AD_____

Award Number: DAMD17-02-1-0230

TITLE: Molecular Imaging for IMRI-Guided Minimally Invasive
Treatment of Prostate Cancer

PRINCIPAL INVESTIGATOR: Baowei Fei, Ph.D.
David L. Wilson, Ph.D.
Jeffrey L. Duerk, Ph.D.
D. Bruce Sodee, M.D.

CONTRACTING ORGANIZATION: Case Western Reserve University
Cleveland, Ohio 44106-7015

REPORT DATE: March 2004

TYPE OF REPORT: Annual Summary

PREPARED FOR: U.S. Army Medical Research and Materiel Command
Fort Detrick, Maryland 21702-5012

DISTRIBUTION STATEMENT: Approved for Public Release;
Distribution Unlimited

The views, opinions and/or findings contained in this report are
those of the author(s) and should not be construed as an official
Department of the Army position, policy or decision unless so
designated by other documentation.

BEST AVAILABLE COPY

20040830 025

REPORT DOCUMENTATION PAGE		Form Approved OMB No. 074-0188

Public reporting burden for this collection of information is estimated to average 1 hour per response, including the time for reviewing instructions, searching existing data sources, gathering and maintaining the data needed, and completing and reviewing this collection of information. Send comments regarding this burden estimate or any other aspect of this collection of information, including suggestions for reducing this burden to Washington Headquarters Services, Directorate for Information Operations and Reports, 1215 Jefferson Davis Highway, Suite 1204, Arlington, VA 22202-4302, and to the Office of Management and Budget, Paperwork Reduction Project (0704-0188), Washington, DC 20503

1. AGENCY USE ONLY (Leave blank)	2. REPORT DATE March 2004	3. REPORT TYPE AND DATES COVERED Annual Summary (25 Feb 03-25 Feb 04)	

4. TITLE AND SUBTITLE Molecular Imaging for IMRI-Guided Minimally Invasive Treatment of Prostate Cancer	5. FUNDING NUMBERS DAMD17-02-1-0230

6. AUTHOR(S)
Baowei Fei, Ph.D.
David L. Wilson, Ph.D.
Jeffrey L. Duerk, Ph.D.
D. Bruce Sodee, M.D.

7. PERFORMING ORGANIZATION NAME(S) AND ADDRESS(ES) Case Western Reserve University Cleveland, Ohio 44106-7015 E-Mail: Baowei.Fei@case.edu	8. PERFORMING ORGANIZATION REPORT NUMBER

9. SPONSORING / MONITORING AGENCY NAME(S) AND ADDRESS(ES) U.S. Army Medical Research and Materiel Command Fort Detrick, Maryland 21702-5012	10. SPONSORING / MONITORING AGENCY REPORT NUMBER

11. SUPPLEMENTARY NOTES

12a. DISTRIBUTION / AVAILABILITY STATEMENT Approved for Public Release; Distribution Unlimited	12b. DISTRIBUTION CODE

13. ABSTRACT (Maximum 200 Words)

Purpose: Our long-range goal is to develop an image-guided, minimally invasive thermal ablation treatment method for the prostate cancer. Before this method can be achieved, significant engineering developments are required.

Scope: Since MRI does not reliably show prostate tumors, we intend to incorporate nuclear medicine images with higher sensitivity for detecting and localizing prostate tumors. We investigated image registration techniques to incorporate other imaging modalities into interventional MRI (iMRI)-guided treatment for improved tumor targeting.

Major Findings: MR imaging techniques were developed for the prostate that could possibly be used for prostate cancer diagnosis and treatment. High resolution MRI and SPECT images were combined and included into interventional MRI-guided procedures such as the applications of thermal ablation treatment for the prostate cancer.

Results and Significance: We created three image registration techniques that could be used to combine high resolution MRI and SPECT images with iMRI images. We demonstrated the feasibility of combining the three modalities for iMRI-guided thermal ablation treatment. With this research, we create a potential minimally invasive treatment method for prostate cancer that requires no radiation, surgery, or hospitalization. We achieved the goals of training and research in the two years.

14. SUBJECT TERMS Localized therapies - Discovery and development (image-guided medical intervention)	15. NUMBER OF PAGES 175
	16. PRICE CODE

17. SECURITY CLASSIFICATION OF REPORT Unclassified	18. SECURITY CLASSIFICATION OF THIS PAGE Unclassified	19. SECURITY CLASSIFICATION OF ABSTRACT Unclassified	20. LIMITATION OF ABSTRACT Unlimited

NSN 7540-01-280-5500

Standard Form 298 (Rev. 2-89)
Prescribed by ANSI Std. Z39-18
298-102

Table of Contents

Annual Summary Report

Award Number: DAMD17-02-1-0230

FY01 Prostate Cancer Research Program (PCRP) Post-Doctoral Traineeship Award
"Molecular Imaging for IMRI-Guided Minimally Invasive Treatment of Prostate Cancer"

Introduction

Our long-term goal is to develop an image-guided, minimally invasive treatment method for prostate cancer. We currently use interventional magnetic resonance imaging (iMRI) to guide biopsy needles for diagnosis and to guide radiofrequency (RF) electrodes for thermal ablation treatment of cancer. We use a low field, open magnet system that allows patient access during imaging. A unique aspect of iMRI-guided thermal ablation therapy is that real time feedback is provided from images of treated regions and from non-invasive three-dimensional (3D) temperature measurements. Before this method can be extended to the prostate, significant engineering developments are required.

Although MRI provides excellent anatomical detail, it does not reliably identify prostate cancer. Fortunately, there are emerging imaging methods that promise to improve detection of prostate tumor. These include nuclear medicine SPECT and MR spectroscopy that promise to help identify prostate tumor. We intend to incorporate this information especially SPECT ProstaScint images into the iMRI-guided paradigm.

Although functional images promise to help identify prostate tumor, they have poor resolution and do not provide the anatomical information required for treatment delivery. The solution is to register and superimpose the functional images with 3D high-resolution MR images. We are investigating method to correlate features from SPECT with high-resolution anatomical MR images to aid identification of prostate cancer. To improve tumor targeting during treatment, the information from the multi-modality will be integrated with freshly acquired iMRI-slice image to guide intervention tools. Accurate registration with anatomy will be necessary for highly accurate, interventional MRI-guided thermal ablations.

Summary Body

As part of my postdoctoral training, I am working with a team of researchers to achieve aims. My specialized role is to develop image registration techniques, but I participated in most, if not all, research aspects of the molecular imaging for iMRI-guided minimally invasive treatment of prostate cancer. [1-11] The following paragraphs outline the training and research associated with the tasks described in the Statement of Work.

As for the Task 1 of image acquisitions, we obtained and analyzed SPECT ProstaScint and high-resolution MR images from patients with verifiable prostate cancer.[12,13] First, we developed methods for SPECT ProstaScint imaging for the prostate cancer.[13-18] Second, we developed high-resolution 3D MR imaging techniques for the prostate.[1-3,7] The imaging techniques are reported in our published papers.[1-3,7] I helped plan image acquisition methods suitable for registration.

As for the Task 2 of image correlation and registration, we have correlated SPECT images with high-resolution MRI volume to improve detection and treatment of prostate cancer.[6,7,13,19,20] First, we created 3D image registration methods suitable for aligning multi-modality volumes to combine anatomic and metabolic information.[6,7,19] We extended our current mutual information methods for robust image registration. Second, we created image software system to visualize and analyze images of the prostate cancer.[1,6,7] Using the visualization software, we compared 3D registered image data using linked cursors and hand-drawn regions-of-interest on side-by-side image frames. From a pair of registered volumes, we applied multi-planar reformatting to visualize registered slices from each of two volumes using multiple types of displays. Statistical analyses were developed to correlate image gray values in ProstaScint and

4

MRI images.[13,17,18] In addition to analysis, we investigated fusion methods for iMRI targeting. These techniques are described in detail in our published papers.[1,6,7] Third, our group compared functional image data with histology of surgically removed prostates.[12,13]

As for the Task 3 of testing the feasibility of iMRI-guided procedure, we have performed simulation experiments,[6] phantom experiments,[6,7] iMRI-guided thermal ablation experiments on dogs and rabbits,[21-23] and simulated clinical experiments using patient data.[6,7] First, we created a robust, accurate and fast registration method for freshly acquired iMRI-slice images and SPECT/MR volume images.[1,3,11] We performed registration experiments at our low field, open magnetic system.[1,3,11] Second, we conducted phantom experiments and evaluated the registration accuracy.[1,6,7] Third, we have performed simulation experiments for the image-guided thermal ablation procedure using patient data.[1,6,7] We have conducted thermal ablation experiments on dogs and rabbits.[21-23]

As for the training, I actively participated in the journal club every week as held in Dr. Wilson's Laboratory. I attended the research seminar once a week in the Biomedical Engineering Department. The Ireland Cancer Center at our institute, a NCI Comprehensive Cancer Center with over 130 scientists and physicians, often has excellent seminars with great training opportunities. I frequently interact with mentors Drs. Wilson, Duerk, and Sodee. I took eight courses in biomedical engineering and computer science at Case Western Reserve University. I had nine international conference presentations during the two years.

Key Research Accomplishments

1. We created a robust image registration method for the combination of high resolution MRI volume and interventional MRI slice.[1,3,8,11] It is significant because it demonstrated feasibility of including other image modalities such as high resolution MRI and SPECT images into iMRI-guided treatment for improved tumor targeting.

2. We created image registration and fusion software that could be used for the iMRI-guided procedures.[6,7] It is important because it could help physician or radiologist better locate and target tumors region and possibly improve treatment.

3. We developed MR imaging techniques for the acquisition of high resolution prostate images.[1-3] Since the imaging techniques well delineates the prostate and its surroundings, they could possibly be used for the prostate cancer screening and other clinical applications.

4. We developed fast imaging techniques for interventional MR imaging of the prostate.[1,3] This is very important because the techniques can acquire prostate images in nearly real-time and thus provide image guidance during interventional procedures.

5. We created image visualization software for image analysis and registration evaluation.[6,7] This byproduct is a very useful image analysis tool with multiple visualization displays. It also allows one to quantitatively measure prostate size, movement, and deformation.

6. We performed more than 1000 slice to volume registration experiments using MR images acquired from patients and volunteers.[1,3,8,11] These experiments simulated and tested a variety of possible conditions in potential applications and thus provide useful information and guidance for future clinical applications.

7. We performed image registration and fusion experiments using SPECT and high resolution MR images from patients with prostate cancer. Registration and fusion of the two modalities could possible improve the diagnosis of prostate tumors.[6,7,19]

8. We conducted a variety of pelvic phantom experiments to test registration accuracy of high resolution MR and SPECT images.[6,7,19] These experiments provided some baseline for accuracy evaluation and simulation.

9. We conducted iMRI-guided thermal ablation experiments on dogs and rabbits.[21-23] The experiments provided some fundamental knowledge for any future human applications.

10. We have applied the volume-to-volume registration technique to vascular images for the potential application in vulnerable plaque classification.[24,25]

11. We have applied our volume-to-volume registration algorithm to micro-PET and high-resolution MR images for the potential application in photodynamic therapy.[26]

12. We have applied our volume-to-volume registration method to small animal images as acquired from micro-CT and SPECT for the application in lung perfusion study.[27]

Reportable Outcomes

1. Our paper entitled "Slice to volume registration and its potential application to interventional MRI guided radiofrequency thermal ablation of prostate cancer"[1] was published in the IEEE Transaction on Medical Imaging, which was the most-cited journal in the biomedical engineering and imaging science & photographic technology categories.[28]

2. One paper entitled "Automatic 3D registration for interventional MRI-guided treatment of prostate cancer"[3] was published in the Computer Aided Surgery, the official journal of the International Society for Computer Aided Surgery (ISCAS).[29]

3. One paper entitled "A comparative study of warping and rigid body registration for the prostate and pelvic MR volumes"[4] was published in the Computerized Medical Imaging and Graphics, the official journal of the Computerized Medical Imaging Society, an international journal on imaging and image-archiving in all medical specialties.[30]

4. One paper entitled "Registration and fusion of SPECT, high resolution MRI, and interventional MRI for thermal ablation of prostate cancer"[7] is published in IEEE Transaction on Nuclear Science.

5. One manuscript entitled "Three-dimensional MR image registration of the prostate and pelvis with semiautomatic warping"[31] was submitted to IEEE Transaction on Medical Imaging in March 2004.

6. Two referred conference papers were published in the Lecture Notes in Computer Science: the proceeding of the Sixth International Conference on Medical Image Computing and Computer Assisted Intervention 2003 [6] and the proceeding of the Second International Workshop on Biomedical Image Registration.[5]

7. Three conference papers were published in the proceedings of International Conference of SPIE on Medical Imaging 2002, 2003, and 2004.[9,10,26]

8. Three conference papers were published in the proceedings of the International Conference of IEEE Engineering in Medicine and Biology 2002 and 2003.[8,24,27]

9. I had five oral presentations and four poster presentations at professional international conferences: The 24th and 25th IEEE Engineering in Medicine and Biology,[8,24,27] The SPIE on Medical Imaging Conferences (2002, 2003, and 2004),[9-11,26] The Sixth International Conference on Medical Image Computing and Computer Assisted Intervention 2003,[6] the Second International Workshop on Biomedical Image Registration,[5] and The 10th Scientific Retreat of the Prostate Cancer Foundation.[26]

10. I wrote two book chapters for the Handbook of Medical Image Analysis: Advanced Segmentation and Registration Models.[32,33]

Conclusions

During the two year of training, we well completed the tasks as outlined in the Statement of Work. We achieved twelve key research accomplishments and ten reportable outcomes. We had seven peer-reviewed referred papers, seven conference proceedings, and nine scientific presentations. We achieved the goals of the training and research.

Reference List

1. B.W.Fei, J.L.Duerk, D.T.Boll, J.S.Lewin, and D.L.Wilson, "Slice to volume registration and its potential application to interventional MRI guided radiofrequency thermal ablation of prostate cancer," *IEEE Transactions on Medical Imaging*, vol. 22, pp. 515-525, 2003.

2. B.W.Fei, A.Wheaton, Z.Lee, J.L.Duerk, and D.L.Wilson, "Automatic MR volume registration and its evaluation for the pelvis and prostate," *Physics in Medicine and Biology*, vol. 47, pp. 823-838, 2002.

3. B.W.Fei, J.L.Duerk, and D.L.Wilson, "Automatic 3D Registration for Interventional MRI-Guided Treatment of Prostate Cancer," *Computer Aided Surgery*, vol. 7, pp. 257-267, 2002.

4. B.W.Fei, C.Kemper, and D.L.Wilson, "A comparative study of warping and rigid body registration for the prostate and pelvic MR volumes," *Computerized Medical Imaging and Graphics*, vol. 27, pp. 267-281, 2003.

5. B.W.Fei, Z.Lee, J.L.Duerk, and D.L.Wilson, "Image Registration for Interventional MRI Guided Procedures: Similarity Measurements, Interpolation Methods, and Applications to the Prostate," *Lecture Notes of Computer Science (LNCS)*, vol. 2717, pp. 321-329, 2003.

6. B.W.Fei, Z.Lee, D.T.Boll, J.L.Duerk, Lewin J.S., and D.L.Wilson, "Image Registration and Fusion for Interventional MRI Guided Thermal Ablation of the Prostate Cancer," *Lecture Notes in Computer Science (LNCS)*, vol. 2879, pp. 364-372, 2003.

7. B.W.Fei, Z.Lee, J.L.Duerk, Lewin J.S., D.B.Sodee, and D.L.Wilson, "Registration and Fusion of SPECT, High Resolution MRI, and interventional MRI for Thermal Ablation of the Prostate Cancer," *IEEE Transactions on Nuclear Science (In Press)*, Feb. 2004.

8. B.W.Fei, D.T.Boll, J.L.Duerk, and D.L.Wilson, "Image Registration For Interventional Mri-Guided Minimally Invasive Treatment Of Prostate Cancer,"The 2nd Joint Meeting of The IEEE Engineering in Medicine and Biology Society and the Biomedical Engineering Society,pp. 1185-1185, 2002.

9. B.W.Fei, Frinkley K., and D.L.Wilson, "Comparison of Different Registration Algorithms for Interventional MRI-guided Treatment of the Prostate Cancer,"proceeding of SPIE on Medical Imaging: Visualization, Image guided procedures, and display,pp. 58-67, 2003.

10. B.W.Fei, C.Kemper, and D.L.Wilson, "Three-dimensional warping registration of the pelvis and prostate,"Proceedings of SPIE Medical Imaging on Image Processing, vol. 4684, pp. 528-537, 2002.

11. B.W.Fei, A.Wheaton, Z.Lee, K.Nagano, J.L.Duerk, and D.L.Wilson, "Robust registration algorithm for interventional MRI guidance for thermal ablation of prostate cancer,"Proceedings of SPIE Medical Imaging on Visualization, Display, and Image-Guided Procedures, vol. 4319, pp. 53-60, 2001.

12. Z.Lee, D.B.Sodee, P.F.Faulhaber, T.L.Lancaster, G.T.MacLennan, and D.L.Wilson, "Comparison of SPECT and PET imaging for prostate cancer with histological correlation," *Journal of Nuclear Medicine*, vol. 42, pp. 1226-1226, 2001.

13. D.B.Sodee, G.T.MacLennan, M.I.Resnick, P.F.Faulhaber, Z.Lee, A.D.Nelson, J.P.Molter, and G.Bakale, "Comparison of CT- or MRI-fused PET-FDG and SPECT-ProstaScint (R) imaging of prostate cancer with the gold standard of histology," *Journal of Nuclear Medicine*, vol. 42, pp. 1222, 2001.

14. D.B.Sodee, R.Conant, M.Chalfant, S.Miron, E.Klein, R.Bahnson, P.Spirnak, B.Carlin, E.M.Bellon, and B.Rogers, "Preliminary imaging results using In-111 labeled CYT-356 (Prostascint(TM)) in the detection of recurrent prostate cancer," *Clinical Nuclear Medicine*, vol. 21, pp. 759-767, 1996.

15. D.B.Sodee, R.J.Ellis, M.A.Samuels, J.P.Spirnak, W.F.Poole, C.Riester, D.M.Martanovic, R.Stonecipher, and E.M.Bellon, "Prostate cancer and prostate bed SPECT imaging with ProstaScint (R): Semiquantitative correlation with prostatic biopsy results," *Prostate*, vol. 37, pp. 140-148, 1998.

16. D.B.Sodee, N.Malguria, A.A.Elgamel, M.J.Troychak, G.P.Murphy, M.J.Blend, R.Conant, P.Spirnak, and J.K.O'Donnell, "Immunodetection of residual recurrent prostatic cancer by In- 111 Capromab Pentedetide imaging in 423 patients," *Journal of Nuclear Medicine*, vol. 40, pp. 1138-1138, 1999.

17. D.B.Sodee, N.Malguria, A.D.Nelson, P.F.Faulhaber, R.J.Ellis, and P.R.Devlin, "Optimization of ProstaScint (R) sensitivity in the diagnosis and staging of prostate cancer," *Journal of Nuclear Medicine*, vol. 41, pp. 456-456, 2000.

18. D.B.Sodee, N.Malguria, P.Faulhaber, M.I.Resnick, J.Albert, and G.Bakale, "Multicenter ProstaScint imaging findings in 2154 patients with prostate cancer," *Urology*, vol. 56, pp. 988-993, 2000.

19. Z.Lee, K.Nagano, J.L.Duerk, D.B.Sodee, and D.L.Wilson, "Automatic registration of MR and SPECT images for treatment planning in prostate cancer," *Academic Radiology*, vol. 10, pp. 673-684, 2003.

20. Z.Lee, D.B.Sodee, J.L.Duerk, A.D.Nelson, and M.S.Berridge, "Automatic registration of SPECT-MRI in the pelvis," *Journal of Nuclear Medicine*, vol. 41, pp. 232, 2000.

21. M.S.Breen, T.L.Lancaster, R.S.Lazebnik, Nour S.G., J.S.Lewin, and D.L.Wilson, "Three Dimensional Method for Comparing in vivo Interventional MR Images of Thermally Ablated Tissue with Tissue Response," *J.Magn.Reson.Imaging*, vol. 18, pp. 90-102, Jun 13, 2003.

22. M.S.Breen, R.S.Lazebnik, J.S.Fitzmaurice, Lewin J.S., and D.L.Wilson, "Radiofrequency Thermal Ablation: Correlation of Hyperacute MR Lesion Images with Tissue Response," *JMRI (Submitted)*, vol. 2003.

23. M.S.Breen, R.S.Lazebnik, and D.L.Wilson, "ThreeDimensional Registration of Medical Image Data with Histological Sections," *Annals of Biomedical Engineering (Submitted)*, vol. 2003.

24. B.W.Fei, S.Zhang, O.Savado, J.Suri, Lewin J.S., and D.L.Wilson, "Three-Dimensional Automatic Volume Registration of Carotid MR Images,"*The 25th Annual International Conference of IEEE Engineering in Medicine and Biology Society*, Cancun, Mexico,pp. 646-648, 2003.

25. B.W.Fei, J.Suri, and D.L.Wilson. Three-Dimensional Automatic Volume Registration of Carotid MR Images. In: *Vascular Plaque Imaging*, eds. J.Suri, D.L.Wilson, and S.Laxminarayan. International Federation for Medical and Biological Engineering (IFMBE), 2004.

26. B.W.Fei, R.Muzic, Z.Lee, C.Flask, R.Morris, J.L.Duerk, and D.L.Wilson, "Registration of micro-PET and high resolution MR images of mice for monitoring photodynamic therapy,"*Proceeding of SPIE on Medical Imaging: Physiology, Function, and Structure from Medical Images,*2004.

27. B.W.Fei, C.Wietholt, A.V.Clough, C.A.Dawson, and D.L.Wilson, "Automatic Registration and Fusion of High Resolution Micro-CT and Lung Perfusion SPECT Images of the Rat,"*The 25th Annual International Conference of IEEE Engineering in Medicine and Biology Society*, Cancun, Mexico,pp. 592-594, 2003.

28. Webpage of IEEE Transaction on Medical Imaging, *http://www.ieee.org/products/citations.html#top*

29. Webpage of Computer Aided Surgery, *http://www.interscience.wiley.com/jpages/1092-9088/*

30. Webpage of Computerized Medical Imaging and Graphics, *http://www.elsevier.com/locate/issn/08956111*

31. D.L.Wilson and B.W.Fei, "Three-dimensional MR image registration of the prostate and pelvis with semiautomatic warping," *IEEE Trans Med Imaging*, vol. (Submitted), 2003.

32. B.W.Fei, J.Suri, and D.L.Wilson. Three-Dimensional Rigid and Non-Rigid Image Registration for the Pelvis and Prostate. In: *Handbook of Medical Image Analysis: Advanced Segmentation and Registration Models*, eds. J.Suri, D.L.Wilson, and S.Laxminarayan. New York: Marcel Dekker, Inc.; 2004.

33. J.Suri, B.W.Fei, and D.L.Wilson. Future of Medical Image Segmentation and Registration. In: *Handbook of Medical Image Analysis: Advanced Segmentation and Registration Models*, eds. J.Suri, D.L.Wilson, and S.Laxminarayan. New York, Marcel Dekker, Inc., 2004.

Appendices

Peer-Review Publications:

1. **BW Fei**, JL Duerk, DT Boll, JS Lewin, DL Wilson, "Slice to volume registration and its potential application to interventional MRI guided radiofrequency thermal ablation of prostate cancer," *IEEE Transactions on Medical Imaging*, Vol. 22, No. 4, pp. 515-525, 2003.

2. **BW Fei**, Z Lee, JL Duerk, JS Lewin, DB Sodee, DL Wilson, "Registration and Fusion of SPECT, High Resolution MRI, and interventional MRI for Thermal Ablation of the Prostate Cancer," *IEEE Transactions on Nuclear Science*, Feb. 2004.

3. **BW Fei**, Z Lee, JL Duerk, DL Wilson, "Image Registration for Interventional MRI Guided Procedures: Similarity Measurements, Interpolation Methods, and Applications to the Prostate," *Lecture Notes in Computer Science (LNCS)* Vol. 2717, pp. 321-329, 2003.

4. **BW Fei**, Z Lee, DT Boll, JL Duerk, JS Lewin, DL Wilson, "Image Registration and Fusion for Interventional MRI Guided Thermal Ablation of the Prostate Cancer," *Lecture Notes in Computer Science (LNCS)*, Vol. 2879, pp. 364-372, 2003.

5. **BW Fei**, C Kemper, DL Wilson, "A comparative study of warping and rigid body registration for the prostate and pelvic MR volumes," *Computerized Medical Imaging and Graphics*, Vol.27, pp. 267-281, 2003

6. **BW Fei**, JL Duerk, DL Wilson, "Automatic 3d registration for interventional MRI-guided treatment of prostate cancer," *Computer Aided Surgery*, Vol. 7, No.5, pp. 257-267, 2002.

7. **BW Fei**, A Wheaton, Z Lee, JL Duerk, DL Wilson, "Automatic MR volume registration and its evaluation for the pelvis and prostate," *Physics in Medicine and Biology*, Vol. 47, pp. 823-838, 2002.

8. DL Wilson, **BW Fei**, "Three-dimensional semiautomatic warping registration of the prostate and pelvis," *IEEE Transactions on Medical Imaging*, (Submitted).

International Conference Proceedings:

1. **BW Fei**, RF Muzic, Z Lee, CA Flask JL Duerk, N Oleinick, DL Wilson, "Registration of micro-PET and high resolution MR images of mice for monitoring photodynamic therapy," *Proceeding of SPIE on Medical Imaging: Physiology, Function, and Structure from Medical Images*, San Diego, CA, 14-19 February 2004.

2. **BW Fei**, SX Zhang, O Savado, J Suri, JS Lewin, DL Wilson, "Three-Dimensional Automatic Volume Registration of Carotid MR Images," *The 25th Annual International Conference of IEEE Engineering in Medicine and Biology Society*, Cancun, Mexico, Sep. 17-21, 2003.

3. **BW Fei**, C Wietholt, AV Clough, CA Dawson, DL Wilson, "Automatic Registration and Fusion of High Resolution Micro-CT and Lung Perfusion SPECT Images of the Rat," *The 25th Annual International Conference of IEEE Engineering in Medicine and Biology Society*, Cancun, Mexico, Sep. 17-21, 2003.

4. **BW Fei**, K Frinkley, DL Wilson, "Comparison of different registration algorithms for interventional MRI-guided treatment of the prostate" *Proceeding of SPIE on Medical Imaging: Visualization, Image Guided Procedures, and Display*, San Diego, CA, 15-20 February 2003.

9

5. **BW Fei**, DT Boll, JL Duerk, DL Wilson, "Image registration for interventional MRI-guided minimally invasive treatment of prostate cancer," *Proceeding of the 2nd Joint International Conference of IEEE Engineering in Medicine and Biology Society and the Biomedical Engineering Society,* pp. 1185, Huston, TX, October 23-26, 2002.

6. **BW Fei**, C Kemper, DL Wilson, "Three dimensional warping image registration of the pelvis and prostate," *Proceeding of SPIE Medical Imaging on Image Processing,* pp. 528-537,San Diego, CA, 17-22 Feb. 2002.

7. **BW Fei**, A Wheaton, K Nagano, Z Lee, JL Duerk, DL Wilson, "Robust registration algorithm for interventional MRI guidance for thermal ablation of prostate cancer," *Proceedings of SPIE Medical Imaging: Visualization, Display, and Image-Guided Procedures,* Vol. 4319, pp. 53-60, San Diego, CA, 17-22 February 2001.

Slice-to-Volume Registration and its Potential Application to Interventional MRI-Guided Radio-Frequency Thermal Ablation of Prostate Cancer

Baowei Fei, Jeffrey L. Duerk, *Member, IEEE*, Daniel T. Boll, Jonathan S. Lewin, and David L. Wilson*, *Member, IEEE*

Abstract—In this study, we registered live-time interventional magnetic resonance imaging (iMRI) slices with a previously obtained high-resolution MRI volume that in turn can be registered with a variety of functional images, e.g., PET, SPECT, for tumor targeting. We created and evaluated a slice-to-volume (SV) registration algorithm with special features for its potential use in iMRI-guided radio-frequency (RF) thermal ablation of prostate cancer. The algorithm features included a multiresolution approach, two similarity measures, and automatic restarting to avoid local minima. Imaging experiments were performed on volunteers using a conventional 1.5-T MR scanner and a clinical 0.2-T C-arm iMRI system under realistic conditions. Both high-resolution MR volumes and actual iMRI image slices were acquired from the same volunteers. Actual and simulated iMRI images were used to test the dependence of SV registration on image noise, receive coil inhomogeneity, and RF needle artifacts. To quantitatively assess registration, we calculated the mean voxel displacement over a volume of interest between SV registration and volume-to-volume registration, which was previously shown to be quite accurate. More than 800 registration experiments were performed. For transverse image slices covering the prostate, the SV registration algorithm was 100% successful with an error of <2 mm, and the average and standard deviation was only 0.4 mm ± 0.2 mm. Visualizations such as combined sector display and contour overlay showed excellent registration of the prostate and other organs throughout the pelvis. Error was greater when

an image slice was obtained at other orientations and positions, mostly because of inconsistent image content such as that from variable rectal and bladder filling. These preliminary experiments indicate that MR SV registration is sufficiently accurate to aid image-guided therapy.

Index Terms—Image registration, interventional magnetic resonance imaging (iMRI), minimally invasive treatment, mutual information, prostate cancer, thermal ablation.

I. INTRODUCTION

WE USE AN interventional magnetic resonance imaging (iMRI) system to guide minimally invasive treatments, including the radio-frequency (RF) thermal ablation of abdominal cancers [1]–[3]. The iMRI system consists of a 0.2-T clinical C-arm open MRI scanner, an in-room RF-shielded liquid crystal monitor, an MR compatible mouse, a foot pedal, and an RF device. We are currently investigating the extension of these techniques to the treatment of prostate cancer. Since MRI does not reliably show prostate tumors, we intend to incorporate nuclear medicine or MR spectroscopy images with higher sensitivity for detecting and localizing prostate tumors [4], [5]. We will first register the low-resolution functional images with a high-resolution MRI volume [6], [7]. Then, by registering the high-resolution MR volume with live-time iMRI acquisitions, we can, in turn, map the functional data and high-resolution anatomic information to live-time iMRI images for improved tumor targeting. As discussed later, since live-time iMRI is used for device guidance, the accuracy requirements for registering these supplemental images might be less strict than required in some other applications.

We previously described a rigid-body volume-to-volume (VV) registration method for the pelvic and prostate MR images that was accurate when images were acquired under similar conditions [8]. We used bony landmarks and three-dimensional (3-D) centroids of segmented prostates to evaluate VV registration. For volume pairs acquired over a short time span from a supine subject with legs flat on the table, registration accuracy of both the prostate centroid (typically <1 mm) and bony landmarks (average 1.6 mm) was on the order of a voxel ($\approx$1.4 mm). The centroid error was slightly smaller because the prostate was at the volume center and rotation errors had less effect on it. The localization error in finding 3-D points from bony landmarks is probably greater than that

of finding centroids of relatively large prostate volumes where segmentation errors average out. We obtained somewhat larger prostate registration errors of about 3.0 mm when volume pairs were obtained under very different conditions that would be avoided in patient studies, e.g., legs flat and legs raised.

In this study, we are investigating methods to register live-time iMRI image slices with a previously obtained high-resolution MRI volume. We call this slice-to-volume (SV) registration. Because of our success with VV prostate registration, we can determine SV accuracy by comparing results to VV registration for volume pairs having low VV registration error.

The application of SV registration to iMRI-guided treatment of prostate cancer raises several challenges. First, a single slice, or a few slices, provides much less information than an entire volume for voxel-based matching. Second, iMRI images often have lower signal-to-noise ratio (SNR) than diagnostic MR images because of the emphasis on fast imaging and because of the typically lower field strength of open iMRI magnets. Third, the normal prostate is a small organ; when healthy, it measures only $\approx$3.8 cm in its widest dimension [9]. The small prostate is located below the much larger bladder that can change its shape and size during imaging. Fourth, the nonhomogenous receive coil response can change from one imaging session to the next. Finally, times for registration and algorithm robustness are of particular concern for this application to treatment.

Previously reported methods for SV registration were mainly applied to the brain for applications of functional MRI [10], postmortem pathology studies [11], and anatomical modeling [12]. There are no reports of SV registration for abdominal organs or iMRI guidance. Voxel-based methods, particularly those based upon mutual information (MI), are robust, require no segmentation that can be prone to error, are suitable for multimodality registration, and are highly accurate for many applications [3], [8], [10], [13]–[15]. However, the MI method has the problem of interpolation artifacts, which can be especially serious in the case of downsampling in a multiresolution approach [16]. Other similarity measures such as the correlation coefficient (CC) can reduce the presence of local minima [17].

In this paper, we first describe a voxel-based registration algorithm with special features for this important new application. Later, we describe the details of imaging experiments on a conventional MR scanner and a clinical iMRI system. Actual and simulated iMRI images are used to test the registration algorithm. Results of SV and VV registration are compared. In this study, we have performed more than 800 registration experiments.

II. REGISTRATION ALGORITHM

A. Similarity Measurements

We used two similarity measures—mutual information and correlation coefficient—in our registration. Suppose one image R is the *reference*, and the other F is *floating*. Their mutual information $\mathrm{MI}(R, F)$ is given as follows [18]:

$$\mathrm{MI}(R, F) = \sum_{r,f} p_{\mathrm{RF}}(r, f) \log \frac{p_{\mathrm{RF}}(r, f)}{p_R(r) \cdot p_F(f)}.$$

The joint probability $p_{\mathrm{RF}}(r, f)$ and the marginal probabilities $p_R(r)$ of the reference image and $p_F(f)$ of the floating image can be estimated from the normalized joint intensity histogram. The correlation coefficient $\mathrm{CC}(R, F)$ is given as follows [19]:

$$\mathrm{CC}(R, F) = \frac{\sum \left(R(r) - \overline{R}(r)\right) \left(F(f) - \overline{F}(f)\right)}{\sqrt{\sum \left(R(r) - \overline{R}(r)\right)^2 \sum \left(F(f) - \overline{F}(f)\right)^2}}.$$

Here $\overline{R}(r)$, $\overline{F}(f)$ denote the average intensities of the reference and floating images and the summation includes all voxels within the overlap of both images.

We compared the two similarity measures at different resolutions in order to determine their suitability for SV registration. At *1/4 resolution*, we resampled images so as to give 1/4 number of the voxels along each linear dimension. At *full resolution*, we used the full number of voxels. In Figs. 1 and 2, we plot the two similarity measures as a function of two translation parameters. After two typical high-resolution MR volumes were registered [8], values were plotted with the origin as the optimal transformation. We calculated CC and MI values while moving the simulated iMRI image relative to the high-resolution MR image along coronal (anterior–posterior) and sagittal (left–right) axes. The simulated iMRI image was obtained as described in Section III.

Features of MI and CC demonstrate their suitability at high and low resolutions, respectively. At 1/4 resolution, CC surfaces are much smoother than MI, which is noisy and contains many local maxima as shown in Fig. 1(a) and (c). In fact, there is a false global maximum at +25 voxels. At full resolution, Fig. 2(a) and (c) shows that MI has a much sharper peak than CC, but once again there is high-frequency noise in the MI curves, far from the optimum, that gives rise to local maxima that must be avoided. From these figures, we infer that CC is better at low resolution and MI is better at full resolution, when one is close to the optimum value. As described next, our registration algorithm makes use of these features.

B. Registration Algorithm with Special Features

The algorithm includes special features to improve robustness for registration of MR prostate images. Suppose the iMRI image slice is the *reference slice*, the matching slice extracted from the high-resolution MRI volume is the *reformatted slice*, and the final reformatted slice is the *registered slice*. We use a multiresolution approach and perform registration from low to high resolution. We use CC at the two lower resolutions because it gives fewer local maxima and because it can be calculated faster than MI. We use MI at full resolution because of its peaked surface. To avoid local maxima, we include a restarting feature where registration is restarted with randomly perturbed parameters obtained from a uniform distribution about the initial transformation values at the current resolution being used. The algorithm restarts until the absolute CC is above a threshold of 0.5 as determined later or the maximum number of restarts is reached. Absolute CC is used rather than MI because it has a well-defined range between 0 and 1 and because it provides an independent check of the MI result at the highest resolution.

We record all important results following an optimization cycle including the CC and/or MI values and the transforma-

MI   CC

(a)   (b)
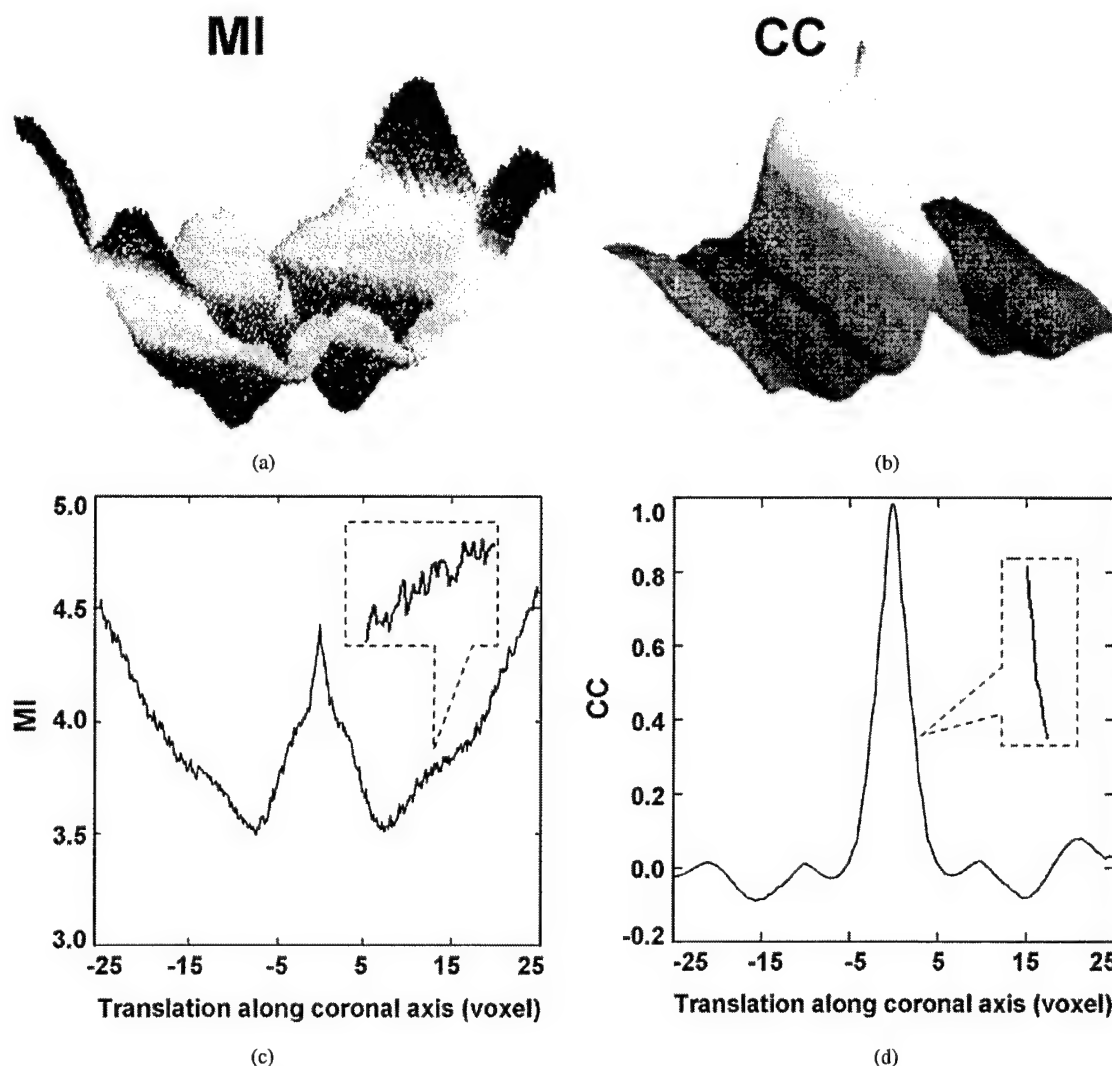

(c)   (d)

Fig. 1.   Similarity functions are plotted as a function of translations at the lowest resolution in the multiresolution registration process. Two high-resolution MRI volumes were registered. From the optimal parameters, we computed the similarity of the simulated iMRI and MRI images as a function of translations along the coronal (anterior–posterior) and sagittal (left–right) axes. MI is plotted in (a) and (c); CC is plotted in (b) and (d). Graphs (a) and (b) are 3-D plots for translations along the coronal and sagittal axis. Graphs (c) and (d) are 2-D plots for translations about the coronal axis. The small insets in (c) and (d) are magnified curves showing noise having local maxima in (c). A false global maximum for MI occurred at +25 voxels. Images are from volunteer S2, and they are downsampled by 1/4 along each linear dimension, giving a distance between voxel centers of ≈ 5.5 mm.

tion parameters. At the end of processing at a lower resolution, we always select the transformation parameters having the maximum CC value. We then scale the translation parameters appropriately and assign the new parameters to be initial values at the next higher resolution. At the highest resolution, MI instead of CC is the similarity measure, and we select the final transformation parameters to be those having the maximum MI value.

C. Additional Details

Additional algorithm details are now described. For registration, we use rigid-body transformation (three translations and three rotations) and trilinear interpolation. For optimization, we use the downhill simplex method of Nelder and Mead [20] or the Powell method [21]. Optimization of similarity ends either when the maximum number of calculations is reached (typically 500) or the fractional change in the similarity function is smaller than a tolerance (typically 0.001). The input MRI volume is a 3-D MR acquisition giving $256 \times 256 \times 128$ nearly isotropic

voxels over a field of view covering the whole pelvis. We create isotropic voxels of about 1.4 mm on a side using 3-D linear interpolation. We use IDL (Interactive Data Language, Research Systems Inc., Boulder, CO) as the programming language.

Typical parameter values are now described. We use an initial guess assuming an identity transformation, i.e., all initial translation and rotation parameters are zero, because the patient is normally oriented approximately the same way from one scan to the next. We set the maximum numbers of restarts at 10, 5, and 3, from low to high resolution, respectively.

III. EXPERIMENTAL METHODS

A. Image Acquisition

High-resolution MRI volumes were acquired using a 1.5-T Siemens MRI system (Magnetom Symphony, Siemens Medical Systems, Erlangen, Germany). An eight-element phased array body coil was used to ensure coverage of the prostate with a
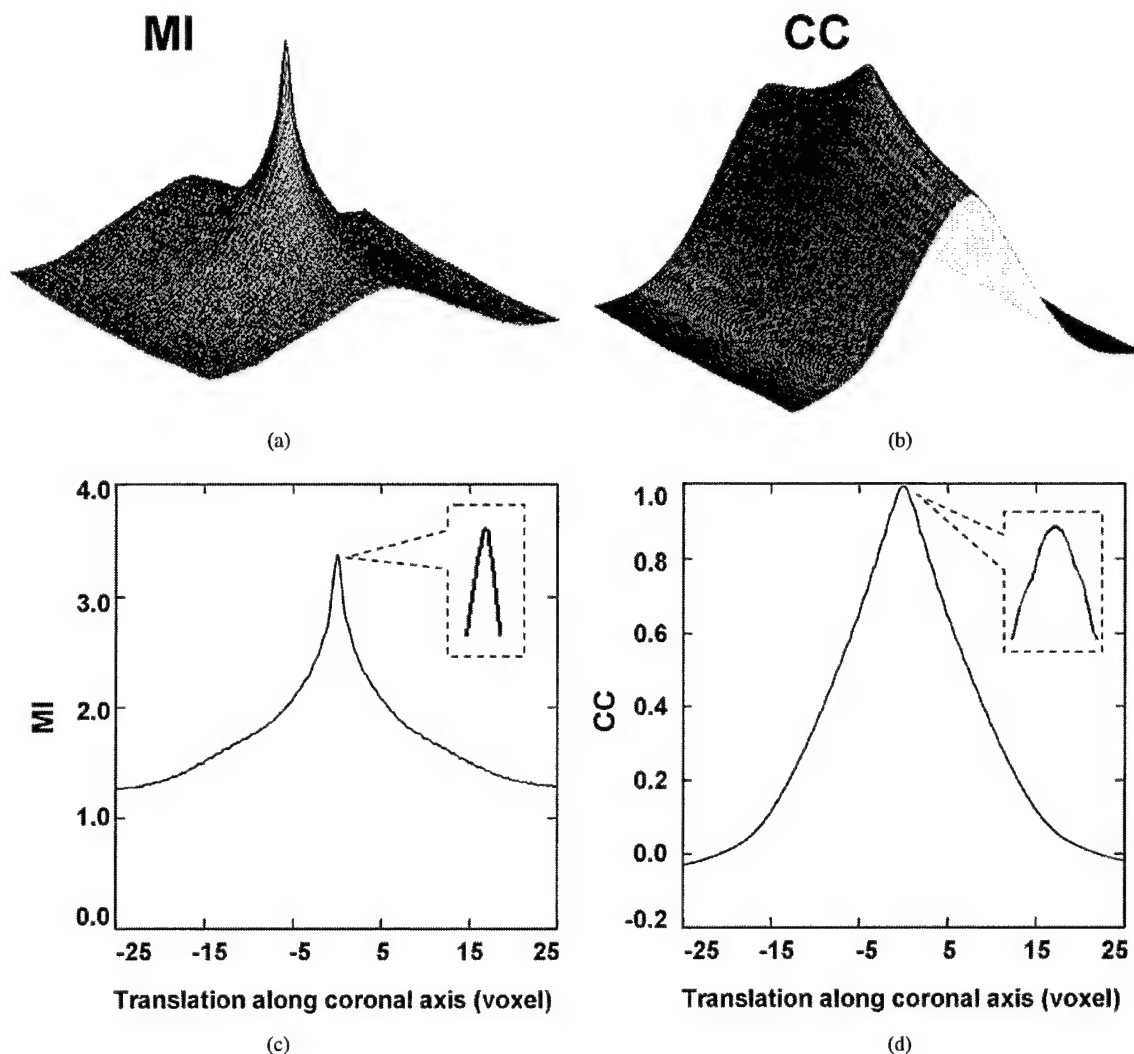
Fig. 2.   Similarity functions are plotted as a function of translations at full resolution. Many details are given in the legend of Fig. 1. Again, MI is plotted in (a) and (c); CC is plotted in (b) and (d). MI in (a) and (c) has a much sharper peak than CC in (b) and (d). The voxel is isotropic with 1.4 mm on a side. Image data are the same used in Fig. 1.

uniform sensitivity. Typically, two anterior and two posterior elements were enabled for signal acquisition. We used two different MR sequences. First, we used a 3-D RF spoiled gradient echo steady-state pulse sequence (FLASH) with TR/TE/flip parameters of 12/5.0/60, which give $256 \times 256 \times 128$ voxels over a $330 \times 330 \times 256$-mm field of view (FOV) to yield $1.3 \times 1.3 \times 2.0$-mm voxels oriented to give the highest resolution for transverse slices. The acquisition time is 5 min and 38 s. This sequence is good for pelvic imaging, but is not ideal for the prostate. It was used to acquire volumes for volunteer S1. Second, we used a 3-D rapid gradient echo sequence (PSIF) designed to acquire the spin-echo component of the steady-state response, rather than the free induction decay. The spin echo component forms immediately prior to the RF pulse; it is shifted toward the prior RF pulse through appropriate gradient waveform design. The sequence with 9.4/5.0/60 (TR/TE/flip) yields $160 \times 256 \times 128$ voxels over a $219 \times 350 \times 192$-mm rectangular FOV and $1.4 \times 1.4 \times 1.5$-mm voxels oriented to give the highest resolution for transverse slices. There is over sampling at 31% in the slice direction to reduce aliasing artifacts. The acquisition time is 4 min and 15 s. This sequence

gave excellent image contrast for the prostate and its surroundings. It was used to acquire volumes for volunteers S2–S4.

We also acquired iMRI images from the same volunteers using a clinical 0.2-T C-arm open MR scanner (Siemens Open Symphony, Erlangen, Germany) modified for interventional MRI procedures and in this paper referred to as the iMRI system. We used a 3-D PSIF with 25/13/60 (TR/TE/FA) for image volume acquisitions and two-dimensional (2-D) PSIF with 15.2/7.4/45 (TR/TE/FA) for image slice acquisitions. The iMRI volumes were $256 \times 256 \times 100$ with voxel size of $1.3 \times 1.3 \times 1.4$ mm. The iMRI slices were 128×128 with in-plane pixel size of 2.8×2.8 mm and with effective slice thickness of 5 mm. We acquired iMRI images from volunteers S1–S3.

B. Simulation of iMRI Image Slices

In experiments, we used high-resolution MRI volumes to simulate iMRI image slices, which are thicker, noisier, and degraded by receive coil inhomogeneity. Clinically, we typically use an iMRI slice thickness of 4.0–6.0 mm. We used trilinear interpolation to create isotropic high-resolution MRI volumes
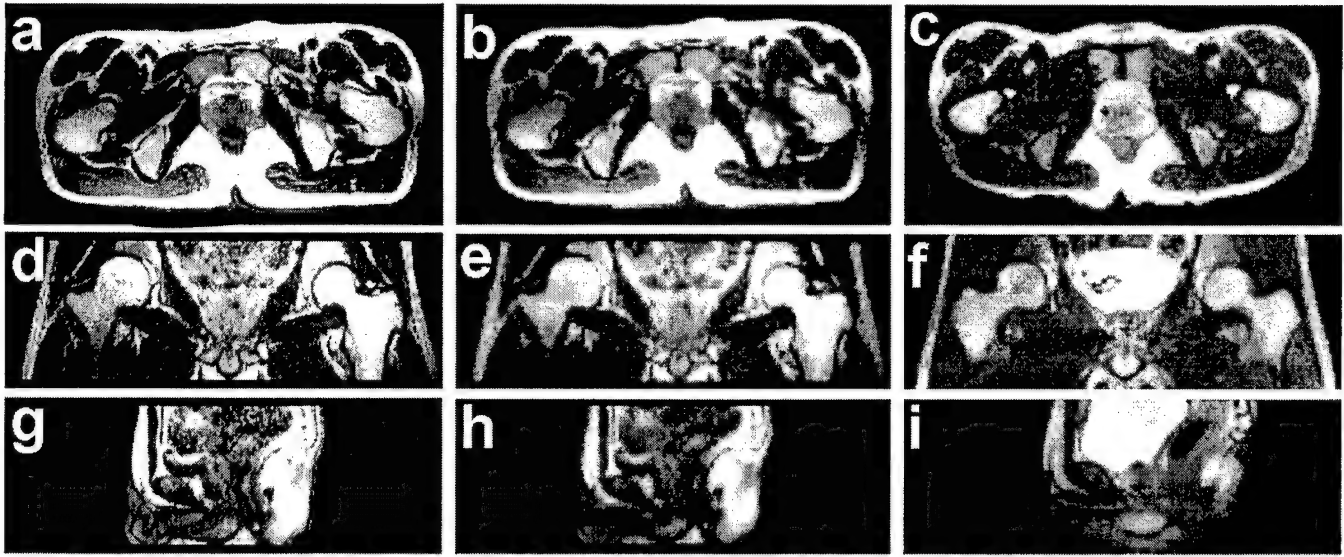
Fig. 3. High-resolution MR images, simulated and actual iMRI image slices. Images on the left column, (a), (d), and (g), are the original high-resolution MR images from the 1.5-T scanner in the transverse, coronal, and sagittal planes, respectively. Images in the middle column are the corresponding, simulated thick iMRI images with noise added to give $SNR = 15$ and with sensitivity fall off from a belt coil. Images on the right panel are actual iMRI slices (0.2-T scanner) from similar spatial locations. The actual iMRI slices seem blurred because of nearly doubled pixel size. Images are from volunteer S2.

with voxel size of $1.4 \times 1.4 \times 1.4$ mm. From the isotropic high-resolution MRI volume, we averaged three 1.4-mm adjacent thin slices to create a 4.2-mm-thick slice. MR noise in a magnitude is described by the Rician distribution [22]. At SNR values of greater than approximately five, the noise can be approximated as being Gaussian white noise [23]. We measured typical signal and noise values on our iMRI system using a homogenous phantom, and volunteer images in the region of the prostate with methods described elsewhere [24], [25]. In all cases, image SNR was greater than 10 in all tissues including the prostate. With this justification, we added Gaussian noise to the simulated iMRI image slices either to match the measured SNR or to give much greater noise to further stress registration. We report noise experiments using the SNR of the simulated image slices. Fig. 3 shows high-resolution MR images as well as simulated and actual iMRI image slices.

We simulated receive coil inhomogeneity from a belt coil used in our clinical iMRI acquisitions. The coil is modeled as a solenoid with parameters shown in Fig. 4. Coil parameters are a, the radius of the coil; $2g$, the length of the coil; I, the current; μ_0, the permeability of free space; n, the turns; and the z axis, the axis along the center line of the coil. The magnetic field in the xy plane can be approximated as [26]

$$(B_1)_{xy} = \frac{\mu_0 n}{2} \frac{I}{[a^2 + g^2]^{1/2}}. \tag{1}$$

The z component of the field is given by [27]

$$(B_1)_z = \frac{\mu_0 n I}{2g} (\cos \alpha_1 + \cos \alpha_2) \tag{2}$$

where the definition of the angles α_1 and α_2 are given in Fig. 4. The magnetic field is highest at the coil center and falls off along the axial direction. According to the Biot–Savart law [28], this model also accounts for the spatial sensitivity of the coil to MR
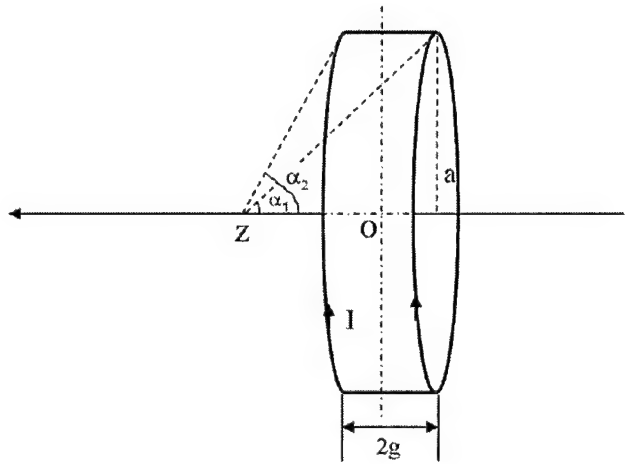

Fig. 4. Geometry of solenoidal receive coil. Model parameters are defined in the figure. The axial line is along the cranial–caudal direction of the patient.

signal sources. Fig. 5 shows a coronal image with simulated inhomogeneity along the axis (head–foot) direction.

Because a needle will often be present during an iMRI intervention, we tested the effect of simulated needles on registration. We used artifact sizes from a previous report on the effects of pulse sequence design and magnetic field orientation on needle artifacts in MR-guided biopsy and aspiration [29]. Fig. 6 shows sagittal images with and without a simulated needle artifact. The simulated artifacts in Fig. 6(b) appeared as straight noisy bars 2 mm in width.

C. Imaging Experiments

1) Imaging Experiments for High-Resolution MR Volumes: When acquiring high-resolution MR volumes, volunteers laid supine in a manner similar to the *diagnostic position* in routine MR scanning. Between volume acquisitions, volunteers got up from the MR table, stretched, and walked
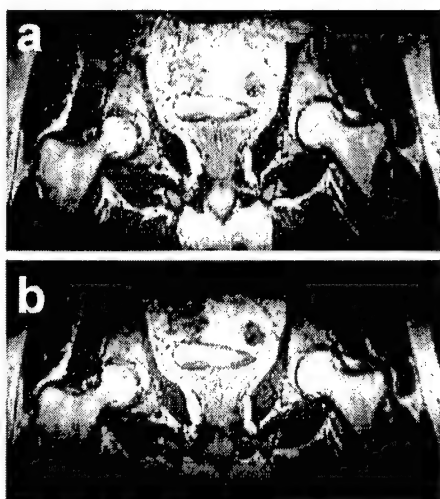
Fig. 5. Simulated signal changes due to receive coil inhomogeneity. The original image (a) is acquired using a phased array coil on a conventional 1.5-T MRI system. Using a belt coil model with a diameter of 350 mm and a width of 50 mm, the simulated iMRI image is shown in (b). The image intensity is highest at the center and decreases along the axial direction.
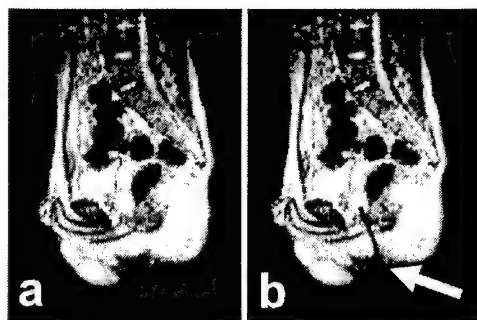

Fig. 6. Synthetic image with simulated needle artifact. Image (a) is the sagittal slice acquired from the 0.2 T iMRI system without a needle artifact. Image (b) is obtained from image (a) with a simulated needle artifact (white arrow) for an RF needle probe inserted into the prostate. Images are from volunteer S3.

around to ensure that they would assume a different position when they laid back on the table. Before the last of three volume acquisitions, the volunteer voided to create an *empty bladder*. The coil array was centered on the prostate. All images of the same volunteer were acquired with the same MRI acquisition parameters. In total, there are 12 volumes, three for each of volunteers S1–S4.

2) Imaging Experiments on iMRI System: We acquired iMRI images under the conditions simulating the treatment application. The volunteer was supine, and his legs were supported at 30°–60° relative to the horizon and separated in a "V" with an angle of 60°–90° between two legs. This is similar to the lithotomy position used in prostate therapies, and it should provide access for needle insertion in brachytherapy or RF thermal ablation. We call this the *treatment position*. Before experiments, the volunteer voided their bladder. For each volunteer, all images were obtained within a 2-h session. Between image acquisitions, volunteers moved to ensure a different position. For each of the volunteers S1–S3, we acquired three volumes and 50 iMRI image slices covering the prostate. They included 30 transverse, ten coronal, and ten sagittal image slices. We call these images "*actual*" iMRI

images to differentiate them from previous experiments using "*simulated*" iMRI slices.

D. Registration Experiments

1) Registration Experiments Using Simulated iMRI Images: We used 12 pairs of high-resolution MR volumes to perform registration experiments. For each volume pair, we extracted data from one volume to simulate thick iMRI image slices; and then we registered the simulated image slices to the other volume. We desire an iMRI slice image acquisition method that gives robust, accurate registrations and is relatively insensitive to acquisition parameters. Hence, we performed experiments to determine the dependence on slice orientation (transverse, sagittal, and coronal), on slice position relative to the prostate (above, centered, and below), on image noise from fast imaging techniques, and on the inhomogeneous sensitivity response from a belt coil.

2) Registration Experiments Using Actual iMRI Image Slices: We also performed two types of SV registration experiments using the actual iMRI images. First, we registered actual iMRI image slices with high-resolution (1.5-T system) MR volumes and visually evaluated results. For each volunteer S1–S3, there were three high-resolution MR volumes and 50 iMRI image slices giving 150 SV registration experiments, and a total of 450 experiments. Second, we registered thick slices simulated from the volume of image data obtained on the iMRI scanner with the corresponding high-resolution (1.5-T scanner) MR volume. In this case, we compared results to VV registration obtained by registering the volume from the iMRI system with the high-resolution volume (1.5-T scanner). We investigated the effect of iMRI slice thickness by averaging 1–10 contiguous image slices to create a thick slice and registering it to the high-resolution volume. The original actual iMRI volumes have a slice thickness of 1.4 mm and in-slice dimensions of 1.3×1.3 mm. We used trilinear interpolation to create isotropic actual iMRI volumes with voxel size of $1.3 \times 1.3 \times 1.3$ mm. Thus, thick slices simulated from actual iMRI volumes are 1.3 to 13 mm.

E. Registration Evaluation

1) Visual Inspection: We evaluated registration experiments by visual inspection. We used *RegViz*, a program created in IDL in our laboratory with multiple visualization and analysis methods. First, we manually segmented prostate boundaries in image slices and copied them to corresponding slices. This enabled visual determination of the overlap of prostate boundaries over the entire volume. Second, color overlay displays were used to evaluate overlap of structures. One image was rendered in gray and the other in the "hot-iron" color scheme available in IDL. To visualize potential differences, it was quite useful to interactively change the contribution of each image using the transparency scale. Third, we used a sector display, which divided the reference and registered images into rectangular sectors and created an output image by alternating sectors from the two input images. Even subtle shifts of edges would be clearly seen.

2) Volume-to-Volume Registration Standard: Our standard evaluation method was to compare SV and VV registration.

The VV registration accuracy was previously evaluated [8]. For volume pairs acquired over a short time span from a supine subject with legs flat on the table, prostates were well aligned and prostate centroid displacements were typically <1 mm. The registration accuracy as determined from displacements of pelvic bony landmarks was 1.6 mm ± 0.2 mm. This error might be overestimated because it includes the uncertainty of locating the bony landmarks. From our success with VV prostate registration, we decided that we could obtain SV accuracy by comparing to VV registration for those volume pairs having low VV registration error.

To compare SV and VV registration results, we defined a rectangular volume of interest (VOI) just covering the prostate over which to calculate registration error. To voxels within the VOI, we applied the transformations obtained by the VV and by SV registrations. We then calculated the 3-D displacements between the transformed voxels. The mean voxel distance over the VOI was used as our metric of SV registration error. For evaluation of algorithm robustness, we defined the SV registration as being *successful* when the mean 3-D displacement was less than 2.0 mm.

IV. RESULTS

A. Experiments with Simulated iMRI Images from the 1.5-T System

As described in Section III, we obtained relatively low-noise high-resolution MR images and simulated SV registration results. These datasets allowed us to test effects of noise and receive coil inhomogeneity in a controlled fashion. And, because we had substantial previous experience showing the accuracy of VV registration under comparable conditions, we could easily determine SV error by comparing results to VV registration.

In Fig. 7, the sector display shows a simulated image slice registered with a high-resolution image volume. The simulated image slice was obtained at a transverse orientation near the center of the prostate. The sector display shows close alignment at this position. Other transverse images were also well aligned, indicating that the registration was successful in three dimensions.

We determined SV registration results for slices near the prostate in the three standard orthogonal orientations. Compared with VV, mean and standard deviation registration errors across 12 volume pairs and 60 SV registration experiments were 0.4 mm ± 0.2 mm, 0.5 mm ± 0.2 mm, and 2.6 mm ± 1.6 mm for transverse, coronal, and sagittal slices covering the prostate, respectively. Transverse slices worked best because they contain many relatively rigid anatomical structures (see Fig. 3). We further found that transverse slices centered on the prostate produced better results than those above or below the prostate. Image slices above included the deformable bladder that could give an inconsistent structure from one volume to the next. Image slices below the prostate mainly contained muscle and fatty regions from the hips that could deform, again giving inconsistent image data. Coronal slices worked next best. Sagittal slices gave the largest error because they contained a large portion of the deformable bladder and rectum.
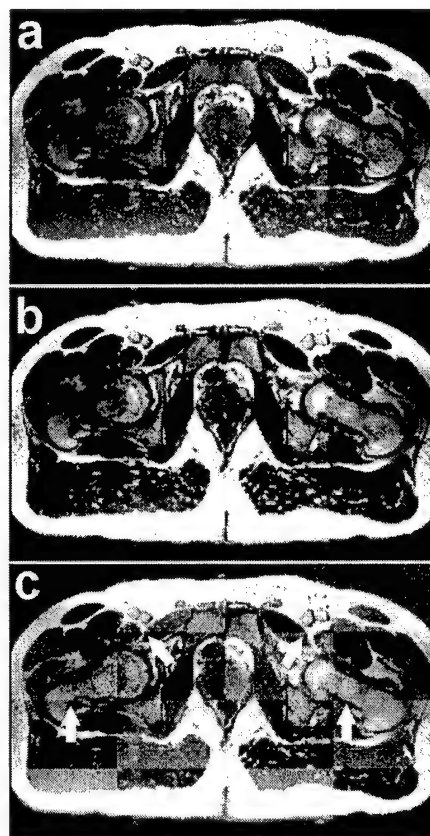

Fig. 7. Sector display showing quality of SV registration. Transverse slices are shown for (a) simulated iMRI and (b) high-resolution MRI images. In the sector display (c), a checker board pattern is created where image sections from (a) and (b) are alternated. Square sections from (a) are made brighter in order to show the boundaries. As indicated by the arrows, the boundaries of bones and other structures are continuous across the sections indicating excellent registration. The prostate registered very well. Images are acquired from volunteer S4.

Simulation experiments showed SV registration to be very insensitive to noise. We performed over 150 registration experiments with noise added to give SNRs ranging from 20 to 5. Using the slice configurations recommended above (transverse slices near the prostate center), we obtained 100% successful registrations (an error <2.0 mm) for SNRs ≥10, a value much worse than the clinical SNR value of ≈25 on our iMRI system.

Receive coil inhomogeneity also had little effect on registration. Registration again was 100% successful for all volume pairs under all receive coil configurations, even when the coil for the slice acquisition was displaced up to 200 mm toward the head from the prostate center, the position of the coil for the volume acquisition.

B. Experiments with Actual iMRI Images

Fig. 8 shows results for an SV registration of actual iMRI image slices with a high-resolution MR volume. The contours overlap and overlay images show that the prostate matches very well. Other visual inspection techniques also demonstrate excellent registration. Note that a single iMRI image was used to produce this registration result.

Fig. 9 shows SV registration error as a function of slice thickness. As described previously, we first registered each volume from the iMRI scanner with the corresponding high-resolution
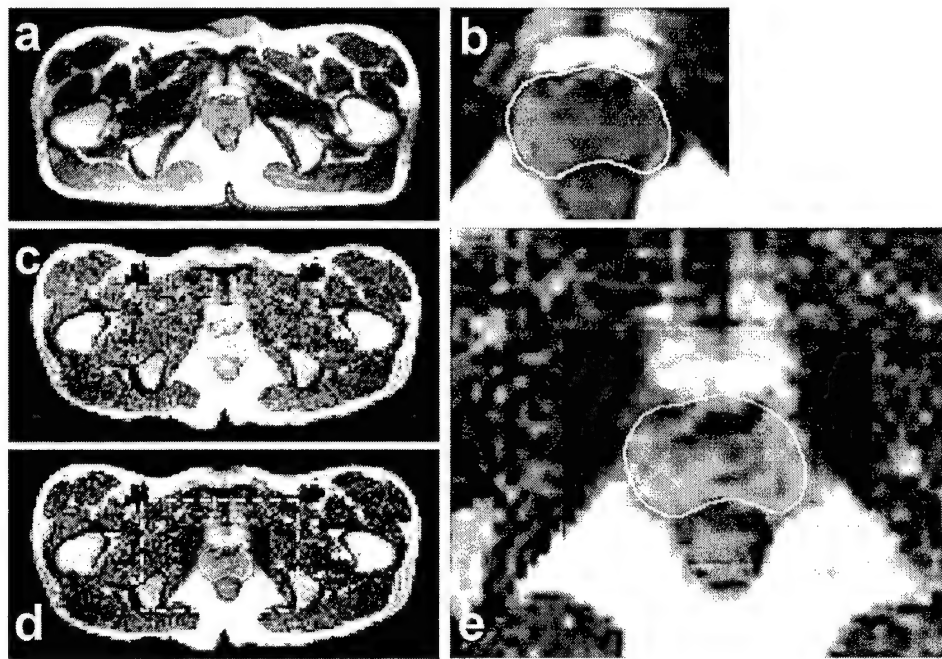
Fig. 8. Images after SV registration of actual iMRI slices from a 0.2-T open MR system. Image (a) is a transverse slice from a high-resolution MR volume (1.5-T scanner). The prostate is segmented and magnified in image (b). Image (c) is the actual iMRI slice (0.2-T scanner). Images (c) and (b) are displayed together in an overlay in image (d), and the white rectangular region is magnified in image (e). The segmented prostate boundary from the high-resolution MR image is copied to the actual iMRI image where it closely matches the prostate in the actual iMRI image slice indicating excellent registration.
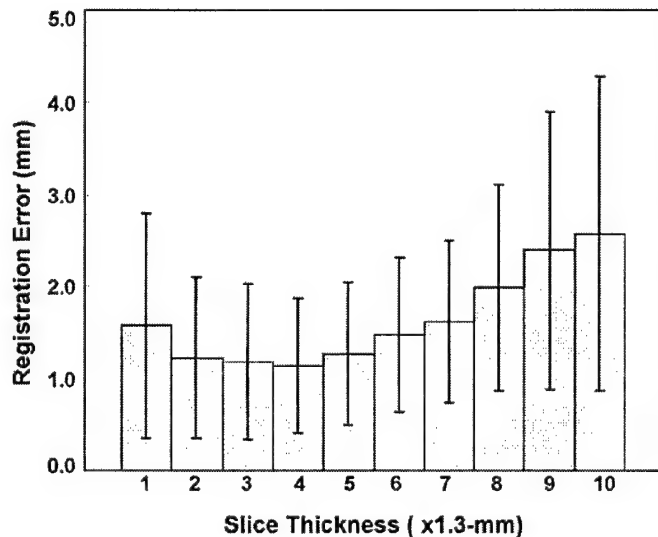

Fig. 9. SV registration using images with different slice thickness. The error metric is the average voxel displacement between the SV and VV registrations. Plotted are mean errors as well as standard deviation from a rectangular VOI surrounding the prostate. One typical datasets of high-resolution MRI volume and actual iMRI slices of volunteer S1 are used for the registration experiments. For each thickness, ten registration experiments were conducted using ten different simulated iMRI transverse slices that intersected the prostate with different distances. Thick iMRI slices were obtained by averaging 1–10 iMRI image slices.

MRI volume (1.5-T scanner) using rigid-body voxel-based registration [8] and used the result as the gold standard for calculating the SV error. Each thick slice image was obtained by averaging several contiguous slices from the actual iMRI volume. As the slice thickness increases from 1×1.3 mm to 4×1.3 mm, the registration error decreases, possibly because of improved

SNR and/or because of the inclusion of more features. Error increases with thicker slices, probably because of the inconsistency of image features between the thick slice and more finely sampled volume.

In Fig. 10, we evaluated SV registration for thick slices at different orientations. The evaluation method was the same as that used in Fig. 9, and the slices were 5 mm thick and intersected the volume near the prostate center. Results were consistent with those from the previous simulation experiments. Transverse slices worked best with an average VOI displacement of only 1.1 mm $\pm$ 0.7 mm and a success rate of 100%. The coronal images gave a reasonable average error, but the success rate dropped to 86%. The sagittal orientation gave the worst result.

Needle artifacts had little effect on the SV registration. In each of 30 the experiments, we registered a high-resolution volume with an actual iMRI image slice containing or not containing a simulated needle artifact. Visual inspection, the correlation coefficient, and mutual information values of registered images showed little effect of the needle artifact. The success rate was 100% in both cases.

C. Algorithmic Robustness and Implementation

The registration algorithm was quite robust for transverse slices covering the prostate. Using simulated iMRI slices from high-resolution MRI volume pairs of four volunteers, the algorithm never failed for any transverse slice covering the prostate. In addition, the final registration result was insensitive to initial guesses within a very large range, $[-60, +60]$ mm for translations and $[-20, +20]$ degrees for rotations. With the restarting algorithm, we even successfully registered slices as much as 80 mm from the optimum. This working range should be quite
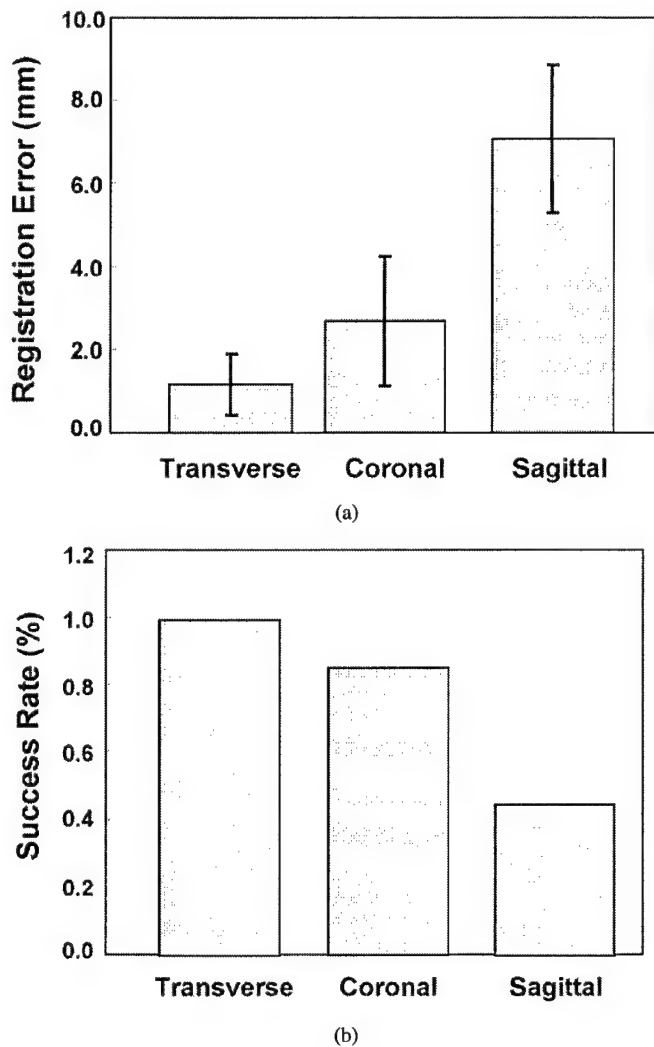
Fig. 10. SV registration error and robustness for iMRI images in the three standard orientations. In (a), registration error relative to VV registration is plotted as a function of image slice orientation. In (b), success rate is also plotted as a function of orientation where registration is successful when the error is <2.0 mm. For volunteer S2, one high-resolution volume and one volume from the iMRI scanner were used in these experiments. Data were extracted from the iMRI volume to simulate iMRI slices with a thickness of about 5 mm. Fifteen transverse, coronal, and sagittal slices from the prostate center were used for SV registration, respectively.

sufficient for clinical applications where we can ensure good starting values. Using the pelvic bones as markers and device localization methods [29], we should be able to position the prostate within about ±20 mm in the imaging field. In addition, the patient normally lies supine in the MR bed with very little rotation (< ±5°).

Using CC and MI at different resolutions was an important feature that increased robustness. MI registrations at low resolution sometimes gave false maxima [Fig. 1(a) and (c)], and only 60% success was achieved when MI was used at all resolutions. The interpolation artifacts at low resolutions often caused failures and required more restarts [16]. CC performed well and gave fewer local maxima at the lower resolutions [Fig. 1(b) and (d)], but MI was more accurate than CC at the highest resolution due to the sharper peak of the MI surface [Fig. 2(a) and (c)] [8]. Our registration algorithm thus combined advantages from the two similarity measures.

The multiresolution approach improved algorithmic robustness and speed. When we used only MI at full resolution, registration was 70% successful compared to the 100% of the full algorithm. This failure of MI was also reported by others [13], [17]. The multiresolution approach enabled the program to quickly approach the final value because of the reduced number of calculations at low resolutions. For a typical image pair, iterations at 1/4 resolution were approximately 4 and 25 times faster than at 1/2 and full resolution, respectively.

Restarting was important for image pairs with large translations and/or rotations from the optimum. In our experience with over 800 SV registration experiments, restarting occurred in about 5% of them. For an example pair with an 80-mm displacement, the number of restarts was 3, 1, and 0 at 1/4, 1/2, and full resolutions, respectively. Without restarting, we found that registrations sometimes failed in cases of volumes with a large mismatch of 54 mm and high noise. The algorithm was insensitive to the CC threshold for restarting. When we decreased the threshold from 0.8 to 0.5 with an interval of 0.05, we found little change in the number of restarts and no change in final registrations. We set the threshold at 0.5 to avoid only the most obvious local maxima.

We now describe some aspects of the implementation. The time for an SV registration was typically about 15 s on a Pentium IV 1.8-GHz CPU with 1 GB of memory. The algorithm was written in IDL and could probably be made much faster in a lower level language such as C. A call to the Simplex optimization typically resulted in 50 to 105 similarity evaluations before the tolerance value (0.001) was reached. The simplex optimization method worked about 1.5–2.0 times faster than the Powell method in our implementation. We used the Simplex method for our experiments in this study.

V. DISCUSSION AND CONCLUSION

Despite complications such as image noise, receive coil inhomogeneity, a limited number of voxels, and needle artifacts, SV voxel-based registration can be quite robust and accurate. For transverse slices covering the prostate, registration results agreed very favorably with VV results. Below, we further discuss the algorithm and its practicality.

A. Mutual Information at Low Resolution

There are probably several reasons why mutual information does not work well at low resolution. First, the similarity curve is noisy with periodic oscillations from the so-called interpolation artifact [8], [16] that is accentuated at reduced resolutions [30]. As a result, there are many local maxima in Fig. 1(a) and (c) that can trap the optimization; and a similar result was reported for brain registration [13]. In additional experiments, we decreased the number of bins for both images to 256, 128, 64, and 32 and plotted mutual information values as a function of translation. With a larger number of bins, we got no discernable effect of bin size. When the number of bins was reduced to 32, the MI surface was degraded. Others showed that Gaussian blurring of images before registration did not improve performance at low resolutions and that there was little difference between standard and normalized mutual information [40]. Second, when images are

of low resolution and there is only a small region of overlap, the mutual information function can even contain incorrect global maxima [30] as found in Fig. 1(a). This false result was obtained at very large displacements where the SV overlap was reduced. This occurs because MI is not only a function of how well the images match in the overlap, but also by how much information is provided by the two images in the overlap [31], [32], [35]. As shown above, using both mutual information and correlation coefficient, at different resolutions, was an important feature that increased robustness.

B. Accuracy Consideration

Essentially, we found that SV is of similar accuracy to VV registration, with an average voxel displacement difference of only 0.4 mm in the prostate for the simulated images and about 1 mm for actual iMRI image data. Hence, the accuracy of the best SV method is essentially that previously reported for VV registration [8].

We recommend that image data are obtained under comparable conditions by keeping a similar posture and by taking clinical measures to reduce rectal and bladder filling. We see no reason to suspect that SV registration will be inaccurate when such conditions are met. When images were acquired under much different conditions, such as legs flat and legs raised, rigid-body registration could result in prostate centroid errors as much as 3.4 mm. Another effect may be the tissue deformation from insertion of the RF needle. From our previous experience observing *in vivo* needle insertion in both animal models and clinical trials with real-time MRI, the amount of tissue deformation that occurs with insertion of a sharp bevel tip needle is minimal and transient in tissues with normal interstitial pressure. In certain lesions, such as cysts or necrotic tumor, persistent deformation is possible; however, we can see such deformations in the live-time interventional MRI images and very probably mentally correct the registered, fused images. We previously reported a warping registration method [38], [39] that can correct deformations at the expense of additional complexity, time, and possibly robustness.

The automatic SV registration provides sufficient accuracy for many potential iMRI applications. As compared to a typical SPECT and/or iMRI slice thickness of ≥ 3.0 mm, SV registration is quite accurate. MR spectroscopy also is done at limited resolution. If one were to use functional or high-resolution MR images directly for targeting, the requirements for registration accuracy would be great. However, fused image data will not be used blindly. Rather, these visualizations will be used as a guide. Physicians will always use the live-time iMRI images for needle guidance. With proper visualization tools, they should be able to mentally account for any small registration errors. In addition, very often there is image evidence of cancer in MR prostate images that can perhaps be identified with the aid of functional images. Such MR-visible lesions can then become the markers for tumor targeting.

C. Practicality and Application

The registration experiments presented here provided fairly comprehensive tests for the potential application in iMRI-guided RF thermal ablation of the prostate. Simulation

provided an efficient way to extensively evaluate registration performance. The algorithm was extremely robust to noise levels, far beyond those encountered in clinical iMRI applications. Similarly, the inhomogeneity seen with a belt coil was not problematic for transverse images, probably due to coil inhomogeneity simply scaling the grayscale values, an operation that should not affect MI or CC similarity measures. Needle artifacts had little effect, probably because they occupy relatively few voxels. The actual iMRI images acquired under more realistic conditions further tested practicality. Images from the iMRI system contained more noise and had less contrast than those from the 1.5-T scanner. Registration quality was comparable to that of simulation experiments. Registration time can probably be improved considerably using optimized C code rather than IDL. If registration is done in the background in a seamless way, the time for registration is probably quite acceptable. Although we normally used T2-weighted image pairs, the registration worked well for pairs of T1-weighted and T2-weighted images.

We conclude that the automatic SV registration algorithm is quite robust for transverse image slices covering the prostate and that the registration provides sufficient accuracy to aid image-guided therapy. From previous reports of MR-PET or MR-SPECT registration accuracy [6], [7], it appears feasible to combine functional images to aid iMRI-guided procedures. We are beginning to explore this application in animal experiments.

REFERENCES

[1] J. S. Lewin, C. F. Connell, J. L. Duerk, Y. C. Chung, M. E. Clampitt, J. Spisak, G. S. Gazelle, and J. R. Haaga, "Interactive MRI-guided radiofrequency interstitial thermal ablation of abdominal tumors: clinical trial for evaluation of safety and feasibility," *J. Magn. Reson. Imag.*, vol. 8, pp. 40–47, 1998.

[2] D. L. Wilson, A. Carrillo, L. Zheng, A. Genc, J. L. Duerk, and J. S. Lewin, "Evaluation of 3D image registration as applied to MR-guided thermal treatment of liver cancer," *J. Magn. Reson. Imag.*, vol. 8, pp. 77–84, 1998.

[3] A. Carrillo, J. L. Duerk, J. S. Lewin, and D. L. Wilson, "Semiautomatic 3-D image registration as applied to interventional MRI liver cancer treatment," *IEEE Trans. Med. Imag.*, vol. 19, pp. 175–185, Mar. 2000.

[4] D. B. Sodee, N. Malguria, P. Faulhaber, M. I. Resnick, J. Albert, and G. Bakale, "Multicenter ProstaScint imaging findings in 2154 patients with prostate cancer," *Urology*, vol. 56, pp. 988–993, 2000.

[5] J. Scheidler, H. Hricak, D. B. Vigneron, K. K. Yu, D. L. Sokolov, L. R. Huang, C. J. Zaloudek, S. J. Nelson, P. R. Carroll, and J. Kurhanewicz, "Prostate cancer: localization with three-dimensional proton MR spectroscopic imaging—clinicopathologic study," *Radiology*, vol. 213, pp. 473–480, 1999.

[6] D. B. Sodee, G. T. MacLennan, M. I. Resnick, P. F. Faulhaber, Z. Lee, A. D. Nelson, J. P. Molter, and G. Bakale, "Comparison of CT- or MRI-fused PET-FDG and SPECT-ProstaScint® imaging of prostate cancer with the gold standard of histology," *J. Nucl. Med.*, vol. 42, p. 1222, 2001.

[7] Z. Lee, D. B. Sodee, J. L. Duerk, A. D. Nelson, and M. S. Berridge, "Automatic registration of SPECT-MRI in the pelvis," *J. Nucl. Med.*, vol. 41, p. 232, 2000.

[8] B. W. Fei, A. Wheaton, Z. Lee, J. L. Duerk, and D. L. Wilson, "Automatic MR volume registration and its evaluation for the pelvis and prostate," *Phys. Med. Biol.*, vol. 47, pp. 823–838, 2002.

[9] H. Gray, *Anatomy—Descriptive and Surgical* (The classic collector's edition). New York: Gramercy Books, 1977, pp. 823–1010.

[10] B. Kim, J. L. Boes, P. H. Bland, T. L. Chenevert, and C. R. Meyer, "Motion correction in fMRI via registration of individual slices into an anatomical volume," *Magn. Reson. Med.*, vol. 41, pp. 964–972, 1999.

[11] T. S. Kim, M. Singh, W. Sungkarat, C. Zarow, and H. Chui, "Automatic registration of postmortem brain slices to MRI reference volume," *IEEE Trans. Nucl. Sci.*, vol. 47, pp. 1607–1613, Aug. 2000.

[12] J. Zhengping and P. H. Mowforth, "Mapping between MR brain images and voxel model," *Med. Inform.*, vol. 16, pp. 183–193, 1991.

[13] F. Maes, A. Collignon, D. Vandermeulen, G. Marchal, and P. Suetens, "Multimodality image registration by maximization of mutual information," *IEEE Trans. Med. Imag.*, vol. 16, pp. 187–198, 1997.

[14] Y. M. Zhu, "Volume image registration by cross-entropy optimization," *IEEE Trans. Med. Imag.*, vol. 21, pp. 174–180, Feb. 2002.

[15] R. Shekhar and V. Zagrodsky, "Mutual information-based rigid and non-rigid registration of ultrasound volumes," *IEEE Trans. Med. Imag.*, vol. 21, pp. 9–22, Jan. 2002.

[16] J. P. W. Pluim, J. B. A. Maintz, and M. A. Viergever, "Interpolation artefacts in mutual information-based image registration," *Comput. Vis. Image Understand.*, vol. 77, pp. 211–232, 2000.

[17] D. L. G. Hill, L. A. Langsaeter, P. N. Poynter-Smith, P. E. Summers, S. F. Keevil, R. Walsh, D. J. Hawkes, and M. J. Gleeson, "Feasibility study of magnetic resonance imaging-guided intranasal flexible microendoscopy," *Comput. Aided Surg.*, vol. 2, pp. 264–275, 1997.

[18] A. Collignon, F. Maes, D. Delaere, D. Vandermeulen, P. Suetens, and G. Marchal, "Automated multimodality image registration using information theory," in *Proc. 14th Int. Conf. Information Processing in Medical Imaging (IPMI'95)*, 1995, pp. 287–298.

[19] W. H. Press, B. P. Flannery, S. A. Teukolsky, and W. T. Vellerling, *Numerical Recipes in C: The Art of Scientific Computing*, 2nd ed. London, U.K.: Cambridge Univ. Press, 1993.

[20] J. Nelder and R. A. Mead, "A simplex method for function minimization," *Comput. J.*, vol. 7, pp. 308–313, 1965.

[21] M. J. D. Powell, "An iterative method for finding stationary values of a function of several variables," *Comput. J.*, vol. 5, pp. 147–151, 1962.

[22] A. Macovski, "Noise in MRI," *Magn. Reson. Med.*, vol. 36, pp. 494–497, 1996.

[23] R. C. Gregg and R. D. Nowak, "Noise removal methods for high resolution MRI," in *Proc. IEEE Nuclear Science Symp.*, vol. 2, 1997, pp. 1117–1121.

[24] L. Kaufman, D. M. Kramer, L. E. Crooks, and D. A. Ortendahl, "Measuring signal-to-noise ratios in MR imaging," *Radiology*, vol. 173, pp. 265–267, 1989.

[25] R. M. Henkelman, "Measurement of signal intensities in the presence of noise in MR images," *Med. Phys.*, vol. 12, pp. 232–233, 1985.

[26] D. I. Hoult and R. E. Richards, "The signal-to-noise ratio of the nuclear magnetic resonance experiment," *J. Magn. Reson.*, vol. 24, pp. 71–85, 1976.

[27] E. M. Haacke, R. W. Brown, M. R. Thompson, and R. Venkatesan, *Magnetic Resonance Imaging: Physical Principles and Sequence Design.* New York: Wiley, 1999, p. 834.

[28] L. K. Forbes, S. Crozier, and D. M. Doddrell, "Rapid computation of static fields produced by thick circular solenoids," *IEEE Trans. Magn.*, vol. 33, pp. 4405–4410, Sept. 1997.

[29] J. S. Lewin, J. L. Duerk, V. R. Jain, C. A. Petersilge, C. P. Chao, and J. R. Haaga, "Needle localization in MR-guided biopsy and aspiration: effects of field strength, sequence design, and magnetic field orientation," *Amer. J. Roentgenol.*, vol. 166, pp. 1337–1345, 1996.

[30] J. P. W. Pluim, J. B. A. Maintz, and M. A. Viergever, "Image registration by maximization of combined mutual information and gradient information," *IEEE Trans. Med. Imag.*, vol. 19, pp. 809–814, Aug. 2000.

[31] C. Studholme, D. L. G. Hill, and D. J. Hawkes, "Automated three-dimensional registration of magnetic resonance and positron emission tomography brain images by multiresolution optimization of voxel similarity measures," *Med. Phys.*, vol. 24, pp. 25–35, 1997.

[32] D. Rueckert, M. J. Clarke, D. L. G. Hill, and D. J. Hawkes, "Non-rigid registration using higher-order mutual information," in *Proceedings of SPIE*, K. M. Hanson, Ed. Bellingham, WA: SPIE, 2000, vol. 3979, Medical Imaging 2000: Image Processing, pp. 438–447.

[33] F. Maes, "Segmentation and registration of multimodal images: from theory, implementation and validation to a useful tool in clinical practice," Ph.D. dissertation, Katholieke Univ. Leuven, Belgium, 1996.

[34] C. Studholme, D. L. G. Hill, and D. J. Hawkes, "An overlap entropy measure of 3D medical image alignment.," *Pattern Recognit.*, vol. 32, pp. 71–86, 1999.

[35] P. A. Viola, "Alignment by maximization of mutual information," Ph.D. dissertation, Massachusetts Institute of Technology, Cambridge, MA, 1995.

[36] J. M. Fitzpatrick, J. B. West, and C. R. Maurer, "Predicting error in rigid-body point-based registration," *IEEE Trans. Med. Imag.*, vol. 17, pp. 694–702, Oct. 1998.

[37] M. V. Herk, A. Bruce, A. P. G. Kroes, T. Shouman, A. Touw, and J. V. Lebesque, "Quantification of organ motion during conformal radiotherapy of the prostate by three dimensional image registration," *Int. J. Radiat. Oncol. Biol. Phys.*, vol. 33, pp. 1311–1320, 1995.

[38] B.W. Fei, C. Kemper, and D. L. Wilson, "Three-dimensional warping registration of the pelvis and prostate," in *Proceedings of the SPIE*, M. Sonka and J. M. Fitzpatrick, Eds. Bellingham, WA: SPIE, 2002, vol. 4684, Medical Imaging 2002: Image Processing, pp. 528–537.

[39] ——, "A comparative study of warping and rigid body registration for the prostate and pelvic MR volumes," *Comput. Med. Imag. Graph.*, vol. 27, pp. 267–281, 2003.

[40] J. P. W. Pluim, J. B. A. Maintz, and M. A. Viergever, "Mutual information matching in multiresolution contexts," *Image Vis. Comput.*, vol. 19, pp. 45–52, 2001.

Registration and Fusion of SPECT, High Resolution MRI, and interventional MRI for Thermal Ablation of Prostate Cancer

Baowei Fei, Zhenghong Lee, Daniel T. Boll, Jeffery L. Duerk,
D. Bruce Sodee, Jonathan S. Lewin, David L. Wilson

Abstract --We are investigating interventional MRI (iMRI) guided radiofrequency thermal ablation for the minimally invasive treatment of the prostate cancer. Nuclear medicine can detect and localize tumor in the prostate not reliably seen in MRI. We intend to combine the advantages of functional images such as nuclear medicine SPECT with iMRI-guided treatments. Our concept is to first register the low-resolution SPECT with a high resolution MRI volume. Then by registering the high-resolution MR image with live-time iMRI acquisitions, we can, in turn, map the functional data and high-resolution anatomic information to live-time iMRI images for improved tumor targeting. For the first step, we used a three dimensional mutual information registration method. For the latter, we developed a robust slice to volume (SV) registration algorithm with special features. The concept was tested using image data from three patients and three volunteers. The SV registration accuracy was 0.4 mm ± 0.2 mm as compared to our volume-to-volume registration that was previously shown to be quite accurate for these image pairs. With our image registration and fusion software, simulation experiments show that it is quite feasible to incorporate SPECT and high resolution MRI into the iMRI-guided minimally invasive treatment procedures.

I. INTRODUCTION

We use an interventional magnetic resonance imaging (iMRI) system to guide minimally invasive treatments, including the radiofrequency (RF) thermal ablation of abdominal cancers [1]-[3]. The iMRI system consists of a

B.W. Fei is with Department of Biomedical Engineering, Case Western Reserve University, Cleveland, OH 44106 (e-mail: Baowei.Fei@case.edu)

D.T. Boll, Z.Lee, J.L.Duerk, D.B.Sodee and J.S.Lewin are with the Departments of Biomedical Engineering and Radiology, Case Western Reserve University and University Hospitals of Cleveland, Cleveland, OH 44106. J.S. Lewin is also with Departments of Oncology and Neurological Surgery, University and University Hospitals of Cleveland, Cleveland, OH 44106 (e-mails: Boll, Lee, Duerk, Sodee, Lewin@uhrad.com).

D.L.Wilson is with the Departments of Biomedical Engineering and Radiology, Case Western Reserve University and University Hospitals of Cleveland, Cleveland, OH 44106 (e-mail: DLW@po.cwru.edu).

0.2 T, clinical C-arm open MRI scanner, an in-room RF-shielded liquid crystal monitor, an MR compatible mouse, a foot pedal, and a RF ablation device. We are currently investigating the extension of these techniques to the treatment of prostate cancer. Since MRI does not reliably show prostate tumors, we intend to incorporate nuclear medicine SPECT or MR spectroscopy images with higher sensitivity for detecting and localizing prostate tumors [4][5].

To incorporate image data from other sources in a live-time iMRI procedure, we intend to register two-dimensional (2D) slice images quickly acquired on the iMRI scanner in live-time with a previously acquired volume of image data. Then, to incorporate an image volume from another modality, it can be registered with the full MR volume. Thus, to incorporate SPECT in an iMRI procedure, we will first register the SPECT image volume with a high resolution MR volume; then, when we register iMRI slice images to the high resolution MR volume, we can also map them to the SPECT functional image data. If this procedure is successful, then a variety of potential visualization tools can help the physician appropriately localize and apply treatments. The live-time iMRI images will be used for guidance, and very probably any small misregistration errors can be mentally corrected by the physician. To simplify and possibly improve the slice-to-volume (SV) registration step, we intend to always use MR images acquired with similar pulse sequences.

The application of SV registration methods to iMRI-guided treatment of prostate cancer raises several challenges. First, iMRI images often have lower signal to noise ratio (SNR) than diagnostic MR images because of the emphasis on fast imaging and because of the typically lower field strength of open iMRI magnets. Second, a single slice, or a few slices, provides many fewer structures than an entire volume for voxel based matching. Third, the prostate can move relative to the pelvic bones due to changes in rectal and bladder filling [6] or changes in patient posture for treatment [7]. That is, alignment of the pelvic bones, prominent anatomical features in MR gray-scale images, does not necessarily ensure that the prostate is aligned. Fourth, the normal prostate is a small organ; when healthy, it measures only ~ 3.8 cm in its widest dimension [8]. The small prostate is located below the much larger bladder that can change its shape and size during

imaging. Finally, times for registration and algorithm robustness are of particular concern for this application.

Previous success with registering one MR prostate volume to another [7] encourages us to pursue this plan. We call this volume-to-volume registration, or VV. We used a rigid body, mutual information registration method with some features to improve robustness [7]. We carefully evaluated registration quality using a variety of methods. For volume pairs acquired over a short time span from a supine subject with legs flat on the table, registration accuracy of both prostate centroids (typically < 1 mm) and bony landmarks (average 1.6 mm) was on the order of a voxel ($\tilde{\ }$ 1.4 mm). For volumes acquired under very different conditions, e.g., legs flat and legs raised into the treatment position, or with and without bladder or rectal filling, we obtained somewhat larger prostate centroids registration errors of about 3.0 mm. From our results with VV prostate registration, we decided that we could assess SV accuracy by comparing results to VV registration for those volume pairs having low VV registration error.

In the next sections, we will report algorithms and results for the slice-to-volume registration between an iMRI thick slice and a high resolution MRI volume, the three dimensional registration of SPECT and high resolution MRI volumes, and the fusion of the three modalities for potential applications in iMRI-guided thermal ablation of the prostate.

II. Registration Algorithms

A. Similarity Measures

For slice to volume registration of iMRI image slice and high resolution MRI volume, we used two similarity measures, mutual information and correlation coefficient, in our registration. Suppose one image R is the *reference*, and the other F is *floating*. Their mutual information $MI(R,F)$ is given below [9].

$$MI(R,F) \Box \Box_{r,f} p_{RF}(r,f) \log \frac{p_{RF}(r,f)}{p_R(r) \Box p_F(f)}$$

The joint probability $p_{RF}(r,f)$ and the marginal probabilities $p_R(r)$ of the reference image and $p_F(f)$ of the floating image, can be estimated from the normalized joint intensity histogram.

The correlation coefficient (CC) is the measure of the interdependence of two random variables that ranges in value from -1 to +1, indicating perfect negative correlation at -1, absence of correlation at zero, and perfect positive correlation at +1. For the reference and floating images, R and F, their correlation coefficient $CC(R,F)$ is given below The correlation coefficient $CC(R,F)$ is given below [10].

$$CC(R,F) \Box \frac{\sum_{i \Box 0}^{N \Box 1} (R(i) \Box \overline{R})(F(i) \Box \overline{F})}{\sqrt{\sum_{i \Box 0}^{N \Box 1} (R(i) \Box \overline{R})^2 \quad \sum_{i \Box 0}^{N \Box 1} (F(i) \Box \overline{F})^2}}$$

Here $\overline{R}$, $\overline{F}$ denote the average intensities of the reference and floating volumes and the summation includes all N voxels within the overlap of both volumes.

B. Registration of iMRI Slice and High Resolution MRI Volume

We used a registration algorithm similar to the one as previously reported by us [11][12]. We used multi-resolution approach and perform registration from low to high resolution. At *1/4 resolution*, we resampled images so as to give 1/4 number of the voxels along each linear dimension. At *full resolution*, we used the full number of voxels. We use correlation coefficient at the two lower resolutions because it gives fewer local maximums and because it can be calculated faster than MI. We use MI at full resolution because the peaked similarity function gives a more precise solution than CC [7]. To avoid local maximums, we include a restarting feature where registration is restarted with randomly perturbed parameters obtained from a uniform distribution about the initial transformation values at the current resolution being used. The algorithm restarts until the absolute CC is above an experimentally determined threshold or the maximum number of restarts is reached. Absolute CC is used rather than MI because it has a well-defined range between 0 and 1 and because it provides an independent check of the MI result at the highest resolution.

We record all important results following an optimization cycle including the CC and/or MI values, the number of restarts, and the transformation parameters. At the end of processing at a lower resolution, we always select the transformation parameters having the maximum CC value. We then scale the translation parameters appropriately and assign the new parameters to be initial values at the next higher resolution. At the highest resolution, MI instead of CC is the similarity measure, and we select the final transformation parameters to be those with the maximum MI value.

Typical parameter values are now described. We use an initial guess assuming an identity transformation, i.e., all initial translation and rotation parameters are zero, because the patient is normally oriented approximately the same way from one scan to the next. The algorithm restarts until the absolute CC is above a threshold of 0.5 or maximum numbers of restarts are reached (10, 5, and 3, from low to high resolution, respectively).

C. Registration of SPECT and High Resolution MRI Volume

The mutual information algorithm was used to register MRI and SPECT volume images because of its ability to align multi-modality images [13][14]. Registration of SPECT and MR images is challenging because the two image types have different spatial resolutions and image features. The radiotracer used for SPECT imaging was ProstaScint$\Box$ (Cytogen Corporation, Princeton, NJ), a monoclonal antibody that binds to prostate-specific membrane antigen (PSMA). Before registration, both SPECT and MRI volumes were resized using trilinear interpolation to create volumes matrix

of 128x128x128 with 3 mm isotropic voxels, a voxel size between that of the two scans. The standard parameter set for automatic registration included: 256 intensity levels for each volume, the entire 2D joint histogram, the full field of view of 128x128x128 voxels for both volumes, and no masking or cropping of either volume. Phantom data were preprocessed in a similar fashion.

III. EXPERIMENTAL METHODS

A. High Resolution MR Image Acquisitions

High-resolution MRI volumes were acquired using a 1.5 T Siemens MRI system (Magnetom Symphony, Siemens Medical Systems, Erlangen, Germany). An 8-element phased array body coil was used to ensure coverage of the prostate with a uniform sensitivity. Typically two anterior and two posterior elements were enabled for signal acquisition. We used two different MR sequences.

First, we used a 3D rapid gradient echo sequence (PSIF) designed to acquire the spin-echo component of the steady state response, rather than the free induction decay. The spin echo component forms immediately prior to the RF pulse; it is shifted toward the prior RF pulse through appropriate gradient waveform design. The sequence with 9.4/5.0/60 (TR/TE/flip) yields 160x256x128 voxels over a 219x350x192-mm rectangular FOV and 1.4x1.4x1.5-mm voxels oriented to give the highest resolution for transverse slices. There is over sampling at 31% in the slice direction to reduce aliasing artifacts. The acquisition time is 4 min and 15 sec. This sequence gave excellent image contrast for the prostate and its surroundings. It was used to acquire volumes for volunteers S1-S3.

Second, we used a 3D RF spoiled gradient echo steady state pulse sequence (FLASH) with TR/TE/flip parameters of 12/5.0/60 which give 256 x 256 x 128 voxels over a 330 x 330 x 256-mm field of view (FOV) to yield 1.3 x 1.3 x 2.0-mm voxels oriented to give the highest resolution for transverse slices. The acquisition time is 5 min and 38 sec. This sequence is good for pelvic imaging but is not ideal for the prostate. It was used to acquire volumes for patients S4-S8.

When acquiring high-resolution MR volumes, volunteers laid supine in a manner similar to the diagnostic position in routine MR scanning. Between volume acquisitions, volunteers got up from the MR table, stretched, and walked around to ensure that they would assume a different position when they laid back on the table. The coil array was centered on the prostate. We acquired three volumes from each of the volunteers S1-S3. For patients S4-S8, we acquired nine MRI volumes and each patient with at least one volume.

B. Interventional MRI Image Acquisitions and Simulation

We acquired iMRI images using a clinical 0.2 T C-arm open MR scanner (Siemens Open Symphony, Erlangen, Germany) modified for interventional MRI procedures and in this paper referred to as the iMRI system. We used a two-dimensional PSIF with 15.2/7.4/45 (TR/TE/FA) for image slice acquisitions. The iMRI slices were 128x128 with in-plane pixel size of 2.8x2.8 mm and with effective slice thickness of 5 mm.

We acquired iMRI images under the conditions simulating the treatment application. The volunteer was supine, and his legs were supported at 30□60□ relative to the horizon and separated in a "V" with an angle of 60□90□ between two legs. This is similar to the lithotomy position used in prostate therapies, and it should provide access for needle insertion in brachytherapy or RF thermal ablation. We call this the treatment position. For each of the volunteers S1-S3, we acquired 30 iMRI image slices covering the prostate. They included 10 transverse, 10 coronal, and 10 sagittal image slices. We call these images *"actual"* iMRI images to differentiate them from *"simulated"* images as described in the next paragraph.

To test a variety of clinical conditions, we used high-resolution MRI volumes to simulate iMRI images by creating thick slices and adding noise and receive coil inhomogeneity [15]. Clinically, we typically use an iMRI slice thickness of 4.0 - 6.0 mm. We averaged 3 slices 1.4 mm thick to create a 4.2 mm thick slice. We added noise to the simulated iMRI image.

C. SPECT Image Acquisition

The study included five patients (S4-S8) with either high Gleason scores (>5) from biopsy or rising PSA level (>10 mcg/L, prostate specific antigen) or palpation staging beyond stage T1. After patient eligibility was established, patients gave informed consent. The Institutional Review Board of the University Hospitals of Cleveland approved the imaging protocol.

Approximately four days after injecting 5 mCi ProstaScint□, the abdominal and pelvic regions were scanned using a two-head Siemens E.CAM+ camera (Siemens Medical System, Inc., Hoffman Estates, Illinois, USA). ProstaScint□ is an [In-111]-labeled monoclonal antibody capromab penditide (^{111}In MoAb 7E11.C5) used for imaging prostate cancer. The evening before scanning, patients performed a bowel prep with Fleet R Prep Kit #3 (Fleet Pharmaceuticals, Lynchburg, VA). Images were acquired with a medium energy collimator and 15% energy window. The acquisition parameters included a step-and-shoot motion, a 128 x 128 pixel matrix for each projection, an imaging time of 25 sec per stop, and a total of 120 stops over a full 360□ rotation. The field of view of was 53.3 x 38.7 cm². The Ordered Subsets Expectation Maximization (OSEM) algorithm was used for image reconstruction [16]. SPECT images were comprised of 4.795 x 4.795 x 4.795-mm isotropic voxels. Each patient had one SPECT scan of the pelvis.

To analyze and validate registration of high resolution MRI and SPECT under a controlled situation, an acrylic phantom of the pelvis and lower abdomen was used. Spheres of proportional size representing portions of the bladder,

acetabula, rectum, and the prostate gland were placed in appropriate positions in the torso phantom. The spheres of acetabulum were filled with potassium phosphate. Other spheres were filled with water. The torso phantom was filled with a small amount of copper sulfate dissolved in deionized water. The SPECT scan was conducted after injecting all spheres with [In-111]-DTPA at relative concentrations comparable to those detected in human scans. The water in the torso was given a background activity of 1 ☐Ci/ml such as to mimic the background in human SPECT scans.

D. Registration Experiments

We used 9 pairs of high-resolution MR volumes of volunteers S1-S3 to perform SV registration experiments. For each volume pair, we extracted data from one volume to simulate thick iMRI image slices; and then we registered the simulated image slices to the other volume. We desire an iMRI slice image acquisition method that gives robust, accurate registrations and is relatively insensitive to acquisition parameters. Hence, we performed experiments to determine the dependence on slice orientation (transverse, sagittal and coronal), on slice position relative to the prostate (above, centered, and below) and on image noise from fast imaging techniques.

We also performed SV registration experiments using the actual iMRI images from volunteers S1-S3. We registered actual iMRI image slices with high-resolution (1.5 T system) MR volumes of the same volunteer and visually evaluated results. For each volunteer, there were three high-resolution MR volumes and 30 iMRI image slices giving 90 SV registration experiments, and a total of 270 experiments.

A number of technical issues were examined for MI registration of MRI and ProstaScint☐ SPECT prostate images. Firstly, MRI acquisition, by varying the MR imaging pulse sequence, various structures can be emphasized or suppressed. Several different acquisition sequences were tested and its effect on registration accuracy and robustness was determined. Secondly, because of the different dynamic ranges between MR and SPECT images, intensity scaling was studied for its effect on registration. This is prompted by a recent study showing that scaling images to 16 gray levels gives better results than 256 gray levels when registering muscle fiber images [17]. Thirdly, because of the sparseness in the histogram, the use of a portion or a section rather than the full joint histogram was evaluated. This effectively restricted the registration to particular intensity ranges. Fourthly, the multi-resolution approach was examined for its ability to expedite the automated search algorithm. Fifthly, the use of spatial masking was investigated to see whether it facilitates the registration of partially overlapping volumes. In all cases, registration experiments were performed with and without these modifications to determine their effect on the success of registration. Success was determined by comparing the results of these experiments to those of manual registration of the same images as described in the next section. Experiments with these parameters should provide insight into improving registration of MR and SPECT prostate images. We performed registration experiments using the SPECT and MRI image volumes from patients S4-S8.

E. Registration Evaluations

We evaluated registration experiments by visual inspection. We used *RegViz,* a program created in IDL (Interactive Data Language, Research System Inc., CO) in our laboratory with multiple visualization and analysis methods. First, we manually segmented prostate boundaries in image slices and copied them to corresponding slices. This enabled visual determination of the overlap of prostate boundaries over the entire volume. Second, color overlay displays were used to evaluate overlap of structures. One image was rendered in gray and the other in the "hot -iron" color scheme. To visualize potential differences, it was quite useful to interactively change the contribution of each image using the transparency scale. Third, we used a sector display, which divided the reference and registered images into rectangular sectors and created an output image by alternating sectors from the two input images. Even subtle shifts of edges would be clearly seen.

Our standard evaluation method for SV registration was to compare SV and VV registration. Since this relies on VV registration accuracy, we now review our previous results [7]. For volume pairs acquired over a short time span from a supine subject with legs flat on the table, prostates were well aligned and prostate centroid displacements were typically < 1 mm. The registration accuracy as determined from displacements of pelvic bony landmarks was 1.6 ± 0.2 mm. From our success with VV prostate registration, we decided that we could measure SV accuracy by comparing results to VV registrations for those volume pairs having low VV registration error. To compare SV and VV registration, we defined a rectangular volume of interest (VOI) just covering the prostate and calculated voxel displacements between the two registrations. To voxels within the VOI, we applied the transformations obtained by VV and by SV registrations. We then calculated the 3D Euclidian displacements between the transformed voxels. The mean voxel distance was used as our metric of SV registration error. For the evaluation of algorithm robustness, we defined the SV registration as being *successful* when the 3D displacement was less than 2.0 mm.

The success of computer registration of SPECT and MRI volumes was determined by comparing results to manual registration. Manual registration was done by two board-certified nuclear medicine radiologists blinded to the automatic registration results. Manual registration was done using a software package with a graphical user interface (GUI) developed in–house, which allows graphical manipulation of volumes with six degrees of freedom in a rigid body registration. A color overlay was used to assess registration quality.

Two radiologists with a nuclear medicine specialty aligned the image volumes, and whenever there was a discrepancy, they reached a consensus for a single transformation. This painstaking cross-validation was a time-consuming process and certainly would not be a routine procedure, but the results served as the gold standard for the automated method. We

defined a successful automatic registration to be obtained when all displacements were < 2 voxels (6 mm) in the x, y, and z directions and angle differences were < 2 degree for all angles about each of the three axes.

Although manual registration is difficult and somewhat operator dependent, it is the only acceptable option for an independent registration on the patient SPECT and MRI volumes. Skin fiducials would be of limited value in the pelvis, and there are no good identifiable point anatomical landmarks in the SPECT images.

We simulated the iMRI-guided procedures using our image registration and fusion software that are specially designed for this application. Before treatment, we acquired SPECT and high resolution MRI volumes from the same patients. Second, we registered the two images and transferred the pair of aligned data sets to a workstation that was used for the slice to volume registration. Third, we connected the workstation to the iMRI scanner and obtained iMRI image slices from the scanner. Fourth, we performed the slice to volume registration. Finally, the software created fused images of the three modalities as would be done for image guidance. All registrations and image fusions are automatic.
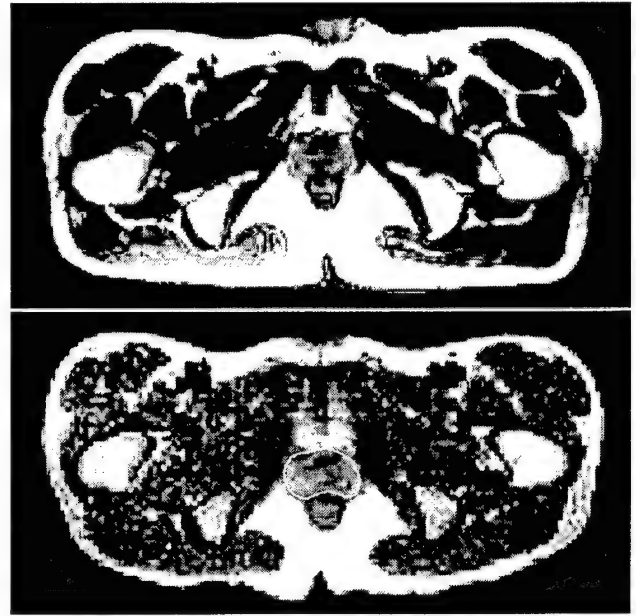

Fig. 1. Prostate MR images. The top is the high resolution MR image. The bottom is the actual iMRI image; the rectangular window at the center is the transparency display of both images. The prostate boundary segmented from high resolution MR image, matches well with the prostate in iMRI image. Images are from the volunteer S3.

IV. RESULTS

A. Registration of an iMRI Slice to a High Resolution MRI Volume

We determined SV registration results for slices near the prostate in the three standard orthogonal orientations. Comparing to VV, mean and standard deviation registration errors across 9 volume pairs were $0.4 \, mm \pm 0.2$ mm, $0.5 \, mm \pm 0.2$ mm, and $2.6 \, mm \pm 1.6 \, mm$ for transverse, coronal and sagittal slices covering the prostate, respectively. Transverse slices worked best because they contain many relatively rigid anatomical structures.

Simulation experiments showed SV registration to be very insensitive to noise. We performed over 100 registration experiments with noise added to give signal to noise ratio (SNR) ranging from 20 to 5. Using the slice configurations recommended above (transverse slices near the prostate center), we obtained 100% successful registrations (an error < 2.0 mm) for SNR's = 10, a value much worse than the clinical SNR value of ~ 25 on our iMRI system.

As for SV registration of actual iMRI image slices with a high-resolution MR volume, the contours overlap and overlay images show that the prostate matches very well (Fig. 1). Other visual inspection techniques also demonstrate excellent registration. Note that a single iMRI image was used to produce this registration result.

We now describe some aspects of the implementation. The time for an SV registration was typically about 3 sec on a Pentium IV, 2.4 GHz CPU, with 1Gbytes of memory. The algorithm was written in IDL and could probably be made much faster in a lower level language such as C.

B. Registration of SPECT and High Resolution MRI Volumes

An example of a successful automatic registration is shown in Fig. 2. All anatomical features including the bone marrow in the femur and pubic symphysis are well aligned in the color overlay. This MR-SPECT volume pair and four others were successfully registered according to the criteria defined earlier. Standard algorithm parameters (Section II.C) were used with the lower-left quadrant of the joint histogram used for calculating MI. Successful image registration was obtained with images from patients S4, S5, and S8. There were four other MR-SPECT volume pairs obtained from patients S6 and S7 that were not successfully registered with our program. In all four cases, the MR images were not acquired using our final, optimized MR sequence (Section III.A). When we used the optimized sequence with full anatomical coverage, registration was always successful. We believe that automated SPECT-MRI registration will be feasible on many patients' images.

We now report the registration results of SPECT and high resolution MRI images of the phantom. Registrations of the phantom images were carried out by displacing the aligned image pair with known rotation and translations. All orientations, axial, sagittal, and coronal, were successfully registered. Other experiments showed that intensity scaling and multi-resolution could not improve the registration ability for both phantom and human data.

C. Image Fusion and Visualization

We created image registration and fusion software for the potential applications in iMRI-guided procedures. In Fig. 3,

we demonstrate the image fusion visualization software in a simulation of clinical usage. SPECT and high resolution MR images were acquired, transferred to a workstation, and registered prior to the "simulated" procedure. We then simulate acquiring thick iMRI slices, register them to the high resolution volume, and prepare the visualization in Fig. 3. In this figure, one can see all. The registered images are shown in the three windows at the top line (Fig. 3). After registration, the program creates fused images as displayed at the bottom.

V. DISCUSSION AND CONCLUSION

This preliminary study has shown promising algorithmic results for bringing nuclear medicine, functional images into the interventional MRI suite. Automatic registration of SPECT and MRI volumes was always successful with "good" MRI volumes obtained using the optimized acquisition sequence and covering all anatomy of interest. Slice-to-volume automatic registration was even more successful with highly accurate, robust registration obtained. Putting these two steps together, a patient's SPECT images can be registered to a high resolution MRI volume prior to an iMRI procedure; live-time iMRI slice images can be registered to the MRI volume; and, finally, one can then display the live-time iMRI slice image with the appropriately reformatted, fused image from the SPECT and high resolution MRI image volumes.

The required registration accuracy is probably less than one might think. The live-time iMRI image obtained in the plane of the advancing needle will always be used for guiding a needle for intervention or biopsy. The corresponding fused SPECT-MRI and/or high resolution MRI images will be used as a planning guide. With proper visualization tools, interventional radiologists should be able to mentally account for any small registration errors. In addition, there is often image evidence of cancer in MR prostate images that can perhaps be identified with the aid of functional images. Such MR-visible lesions can then become the markers for tumor targeting. Any potential gross registration errors should be easily recognized resulting in a failure to include the functional image data in the iMRI suite but not in a catastrophic misguidance of the therapy needle.

More analysis of registration error is possible. The overall registration error of placing a SPECT image with a live-time iMRI image depends upon both SPECT-MRI and the slice-to-volume errors. The slice to volume error for voxels near the prostate is $\square$1.4 mm, as argued elsewhere [11][12]. The SPECT-MRI error can be roughly estimated from the requirements for acceptable registration ($\square$6 mm and $\square$2 degrees). Slice-to-volume registration has an error less than obtained with SPECT-MRI, as would be expected from the low resolution and reduced number of features with

SPECT. The automatic SPECT-MRI registration error is comparable to the uncertainty of manual registration. (After all, that is how we specified the requirements for "acceptability.") Despite such uncertainty, SPECT images have been routinely registered with CT and MR images at our institution to use ProstaScint$\square$ for diagnostic studies of prostate cancer. If SPECT-MRI can be used for diagnostic procedures and slice-to-volume registration has much less error, then we anticipate that the combined process will fulfill needs for guidance as argued in the last paragraph.

To minimize registration error, we recommend that image data are obtained under comparable conditions by keeping a similar posture and by taking clinical measures to reduce rectal and bladder filling. Warping registration method may be useful to correct significant deformations at the expense of additional complexity, time, and possibly robustness [18][19].

Finally, we believe that it is quite feasible to include previously acquired nuclear medicine SPECT images and high-resolution MRI data into iMRI-guided minimally invasive treatment procedures. We are beginning to explore this application in animal experiments.
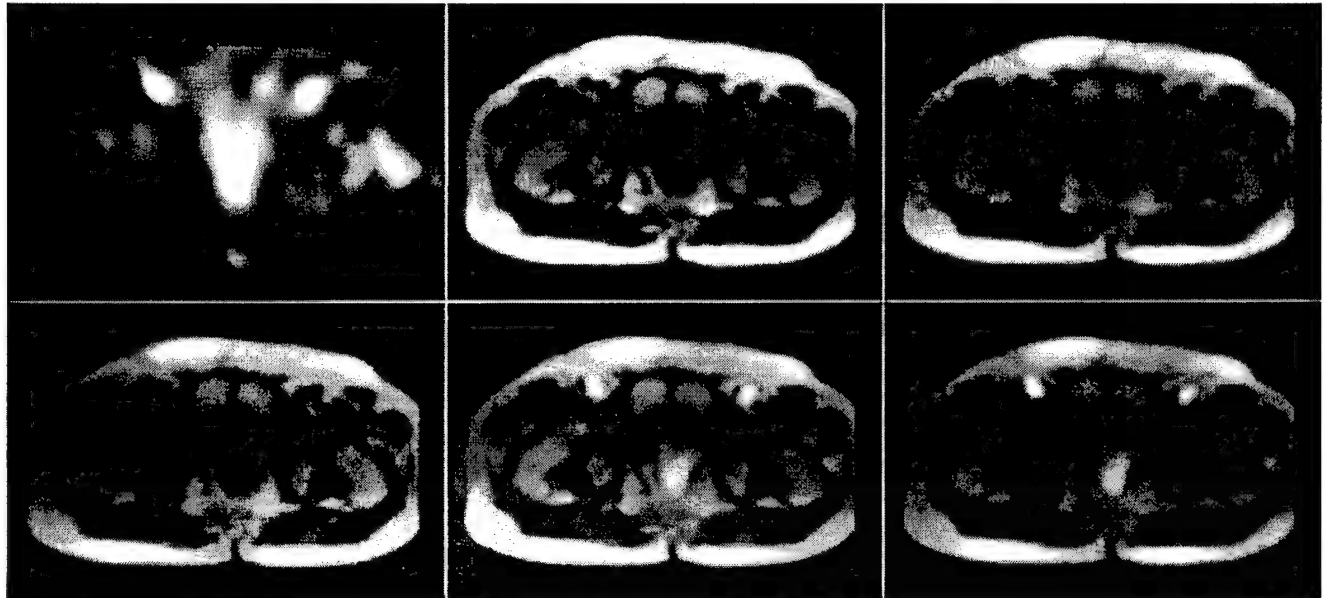
Fig. 2. Registration results of patient data. The top three images show corresponding registered SPECT, high resolution MRI, and simulated iMRI images, respectively. The bottom three windows show the fused images of the three modalities, from left to right, iMRI/MRI, SPECT/MRI, and SPECT/iMRI, respectively. Images are from Patient S4.
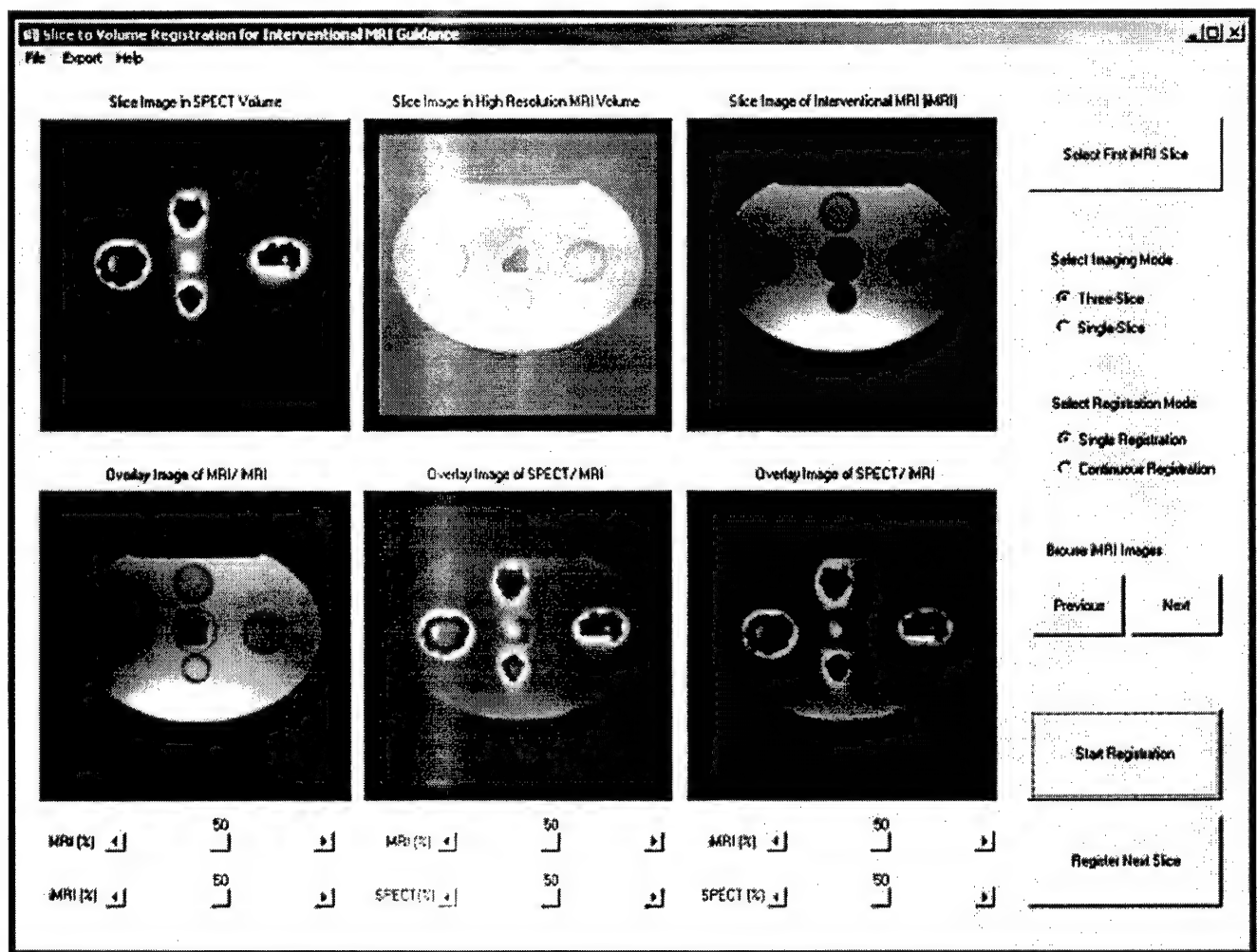

Fig. 3. Simulation experiments with phantom using registration and fusion software. The top three windows from left to right show corresponding registered SPECT, high resolution MRI, and iMRI images, respectively. The bottom three windows from left to right show the fused images, iMRI/MRI, SPECT/MRI, and SPECT/iMRI, respectively. Other buttons and sliders control the configuration and registration.

Reference List

[1] J.S.Lewin, C.F.Connell, J.L.Duerk, Y.C.Chung, M.E.Clampitt, J.Spisak, G.S.Gazelle, and J.R.Haaga, "Interactive MRI-guided radiofrequency interstitial thermal ablation of abdominal tumors: Clinical trial for evaluation of safety and feasibility," *Journal of Magnetic Resonance Imaging*, vol. 8, pp. 40-47, 1998.

[2] D.L.Wilson, A.Carrillo, L.Zheng, A.Gene, J.L.Duerk, and J.S.Lewin, "Evaluation of 3D image registration as applied to MR-guided thermal treatment of liver cancer," *Journal of Magnetic Resonance Imaging*, vol. 8, pp. 77-84, 1998.

[3] A.Carrillo, J.L.Duerk, J.S.Lewin, and D.L.Wilson, "Semiautomatic 3-D image registration as applied to interventional MRI liver cancer treatment," *IEEE Transactions on Medical Imaging*, vol. 19, pp. 175-185, 2000.

[4] D.B.Sodee, N.Malguria, P.Faulhaber, M.I.Resnick, J.Albert, and G.Bakale, "Multicenter ProstaScint imaging findings in 2154 patients with prostate cancer," *Urology*, vol. 56, pp. 988-993, 2000.

[5] J.Scheidler, H.Hricak, D.B.Vigneron, K.K.Yu, D.L.Sokolov, L.R.Huang, C.J.Zaloudek, S.J.Nelson, P.R.Carroll, and J.Kurhanewicz, "Prostate cancer: Localization with three-dimensional proton MR spectroscopic imaging - Clinicopathologic study," *Radiology*, vol. 213, pp. 473-480, 1999.

[6] R.K.Tenhaken, J.D.Forman, D.K.Heimburger, A.Gerhardsson, D.L.Mcshan, C.Pereztamayo, S.L.Schoeppel, and A.S.Lichter, "Treatment planning issues related to prostate movement in response to differential filling of the rectum and bladder," *International Journal of Radiation Oncology Biology Physics*, vol. 20, pp. 1317-1324, 1991.

[7] B.W.Fei, A.Wheaton, Z.Lee, J.L.Duerk, and D.L.Wilson, "Automatic MR volume registration and its evaluation for the pelvis and prostate," *Physics in Medicine and Biology*, vol. 47, pp. 823-838, 2002.

[8] H.Gray. *Anatomy, Descriptive and Surgical (The classic collector's edition).* New York: Gramercy Books, 1977.

[9] A.Collignon, F.Maes, D.Delaere, D.Vandermeulen, P.Suetens, and G.Marchal, "Automated multimodality image registration using information theory,"*Information Processing in Medical Imaging:* *Proc. 14th International Conference (IPMI'95)*, Computational Imaging and Vision,pp. 287-298, 1995.

[10] W.H.Press, S.A.Teukolsky, W.T.Vellerling, and B.P.Flannery. *Numerical Recipes in C: The Art of Scientific Computing, Second Edition.* New York: The Press Syndicate of the Cambridge University, 1992.

[11] B.W.Fei, J.L.Duerk, D.T.Boll, J.S.Lewin, and D.L.Wilson, "Slice to volume registration and its potential application tointerventional MRI guided radiofrequency thermal ablation of prostate cancer," *IEEE Transactions on Medical Imaging*, vol. 22, no. 4, pp. 515-525, 2003.

[12] B.W.Fei, J.L.Duerk, and D.L.Wilson, "Automatic 3D Registration for Interventional MRI-Guided Treatment of Prostate Cancer," *Computer Aided Surgery*, vol. 7, pp. 257-267, 2002.

[13] F.Maes, A.Collignon, D.Vandermeulen, G.Marchal, and P.Suetens, "Multimodality image registration by maximization of mutual information," *IEEE Transactions on Medical Imaging*, vol. 16, pp. 187-198, 1997.

[14] D.B.Sodee, R.J.Ellis, M.A.Samuels, J.P.Spirnak, W.F.Poole, C.Riester, D.M.Martanovic, R.Stonecipher, and E.M.Bellon, "Prostate cancer and prostate bed SPECT imaging with ProstaScint (R): Semiquantitative correlation with prostatic biopsy results," *Prostate*, vol. 37, pp. 140-148, 1998.

[15] A.Macovski, "Noise in MRI," *Magnetic Resonance in Medicine*, vol. 36, pp. 494-497, 1996.

[16] H.M.Hudson and R.S.Larkin, "Accelerated image-reconstruction using ordered subsets of projection data," *IEEE Transactions on Medical Imaging*, vol. 13, pp. 601-609, 1994.

[17] B.Likear and F.Pernus, "Registration of serial transverse sections of muscle fibers," *Cytometry*, vol. 37, pp. 93-106, 1999.

[18] B.W.Fei, C.Kemper, and D.L.Wilson, "Three-dimensional warping registration of the pelvis and prostate,"*Proceedings of SPIE Medical Imaging on Image Processing*, vol. 4684, pp. 528-537, 2002.

[19] B.W.Fei, C.Kemper, and D.L.Wilson, "A comparative study of warping and rigid body registration for the prostate and pelvic MR volumes," *Computerized Medical Imaging and Graphics*, vol. 27, pp. 267-281, 2003.

Image Registration for Interventional MRI Guided Procedures: Interpolation Methods, Similarity Measurements, and Applications to the Prostate

Baowei Fei,[1] Zhenghong Lee,[2,1] Jeffery L. Duerk,[2,1] David L. Wilson[1,2]

[1] Department of Biomedical Engineering
Case Western Reserve University, Cleveland, OH 44106, USA
{BXF18, DLW} @po.cwru.edu

[2] Department of Radiology, University Hospitals of Cleveland
Cleveland, OH 44106, USA. {Lee, Duerk}@uhrad.com

Abstract. Nuclear medicine can detect and localize tumor in the prostate not reliably seen in MR. We are investigating methods to combine the advantages of SPECT with interventional MRI (iMRI) guided radiofrequency thermal ablation of the prostate. Our approach is to first register the low-resolution functional images with a high resolution MR volume. Then, by combining the high-resolution MR image with live-time iMRI acquisitions, we can, in turn, include the functional data and high-resolution anatomic information into the iMRI system for improved tumor targeting. In this study, we investigated registration methods for combining noisy, thick iMRI image slices with high-resolution MR volumes. We compared three similarity measures, i.e., normalized mutual information, mutual information, and correlation coefficient; and three interpolation methods, i.e., re-normalized sinc, tri-linear, and nearest neighbor. Registration experiments showed that transverse slice images covering the prostate work best with a registration error of ≈ 0.5 mm as compared to our volume-to-volume registration that was previously shown to be quite accurate for these image pairs.

1 Introduction

Nuclear medicine can detect and localize tumor in the prostate not reliably seen in MR.[1] We are investigating methods to combine the advantages of SPECT with interventional MRI (iMRI) guided radiofrequency (RF) thermal ablation for the treatment of the prostate cancer. Our idea is to first register the low-resolution functional images with a high resolution MRI.[2] Then by registering the high-resolution MR volume with live-time iMRI acquisitions, we can, in turn, map the functional data and high-resolution anatomic information to iMRI images to aid tumor targeting. We previously reported a method for the registration of noisy, thick iMRI image slices with high-resolution MR volumes with simulated [3] and actual iMRI images.[4] In this report, we compared three interpolation methods and three similarity measures for this application. Hundreds of registration experiments were performed with 12 pairs of MR volume images acquired from four healthy volunteers.

2 Registration Algorithms

2.1 Three Interpolation Methods

We investigated three interpolation methods, i.e., re-normalized sinc interpolation,[5] tri-linear, and nearest neighbor.

Let the original data set be I_{org}, the re-formatting data set I_{new}. The conventional sinc interpolation with a cosine Hamming window is described as below.[5,6]

$$I_{new}(x, y, z) = \sum_X \sum_Y \sum_Z I_{org}(X, Y, Z) \cdot H(x, X, R) \cdot H(y, Y, R) \cdot H(z, Z, R)$$

where $H(a, A, R) = \dfrac{\sin[\pi(a - A)]}{2\pi(a - A)} \cdot \left\{ 1 + \cos[\pi(a - A) / R + 1] \right\}$,

and X, Y, Z, represent the coordinates of (I_{org}); x, y, z the coordinates of (I_{new}); A is a symbol representing X, Y, or Z, and a represents x, y, or z; and R is the kernel size. The Hamming function eliminates problems with oscillatory effects at discontinuities and guarantees that the convolution coefficients fall of to zero at the edge of the sinc kernel (i.e., at $|a|=R+1$, where $R=5$ in this study).[5]

In our implementation, we used the re-normalized sinc interpolation method because it could make significant improvement in performance of the conventional sinc interpolation.[5] We replaced H in the above equation with

$$H_{new}(a, A, R) = H(a, A, R) \Big/ \sum_A H(a, A, R) = H(a, A, R) \Big/ |H(a)|.$$

2.2 Three Similarity Measurements

We used three similarity measures, normalized mutual information (NMI), mutual information (MI), and correlation coefficient (CC), in our registration. One image R is the *reference*, and the other F is *floating*. Their mutual information MI is given below.[7,8]

$$MI = \sum_{r,f} p_{RF}(r, f) \log \frac{p_{RF}(r, f)}{p_R(r) \cdot p_F(f)}$$

The joint probability $p_{RF}(r, f)$ and the marginal probabilities $p_R(r)$ of the reference image and $p_F(f)$ of the floating image, can be estimated from the normalized joint intensity histograms. We used the NMI version proposed by Maes.[8]

$$NMI = \frac{2MI}{H(R) + H(F)}$$

where $H(R) = -\sum_r p_R(r) \log p_R(r)$ and $H(F) = -\sum_f p_F(f) \log p_F(f)$.

The correlation coefficient CC is given below.[9]

$$CC = \frac{\sum (R(r) - \overline{R})(F(f) - \overline{F})}{\sqrt{\sum (R(r) - \overline{R})^2 \sum (F(f) - \overline{F})^2}}$$

Here $\overline{R}$, $\overline{F}$ denote the average intensities of the reference and floating images and the summation includes all voxels within the overlap of both images.
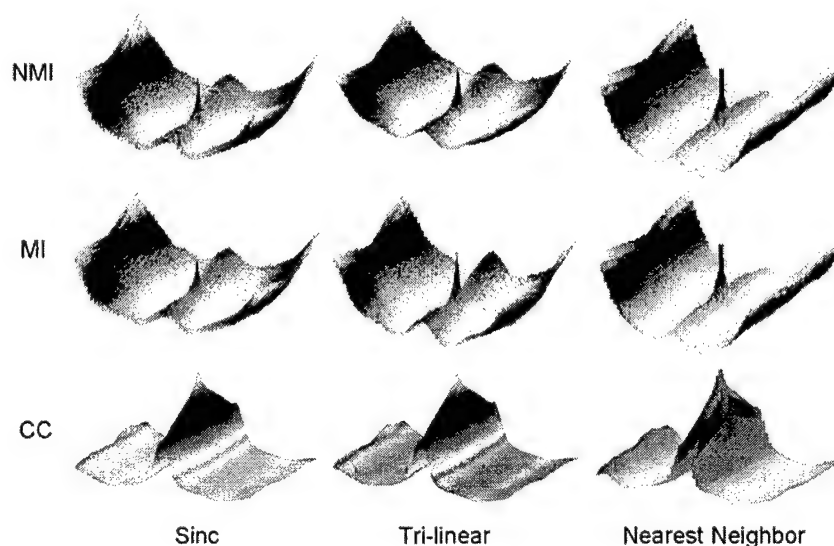

Fig. 1 Similarity surfaces are plotted as a function of translations at the 1/4 resolution in the multi-resolution registration process. Two high-resolution MRI volumes were registered, and they are down sampled by 1/4 along each linear dimension, giving a distance between voxel centers of ≈ 5.5 mm. From the optimal parameters, we computed the similarity values of the simulated iMRI and MRI images as a function of translations along the coronal (anterior-posterior) and sagittal (left-right) axis. From top to bottom, normalized mutual information (NMI), mutual information (MI), and correlation coefficient (CC) surfaces are plotted. From left to right, sinc, tri-linear, and nearest neighbor interpolations are used to obtain the floating images, respectively. The noisey NMI/MI surfaces show a false global maximum and many local maxima. CC surfaces are much smoother indicating its suitability for low resolution. Nearest neighbor has a flat peak with a width of one voxel in similarity surfaces. Images are from volunteer S2.

2.3 Comparison of Similarity Surfaces

We plot the similarity surfaces for the three similarity measures, NMI, MI, and CC, at different resolutions; and we determine their suitability for SV registration. At *1/4 resolution*, we resampled images so as to give 1/4 number of the voxels along each linear dimension. At *full resolution*, we used the full number of voxels. We plot the similarity measures as a function of translations. After two typical high-resolution MR volumes were registered,[10] values were plotted with the origin as the optimal

transformation. We calculated similarity values while moving the simulated iMRI image relative to the high-resolution MR image along coronal (anterior-posterior) and sagittal (left-right) axis. When obtaining floating images, we used the three different interpolation methods.

At 1/4 resolution (Fig. 1), CC surfaces are much smoother than NMI and MI, which are noisy and contain a false global maximum that could lead to a false answer and many local maxima.[11] From these figures, we infer that CC is better at low resolution. Comparing CC surfaces of different interpolations, sinc and tri-linear have similar surfaces, and tri-linear is better than nearest neighbor. For this application, we chose tri-linear interpolation instead of sinc because it is much faster and because it has comparable performance. Finally, we used CC and tri-linear at low resolution.

At full resolution (Fig. 2), NMI and MI surfaces are much more peaked than CC that infers good optimization accuracy, but once again there is high frequency noise in the NMI and MI curves, far from the optimum, that gives rise to local maxima that must be avoided. Comparing three interpolation methods, sinc gave the sharpest peak at the optimum; nearest neighbor interpolation gave a flat peak with a width of one voxel; and tri-linear gave a result between the other two. As stated above, tri-linear is much faster that sinc with similar performance. NMI and MI have no significant difference but NMI is a little bit robust in our implementation. We chose NMI and tri-linear at the full resolution.
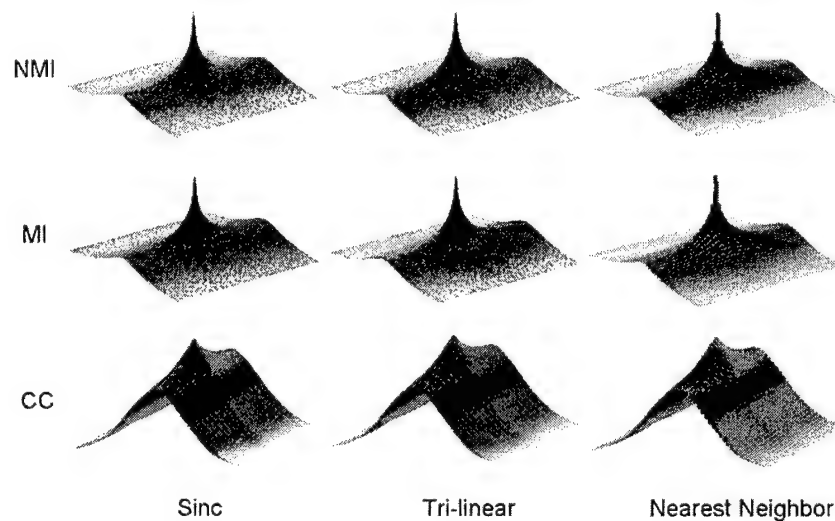

Fig. 2 Similarity functions are plotted as a function of translations at full resolution. Many details are given in the legend of Fig. 1. NMI and MI surfaces are much peaked than CC, especially with sinc and tri-linear interpolation. The voxel is isotropic with 1.4 mm on a side. Image data are the same used in Fig. 1.

2.4 Combination of Normalized Mutual Information and Correlation Coefficient

As a result of the above analyses, we created a registration algorithm for prostate MR images. We define the iMRI image slice to be the *reference* image; the matching slice from the high-resolution MRI volume is the *floating* image. We use a multi-resolution approach and perform registration from low to high resolution. We use CC at the two lower resolutions because it gives fewer local maxima and because it can be calculated faster than NMI. We use NMI at full resolution because of its peaked surface. To avoid local maxima, we include a restarting feature where registration is restarted with randomly perturbed parameters obtained from a uniform distribution about the initial transformation values at the current resolution being used. The algorithm restarts until the absolute CC is above a threshold of 0.5 as experimentally determined or the maximum number of restarts is reached.

For registration, we use a rigid body transformation (three translations and three rotations). For optimization, we use the downhill simplex method of Nelder and Mead.[12] Optimization of similarity ends either when the maximum number of calculations is reached (typically 500) or when the fractional change in the similarity function is smaller than a tolerance (typically 0.001). We use IDL (Interactive Data Language, Research System Inc., Boulder, CO.) as the programming language. We use an initial guess assuming an identity transformation, i.e., all initial translation and rotation parameters are zero, because the patient is normally oriented approximately the same way from one scan to the next. We set the maximum numbers of restarts at 10, 5, and 3, from low to high resolution, respectively.

2.5 Registration Evaluation

We used a variety of evaluation methods. We used *RegViz*, a program created in IDL in our laboratory with multiple visualization and analysis methods. First, we manually segmented prostate boundaries in image slices and copied them to corresponding slices. This enabled visual determination of the overlap of prostate boundaries over the entire volume. Second, color overlay displays were used to evaluate overlap of structures. To visualize potential differences, it was quite useful to interactively change the contribution of each image using the transparency scale. Third, we used a sector display, which divided the reference and registered images into rectangular sectors and created an output image by alternating sectors from the two input images. Even subtle shifts of edges would be clearly seen.

Our quantitative evaluation method for slice to volume registration was to compare SV and VV registration.[10] For volume pairs acquired over a short time span from a supine subject with legs flat on the table, prostates were well aligned and prostate centroid displacements were typically < 1 mm. The registration accuracy as determined from displacements of pelvic bony landmarks was 1.6 ± 0.2 mm, a value comparable to error associated with locating the landmarks.[10] To compare SV and VV registration, we defined a rectangular volume of interest (VOI) just covering the prostate and calculated voxel displacements between the two registrations. We defined the SV registration as being *successful* when the 3D displacement was less than 2.0 mm.

3 Experimental Methods

3.1 Imaging Experiments

We acquired high resolution MRI volumes from a 1.5 T Siemens MRI system (Magnetom Symphony, Siemens Medical Systems, Erlangen, Germany). An 8-element phased array body coil was used to ensure coverage of the prostate with a uniform sensitivity. We used a 3D rapid gradient echo sequence (PSIF) designed to acquire the spin-echo component of the steady state response, rather then the free induction decay. The sequence with 9.4/5.0/60 (TR/TE/flip) yielded 160 x 256 x 128 voxels over a 219 x 350 x 192-mm rectangular FOV and 1.4 x 1.4 x 1.5-mm voxels oriented to give the highest resolution for transverse slices. There was over sampling at 31% in the slice direction to reduce aliasing artifacts. The acquisition time was 4.3 min. The sequence gave excellent image contrast for the prostate and its surroundings.

We acquired high resolution MRI volumes from four volunteers S1-S4. For each volunteer, three image volumes were obtained with an imaging session. Each volume was acquired with compatible conditions. Volunteers laid supine with legs flat similar to the position in routine MR scanning. Between volume acquisitions, volunteers got off the MRI table, stretched, and walked around to ensure that they would assume a different position when they laid back on the table. The coil array was centered on the prostate. All images of a volunteer were acquired with the same MRI acquisition parameters. In total, there are 12 pairs of high-resolution MRI volumes for registration.

We used the high-resolution MRI volumes to simulate iMRI images by creating thick slices and adding noise. MR noise is described by the Rician distribution,[13] but at reasonably high signal values, the noise is accurately approximated with Gaussian white noise.[14] We added Gaussian noise to the simulated iMRI slice images. Clinically, we typically use an iMRI slice thickness of 4.0 - 6.0 mm. We averaged 3 1.4 mm thick slices to create a 4.2 mm thick slice.

Additionally, we acquired real iMRI images from volunteers S1-S3 using a clinical 0.2 T C-arm open MR scanner (Siemens Open Symphony, Erlangen, Germany). We used a two-dimensional (2D) PSIF sequence with 15.2/7.4/45 (TR/TE/FA) for image slice acquisitions. The iMRI slices were 128x128 with in-plane pixel size of 2.8x2.8 mm and with effective slice thickness of 5 mm.

3.2 Registration Experiments

We used 12 pairs of high-resolution MR volumes to perform registration experiments. For each volume pair, we extracted data from one volume to simulate thick iMRI image slices; and then we registered the simulated image slices to the other volume. We desire an iMRI slice image acquisition method that gives robust, accurate registrations and is relatively insensitive to acquisition parameters. Hence, we performed experiments to determine the dependence on slice orientation (transverse, sagittal and coronal), on slice position relative to the prostate (above, centered, and below) and on image noise from fast imaging techniques.

We also performed SV registration experiments using actual iMRI images. We registered actual iMRI image slices with high-resolution (1.5 T system) MR volumes

and visually evaluated results. For each volunteer S1-S3, there were three high-resolution MR volumes and 30 iMRI image slices giving 90 SV registration experiments, and a total of 270 experiments.
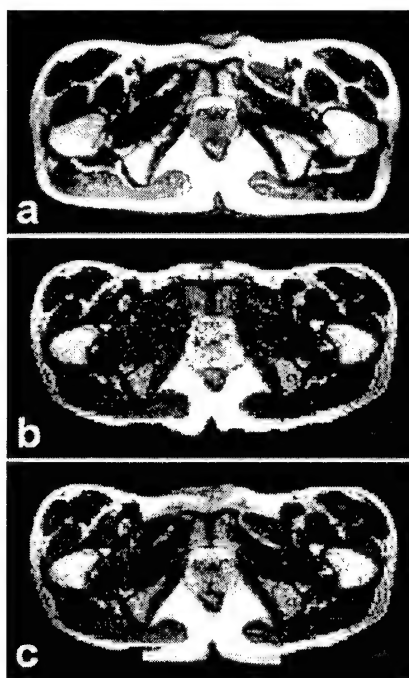

Fig. 3 Prostate images of high resolution MRI (a) and interventional MRI (b). The rectangular region at the center of image (c) is the overlay display of both images. The prostate matches well. Images are from S3.

4 Results

4.1 Simulated Images

Using simulated iMRI images, we determined SV registration results for slices near the prostate in the three standard orthogonal orientations. Comparing to VV, average registration errors were 0.4 mm, 0.5 mm, and 2.6 mm for transverse, coronal and sagittal slices covering the prostate, respectively. Transverse slices worked best because they contained many relatively rigid anatomical structures. Coronal slices worked next best. Sagittal slices gave the largest error because they contained a large portion of the deformable bladder and rectum.

The registration is insensitive to noise. Typical iMRI SNR under clinical conditions is about 25. Even when noise much exceeded this normal situation, registration results were quite good. A 100% success rate was achieved with an acceptance criterion of < 2.0 mm even when SNR was as bad as 10.

4.2 Actual iMRI Images

Registration of actual iMRI image slices with a high-resolution MR volume was successful. The contours overlap and overlay images show that the prostate matches very well. Other visual inspections also demonstrate excellent registration. Note that a single iMRI image was used to produce this registration result.

4.3 Algorithm Implementation

Computation time and registration accuracy are two main factors to consider when choosing interpolation methods. Using tri-linear interpolation, the time for an SV registration was typically about 5 sec on a Pentium IV, 1.8 GHz CPU, with 1Gbyte of memory. When the re-normalized sinc interpolation method was used, the time was ≈ 10 min, a duration not acceptable for our application. The algorithm was written in IDL and could probably be made faster in a lower level language such as C. We did not use nearest neighbor because of insufficient accuracy as deduced from its flat peak of the similarity surfaces in Figure 2. A call to the Simplex optimization typically resulted in 50 to 150 similarity evaluations before the tolerance value (0.001) was reached.

4 Discussion and Conclusion

The comparison of similarity surfaces enabled us to design a robust, fast, and accurate registration algorithm for the potential applications of iMRI-guided thermal ablation of the prostate cancer. A single iMRI image slice achieved nearly the same accuracy as obtained from volume-to-volume registration. Since live-time iMRI images are used for guidance and registered images are used for adjunctive information, the registration accuracy is very probably adequate. As compared to a typical SPECT and/or iMRI slice thickness of ≥ 3.0 mm, SV registration is quite accurate.

If one were to use functional or high-resolution MR images directly for tumor targeting within the relatively small prostate, the requirements for registration accuracy would be great. However, fused image data will not be used blindly. Rather, these visualizations will be used as a guide. Physicians will always use the live-time iMRI images for needle guidance. With proper visualization tools, physicans should be able to mentally account for any small registration errors. Moreover, the functional images might enable one to find cancer features in the iMRI images.

Finally, we conclude that it is quite feasible to include previously acquired high-resolution MRI and nuclear images into iMRI-guided treatment procedures. We are beginning to explore this application in animal experiments.

Acknowledgements

References

1. D.B.Sodee, N.Malguria, P.Faulhaber, M.I.Resnick, J.Albert, and G.Bakale, "Multicenter ProstaScint imaging findings in 2154 patients with prostate cancer," *Urology*, vol. 56, pp. 988-993, 2000.
2. Z.Lee, D.B.Sodee, J.L.Duerk, A.D.Nelson, and M.S.Berridge, "Automatic registration of SPECT-MRI in the pelvis," *Journal of Nuclear Medicine*, vol. 41, pp. 232, 2000.
3. B.W.Fei, J.L.Duerk, and D.L.Wilson, "Automatic 3D Registration for Interventional MRI-Guided Treatment of Prostate Cancer," *Computer Aided Surgery*, vol. 7, pp. 257-267, 2002.
4. B.W.Fei, J.L.Duerk, D.T.Boll, J.S.Lewin, and D.L.Wilson, "Slice to volume registration and its potential application tointerventional MRI guided radiofrequency thermal ablation of prostate cancer," *IEEE Transactions on Medical Imaging*, vol. 22, 2003.
5. N.A.Thacker, A.Jackson, D.Moriarty, and E.Vokurka, "Improved quality of re-sliced MR images using re-normalized sinc interpolation," *Journal of Magnetic Resonance Imaging*, vol. 10, pp. 582-588, 1999.
6. J.V.Hajnal, N.Saeed, E.J.SOAR, A.Oatridge, I.R.Young, and G.Bydder, "A registration and interpolation procedure for subvoxel matching of serially acquired MR images," *Journal of Computer Assisted Tomography*, vol. 19, pp. 289-296, 1995.
7. A.Collignon, F.Maes, D.Delaere, D.Vandermeulen, P.Suetens, and G.Marchal, "Automated multimodality image registration using information theory,"*Information Processing in Medical Imaging: Proc. 14th International Conference (IPMI'95)*, Computational Imaging and Vision,pp. 287-298, 1995.
8. F.Maes, A.Collignon, D.Vandermeulen, G.Marchal, and P.Suetens, "Multimodality image registration by maximization of mutual information," *IEEE Transactions on Medical Imaging*, vol. 16, pp. 187-198, 1997.
9. W.H.Press, S.A.Teukolsky, W.T.Vellerling, and B.P.Flannery. *Numerical Recipes in C: The Art of Scientific Computing, Second Edition.* New York: The Press Syndicate of the Cambridge University, 1992.
10. B.W.Fei, A.Wheaton, Z.Lee, J.L.Duerk, and D.L.Wilson, "Automatic MR volume registration and its evaluation for the pelvis and prostate," *Physics in Medicine and Biology*, vol. 47, pp. 823-838, 2002.
11. J.P.W.Pluim, J.B.A.Maintz, and M.A.Viergever, "Image registration by maximization of combined mutual information and gradient information," *IEEE Transactions on Medical Imaging*, vol. 19, pp. 809-814, 2000.
12. J.Nelder and R.A.Mead, "A simplex method for function minimization," *Computer Journal*, vol. 7, pp. 308-313, 1965.
13. A.Macovski, "Noise in MRI," *Magnetic Resonance in Medicine*, vol.36, pp. 494-497, 1996.
14. R.C.Gregg and R.D.Nowak, "Noise removal methods for high resolution MRI," *IEEE Nuclear Science Symposium*, vol. 2, pp. 1117-1121, 1997.

Image Registration and Fusion for Interventional MRI Guided Thermal Ablation of the Prostate Cancer

Baowei Fei [1], Zhenghong Lee [2,1], Daniel T. Boll [2],
Jeffery L. Duerk [2,1], Jonathan S. Lewin [2,1,3], David L. Wilson [1,2]

[1] Department of Biomedical Engineering
Case Western Reserve University, Cleveland, OH 44106, USA
{BXF18, DLW} @po.cwru.edu

[2] Department of Radiology
University Hospitals of Cleveland, Cleveland, OH 44106, USA
{Lee, Boll, Duerk, Lewin}@uhrad.com

[3] Departments of Oncology and Neurological Surgery,
University Hospitals of Cleveland, OH 44106, USA

Abstract. We are investigating interventional MRI (iMRI) guided thermal ablation treatment of the prostate cancer. Functional images such as SPECT can detect and localize tumor in the prostate not reliably seen in MRI. We intend to combine the advantages of SPECT with iMRI-guided treatments. Our concept is to first register the low-resolution SPECT with a high resolution MRI volume. Then by registering the high-resolution MR image with iMRI acquisitions, we can, in turn, map the functional data and high-resolution anatomic information to iMRI images for improved tumor targeting. For the first step, we used a mutual information registration method. For the latter, we developed a robust slice to volume (SV) registration algorithm. Image data were acquired from patients and volunteers. Compared to our volume-to-volume registration that was previously evaluated to be quite accurate, the SV registration accuracy is about 0.5 mm for transverse images covering the prostate. With our image registration and fusion software, simulation experiments show that it is feasible to incorporate SPECT and high resolution MRI into the iMRI-guided treatment.

1 Introduction

We use an interventional magnetic resonance imaging (iMRI) system to guide minimally invasive treatments, including the radiofrequency (RF) thermal ablation of abdominal cancers. [1-3] The iMRI system consists of a 0.2 T, clinical C-arm open MRI scanner, an in-room RF-shielded liquid crystal monitor, an MR compatible mouse, a foot pedal, and a RF device. We are currently investigating the extension of these techniques to the treatment of prostate cancer. Since MRI does not reliably show prostate tumors, we intend to incorporate nuclear medicine images with higher sensitivity for detecting and localizing prostate tumors. [4,5] We will first register the low-resolution functional SPECT images with a high resolution MRI volume. Then by registering the high-resolution MR volume with iMRI acquisitions, we can, in turn, map the functional data and high-resolution anatomic information to iMRI images for improved tumor targeting. If this procedure is successful, then a variety of potential visualization tools can help the physician appropriately localize and apply treatments.

In next sections, we will report a three dimensional registration method for SPECT and high resolution MRI volumes, a slice to volume registration algorithm for iMRI thick slices and high resolution MRI volume, and image registration and fusion software for potential applications in iMRI-guided thermal ablation of the prostate.

2 Registration Algorithms

2.1 Registration of SPECT and High Resolution MRI Volumes

A mutual information algorithm was applied in this study to the registration of pelvic image volumes from MRI and SPECT for potential use in prostate cancer diagnosis, staging, and treatment planning. Mutual information (MI) was chosen because of its potential to align multi-modality images[6,7]. Registration of SPECT and MR images is challenging because the two image types have very different spatial resolutions and image features. The pelvic region is difficult for alignment between images from the two scans. Before registration, both SPECT and MRI volumes were resized using tri-linear interpolation to create volumes matrix of 128x128x128 with 3 mm isotropic voxels, a voxel size between that of the two scans. The standard parameter set for automatic registration include: 256 intensity levels for each volume, the entire 2D joint histogram, the full field of view of 128x128x128 voxels for both volumes, and no masking or cropping of either volume.

2.2 Registration of iMRI Slice and High Resolution MRI Volume

We used two similarity measures, mutual information[8] and correlation coefficient (CC),[9] in our registration. We used a similar algorithm as previously reported by us.[10] We use a multi-resolution approach and perform registration from low to high resolution. We use correlation coefficient at the two lower resolutions because it gives fewer local maximums and because it can be calculated faster than MI.[11] We use MI at full resolution because the peaked similarity function gives a more precise solution than CC.[12] To avoid local maximums, we include a restarting feature where registration is restarted with randomly perturbed parameters obtained from a uniform distribution about the initial transformation values at the current resolution being used.[13] The algorithm restarts until the absolute CC is above an experimentally determined threshold or the maximum number of restarts is reached.

3 Experimental Methods

3.1 SPECT Image Acquisition

We acquired SPECT images from three patients S1-S3 with either high Gleason scores (>5) from biopsy or rising PSA level (>10 mcg/L, prostate specific antigen) or palpatation staging beyond stage T1. After patient eligibility was established, patients gave informed consent. The Institutional Review Board of the University Hospitals of Cleveland approved the imaging protocol. The radiotracer used for SPECT imaging is ProstaScint® (Cytogen Corporation, Princeton, NJ), a monoclonal antibody that binds to prostate-specific membrane antigen (PSMA).

Approximately four days after injecting 5 mCi ProstaScint®, the abdominal region and pelvic region were scanned using a two-head Siemens E.CAM⁺ camera (Siemens Medical System, Inc., Hoffman Estates, IL). The evening before the scanning, patients were asked to perform a bowel prep with Fleet R Prep Kit #3 (Fleet Pharmaceuticals, Lynchburg, VA). Images were acquired with a medium energy collimator and 15% energy window. The acquisition parameters included a step-and-shoot motion, a 128 x 128 pixel matrix for each projection, an imaging time of 25 sec per stop, and a total of 120 stops over a full 360° rotation. The field of view of was 53.3 x 38.7-cm. The iterative image reconstruction algorithm OSEM (ordered subsets expectation maximization) [14] was used to reconstruct the SPECT images with 8 subsets and 10 iterations. The SPECT images were comprised of isotropic voxels with size of 4.8x4.8x4.8-mm. Each patient had one SPECT scan of the pelvis.

3.2 High Resolution MR Image Acquisitions

High-resolution MRI volumes were acquired using a 1.5 T Siemens MRI system (Magnetom Symphony, Siemens Medical Systems, Erlangen, Germany). An 8-element phased array body coil was used to ensure coverage of the prostate with a uniform sensitivity. Typically two anterior and two posterior elements were enabled for signal acquisition. We used two different MR sequences.

First, we used a 3D rapid gradient echo sequence (PSIF) designed to acquire the spin-echo component of the steady state response, rather than the free induction decay. The spin echo component forms immediately prior to the RF pulse; it is shifted toward the prior RF pulse through appropriate gradient waveform design. The sequence with 9.4/5.0/60 (TR/TE/flip) yields 160x256x128 voxels over a 219x350x192-mm rectangular FOV. There is over sampling at 31% in the slice direction to reduce aliasing artifacts. The acquisition time is 4 min and 15 sec. This sequence gave excellent image contrast for the prostate and its surroundings. It was used to acquire volumes for volunteers S4-S6. Second, we used a 3D RF spoiled gradient echo steady state pulse sequence (FLASH) with TR/TE/flip parameters of 12/5.0/60 which give 256 x 256 x 128 voxels over a 330x330x256-mm field of view (FOV) to yield 1.3x1.3x2.0-mm voxels oriented to give the highest resolution for transverse slices. The acquisition time is 5 min and 38 sec. This sequence is good for pelvic imaging but is not ideal for the prostate. It was used to acquire volumes for patients S1-S3.

When acquiring MR volumes, volunteers laid supine in a manner similar to the diagnostic position in routine MR scanning. Between volume acquisitions, volunteers got up from the MR table, stretched, and walked around to ensure that they would assume a different position when they laid back on the table. The coil array was centered on the prostate. We acquire one volume from each of patients S1-S3 and three volumes from each of volunteers S4-S6.

3.3 Interventional MRI Image Acquisitions and Simulation

We acquired iMRI images using a clinical 0.2 T C-arm open MR scanner (Siemens Open Symphony, Erlangen, Germany) modified for interventional MRI procedures and in this paper referred to as the iMRI system. We used a 3D PSIF with 25/13/60 (TR/TE/FA) for image volume acquisitions and two-dimensional (2D) PSIF with

15.2/7.4/45 (TR/TE/FA) for image slice acquisitions. The iMRI volumes were 256x256x100 with voxel size of 1.3x1.3x1.4 mm. The iMRI slices were 128x128 with in-plane pixel size of 2.8x2.8 mm and with effective slice thickness of 5 mm.

We acquired iMRI images under the conditions simulating the treatment application. The volunteer was supine, and his legs were supported at 30°-60° relative to the horizon and separated in a "V" with an angle of 60°-90° between two legs. This is similar to the lithotomy position used in prostate therapies, and it should provide access for needle insertion in brachytherapy or RF thermal ablation. We call this the treatment position. For each of the volunteers S4-S6, we acquired two volumes and 30 iMRI image slices covering the prostate. They included 10 transverse, 10 coronal, and 10 sagittal image slices. We call these images *"actual"* iMRI images to differentiate them from later experiments using *"simulated"* iMRI slices.

To test a variety of clinical conditions, we used high-resolution MRI volumes to simulate iMRI images by creating thick slices and adding noise and receive coil inhomogeneity. Clinically, we typically use an iMRI slice thickness of 4.0 - 6.0 mm. We averaged 3 slices 1.4 mm thick to create a 4.2 mm thick slice. We added noise to the simulated iMRI image.[15,16]

3.4 Registration and Fusion Experiments

We performed three dimensional MI registration of MRI and SPECT images using three pairs of data sets from patients S1-S3. Before registration, we preprocessed both MR and SPECT images such as intensity scaling and isotropic processing.

We used nine pairs of high-resolution MR volumes to perform simulated slice to volume registration experiments. For each volume pair, we extracted data from one volume to simulate thick iMRI image slices; and then we registered the simulated image slices to the other volume. We desire an iMRI slice image acquisition method that gives robust, accurate registrations and is relatively insensitive to acquisition parameters. Hence, we performed experiments to determine the dependence on slice orientation (transverse, sagittal and coronal), on slice position relative to the prostate (above, centered, and below) and on image noise from fast imaging techniques.

We performed SV registration experiments using actual iMRI images. We visually evaluated results. For each volunteer S4-S6, there were three high-resolution MR volumes and 30 iMRI image slices giving 90 SV registration experiments, and a total of 270 experiments.

We simulated the iMRI-guided procedures using our image registration and fusion software that are specially designed for this application. Before treatment, we acquired SPECT and high resolution MRI volumes from the same patient. Second, we registered the two images and transferred the pair of aligned data sets to a workstation that was used for slice to volume registration. Third, we connected the workstation to the iMRI scanner and obtained iMRI image slices from the scanner. Fourth, we performed slice to volume registration. Finally, the software created fused images of the three modalities for image guidance. All registration and fusion are automatic.

3.5 Registration Evaluation

Although we evaluated registration using a variety of quanitative measures, visual inspection was also employed. We used *RegViz,* a program created in IDL in our

laboratory with multiple visualization and analysis methods. First, we manually segmented prostate boundaries in image slices and copied them to corresponding slices. This enabled visual determination of the overlap of prostate boundaries over the entire volume. Second, color overlay displays were used to evaluate overlap of structures. To visualize potential differences, it was quite useful to interactively change the contribution of each image using the transparency scale. Third, we used a sector display, which divided the reference and registered images into rectangular sectors and created an output image by alternating sectors from the two input images. Even subtle shifts of edges would be clearly seen.

Registration between SPECT and MRI was devaluated by comparing automatic registration results to manual registration, our gold standard. Manual registration was done by two board-certified nuclear medicine radiologists who were blinded to the automatic registration results prior to performing registration. Manual registration was done using a software package with a graphical user interface (GUI) developed in–house, which allows graphical manipulation of volumes with six degrees of freedom in a rigid body registration. A successful automatic registration is defined as when the transformation parameters are almost equal to that of the manual registration. Displacements must be < 2 voxels (6 mm) in the x, y, or z directions and < 2 degree in rotation for the three angles measured about each of the 3 axes.

The standard evaluation method for the slice to volume registration was to compare SV and volume to volume (VV) registration.[17] It is quite reasonable to use VV registration as our gold standard because it was previously identified to be quite accurate. For volume pairs acquired over a short time span from a supine subject with legs flat on the table, following VV registration, prostates were well aligned and prostate centroid displacements typically < 1 mm. The VV registration accuracy as determined from displacements of pelvic bony landmarks was 1.6 ± 0.2 mm. To compare SV and VV registration, we defined a rectangular volume of interest (VOI) just covering the prostate and calculated voxel displacements between the two registrations. We report the average voxel displacement as an error measure. In addition, we defined the SV registration as being *successful* when the 3D displacement was less than 2.0 mm.

4 Results

4.1 Registration of iMRI Slice to High Resolution MRI Volume

We reported SV registration results for slices near the prostate in the three standard orthogonal orientations. Comparing to VV, mean and standard deviation registration errors across 9 volume pairs and 60 SV registration experiments were 0.4 mm ± 0.2 mm, 0.5 mm ± 0.2 mm, and 2.6 mm ± 1.6 mm for transverse, coronal and sagittal slices covering the prostate, respectively. Transverse slices worked best because they contain many relatively rigid anatomical structures.

Registration experiments with simulated iMRI images showed the SV registration was very insensitive to noise. We performed over 100 registration experiments with noise added to give signal to noise ratio (SNR) ranging from 20 to 5. Using the slice configurations recommended above (transverse slices near the prostate center), we

obtained 100% successful registrations (an error < 2.0 mm) for SNR's = 10, a value much worse than the clinical SNR value of ˜ 25 on our iMRI system.

For registration of actual iMRI image slices and a high-resolution MR volume, the contours overlap and overlay images show that the prostate matches very well. Other visual inspection techniques also demonstrate excellent registration. Note that a single iMRI image was used to produce this registration result.

The time for an SV registration was typically about 5 sec on a Pentium IV, 1.8 GHz CPU, with 1Gbytes of memory. The algorithm was written in IDL (Interactive Data Language, Research System Inc., CO) and could probably be made much faster in a lower level language such as C.
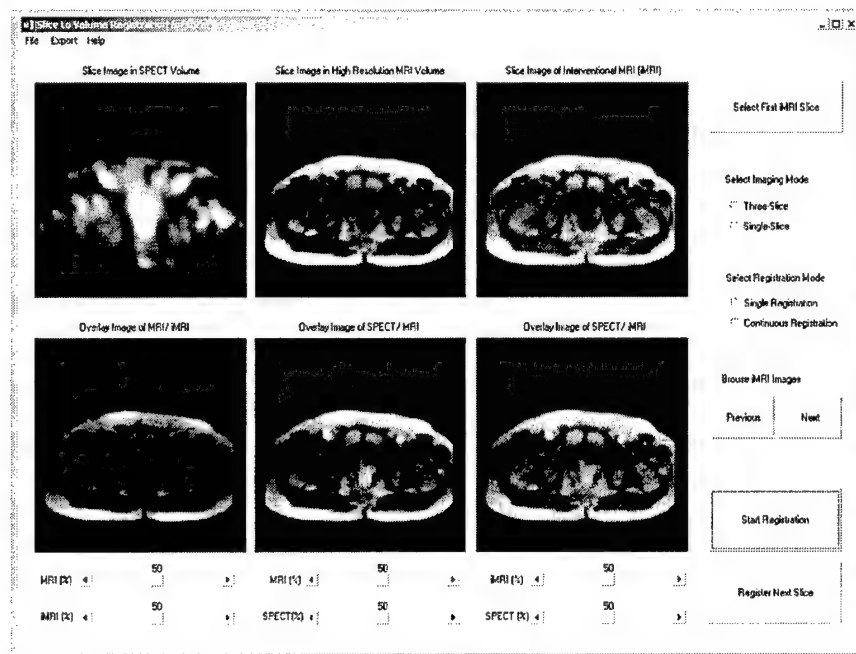

Fig. 1. User interface of the image registration and fusion software. The top three windows from left to right show corresponding registered SPECT, high resolution MRI, and iMRI images, respectively. The bottom three windows from left to right show the fused images, iMRI/MRI, SPECT/MRI, and SPECT/iMRI, respectively. Other buttons and sliders control the configuration and registration. High resolution MRI and SPECT images are from the patient S1 and the iMRI image was simulated from the high resolution MRI image.

4.2 Registration Results of SPECT and High Resolution MRI Volumes

In Figure 1, we show an example of a successful registration of SPECT and MRI. All anatomical features including the bone marrow in the femur and pubic symphysis are well aligned in the color overlay. Using the standard algorithm in Section 2.1, the MI program successfully registered the three volume pairs. The standard parameter set was defined above with the only exception that the lower-left quadrant of the joint

histogram was used for calculating MI. A successful registration was judged by the criteria defined previously.

4.3 Image Fusion and Visualization

In Fig. 1, we demonstrate the image fusion visualization software in a simulation of clinical usage. SPECT and high resolution MR images were acquired, transferred to a workstation, and registered prior to the "simulated" procedure. We then simulate acquiring thick iMRI slices, register them to the high resolution volume, and prepare the visualization. In this figure, one can see all. The registered images are shown in the three windows at the top line. After registration, the program creates fused images as displayed in the bottom windows.

5 Discussion and Conclusion

The automatic slice to volume registration algorithm is quite robust for transverse slice images covering the prostate and the registration accuracy is probably sufficiently accurate to aid iMRI-guided thermal ablation treatment. In clinical applications, physicians will always use the live-time iMRI images for needle guidance. With fused image data and visualization tools, they should be able to mentally account for any small registration errors. In addition, very often there is image evidence of cancer in MR prostate images that can perhaps be identified with the aid of functional images.

We recommend that images are obtained under comparable conditions by keeping a similar posture and by taking clinical measures to reduce rectal and bladder filling. For images acquired in quite different positions with significant deformation, we previously reported a warping registration method[18] that can correct the deformations at the expense of additional complexity, time, and possibly robustness.

We think that it is feasible to include previously acquired high-resolution MRI and nuclear images into iMRI-guided treatment procedures. Image registration and fusion would provide a useful tool for the image-guided application.

Acknowledgements

References

1. J.S.Lewin, C.F.Connell, J.L.Duerk, Y.C.Chung, M.E.Clampitt, J.Spisak, G.S.Gazelle, and J.R.Haaga, "Interactive MRI-guided radiofrequency interstitial thermal ablation of abdominal tumors: Clinical trial for evaluation of safety and feasibility," *Journal of Magnetic Resonance Imaging*, vol. 8, pp. 40-47, 1998.

2. D.L.Wilson, A.Carrillo, L.Zheng, A.Genc, J.L.Duerk, and J.S.Lewin, "Evaluation of 3D image registration as applied to MR-guided thermal treatment of liver cancer," *Journal of Magnetic Resonance Imaging*, vol. 8, pp. 77-84, 1998.

3. A.Carrillo, J.L.Duerk, J.S.Lewin, and D.L.Wilson, "Semiautomatic 3-D image registration as applied to interventional MRI liver cancer treatment," *IEEE Transactions on Medical Imaging*, vol. 19, pp. 175-185, 2000.

4. D.B.Sodee, N.Malguria, P.Faulhaber, M.I.Resnick, J.Albert, and G.Bakale, "Multicenter ProstaScint imaging findings in 2154 patients with prostate cancer," *Urology*, vol. 56, pp. 988-993, 2000.

5. J.Scheidler, H.Hricak, D.B.Vigneron, K.K.Yu, D.L.Sokolov, L.R.Huang, C.J.Zaloudek, S.J.Nelson, P.R.Carroll, and J.Kurhanewicz, "Prostate cancer: Localization with three-dimensional proton MR spectroscopic imaging - Clinicopathologic study," *Radiology*, vol. 213, pp. 473-480, 1999.

6. F.Maes, A.Collignon, D.Vandermeulen, G.Marchal, and P.Suetens, "Multimodality image registration by maximization of mutual information," *IEEE Transactions on Medical Imaging*, vol. 16, pp. 187-198, 1997.

7. D.B.Sodee, R.J.Ellis, M.A.Samuels, J.P.Spirnak, W.F.Poole, C.Riester, D.M.Martanovic, R.Stonecipher, and E.M.Bellon, "Prostate cancer and prostate bed SPECT imaging with ProstaScint (R): Semiquantitative correlation with prostatic biopsy results," *Prostate*, vol. 37, pp. 140-148, 1998.

8. A.Collignon, F.Maes, D.Delaere, D.Vandermeulen, P.Suetens, and G.Marchal, "Automated multimodality image registration using information theory,"*Information Processing in Medical Imaging: Proc. 14th International Conference (IPMI'95)*, Computational Imaging and Vision,pp. 287-298, 1995.

9. W.H.Press, S.A.Teukolsky, W.T.Vellerling, and B.P.Flannery. *Numerical Recipes in C: The Art of Scientific Computing, Second Edition.* New York: The Press Syndicate of the Cambridge University, 1992.

10. B.W.Fei, J.L.Duerk, and D.L.Wilson, "Automatic 3D Registration for Interventional MRI-Guided Treatment of Prostate Cancer," *Computer Aided Surgery*, vol. 7, pp. 257-267, 2002.

11. B.W.Fei, J.L.Duerk, D.T.Boll, J.S.Lewin, and D.L.Wilson, "Slice to volume registration and its potential application to interventional MRI guided radiofrequency thermal ablation of prostate cancer," *IEEE Transactions on Medical Imaging*, vol. 22, no. 4, pp. 515-525, 2003.

12. B.W.Fei, Frinkley K., and D.L.Wilson, "Comparison of Different Registration Algorithms for Interventional MRI-guided Treatment of the Prostate Cancer," Proceeding of SPIE on Medical Imaging: Visualization, Image guided procedures, and display, 2003.

13. B.W.Fei, A.Wheaton, Z.Lee, K.Nagano, J.L.Duerk, and D.L.Wilson, "Robust registration algorithm for interventional MRI guidance for thermal ablation of prostate cancer," Proceedings of SPIE Medical Imaging on Visualization, Display, and Image-Guided Procedures, vol. 4319, pp. 53-60, 2001.

14. H.M.Hudson and R.S.Larkin, "Accelerated image-reconstruction using ordered subsets of projection data," *IEEE Transactions on Medical Imaging*, vol. 13, pp. 601-609, 1994.

15. A.Macovski, "Noise in MRI," *Magnetic Resonance in Medicine*, vol. 36, pp. 494-497, 1996.

16. R.C.Gregg and R.D.Nowak, "Noise removal methods for high resolution MRI," *IEEE Nuclear Science Symposium*, vol. 2, pp. 1117-1121, 1997.

17. B.W.Fei, A.Wheaton, Z.Lee, J.L.Duerk, and D.L.Wilson, "Automatic MR volume registration and its evaluation for the pelvis and prostate," *Physics in Medicine and Biology*, vol. 47, pp. 823-838, 2002.

18. B.W.Fei, C.Kemper, and D.L.Wilson, "A comparative study of warping and rigid body registration for the prostate and pelvic MR volumes," *Computerized Medical Imaging and Graphics*, vol. 27, pp. 267-281, 2003.

A comparative study of warping and rigid body registration for the prostate and pelvic MR volumes

Baowei Fei[a], Corey Kemper[a], David L. Wilson[a,b,*,1]

[a]Department of Biomedical Engineering, Case Western Reserve University, 10900 Euclid Avenue, Cleveland, OH 44106, USA
[b]Department of Radiology, University Hospitals of Cleveland and Case Western Reserve University, Cleveland, OH 44106, USA

Abstract

A three-dimensional warping registration algorithm was created and compared to rigid body registration of magnetic resonance (MR) pelvic volumes including the prostate. The rigid body registration method combines the advantages of mutual information (MI) and correlation coefficient at different resolutions. Warping registration is based upon independent optimization of many interactively placed control points (CP's) using MI and a thin plate spline transformation. More than 100 registration experiments with 17 MR volume pairs determined the quality of registration under conditions simulating potential interventional MRI-guided treatments of prostate cancer. For image pairs that stress rigid body registration (e.g. supine, the diagnostic position, and legs raised, the treatment position), both visual and numerical evaluation methods showed that warping consistently worked better than rigid body. Experiments showed that $\approx$ 180 strategically placed CP's were sufficiently expressive to capture important features of the deformation.
© 2002 Elsevier Science Ltd. All rights reserved.

Keywords: Image registration; Mutual information; Thin plate spline; Prostate cancer therapy; Interventional magnetic resonance imaging

1. Introduction

We are investigating three-dimensional (3D) image registration, particularly with regard to minimally invasive, interventional magnetic resonance imaging (iMRI) guided treatment of prostate cancer. At our institution, we currently use iMRI on a low-field open magnet system to guide radiofrequency (RF) thermal ablation of abdominal cancer [1,2], and we are investigating this method for prostate cancer treatment. A unique feature of iMRI-guided thermal ablation is that therapy can be monitored with MR either by acquiring images of the thermally induced lesion or by measuring temperature. In addition, MR imaging of the prostate is desirable because it more accurately delineates the prostate than does CT [3], which can overestimate the prostate volume [4], and ultrasound, which has a tendency to underestimate the extent of lesions [5].

Several applications in prostate cancer diagnosis, staging, and therapy require registration of MR volumes and/or volumes from other imaging modalities. First, registration of serial examinations can be used to follow regression/progression of tumor. Second, comparison of registered MR images acquired before and immediately after RF thermal ablation can be used to determine whether a tumor is adequately treated. This is particularly helpful in instances where the edematous response to treatment can be confused with a highly perfused tumor. Third, registration of functional, biochemical images such as single photon emission computed tomography, positron emission tomography (PET), and MR spectroscopy, to anatomical MR or CT images is useful for detecting and localizing cancer [6]. Fourth, incorporating the functional, biochemical images into the iMRI paradigm should aid image-guided treatments [7]. Finally, other treatment methods such as external radiation therapy, brachytherapy [8], and surgery, are aided by registration of images from pre-, intra-, and post-therapy for treatment planning, guidance, and assessment.

A few reports describe methods for registration in the pelvis or prostate. Manual registration has been used where an operator cues on segmented vascular structures [9] or other anatomical landmarks in the pelvis [6,10–12]. Others have used automated 3D schemes that match contours of

---

* Corresponding author. Tel: +1-216-368-4099; fax: +1-216-368-4969.
E-mail address: dlw@po.cwru.edu (D.L. Wilson).
[1] http://imaging.ebme.cwru.edu

bones and sometimes other structures that are extracted using manual or interactive segmentation [13–15]. Manual segmentation has also been used to create surfaces for automatic registration [16,17]. All of these methods were based on rigid body registration and required either segmentation or visual identification of structures.

We recently reported a rigid body transformation method for prostate registration [18]. For volume pairs acquired over a short time span from a supine subject with legs flat on the table, registration accuracy of both prostate centroids (typically < 1 mm) and bony landmarks (average 1.6 mm) was on the order of a voxel ($\approx$ 1.4 mm). We obtained somewhat larger prostate registration errors of about 3.0 mm when volume pairs were obtained under very different conditions, e.g. legs flat and legs raised, or with and without bladder or rectal filling. Rigid body registration of the pelvis cannot follow prostate movements due to changes in the postures of legs and deformation of the bladder and rectum, as reported by us [18] and others [19,20]. In this report, we investigate the ability of warping registration to express this deformation.

Warping registration studies are reported for the brain [21,22], for the breast [23–25], for a variety of other organs [26–29], and for excised tissue [30]. Far few reports described results of the pelvis and prostate. Bharaha et al. recently reported a method using manually segmented prostate for rigid body registration followed by finite element-based warping in the application of prostate brachytherapy [31]. Voxel based methods, particularly those based upon mutual information (MI), are robust, require no segmentation that can be prone to error, are highly accurate for brain registration [32], and are suitable for abdominal registration where there can be deformation [2]. We are investigating voxel-based warping registration for the particular application in the pelvis and prostate.

There are challenges to pelvis and prostate registration. First, pelvic regions can change shape significantly, unlike the brain to which registration has been most often applied. Different patient positions such as legs flat and raised significantly change the legs in lower portions of image volumes as well as cause movement and deformation of internal organs in the pelvis. Second, the normal prostate is a small organ that when healthy measures only about 3.8 cm in its widest dimension transversely across the base [33]. Third, the small prostate is located below a much larger bladder that can change shape and size. Fourth, the prostate might move relative to the pelvic bones due to changes in bladder and rectal filling [19,20]. The alignment of the pelvic bones, a most prominent anatomical feature in MR gray-scale images, does not necessarily mean that the prostate is aligned. Finally, efficacious application of warping registration [29,30] to interventional use requires computational efficiency.

In the present study, we perform experiments to compare warping and rigid body registration for the prostate and pelvis. By using high-resolution MR images giving

distinctive anatomic detail, we test the ability of a warping algorithm to correct anatomical variations throughout the pelvic region. We include conditions with very significant changes in posture possible in interventional applications; that is, we ttempt to register image volumes from a diagnostic scan with legs flat to those from a treatment acquisition with legs raised. We qualitatively and quantitatively evaluated registration results using 17 volume pairs from three volunteers.

2. Registration algorithm

2.1. Similarity measurements

We used two similarity measures, MI and correlation coefficient (CC), in our registration. Suppose one volume R is the *reference*, and the other F is *floating*. Their MI $\mathrm{MI}(R, F)$ is given below [34]

$$\mathrm{MI}(R, F) = \sum_{r,f} p_{RF}(r,f) \log \frac{p_{RF}(r,f)}{p_R(r) \cdot p_F(f)}$$

The joint probability $p_{RF}(r,f)$ and the marginal probabilities $p_R(r)$ of the reference image and $p_F(f)$ of the floating image, can be estimated from the normalized joint and marginal intensity histogram, respectively. The CC $\mathrm{CC}(R, F)$ is given below [35].

$$\mathrm{CC}(R, F) = \frac{\sum (R(r) - \bar{R}(r))(F(f) - \bar{F}(f))}{\sqrt{\sum (R(r) - \bar{R}(r))^2 \sum (F(f) - \bar{F}(f))^2}}$$

Here $\bar{R}(r)$, $\bar{F}(f)$ denote the average intensities of the reference and floating volumes and the summation includes all voxels within the overlap of both volumes.

2.2. Rigid body registration algorithm with special features

Prior to warping registration, we perform rigid body registration using a method with features that make it particularly robust for MR pelvic images. We previously reported a similar method [18]. We use two similarity measures, MI and CC. We use a multi-resolution approach. At low resolution, we resample both images at 1/4 or 1/2 number of voxels along each linear dimension, respectively. We use the CC at these resolutions because it gives fewer local maximums than MI [7,18] and because it can be calculated faster than MI. We use MI at full resolution because the peaked similarity function gives a more precise solution than CC [18]. To avoid local maximums, we restart with randomly perturbed parameters obtained from a uniform distribution about the initial transformation values at the current resolution. The algorithm restarts until the absolute CC is above an experimentally determined threshold or the maximum number of restarts is reached. Absolute CC is used for the restart test rather than MI because CC has a well-defined range between 0 and 1,

because CC provides an independent check of the MI result, and because CC has fewer problems with local and incorrect global maximums for registrations at low resolution far from the optimum value [18].

We record all important results following an optimization cycle including the CC and/or MI values, the number of restarts, and the transformation parameters. At the end of processing at a lower resolution, we always select the transformation parameters having the maximum CC value. We then scale the translation parameters appropriately and assign the new parameters to be initial values at the next higher resolution. At the highest resolution, we select the final transformation parameters to be those with the maximum MI value.

Other details follow. A simplex algorithm varies the six rigid body transformation parameters (three translations and three angles) to optimize the similarity measures [36]. We use an initial guess at the lowest resolution of all zeros because the patient is normally oriented approximately the same way from one scan to the next. We set the CC thresholds at a fixed value of 0.50, and the maximum numbers of restarts at 10, 5, and 3, from low to high-resolution, respectively.

2.3. Warping registration using optimized control points

Fig. 1 outlines the warping registration algorithm that includes three major steps: control point selection, control point optimization, and thin plate spline warping. The unchanging volume is the reference, and the one to be warped is floating.

The manual selection of CP's is an important step. We used *RegViz*, a program written in Interactive Data Language (IDL, Research System Inc., Boulder, CO) and created in our laboratory for visualizing and analyzing image volumes. Following rigid body registration, the aligned two volumes are displayed in two rows slice-by-slice. Images can be transverse, coronal, or sagittal slices. It is quite straightforward to find corresponding features at the pelvis, prostate, bladder, and rectum. We normally select control points (CP's) using recognizable organ features such as corners and intersections of edges because of their unique positions. Corresponding CP's in the two volumes are placed using a cursor, and sometimes they are in different image slices. The 3D coordinates are automatically stored in a file. Because of the optimization that occurs later, the correspondence can be up to 15 mm or ≈ 10 voxels in error. Experiences with CP selection are described in Section 4. Typically, we used 180 CP's for a volume with $256 \times 256 \times 140$ isotropic voxels.

The next step of the warping algorithm (Fig. 1) is the CP optimization. We define a small cubic volume of interest (VOI) centered at each CP. The VOI can be 16, 32, 48 or 64 voxels on a side. As reported later, the selection of VOI size depends on the amount of warping required. A simplex optimization algorithm varies the x, y, and z transformation parameters of the floating VOI until the MI with the reference VOI is optimized. Each control point is optimized independently and the 3D coordinates of the optimal CP's are recorded.

The final major step is to warp the floating volume using the corresponding optimal CP's coordinates to establish

---

Register two volumes using rigid body registration

Create a new floating volume from rigid body registration parameters

Select *N* control points (CP) in the reference and new floating volumes

Record 3D coordinates of the CP's in both volumes

Initialize the size of volume of interest (VOI) centered at CP's

Bin the reference and floating volumes to 256 gray levels

FOR *CP* **FROM** *0* to *N-1* **DO BEGIN**

　Optimize mutual information (MI) between the reference and floating VOI's

　　1. **Transform** the floating VOI using three translation parameters

　　2. **Interpolate** to get a reformatted VOI

　　3. **Calculate** MI between the reference and reformatted VOI's

　　4. **Vary** the three translation parameters

　　5. **Repeat** the above steps 1-4 until meeting function tolerance or maximum iteration number

　Record the optimized CP coordinates in the floating volume

END

Calculate thin plate spline transformation using the reference and optimized CP's

Interpolate the floating volume and get a warped volume

Fig. 1. Flow chart of the warping registration algorithm. Following rigid body registration, *N* CP's are selected in both the reference and floating volumes. A small cubic VOI is centered on each control point. Optimization is performed by varying the *x*, *y*, and *z* locations of the floating VOI until the MI between corresponding voxels is maximized. Each control point is optimized independently, and then the optimized CP's are used to establish a three-dimensional thin plate spline transformation for the entire volume.

a 3D thin-plate spline (TPS) transformation [37,38]. We now briefly go through the three computing steps for the TPS transformation.

First, let $P_1 = (x_1, y_1, z_1)$, $P_2 = (x_2, y_2, z_2)$,..., $P_n = (x_n, y_n, z_n)$ be n control points in the image coordinate of the reference volume. Write $r_{ij} = |P_i - P_j|$ for the distance between point i and j. We define matrices

$$P = \begin{bmatrix} 1 & x_1 & y_1 & z_1 \\ 1 & x_2 & y_2 & z_2 \\ \cdots & \cdots & \cdots & \cdots \\ 1 & x_n & y_n & z_n \end{bmatrix}, \quad n \times 4;$$

$$K = \begin{bmatrix} 0 & r_{12} & r_{13} & \cdots & r_{1n} \\ r_{21} & 0 & r_{23} & \cdots & r_{2n} \\ \cdots & \cdots & \cdots & \cdots & \cdots \\ r_{n1} & r_{n2} & r_{n3} & \cdots & 0 \end{bmatrix}, \quad n \times n;$$

and

$$L = \begin{bmatrix} K & P \\ P^T & O \end{bmatrix}, \quad (n+4) \times (n+4);$$

where T is the matrix transpose operator and O is a 4×4 matrix of zero.

Second, let $Q_1 = (u_1, v_1, w_1)$, $Q_2 = (u_2, v_2, w_2)$,..., $Q_n = (u_n, v_n, w_n)$ be n corresponding CP's in the image coordinate of the floating volume. We get matrices

$$V = \begin{bmatrix} u_1 & u_2 & \cdots & u_n \\ v_1 & v_2 & \cdots & v_n \\ w_1 & w_2 & \cdots & w_n \end{bmatrix}, \quad 3 \times n,$$

$$Y = (V | 0 \quad 0 \quad 0 \quad 0)^T, \quad 3 \times (n+4),$$

and define the vector $W = (w_1, w_2, ..., w_n)$ and the coefficients α_1, α_x, α_y, and α_z by the equation

$$L^{-1}Y = (W | \alpha_1 \quad \alpha_u \quad \alpha_v \quad \alpha_w)^T.$$

Third, use the elements of $L^{-1}Y$ to define a function $f(u', v', w')$ everywhere in the entire volume

$$f(u', v', w') = \alpha_1 + \alpha_u u + \alpha_v v + \alpha_w w + \sum_{i=0}^{n} w_i |P_i - (u, v, w)|.$$

Thus any voxel (u_i, v_i, w_i) in the floating volume is transformed to a new coordinate (u'_i, v'_i, w'_i) and a warped volume can be obtained by trilinear interpolation.

Additional algorithm details are now described. For both VOI optimization and rigid body registration, we use trilinear interpolation. Optimization of similarity ends either when the maximum number of calculations is reached (typically 500) or the fractional change in the similarity function is smaller than a tolerance (typically 0.001). We use IDL as the programming language.

3. Experimental methods

3.1. Image acquisition

All MRI volumes were acquired using a 1.5 T Siemens MRI system (Magnetom Symphony, Siemens Medical Systems, Erlangen, Germany). An 8-element phased array body coil was used to ensure coverage of the prostate with a uniform sensitivity. Typically two anterior and two posterior elements were enabled for signal acquisition. We used two different MR sequences. First, a 3D FLASH sequence with TR/TE/flip parameters of 12/5.0/60 gave $256 \times 256 \times 128$ voxels over a $330 \times 330 \times 256$ mm^3 field of view (FOV) to yield $1.29 \times 1.29 \times 2.0$ mm^3 voxels oriented to give the highest resolution for transverse slices. This sequence was good for pelvic imaging but was not ideal for prostate visualization and it was used for volunteer S1. Second, a 3D PSIF sequence with 9.4/5.0/60 (TR/TE/flip) yielded $160 \times 256 \times 128$ voxels over a $219 \times 350 \times 192$ mm^3 rectangular FOV and $1.4 \times 1.4 \times 1.5$ mm^3 voxels oriented to give the highest resolution for transverse slices. There was over sampling at 31% in the slice direction to reduce aliasing artifacts. The second sequence gave excellent image contrast for the prostate and its surroundings and it was used for volunteers S2 and S3.

3.2. Imaging experiments

We acquired 3D MRI volume images from three normal volunteers under a variety of conditions simulating anticipated conditions in diagnostic and treatment applications. Before image acquisition, each volunteer drank water and had a relatively *full bladder*. In the *diagnostic position*, the subject laid supine throughout MR scanning. In the *treatment position*, the subject was supine, and his legs were supported at 30–60° relative to the horizon and separated in a 'V' with an angle of 60–90° between two legs. This is similar to the lithotomy position used in prostate therapies, and it should provide access for needle insertion in brachytherapy or RF thermal ablation. In some experiments, the subject micturated to create an *empty bladder* prior to imaging. For each subject, image volumes were typically obtained on the same day within a 2 h session. We imaged one volunteer (S3) a week before the standard imaging session, and we refer to these volumes as *diagnosis 1 week*. Between volume acquisitions, volunteers got off the MRI table, stretched, and walked around to ensure that they would assume a different position when they laid back on the table. The coil array was centered on the prostate. All images of a volunteer were acquired with the same MRI acquisition parameters so as to ensure very similar gray values. In total, there are 4, 4, and 8 volumes for volunteer S1, S2, and S3, respectively.

The permutation of the volumes gives many possible volume pairs for registration experiments.

3.3. Volumes for registration experiments

We registered 17 volume pairs under five different conditions as defined above. Five pairs are *treatment-diagnosis*; seven pairs are *full bladder–empty bladder*; two pairs are *diagnosis 1 week-diagnosis*; and three pairs are *diagnosis–diagnosis*. For each case, other conditions were controlled. For example, for the case of diagnosis 1 week-diagnosis, both volumes were acquired with empty bladder and comparable conditions. Rigid body and warping registration were applied to each of the volume pairs. Results were evaluated as described next.

3.4. Registration evaluation

We used the multiple visualization features of RegViz to visually evaluate registration results. First, we manually segmented prostate boundaries in image slices and copied them to corresponding slices from the other volume. This enabled visual determination of the overlap of prostate boundaries over the entire volume. We applied the same method to evaluate pelvic registration. Second, color overlay displays were used to evaluate overlap of structures. One image was rendered in gray and the other in the 'hot-iron' color scheme available in IDL. To visualize potential differences, it was quite useful to interactively change the contribution of each image using the transparency scale. Third, we used a sector display, which divided the reference and registered images into rectangular sectors and created an output image by alternating sectors from the two input images. Even subtle shifts of edges could be clearly seen [18].

Voxel gray value measures were calculated as indicators of registration quality. MI and CC between registered volumes were computed. Since volumes to be registered were acquired using the same acquisition parameters, high absolute CC values were obtained when registration was good [24]. Because voxel intensities were comparable, we created difference images and calculated statistics such as the voxel mean and standard deviation following registration.

Finally, we used a variety of tools in RegViz to evaluate registration quality. We used contour overlap and color overlay to assess the prostate registration. We manually segmented the prostate across all slices and calculated the potential displacements of the prostate 3D centroid.

4. Results

4.1. Effect of control point selection on registration quality

In well over 100 registration experiments using different numbers and placement of CP's, we investigated

effects on warping registration quality. For each of the three volunteers, we selected one typical volume pair from the diagnostic-treatment positions for systematic experiments. We progressively increased the number of CP's from 15 to 250. We found that less than 120 CP's did not produce good visual matching of our high-resolution MR images showing great anatomical detail. More than 220 CP's did not give significant improve results but required more time for manual selection and optimization. When we used ≈180 CP's placed strategically using rules described later, we obtained excellent results over the entire pelvis and internal organs. As a result of our experience, we modified the registration method to be suitable for many CP's (Section 5).

Some rules follow for strategic placement of CP's. For registration of treatment and diagnostic image volumes, most CP's were selected using transverse slices because they best showed the pelvic displacement when moving the legs to the treatment position (Fig. 2). About 25 CP pairs were placed near edge and point features having recognizable correspondence on each of 5–8 transverse slices with a z interval of ≈8 mm, covering the entire pelvic region. Additionally, we placed about 25 CP's from sagittal slices because they
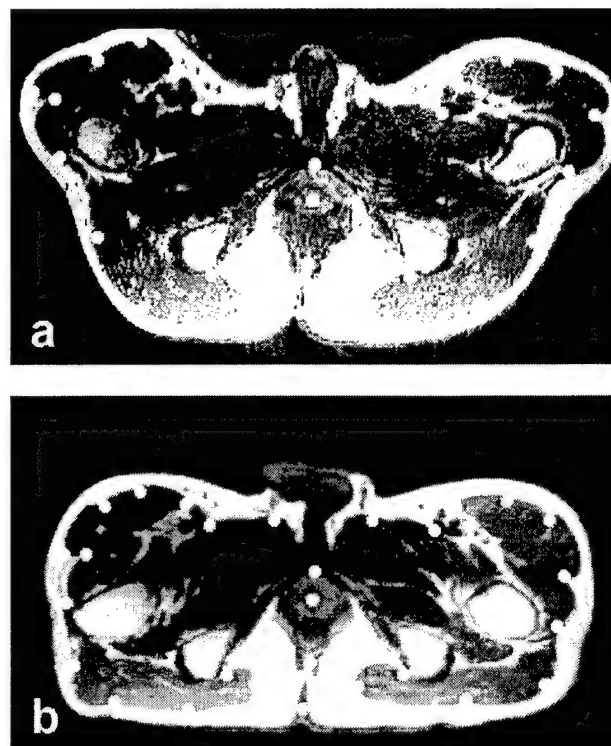

Fig. 2. Control point selection when images are acquired in the treatment and diagnostic positions. Image (a) is from the reference volume acquired in the treatment position with legs raised. Image (b) is to be warped and is from the volume acquired in the diagnostic position with the subject supine on the table. Transverse slices best show the deformations, especially at the legs. As described in the text, CP's indicated by the white dots are selected around the pelvic surface and the prostate. Each control point is located at one voxel but displayed much bigger for better visualization. Volumes are from volunteer S2.

provided other structures that can be missed in the transverse images. It was also important to include CP's from organs other than the prostate because they constrained warps. We always placed CP's at critical regions such as the prostate center, pelvic surface, bladder border, and rectal walls.

For registration of image volumes with full and empty bladder, most CP's were placed from sagittal slices because they best showed the deformation of the bladder and rectum (Fig. 3). About 10–20 CP's were placed at the borders of the bladder and rectum on each of 8–10 sagittal slices with an equal interval of ≈ 8 mm, covering the entire pelvic region including the prostate, bladder, and rectum.

4.2. Registration quality of warping and rigid body registration

In Fig. 4, we compare warping and rigid body registration for a typical volume pair in the treatment and diagnostic positions. Following warping registration, the prostate boundary overlap is excellent (Fig. 4(e)) and probably within the manual segmentation error. Similar results were obtained in other transverse slices throughout the prostate. The prostate 3D centroid calculated from segmented images displaced by only 0.6 mm, or 0.4 voxels, following warping. Following rigid body registration, the prostate was misaligned with a displacement to the posterior of ≈ 3.4 mm when in the treatment position (Fig. 4(d)), as previously reported by us [18]. Using rigid body registration, there is significant misalignment throughout large regions in the pelvis (Fig. 4(f)) that is greatly reduced with warping (Fig. 4(g)). Note that warping even allows the outer surfaces to match well. Other visualization methods such as
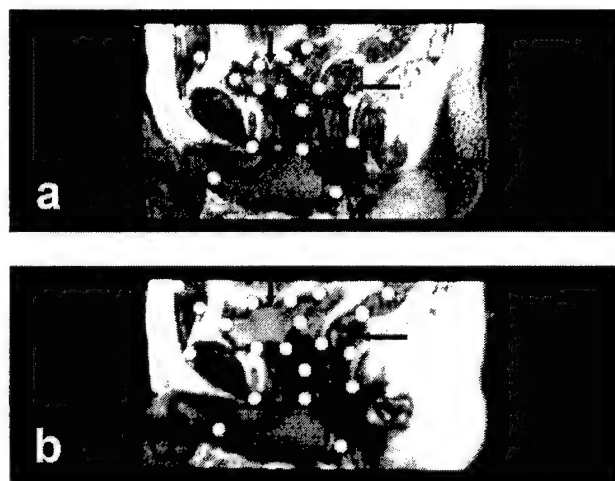

Fig. 3. Control point selection when images are acquired with a week interval between them. Image (a) is from the reference volume acquired 1 week later with an empty bladder. Image (b) is to be warped and is from the volume acquired earlier with a full bladder. Sagittal slices best show the deformations at the bladder (vertical arrow) and rectum (horizontal arrow) where most CP's are placed. Volumes are from volunteer S3.

two-color overlays and difference images, quickly show matching of structures without segmentation but do not reproduce well on a printed page.

We next examine the effect of conditions such as bladder and rectal filling that might change from one imaging session to the next. In Fig. 5, we compare warping and rigid body registration for a volume pair with 1 week between imaging sessions. One volume is with an empty bladder and the other is with a relatively full bladder. There is also a difference in rectal filling. Warping registration closely aligns the prostate Fig. 5(e)) while rigid body does not (Fig. 5(d)). In addition, rigid body registration does not align the bladder and parts of the rectum (Fig. 5(f)). With warping, the bladder closely matches the reference, and the rectum is better aligned (Fig. 5(g)). Other visualization methods showed excellent alignment of internal and surface edges. Difference images show that warping greatly improves alignment of internal structures as compared to rigid body registration (Fig. 6). The difference image following rigid body registration shows bright regions indicating misalignments (Fig. 6(d)) that are removed with warping (Fig. 6(e)).

We also examined volume pairs with both volumes acquired in the diagnostic position under comparable conditions. In the current data set, five volume pairs fit these criteria. In all such cases, rigid body registration worked as well as warping. There were no noticeable deformations in the pelvis, and prostate centroids typically displaced less than 1.0 mm between the two registered volumes. Note that this was obtained even though subjects always got up from the table and moved around before being imaged again.

4.3. Quantitative evaluation of warping registration

Fig. 7 shows the CC and MI values between registered volumes. Warping increased CC and MI values in every case, and a paired two-tailed t test indicated a significant effect of warping at $p < 0.5\%$. The most significant improvement was in the case of treatment-diagnosis where improvements in CC and MI were as high as 102.7 and 87.8%, respectively.

Statistics of image differences following rigid body and warping registration are shown in Fig. 8. Warping reduces the absolute intensity difference between corresponding voxels (Fig. 8(a)), and the mean across all image volumes is only 4.2 gray levels, a value corresponding to only 4.7% of the mean image value of 90. We used the absolute intensity difference because signed values canceled when averaged over the entire image. The standard deviation of absolute difference is also reduced (Fig. 8(b)).

These quantitative measures match observation from visual inspection. For example, the third pair of the first group (diagnosis-treatment) in Fig. 7 and 8 corresponds the images in Fig. 4. After warping, registration greatly
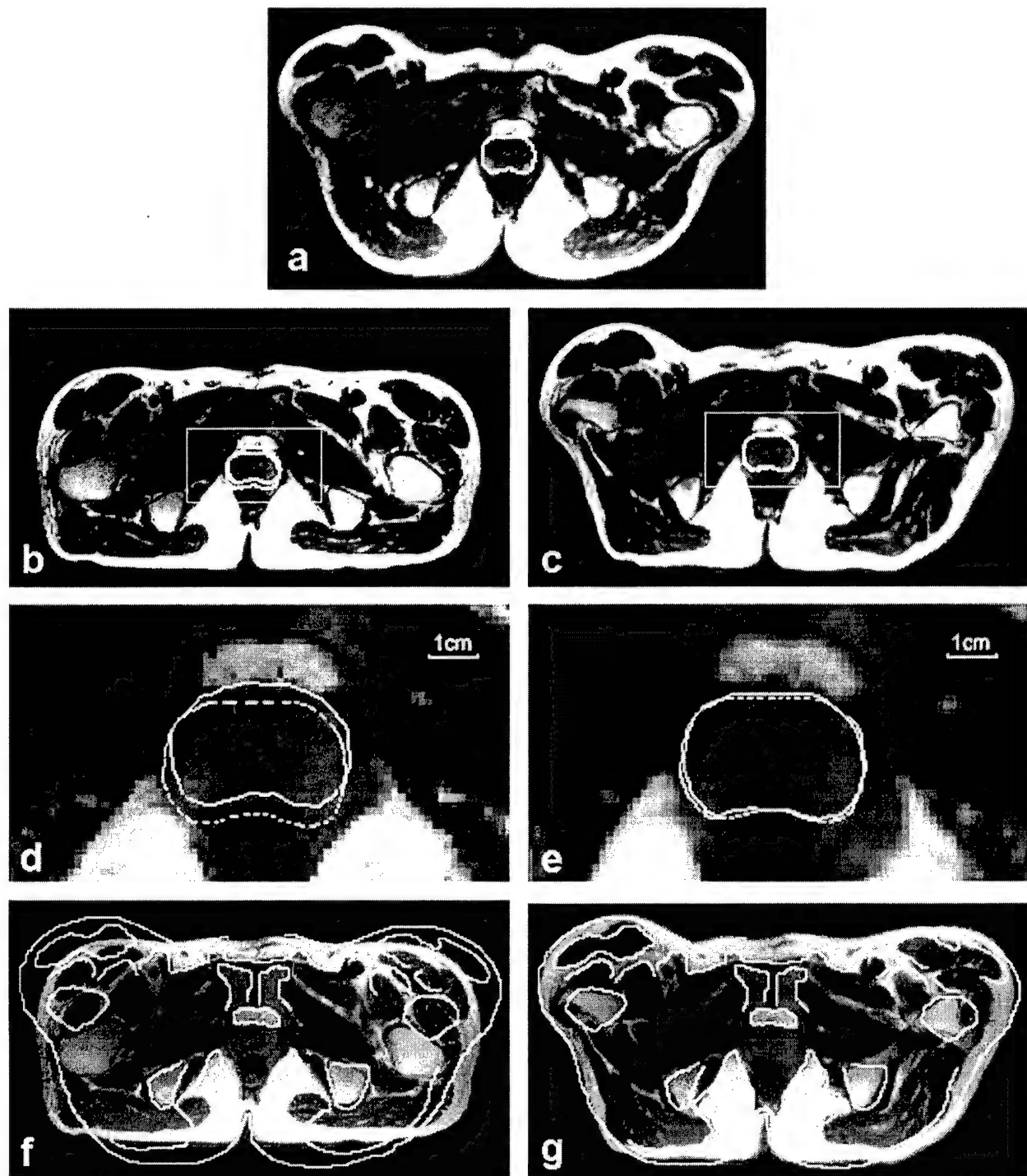
Fig. 4. Comparison of warping and rigid body registration for volumes acquired in the treatment and diagnostic positions. Image (a) is from the reference volume acquired in the treatment position, and the prostate is manually segmented. Images in the left and right columns are from the floating volume acquired in the diagnostic position following rigid body and warping registration, respectively. To show potential mismatch, the prostate contour from the reference in (a) is copied to (b) and (c) and magnified as the dashed contours in (d) and (e). The 3 mm movement of the prostate to the posterior is corrected with warping (e) but not rigid body registration (d). Pelvic boundaries manually segmented from the reference show significant misalignment with rigid body (f) that is greatly improved with warping (g). Images are transverse slices from volunteer S2.

improved. Another interesting example is the difference images in Fig. 6(d) and (e) that correspond to the last pair of the second group (full–empty bladder) in Fig. 8. Once again, the statistical measures reflect the great change in visual quality.

4.4. Algorithmic implementation

In rigid body registration, the multi-resolution approach and restarting algorithm were important modifications. First, these two features improved robustness.
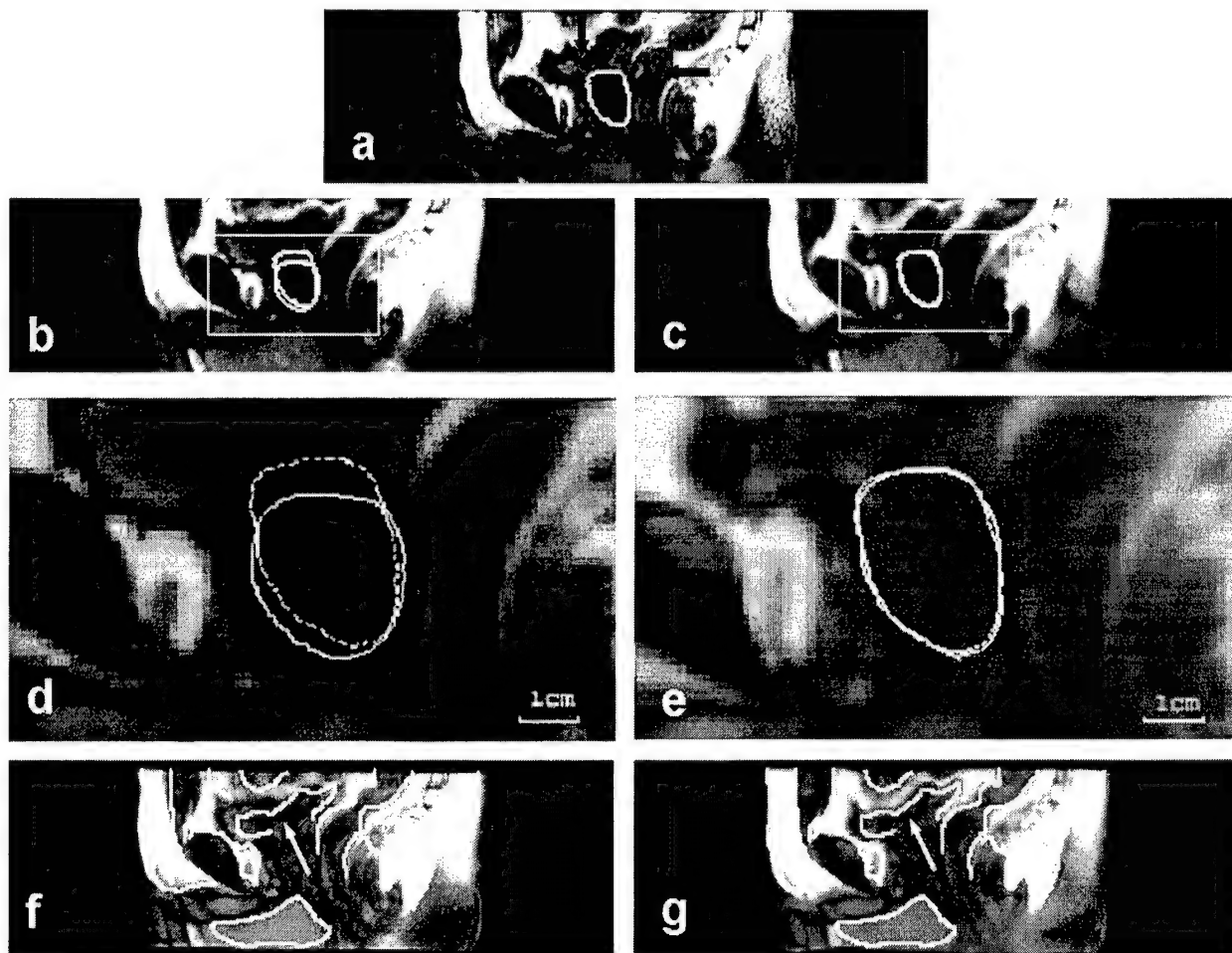
Fig. 5. Comparison of rigid body and warping registration for volumes acquired with an interval of 1 week between imaging sessions. The reference image (a) with a manually segmented prostate was acquired later with an empty bladder (vertical arrow) and partial rectal filling (horizontal arrow). Images in the left and right columns are from the floating volume acquired earlier following rigid body and warping registration, respectively. To show potential mismatch, contours from the reference are shown on images following registration, as described in Fig. 4. The full bladder in (d) has pushed the prostate, shown by the continuous curve, in the caudal direction. After warping, prostate contours match closely (e). The bladder, rectum, and other organs closely align following warping (g). With rigid body (f), proceeding from left to right, the front of the pelvis, the bladder (arrow), and the rectum are all misaligned. Images are sagittal slices from volunteer S3.

The algorithm always gave very nearly the same transformation parameters (<0.01 voxels and 0.01 degrees) for the 17 volume pairs in this study using a wide variety of initial guesses. We also found that MI was more accurate than CC at the highest resolution [18]. Second, the multi-resolution approach enabled the program to get close to the final value quickly because of the reduced number of calculations. That is, the time for reformatting at the lowest resolution of 1/4 number of voxels in a linear dimension was 0.16 min, less than 1/63 times that at the highest resolution, a value nearly equal to the 1/64 expected from the change in the number of voxels. In a typical example, the number of restarts was 5, 1, and 1 for resolutions at 1/4, 1/2, and the full number of voxels in a linear dimension, respectively. When we checked the restarts at the resolution of 1/4 number of voxels, we determined that none of the five restarts converged to the same transformation. It has been

our experience that more restarts are desirable at the lower resolutions, and the algorithm includes this feature. Each call to the simplex optimization resulted in 50–100 MI evaluations before the tolerance (0.001) was reached. In some experiments on multiple volumes, we reduced the tolerance value but found little difference in registration quality, probably because of the restarting and multi-resolution features. The time for rigid body registration, typically 5–10 min on a Pentium IV, 1.8 GHz CPU, with 1.0 GB of memory, could possibly be reduced to within 1 min with optimized C code rather than the high level language IDL.

Some technical aspects of warping registration are of interest. Fig. 9 shows the optimization time and MI values between registered volumes as a function of VOI size. The optimization time for 180 CP's increases roughly linearly with the number of voxels within a VOI, about 0.5 min for VOI's with 16 voxels on one side and 30 min for VOI's with
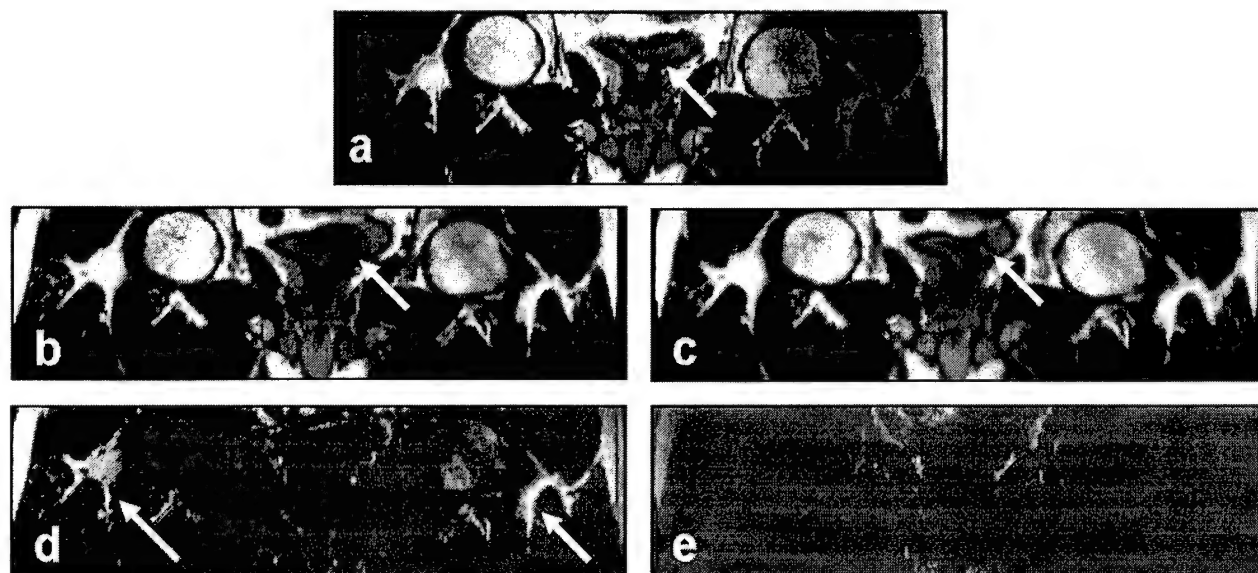
Fig. 6. Comparison of registration quality for rigid body and warping registration. The reference image (a) was acquired with a relatively empty bladder (arrow). Images (b) and (c) are from the floating volume acquired with a full bladder following rigid body and warping registration, respectively. Images (d) and (e) are the absolute difference images between the reference and registered images, respectively. Bright regions following rigid body indicate misalignments (d) that are removed with warping (e). Images (d) and (e) are displayed using the same gray-scale window and level values. Images are coronal slices from S3 volumes shown in Fig. 5.

64 voxels on a side. In Fig. 9, the MI curve saturates at the VOI size of 64 voxels on a side that means the size of 64 gave better MI value. These curves are for the case of treatment-diagnosis for volunteer S2. When we examined the cases of full–empty bladder and volumes acquired over 1 week time interval, we found that the VOI size of 16 voxels on a side worked best. Using the same computer above, for a volume with $256 \times 256 \times 140$ voxels and 180 CP's, the warping registration typically takes about 15–45 min depending on the VOI size.

We report some details on VOI optimization for a typical treatment-diagnosis volume pair from subject S2. Following rigid body registration, the mean distance between the manually selected reference and floating CP's was 15.5 ± 10.7 mm, where the latter number is the standard deviation. The maximum distance was 53.2 mm. After VOI optimization, the algorithm moved the floating CP's an average of 9.0 ± 6.5 mm. This value shows that one does not have to be very careful in marking corresponding CP's.

5. Discussions and conclusions

5.1. Applicability of warping registration

For MR images of the pelvis and prostate, warping registration is desirable whenever images are acquired in different positions or with different conditions of bladder and rectal filling. Local deformations throughout the pelvis can be corrected, and, more importantly, the prostate can be accurately registered. However, when images are acquired

in the same position under comparable conditions such as our case called diagnosis–diagnosis, rigid body registration worked satisfactorily as previously reported by us [18]. Similarly, if one were to reproduce the treatment position with reasonable accuracy, we believe that prostate registration would be very good.

Our goal is to get good matching throughout the entire pelvic region not just at the prostate because proper localization of other organs is important for interpretation of some functional images and because anatomical spatial integrity is important for treatment planning. Hence, we used high-resolution MR images that provide a very stringent test for warping. Many anatomical details are evident, and even a small mismatch can clearly be seen. As a result, we found that ≈ 180 CP's were required to get excellent quality registration. When we applied the method to register CT images with PET images of the lung having much less resolution, many fewer points (≈ 50) were required [39]. With a sufficient number of CP's, the TPS transformation excellently approximated the deformations of the pelvis and internal structures of our MR images. Even when we warped the volume in the diagnostic position to one in the treatment position, most organs were closely aligned, despite very significant movements. The method performed equally well for correcting the deformation and organ displacement arising from changes in bladder and rectal filling.

With our graphical user interface, interactive control point selection is quite easy after training. It usually took an experienced user about 15 min to select 180 CP's. Based on our experience, we think that it is possible to create an
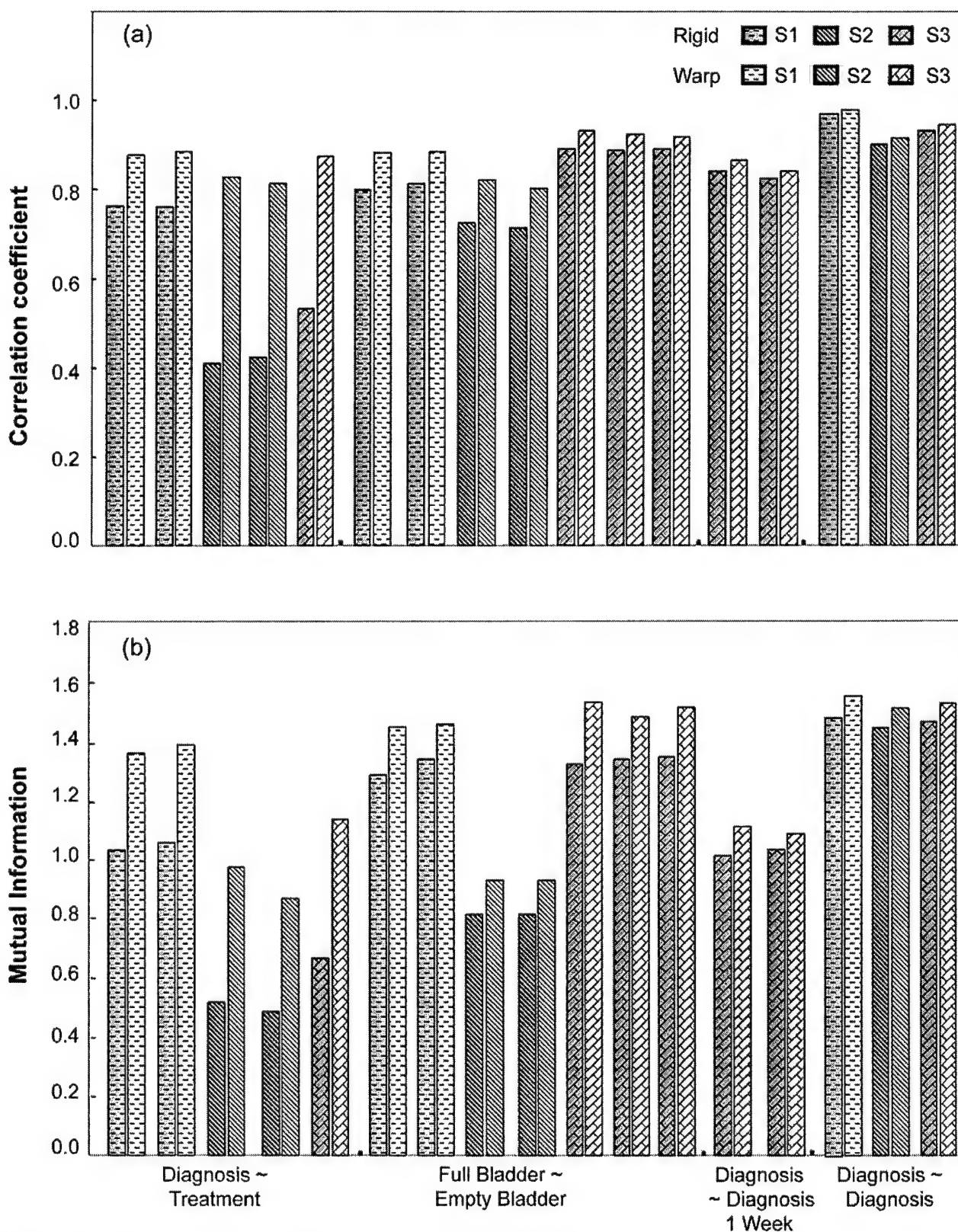
Fig. 7. Voxel similarity measures for rigid body and warping registration. CC (a) and MI (b) following registration with (light bars) and without (dark bars) warping are plotted. Conditions described in Section 3 are listed on the x-axis. Warping increased CC and MI in all cases. The most significant increases occurred in the case of the treatment-diagnosis volume pairs where maximum increases in CC and MI are 102.7% and 87.8%, respectively. For volumes acquired with in the same diagnostic position and comparable conditions (two right most groups), warping did not have significant improvement over rigid body method.
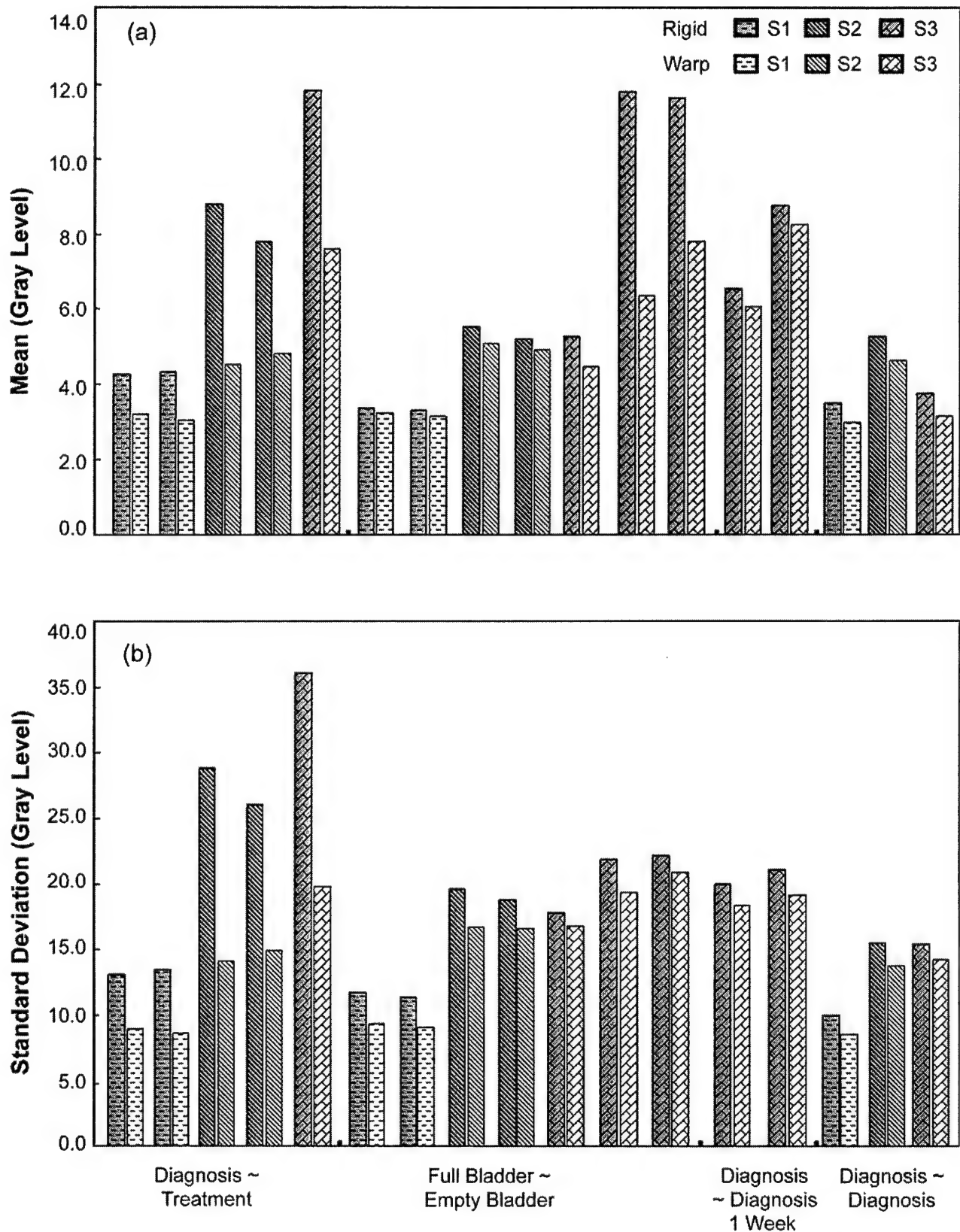
Fig. 8. Image statistics of absolute intensity difference images for rigid body and warping registration. The mean (a) and standard deviation (b) are plotted. See the legend of Fig. 7 for other details. Warping decreased the mean and standard deviation in each case, but the most significant decreases occurred in the case of the treatment-diagnosis volume pairs. After warping, the intensity averaged over all data is 4.2 ± 1.9 gray levels, a value corresponding to only ≈4.7% of the mean image value of ≈90 gray levels.
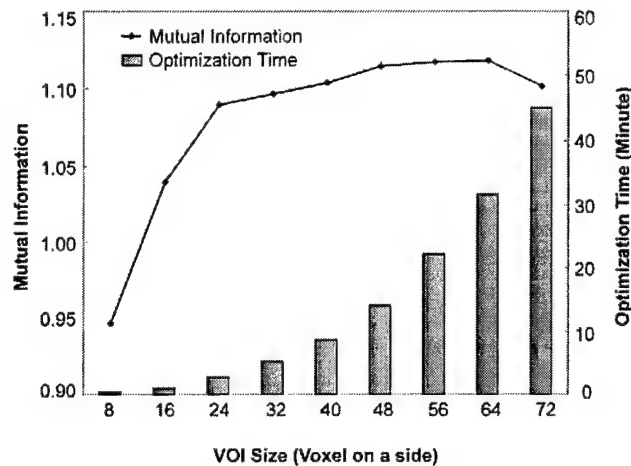
Fig. 9. Optimization time and MI as a function of VOI size. The left vertical axis is MI, and the right vertical axis is the total VOI's optimization time. The horizontal axis is the size of the VOI on a side. In each case, the VOI is centered on the CP, but since even numbers of voxels are used, the CP is displaced consistently to the upper left hand corner by one voxel. With increasing VOI size, time increases linearly with the number of voxels within the VOI. The peak MI value is at a VOI size of 64 on a side. A treatment-diagnosis volume pair is used from S2 with 180 CP's.

automatic or semiautomatic method for selection of appropriate CP's in the pelvis. For example, one might use a gray scale threshold to detect the pelvic outer boundaries and apply edge enhancement to extract feature of internal structures. CP's would be placed on such structures automatically. We are investigating this and other methods for CP selection followed by automatic warping registration.

One way to adjust the movement of CP's is to change the size of the VOI. In the case of treatment-diagnosis volume pairs, a large VOI size of 64 on a side worked better than smaller ones because displacements were large, because larger VOI's tend to give a more robust optimization, and because no small local deformations were required. However, a size of 16 on a side worked better for the case of full–empty bladder volume pairs because small VOI's better capture the small, local deformations. VOI's with a size of 64 on a side covered most of the bladder and could not generate small local deformations. For volumes with both large and small-scale deformations, we suggest using different VOI sizes for different CP's.

With warping registration, we have to be concerned about potential warping errors affecting the application of interest. For the prostate, we used 3–5 CP's near the prostate center because we desired to maintain the spatial integrity of the organ and to preserve the tissue volume. We placed many CP's around the pelvic surface to produce reasonable warping.

5.2. Evaluation of warping registration

Since there is no gold standard for warping registration of anatomical images, we used a variety of methods to evaluate

registration quality. First, for routine evaluation, a color overlay is simple, fast, and intuitive. To better visualize the two data sets, we interactively adjust the transparency scale of each image. Second, for illustration of subtle difference along an edge, we recommend a sector display because it best shows small shifts. Third, for visual evaluation of a specific organ such as the prostate, we like to superimpose manually marked contours from one image onto another as shown in Figs. 4 and 5. This clearly shows any displacement or deformation even in a printed figure. Fourth, a more quantitative approach is obtained by calculating the displacement in millimeters from the 3D centroid of a segmented organ such as the prostate. Finally, when images have comparable gray levels, a difference image can provide a visual evaluation or a quantitative evaluation from image statistics. A downside with MR difference images is that the inhomogeneity of the signal response and interpolation can introduce artifacts in difference images. Since MR image intensity can vary with different MR sequence parameters and the signal response of MR coil, gray value statistic may have some limitations when image acquisitions are not carefully repeated.

5.3. Algorithmic robustness and efficiency

The rigid body algorithm is robust for a global registration. Because of two principal design features, the algorithm is quite robust and accurate for volume pairs acquired in the same positions and with comparable conditions [18]. First, using both CC and MI at different resolutions was an important feature that increased robustness. CC gave fewer local minimums at low resolutions and MI was more accurate at high-resolution [7,18]. Second, the restarting mechanism was also quite important. Without restarting, we found that registrations sometimes failed in cases of volumes with large mismatches and significant deformation. Even these cases resulted in a proper solution when restarting was employed.

Based upon our initial experiments with interactive CP selection, we determined that many CP's were required for good matching throughout the pelvis. As a result, we designed algorithm features to be computationally efficient for TPS warping with hundreds of CP's. First, the optimization of small VOI's is very fast. Second, we optimized each CP separately because the optimization of three parameters (x, y, and z) is simple and fast. Conversely, as previously reported by others [26,27], the simultaneous optimization of many CP's leads to a much more complicated error surface and local maximums. If one were to use 180 CP's and optimizes the 540 free parameters simultaneously, the optimization process would become extraordinarily complex. Third, we applied the TPS transformation once to the final, optimal CP's; this saved considerable time. If TPS was applied in each iteration, the registration time would be unacceptable for our application. If we were to use optimized

C code, the total time for rigid body and warping registration should reduce to within 5 min.

5.4. Applications

We discuss several points on volume interpolation. We used trilinear interpolation in the algorithm because it is fast. The final floating volume following rigid body registration is important because it is used for CP selection and warping registration. A high accurate interpolation such as sinc spline [40] can be applied to obtain this volume with reduced interpolation errors. For optimization, partial volume interpolation that was reported robust for MI-based registration [34] is another option for improvement.

The flexibility introduced with manual selection of CP's makes the current software suitable for warping registration in many applications in addition to the clinical procedures described in Section 1. We have successfully applied it to human MR–MR prostate images as shown here, rat CT–CT images, and CT–PET lung images [39]. We believe that the registration method can be applied to many organs other than the pelvis and prostate, multi-modality images, and inter-subject images. In addition, we think it applicable to a variety of animal experiments in which we are involved, including iMRI-guided thermal ablation in pig and rabbit, prostate imaging studies in dog, and controlled drug release studies in rat.

We conclude that our MI warping registration is fast and can be applied to a variety of applications. For prostate and pelvic imaging, it works better than rigid body registration whenever the subject position or condition is greatly changed between acquisitions. It will probably be a useful tool for many applications in prostate diagnosis, staging, and therapy.

6. Summary

Many applications in prostate cancer management such as tumor localization, possibly tumor staging, tumor targeting during therapy, assessment of adequate treatment, and treatment follow up, require image registration of MRI volumes and/or volumes from other imaging modalities. With regard to interventional MRI guided RF thermal ablation for the minimally invasive treatment of prostate cancer, registration applications include the comparison of registered MR images acquired before and immediately after RF ablation to determine whether a tumor is adequately treated. When images are acquired in different patient positions and/or different conditions, the pelvis, prostate, bladder, and rectum can deform and displace. Warping registration is desired to correct for such deformations.

We created a two-step, 3D registration algorithm using MI and thin plate spline warping for the prostate MR images. First, automatic rigid body registration was used to capture the global transformation. Features included a multi-resolution approach, two similarity measures, and automatic restarting to avoid local minimums. Second, local warping registration was applied. Interactively placed CP's were automatically optimized by maximizing the MI of corresponding voxels in small volumes of interest and by using a three dimensional thin plate spline to express the deformation throughout the image volume. More than 100 registration experiments with 17 MR volume pairs determined the quality of registration under conditions simulating potential interventional MRI-guided treatments of prostate cancer. Evaluations included visual inspection; voxel gray value measures such as MI, CC, and intensity difference; and displacement of the centroids of segmented prostates. For image pairs that stress rigid body registration (e.g. supine, the diagnostic position, versus legs raised, the treatment position), both visual and numerical evaluation methods showed that warping consistently worked better than rigid body. Warping registration rectified the misalignment in the pelvis following rigid body registration. The prostate centroid displacement for a typical volume pair was reduced from 3.4 to 0.6 mm when warping was added. Experiments showed that ≈ 180 strategically placed CP's were sufficiently expressive to capture important features of the deformation. When only 120 CP's were used, warping throughout the pelvis was visually less satisfactory but the prostate was aligned reasonably well. For volume pairs with images acquired in the same position (diagnosis–diagnosis) and comparable conditions, the rigid body method worked sufficiently well, and the prostate centroid displacements were < 1.0 mm. In conclusion, the warping registration method works better than rigid body registration whenever patient position or condition is greatly changed between acquisitions. It is very computational efficient for hundreds of CP's and can very well approximate the deformation of the pelvis and internal organs. It will probably be a useful tool for many applications.

Acknowledgements

References

[1] Lewin JS, Connell CF, Duerk JL, Chung YC, Clampitt ME, Spisak J, Gazelle GS, Haaga JR. Interactive MRI-guided radiofrequency interstitial thermal ablation of abdominal tumors: clinical trial for evaluation of safety and feasibility. J Magn Resonance Imag 1998; 8(1):40–7.

[2] Carrillo A, Duerk JL, Lewin JS, Wilson DL. Semiautomatic 3D image registration as applied to interventional MRI liver cancer treatment. IEEE Trans Med Imag 2000;19(3):175–85.

[3] Milosevic M, Voruganti S, Blend R, Alasti H, Warde P, McLean M, Catton P, Catton C, Gospodarowicz M. Magnetic resonance imaging (MRI) for localization of the prostatic apex: comparison to computed tomography (CT) and urethrography. Radiotherapy Oncol 1998; 47(3):277–84.

[4] Rasch C, Barillot I, Remeijer P, Touw A, van Herk M, Lebesque JV. Definition of the prostate in CT and MRI: a multi-observer study. Int J Radiat Oncol Biol Phys 1999;43(1):57–66.

[5] Boni RAH, Boner JA, Debatin JF, Trinkler F, Knonagel H, Vonhochstetter A, Helfenstein U, Krestin GP. Optimization of prostate carcinoma staging—comparison of imaging and clinical methods. Clin Radiol 1995;50(9):593–600.

[6] Sodee DB, MacLennan GT, Resnick MI, Faulhaber PF, Lee Z, Nelson AD, Molter JP, Bakale G. Comparison of CT- or MRI-fused PET-FDG and SPECT-ProstaScint (R) imaging of prostate cancer with the gold standard of histology. J Nucl Med 2001;42(5):1222.

[7] Fei B, Wheaton A, Lee Z, Nagano K, Duerk JL, Wilson DL. Robust registration algorithm for interventional MRI guidance for thermal ablation of prostate cancer. Ki Mun S, editor. Procedings of SPIE Medical Imaging on Visualization, Display, and Image-Guided Procedures. Bellingham WA; 2001; 4319: 53–60.

[8] Ellis RJ, Sodee DB, Spirnak JP, Dinchman KH, O'Leary AW, Samuels MA, Resnick MI, Kinsella TJ. Feasibility and acute toxicities of radioimmunoguided prostate brachytherapy. Int J Radiat Oncol Biol Phys 2000;48(3):683–7.

[9] Hamilton RJ, Blend MJ, Pelizzari CA, Milliken BD, Vijayakumar S. Using vascular structure for CT–SPECT registration in the pelvis. J Nucl Med 1999;40(2):347–51.

[10] Liehn JC, Loboguerrero A, Perault X, Demange L. Superimposition of computed-tomography and single photon emission tomography immunoscinti-graphic images in the pelvis-validation in patients with colorectal or ovarian carcinoma recurrence. Eur J Nucl Med 1992;19(3):186–94.

[11] Balter JM, Sandler HM, Lam K, Bree RL, Lichter AS, Ten Haken RK. Measurement of prostate movement over the course of routine radiotherapy using implanted markers. Int J Radiat Oncol Biol Phys 1995;31(1):113–8.

[12] Narayana V, Roberson PL, Winfield RJ, McLaughlin PW. Impact of ultrasound and computed tomography prostate volume registration on evaluation of permanent prostate implants. Int J Radiat Oncol Biol Phys 1997;39(2):341–6.

[13] van Herk M, de Munck JC, Lebesque JV, Muller S, Rasch C, Touw A. Automatic registration of pelvic computed tomography data and magnetic resonance scans including a dull circle method for quantitative accuracy evaluation. Med Phys 1998;25(10):2054–67.

[14] Antolak JA, Rosen II, Childress CH, Zagars GK, Pollack A. Prostate target volume variations during a course of radiotherapy. Int J Radiat Oncol Biol Phys 1998;42(3):661–72.

[15] Remeijer P, Geerlof E, Ploeger L, Gilhuijs K, van Herk M, Lebesque JV. 3D portal image analysis in clinical practice: an evaluation of 2-D and 3D analysis techniques as applied to 30 prostate cancer patients. Int J Radiat Oncol Biol Phys 2000;46(5):1281–90.

[16] Roeske JC, Forman JD, Mesina CF, He T, Pelizzari CA, Fontenla E, Vijayakumar S, Chen GTY. Evaluation of changes in the size and location of the prostate, seminal vesicles, bladder, and rectum during a course of external beam radiation therapy. Int J Radiat Oncol Biol Phys 1995;33(5):1321–9.

[17] Scott AM, Macapinlac HA, Divgi CR, Zhang JJ, Kalaigian H, Pentlow K, Hilton S, Graham MC, Sgouros G, Pelizzari C, Chen G, Schlom J, Goldsmith SJ, Larson SM. Clinical validation of SPECT and CT/MRI image registration in radiolabeled monoclonal-antibody studies of colorectal carcinoma. J Nucl Med 1994; 35(12):1976–84.

[18] Fei B, Wheaton A, Lee Z, Duerk JL, Wilson DL. Automatic MR volume registration and its evaluation for the pelvis and prostate. Phys Med Biol 2002;47:823–38.

[19] vanHerk M, Bruce A, Kroes APG, Shouman T, Touw A, Lebesque JV. Quantification of organ motion during conformal radiotherapy of the prostate by three dimensional image registration. Int J Radiat Oncol Biol Phys 1995;33(5):1311–20.

[20] Tenhaken RK, Forman JD, Heimburger DK, Gerhardsson A, Mcshan DL, Pereztamayo C, Schoeppel SL, Lichter AS. Treatment planning issues related to prostate movement in response to differential filling of the rectum and bladder. Int J Radiat Oncol Biol Phys 1991;20(6):1317–24.

[21] Rohr K, Stiehl HS, Sprengel R, Buzug TM, Weese J, Kuhn MH. Landmark-based elastic registration using approximating thin-plate splines. IEEE Trans Med Imag 2001;20(6):526–34.

[22] Maurer CR, Hill DLG, Martin AJ, Liu HY, McCue M, Rueckert D, Lloret D, Hall WA, Maxwell RE, Hawkes DJ, Truwit CL. Investigation of intraoperative brain deformation using a 1.5-t interventional MR system: preliminary results. IEEE Trans Med Imag 1998;17(5):817–25.

[23] Davis MH, Khotanzad A, Flamig DP, Harms SE. A physics-based coordinate transformation for 3D image matching. IEEE Trans Med Imag 1997;16(3):317–28.

[24] Rueckert D, Sonoda LI, Hayes C, Hill DLG, Leach MO, Hawkes DJ. Nonrigid registration using free-form deformations: application to breast MR images. IEEE Trans Med Imag 1999;18(8):712–21.

[25] Denton ERE, Sonoda LI, Rueckert D, Rankin SC, Hayes C, Leach MO, Hill DLG, Hawkes DJ. Comparison and evaluation of rigid, affine, and nonrigid registration of breast MR images. J Comp Assisted Tomography 1999;23(5):800–5.

[26] Meyer CR, Boes JL, Kim B, Bland PH, Zasadny KR, Kison PV, Koral K, Frey KA, Wahl RL. Demonstration of accuracy and clinical versatility of mutual information for automatic multimodality image fusion using affine and thin-plate spline warped geometric deformations. Med Image Anal 1996;1(3):195–206.

[27] Krucker JF, Meyer CR, LeCarpentier GL, Fowlkes JB, Carson PL. 3D spatial compounding of ultrasound images using image-based nonrigid registration. Ultrasound Med Biol 2000;26(9):1475–88.

[28] Kimiaei S, Noz M, Jonsson E, Crafoord J, Maguire GQ. Evaluation of polynomial image deformation using anatomical landmarks for matching of 3D-abdominal MR-images and for atlas construction. IEEE Trans Nucl Sci 1999;46(4):1110–3.

[29] Wilson DL, Carrillo A, Zheng L, Genc A, Duerk JL, Lewin JS. Evaluation of 3D image registration as applied to MR-guided thermal treatment of liver cancer. J Magn Resonance Imag 1998; 8(1):77–84.

[30] Kim B, Boes JL, Frey KA, Meyer CR. Mutual information for automated unwarping of rat brain autoradiographs. Neuroimage 1997; 5(1):31–40.

[31] Bharatha A, Hirose M, Hata N, Warfield SK, Ferrant M, Zou KH. Three-dimensional finite element-based deformable registration of pre- and intraoperative prostate imaging. Radiology 2001;221:224.

[32] West J, Fitzpatrick JM, Wang MY, Dawant BM, Maurer CR, Kessler RM, Maciunas RJ, Barillot C, Lemoine D, Collignon A, Maes F, Suetens P, Vandermeulen D, vandenElsen PA, Napel S, Sumanaweera TS, Harkness B, Hemler PF, Hill DLG, Hawkes DJ, Studholme C, Maintz JBA, Viergever MA, Malandain G, Pennec X, Noz ME, Maguire GQ, Pollack M, Pelizzari CA, Robb RA, Hanson D, Woods RP. Comparison and evaluation of retrospective intermodality brain image registration techniques. J Comp Assisted Tomography 1997; 21(4):554–66.

[33] Gray H. Anatomy, Descriptive and Surgical (The classic collector's edition). New York: Gramercy Books; 1977. p. 1010.

[34] Maes F, Collignon A, Vandermeulen D, Marchal G, Suetens P. Multimodality image registration by maximization of mutual information. IEEE Trans Med Imag 1997;16(2):187–98.

[35] Press WH, Flannery BP, Teukolsky SA, Vellerling WT. Numerical recipes in C: the art of scientific computing, 2nd ed. New York: Cambridge University Press; 1993.

[36] Nelder J, Mead RA. A simplex method for function minimization. Comp J 1965;7:308–13.

[37] Goshtasby A. Registration of images with geometric distortions. IEEE Trans Geosci Remote Sensing 1988;26(1):60–4.

[38] Bookstein FL. Thin-plate splines and the atlas problem for biomedical images. Lecture Notes in Comp Sci 1991;511:326–42.

[39] Lee Z, Kemper C, Muzic RF, Berridge MS, Wilson DL. Quantitative pulmonary imaging based on PET–CT co-registration with warping. J Nucl Med 2001;42:10–11.

[40] Thacker NA, Jackson A, Moriarty D, Vokurka E. Improved quality of re-sliced MR images using re-normalized sinc interpolation. J Magn Resonance Imag 1999;10(4):582–8.

Corey Kemper received her BS in Biomedical Engineering from Case Western Reserve University (CWRU) in 2001. In the same year, she was also named CWRU's Engineering Student of the Year. Currently, she is pursuing a PhD in the Electrical Engineering and Computer Science Department at the Massachusetts Institute of Technology (MIT) on a fellowship awarded by the Whitaker Foundation. She continues to work in biomedical imaging research as part of the Medical Vision Group in the Artificial Intelligence Laboratory at MIT and in the Surgical Planning Laboratory at the Brigham and Women's Hospital.

Baowei Fei received his B.S. (1990) and M.S. (1995) in Biomedical Engineering from Xi'an Jiaotong University, China, where he received the Science and Technological Award from the National Department of Education in 1993. He obtained his PhD (1998) from Shanghai Jiao Tong University, China, where he was awarded the Honor of Excellent Graduate Student of the Year 1998 of Shanghai. From 1998 to 2000, he worked as a Research Fellow at the Computer Integrated Medical Intervention Laboratory of Nanyang Technological University, Singapore. He is currently a Senior Research Associate in the Department of Biomedical Engineering at Case Western Reserve University. In 2001, he won the Postdoctoral Traineeship Award from the US Department of Defense Congressionally Directed Medical Research Program. He is an active member of IEEE and SPIE. He has over 10 years of experience in biomedical engineering with research interests in biomedical image analysis and registration, interventional MRI, medical robotics and computer-aided surgery.

David L. Wilson is currently a Professor in the Departments of Biomedical Engineering and Radiology at Case Western Reserve University (CWRU). His PhD is from Rice University. He has authored over 60 refereed journal papers and over 80 proceedings papers and book chapters, and he holds six patents in interventional medical imaging. He has served as an organizer of biomedical engineering conferences and reviewer for federal funding agencies. He has a history of substantial federal funding in biomedical imaging. He has been a leader in developing biomedical imaging research and education at CWRU including teaching core courses, advising a large number of graduate and undergraduate students, chairing faculty search committees, and co-authoring several successful developmental proposals to foundations and to state and federal agencies. His research interests include biomedical image analysis, interventional MRI, quantitative image quality, and molecular imaging.

Biomedical Paper

Automatic 3D Registration for Interventional MRI-Guided Treatment of Prostate Cancer

Baowei Fei, Ph.D., Jeffrey L. Duerk, Ph.D., and David L. Wilson, Ph.D.

Department of Biomedical Engineering, Case Western Reserve University (B.F., J.L.D., D.L.W.) and Department of Radiology, University Hospitals of Cleveland and Case Western Reserve University (J.L.D., D.L.W.), Cleveland, Ohio

ABSTRACT

The goal of this research is to register real-time interventional magnetic resonance imaging (iMRI) slice images with a previously obtained high-resolution MRI image volume, which in turn can be registered with functional images such as those from SPECT. The immediate application is in iMRI-guided treatment of prostate cancer, where additional images are desired to improve tumor targeting. In this article, simulation experiments are performed to demonstrate the feasibility of slice-to-volume registration for this application. We acquired 3D volume images from a 1.5-T MRI system and simulated low-field iMRI image slices by creating thick slices and adding noise. We created a slice-to-volume mutual information registration algorithm with special features to improve robustness. Features included a multiresolution approach, two similarity measures, and automatic restarting to avoid local minima. To assess the quality of registration, we calculated 3D displacements on a voxel-by-voxel basis over a volume of interest between slice-to-volume registration and volume-to-volume registration, which was previously shown to be quite accurate. More than 800 registration experiments were performed on MR images of three volunteers. The slice-to-volume registration algorithm was very robust and accurate for transverse slice images covering the prostate, with a registration error of only 0.4 ± 0.2 mm. Error was greater at other slice orientations and positions. The automatic slice-to-volume mutual information registration algorithm is robust and probably sufficiently accurate to aid in iMRI-guided treatment of prostate cancer. Comp Aid Surg 7: 257–267 (2002). ©2003 Wiley-Liss, Inc.

INTRODUCTION

We use a low-field open magnet system to guide minimally invasive treatments, including radiofrequency (RF) thermal ablation of abdominal cancer.[1–3] We are currently investigating the incorporation of other medical images for use in live-time treatment planning and execution. Examples of images for possible incorporation include high-resolution MR images from another scanner or from a

---

very-long-duration acquisition in the iMRI scanner, MR spectroscopy images, functional MR images, MR angiography images, PET images, and SPECT images. In some cases, these other images can be used to localize a disease process such as a tumor; in other cases, the images can be used to locate a structure that should be avoided, such as a critical brain structure identified with functional MRI. iMRI is currently under investigation for possible use in the treatment of prostate cancer. Because MRI does not reliably show prostate tumor, we intend to incorporate nuclear medicine or MR spectroscopy images with an improved ability to detect and localize the tumor.[4,5]

To incorporate image data from other sources in a real-time iMRI procedure, we intend to register two-dimensional (2D) slice images acquired quickly on the iMRI scanner with a previously acquired volume of image data. An image volume from another modality can then be registered with the full MR volume. Thus, to incorporate SPECT in an iMRI procedure, we will first register the SPECT image volume with an MR volume.[6] Then, when registering iMRI slice images to the MR volume, they can also be mapped to the SPECT functional image data. If this procedure is successful, a variety of potential visualization tools will be available to help the physician localize and apply treatments appropriately. The real-time iMRI images will be used for guidance, and any small misregistration errors can very probably be mentally corrected by the physician. To simplify and improve the slice-to-volume (SV) registration step, we intend to always use MR images acquired with similar pulse sequences. In this report, we investigate SV registration of MR images.

Previous success with registering one MR prostate volume to another[7] encourages us to pursue this plan. We call this process volume-to-volume or VV registration. A rigid-body mutual information registration method was used, with some features to improve robustness.[7] We carefully evaluated registration quality using a variety of methods. For volume pairs acquired over a short timespan from a supine subject with legs flat on the table, registration accuracy for both prostate centroids (typically <1 mm) and bony landmarks (average 1.6 mm) was in the order of one voxel ($\approx$1.4 mm). For volumes acquired under very different conditions, for example, with legs flat or raised into the treatment position, or with and without bladder or rectal filling, we obtained somewhat larger prostate centroid registration errors of about 3.0 mm. From our results with VV prostate registration, it

was decided that SV accuracy could be assessed by comparing results to VV registration for those volume pairs having low VV registration error.

SV registration is an alternative, fast approach for including other modalities in iMRI-guided treatment. Previously, image registration was used to combine preoperative MRI and CT volumes for iMRI-guided intranasal microendoscopy where iMRI volumes were acquired and registered with preoperative data.[8] Here, it is anticipated that the SV method will be faster, because image acquisition is faster and because registration of a slice should require many fewer calculations for a volume. In addition, our experience is that 2D slice acquisitions are routinely acquired during iMRI interventions, whereas volume acquisitions are only acquired infrequently. In previously published reports, SV registration was mainly applied to the brain for applications of functional MRI,[9,10] postmortem pathology studies,[11] and anatomical modeling.[12] There are no reports of SV registration for abdominal organs or iMRI guidance.

The application of SV registration methods to iMRI-guided treatment of prostate cancer raises several challenges. First, iMRI images often have a lower signal-to-noise ratio (SNR) than diagnostic MR images because of the emphasis on fast imaging and because of the typically lower field-strength of open iMRI magnets. Second, a single slice, or a few slices, provides many fewer structures than an entire volume for voxel-based matching. Third, the prostate can move relative to the pelvic bones due to changes in rectal and bladder filling[13,14] or changes in patient posture for treatment.[7] That is, alignment of the pelvic bones (prominent anatomical features in MR gray-scale images) does not necessarily ensure that the prostate is aligned. Fourth, the normal prostate is a small organ; when healthy, it measures only ~3.8 cm in its widest dimension.[15] The prostate is located below the much larger bladder, which can change its shape and size during imaging. Finally, times for registration and algorithm robustness are of particular concern in this application.

In this study, we test the performance of SV registration. In the next section, we first describe a voxel-based registration method with special features to improve robustness. This is followed by details of how entire MR volume pairs are acquired on a conventional MR scanner and how realistic iMRI images are simulated. Later, results are presented from over 800 registration experiments comparing slice-to-volume with volume-to-volume registration.

MATERIALS AND METHODS

Registration Algorithm

We used an algorithm with special features for the slice-to-volume, or SV, registration. A similar algorithm was previously successfully applied to MR volume-to-volume registration of the prostate.[7] The algorithm is outlined in the following paragraphs.[7,16]

We used two similarity measures, mutual information (MI) and correlation coefficient (CC), in the registration. One image, *R*, is the *reference*, and the other, *F*, is *floating*. Their mutual information *MI(R, F)* is given below.[17]

$$MI(R, F) = \sum_{r,f} P_{RF}(r, f) \log \frac{p_{RF}(r, f)}{p_R(r) \cdot p_F(f)}$$

The joint probability, $p_{RF}(r, f)$, and the marginal probabilities of the reference image, $p_R(r)$, and the floating image, $p_F(f)$, can be estimated from the normalized joint intensity histogram. The correlation coefficient *CC(R, F)* is given below.[18]

$$CC(R, F)$$
$$= \frac{\sum (R(r) - \bar{R}(r))(F(f) - \bar{F}(f))}{\sqrt{\sum (R(r) - \bar{R}(r))^2 \sum (F(f) - \bar{F}(f))^2}}$$

Here, $\bar{R}(r)$, $\bar{F}(f)$ denote the average intensities of the reference and floating images, respectively, and the summation includes all voxels within the overlap region.

We compared the two similarity measures at different resolutions to determine their suitability for SV registration. At $\frac{1}{4}$ resolution, we resampled images so as to give one-quarter the number of voxels along each linear dimension. At *full resolution*, we used the full number of voxels. In Figure 1, the two similarity measures are plotted as a function of translations. Two high-resolution MR volumes were registered as described previously,[7] and values were plotted with the origin as the optimal transformation. We calculated CC and MI values while moving the simulated iMRI image relative to the high-resolution MR image along the coronal (anterior–posterior) axis. The simulated iMRI image was obtained as described later.

We use a multiresolution approach and perform registration from low to high resolution. We use CC at the two lower resolutions because it gives fewer local maxima (Fig. 1) and can be calculated faster than MI. We use MI at full resolution because the peaked similarity function gives

a more precise solution than CC (Fig. 1). To avoid local maxima, we include a restarting feature where registration is restarted with randomly perturbed parameters obtained from a uniform distribution about the initial transformation values at the current resolution being used. The algorithm restarts until the absolute CC is above an experimentally determined threshold or the maximum number of restarts is reached. Absolute CC is used rather than MI because it has a well-defined range between 0 and 1, and because it provides an independent check of the MI result at the highest resolution.

All important results are recorded following an optimization cycle, including the CC and/or MI values, the number of restarts, and the transformation parameters. At the end of processing at a lower resolution, we always select the transformation parameters having the maximum CC value. We then scale the translation parameters appropriately and assign the new parameters to be initial values at the next-higher resolution. At the highest resolution, MI rather than CC is the similarity measure, and we select the final transformation parameters to be those with the maximum MI value.

For registration, we use rigid-body transformation (three translations and three rotations) and trilinear interpolation, as described previously.[19] For optimization, we use the downhill simplex method of Nelder and Mead.[20] Optimization of similarity ends either when the maximum number of calculations is reached (typically 500) or when the fractional change in the similarity function is smaller than a tolerance (typically 0.001). There are several preprocessing details to note: The input MRI volume is a 3D MR acquisition giving 256 × 256 × 128 nearly isotropic voxels over a field of view covering the whole pelvis. We create isotropic voxels of about 1.37 mm on each side using 3D linear interpolation. IDL (Interactive Data Language, Research System Inc., Boulder, CO) is used as the programming language.

Typical parameter values are now described. An initial guess is used at the lowest resolution of all zeros because the patient is normally oriented approximately the same way from one scan to the next. All CC thresholds are set at 0.5, and the maximum number of restarts is set at 20, 10, and 5, from low to high resolution, respectively.

Image Acquisition

High-resolution MRI volumes were acquired using a 1.5-T Siemens MRI system (Magnetom Symphony, Siemens Medical Systems, Erlangen, Germany). An eight-element phased-array body coil was
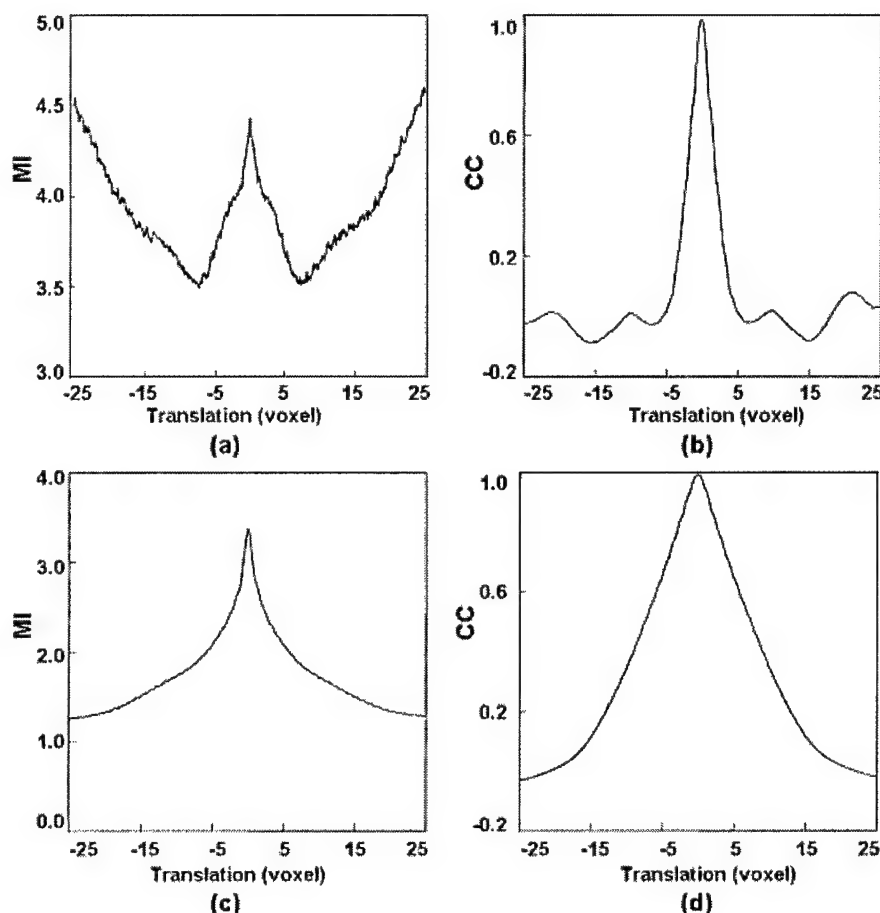
Fig. 1. Similarity functions are plotted as a function of translations in the multiresolution registration process. Two high-resolution MRI volumes were registered. From the optimal parameters, we computed the similarity of the simulated iMRI and MRI images as a function of translations along the coronal (anterior–posterior) axis. MI is plotted in (a) and (c); CC is plotted in (b) and (d). Graphs (a) and (b) are at the lowest resolution where images are down-sampled by 1/4 along each linear dimension, giving a distance between voxel centers of ~5.5 mm. A false global maximum for MI occurred at +25 voxels. Graphs (c) and (d) are plots at full resolution. Images are from volunteer S2.

used to ensure coverage of the prostate with a uniform sensitivity. Typically, two anterior and two posterior elements were enabled for signal acquisition.

Two different MR sequences were used. The first was a 3D RF spoiled gradient echo steady-state pulse sequence (FLASH) with TR/TE/flip parameters of 12/5.0/60, giving 256 × 256 × 128 voxels over a 330 × 330 × 256-mm field of view (FOV) to yield 1.3 × 1.3 × 2.0-mm voxels oriented to give the highest resolution for transverse slices. The acquisition time is 5.6 min. This sequence is good for pelvic imaging, but is not ideal for the prostate. It was used to acquire volumes for volunteer S1.

The second sequence was a 3D rapid gradient echo sequence (PSIF) designed to acquire the spin-echo component of the steady-state response, rather than the free induction decay. The spin-echo com-

ponent forms immediately prior to the RF pulse, and is shifted toward the prior RF pulse through appropriate gradient waveform design. The sequence with 9.4/5.0/60 (TR/TE/flip) yields 160 × 256 × 128 voxels over a 219 × 350 × 192-mm rectangular FOV and 1.4 × 1.4 × 1.5-mm voxels oriented to give the highest resolution for transverse slices. There is oversampling at 31% in the slice direction to reduce aliasing artifacts. The acquisition time is 4.3 min. This sequence gave excellent image contrast for the prostate, and was used to acquire volumes for volunteers S2 and S3.

Imaging Experiments

We acquired high-resolution MRI volumes from three volunteers. For each volunteer, three image volumes were obtained with an imaging session.
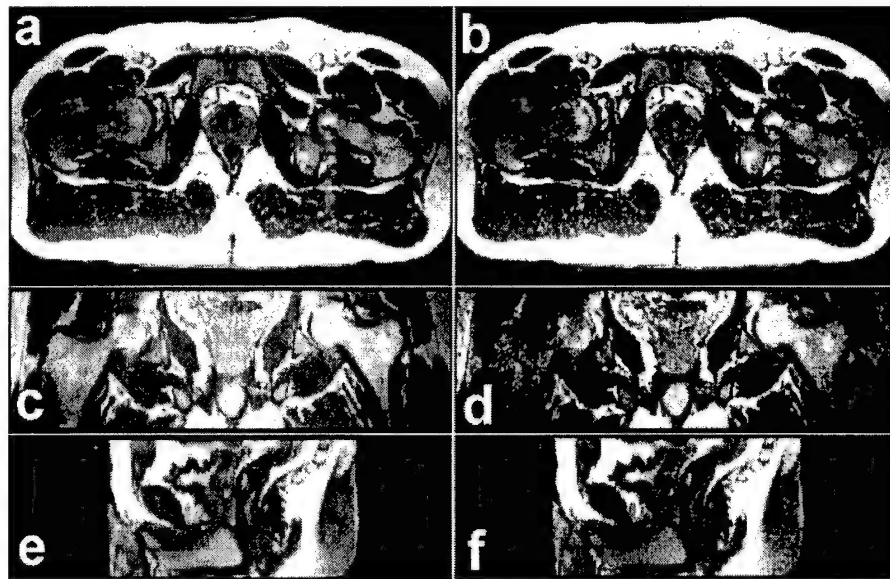
Fig. 2. Simulated iMRI images. Images on the left, (a), (c), and (e), are the original high-resolution MR images in the transverse, coronal, and sagittal planes, respectively. Images on the right are corresponding simulated thick iMRI images with SNR = 10. Images are from volunteer S2.

Each volume was acquired with compatible conditions. Volunteers laid supine with legs flat, similar to the position in routine MR scanning. Between volume acquisitions, volunteers got off the MRI table, stretched, and walked around to ensure that they would assume a different position when they laid back on the table. The coil array was centered on the prostate. All images of a volunteer were acquired with the same MRI acquisition parameters. In total, there were nine pairs of high-resolution MRI volumes for registration.

Simulation of iMRI Slice Images

We used high-resolution MRI volumes to simulate iMRI images by creating thick slices and adding noise and receive-coil inhomogeneity. Clinically, we typically use an iMRI slice thickness of 4.0–6.0 mm. We averaged three slices 1.4 mm thick to create a 4.2-mm-thick slice.

Noise was added to the simulated iMRI image. MR noise is described by the Rician distribution,[21] but at reasonably high signal values it is accurately approximated with Gaussian white noise.[22] We measured typical signal and noise values on our open magnet system using a homogenous phantom and methods described elsewhere.[23,24] Gaussian noise was then added to the simulated iMRI slice images either to match the measured SNR or to give much greater noise to further stress registration. We report noise experiments using the SNR of the simulated slice images. Figure 2 shows high-resolution MRI and noisy simulated iMRI slice images.

We simulated receive-coil inhomogeneity from a belt coil used in the clinical iMRI acquisitions. The coil is modeled as a solenoid, and the magnetic field is highest at the coil center, falling off in the axial direction. According to the Biot-Savart law,[25] this model also accounts for the spatial sensitivity of the coil to MR signal sources.

Registration Experiments

We desire an iMRI slice imaging method that gives robust, accurate registrations, and is relatively insensitive to acquisition parameters. Experiments were perfomed to determine the dependence on slice orientation (transverse, sagittal, and coronal), on slice position relative to the prostate (above, centered, and below), and on image noise from fast imaging techniques. For each volume pair, we extracted data from one volume and registered slice images to the other volume. Many different slices were used in experiments. Slice images are simulated as described above.

Registration Evaluation

Visual Inspection

Registration experiments were evaluated by visual inspection. We used *RegViz,* a program created in

IDL in our laboratory with multiple visualization and analysis methods. First, we manually segmented prostate boundaries in image slices and copied them to corresponding slices. This enabled visual determination of the overlap of prostate boundaries over the entire volume. Second, color overlay displays were used to evaluate overlap of structures. One image was rendered in gray and the other in the "hot iron" color scheme available in IDL. To visualize potential differences, it was useful to interactively change the contribution of each image using the transparency scale. Third, we used a sector display that divided the reference and registered images into rectangular sectors and created an output image by alternating sectors from the two input images. This way, even subtle shifts of edges would be clearly seen.

Comparison to Volume-to-Volume Registration Standard

Our standard evaluation method was to compare SV and VV registration. Because this relies on VV registration accuracy, we will now review our previous results.[7] For volume pairs acquired over a short time-span from a supine subject with legs flat on the table, prostates were well aligned, and prostate centroid displacements were typically <1 mm. The registration accuracy, as determined from displacements of pelvic bony landmarks, was 1.6 ± 0.2 mm. This error might be overestimated because it includes the uncertainty of locating the bony landmarks. The centroid error was slightly smaller because the prostate was at the volume center and rotation errors had less effect. From our success with VV prostate registration, it was decided that we could obtain SV accuracy by comparison with VV registrations for those volume pairs having low VV registration error.

To compare SV and VV registration, we defined a rectangular volume of interest (VOI) that just covered the prostate and calculated voxel displacements between the two registrations. To voxels within this VOI, we applied the transformations obtained by VV and SV registrations. We then calculated the 3D displacements between the transformed voxels. The mean voxel distance was used as the metric of SV registration error. For the evaluation of algorithm robustness, we defined the SV registration as being *successful* when the 3D displacement was less than 2.0 mm.
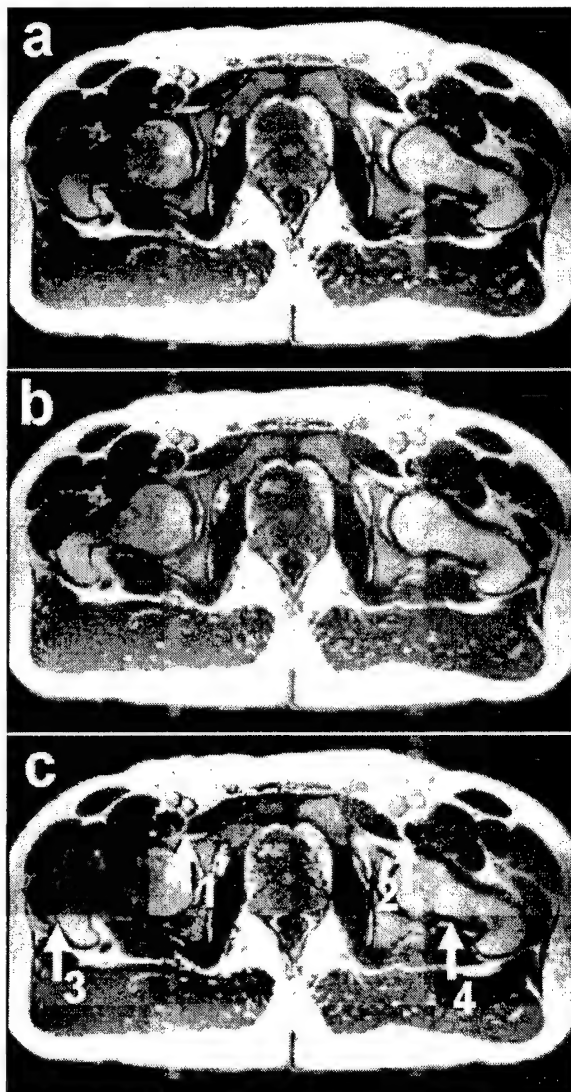

Fig. 3. Sector display showing excellent pelvic registration. Image (a) is a transverse slice from a high-resolution MRI volume. Image (b) is the corresponding noise iMRI slice. In the sector display shown in (c), alternating rectangular sections from (b) are made brighter and combined with sections from (a) to show the matching boundaries. The boundaries of bones and other structures are continuous, as shown particularly at locations 1–4. Other slices from this volume were also perfectly aligned, indicating good 3D alignment. Image volumes are from Volunteer S2.

RESULTS

Slice Orientation

In Figure 3, the sector display shows a simulated slice image registered with a high-resolution volume image. The slice image was obtained at a transverse orientation near the center of the prostate. The sector display shows excellent alignment
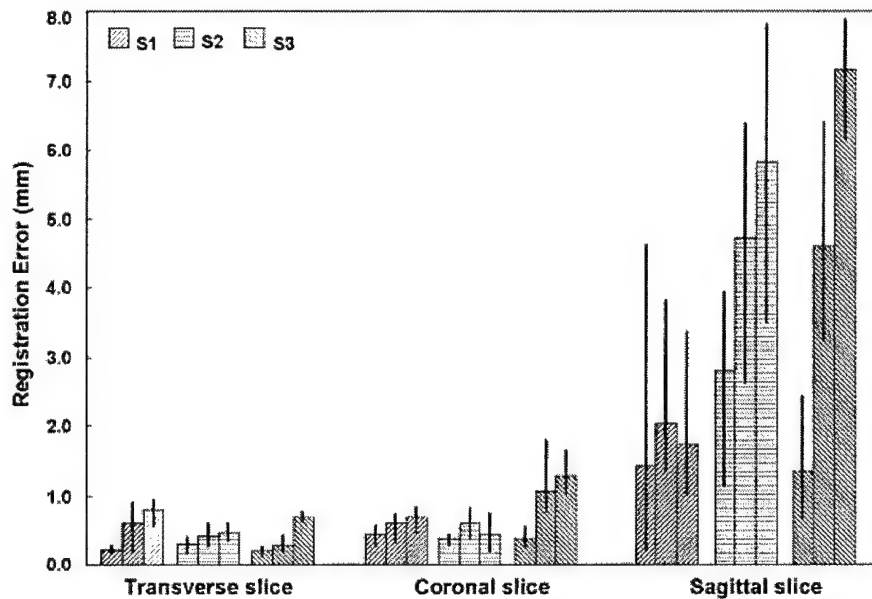
Fig. 4. SV registration using slices at different orientations. The error metric is the voxel displacement between the SV and VV transformations. Plotted are mean errors, as well as maxima and minima over a rectangular VOI surrounding the prostate. For each volunteer, S1, S2, and S3, we registered three volume pairs. For each pair, five registration experiments were conducted using five different simulated iMRI transverse slices intersecting the prostate. The simulated SNR was 25. Averaging data across all volunteers gives 0.4 ± 0.2 mm, 0.5 ± 0.2 mm, and 2.6 ± 1.6 mm errors for transverse, coronal, and sagittal slices, respectively.

at this position. Other transverse images were also well aligned, indicating that the registration was successful in three dimensions.

Figure 4 shows results for single slices oriented in the three traditional orthogonal directions. All slices are near the center of the prostate. Compared to VV transformations, registration error is smallest for transverse slices and largest for sagittal slices. Averaging across all transverse data, the error is only 0.4 ± 0.2 mm, where the latter number is a standard deviation. Coronal slices also gave quite small errors of 0.5 ± 0.2 mm. As shown in Figure 5c, transverse slices work best because they contain abundant anatomical structures that do not deform relative to the prostate. That is, a transverse slice centered at the prostate excludes the bladder that can deform and create an inconsistent match for registration. Figure 5a,b shows that coronal and sagittal views contain large regions of the bladder and rectum that can deform with filling. The following analyses are all based on transverse slices.

Slice Position

Figure 6 shows registration results for transverse slices at different distances from the prostate center. Slices centered on the prostate produced the best results, with a displacement error always less

than 1.0 mm. The reason is that slices centered at the prostate include an abundance of bony structures giving good information for registration. They also exclude portions of the bladder that can deform and create inconsistent matches for registration (Fig. 7). Slices above the prostate include the deformable bladder, which can stress the registration algorithm, especially for volunteer S3 (Fig. 6). Slices below the prostate mainly contain muscle and fatty regions from the hips that can deform, and there is less information for rigid-body registration. This effect was more pronounced for volunteer S2 (Fig. 6).

Noise Level

Figure 8 shows registration results for transverse slices with added noise. The typical iMRI SNR under clinical conditions is about 25. Even when noise far exceeded this normal situation, registration results were still quite good. A 100% success rate was achieved with an acceptance criterion of <2.0 mm, even when the SNR was as bad as 10.

Robustness and Calculation Time

The registration algorithm was quite robust for transverse slices covering the prostate. Using the
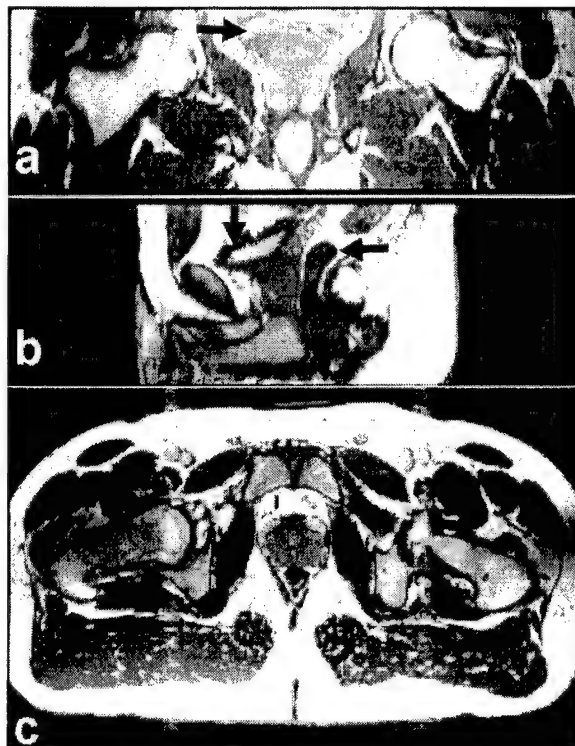
Fig. 5. Image slices showing the advantage of transverse images. The coronal slice in (a) contains the bladder, as indicated by the black arrow. The sagittal slice in (b) contains both the bladder (vertical arrow) and rectum (horizontal arrow). The transverse slice in (c) excludes the bladder and contains abundant bony structures.

nine volume pairs from three volunteers, the algorithm never failed for any transverse slice covering the prostate. In addition, the final registration result was insensitive to initial guesses within a large range: [−60, +60] mm for translations and [−20, +20] degrees for rotations. With the restarting algorithm, we even successfully registered slices as much as 80 mm from the optimum. This working range is probably sufficient for clinical applications where we can ensure good starting values. Using the pelvic bones as markers and needle localization methods,[26] we should be able to position the prostate within about ±20 mm. In addition, the patient normally lies supine in the MR bed with very little rotation (<±5 degrees).

The time for an SV registration was typically about 5 s on a Pentium IV 1.8-GHz CPU with 1 GB of memory. The algorithm was written in IDL and could probably be made much faster in a lower-level language such as C. A call to the simplex optimization typically resulted in 50 to 105 similarity evaluations before the tolerance value (0.001) was reached.

DISCUSSION

For transverse slices covering the prostate, the slice-to-volume registration results agreed very favorably with the volume-to-volume results. That is,
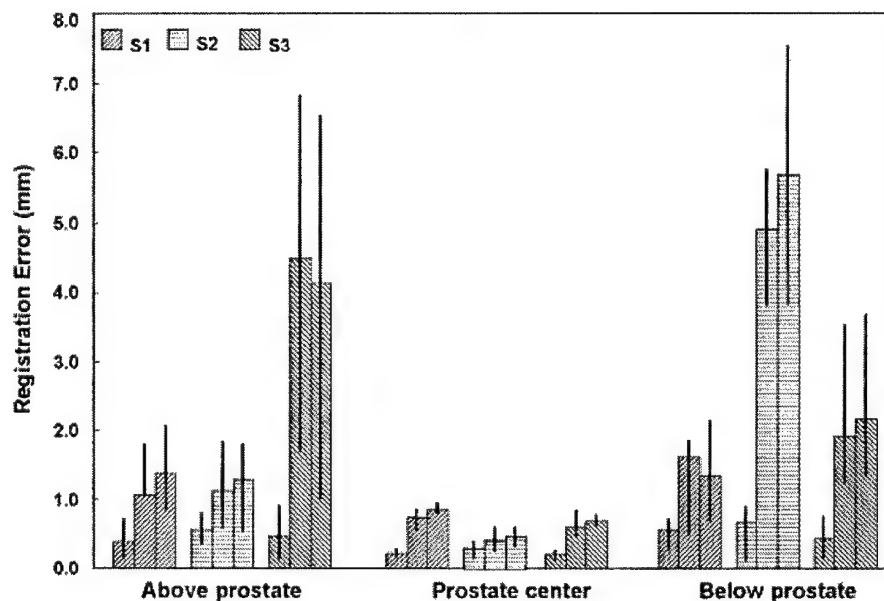

Fig. 6. SV registration using transverse slices at different positions. Groups of five iMRI slices each were extracted near the prostate center, ~35 mm above the prostate base, and ~35 mm below the prostate apex and registered to the MR volume. Other details are given in Figure 4. Slices at the prostate center worked best.
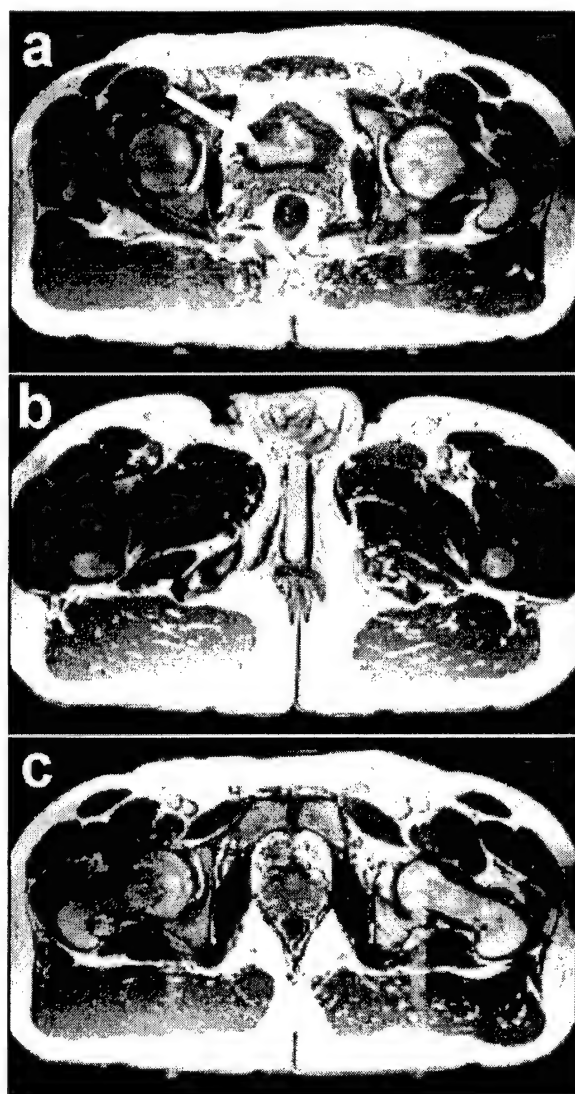
Fig. 7. Transverse images at different positions relative to the prostate. The image 35 mm above the prostate in (a) includes the bladder, indicated by the white arrow. A slice 35 mm below the prostate in (b) mainly contains muscle (dark) and fatty regions (white). A slice centered at the prostate in (c) has abundant bony structures.

we found that SV is equal to VV registration, with an average voxel displacement between them of only 0.4 mm in the prostate. The accuracy of SV is essentially the same as that previously reported for VV registration.[7] In our previous report, it was found that, whenever the subject was in comparable conditions, the prostate centroid registration error was typically <1 mm, or less than a voxel of 1.4 mm. Hence, for SV applied to images in this report, we predict a prostate error of very nearly 1.4 mm or less. In the previous report, it was found that when-

ever supine subjects raised their legs, the prostate moved towards the posterior direction by about 3 mm.[7] Another factor that affects prostate registration is rectal filling.[7,13] Hence, we recommend that prostate registration be done with the patient under similar conditions by maintaining a similar posture and by taking clinical measures to reduce rectal and bladder filling. We see no reason to suspect that SV registration would not be very accurate in these cases.

Slice-to-volume registration is probably sufficiently accurate for many iMRI applications. Compared to a typical iMRI slice thickness of ~3.0 mm, SV registration is quite accurate. The accuracy of SV is probably much better than that of multimodality registration, where the typical functional image has a thickness of 3.0–4.0 mm. If one were to use functional or high-resolution MR images directly for targeting, the requirements for registration accuracy would be great. However, fused image data will not be used blindly. Rather, one can use fused images as a guide. Physicians will always use the real-time anatomical iMRI images for needle guidance.[26,27] With proper visualization tools, they should be able to mentally account for any small registration errors. In addition, there is very often image evidence of cancer in MR prostate images that can perhaps be identified with the aid of functional images. Such MR-visible lesions can become the markers for tumor targeting. As a result of these considerations, we believe that the accuracy of SV registration is sufficient to justify further investigation of its application in iMRI.

The algorithm is quite robust for the SV registration. Significantly, the registration never failed for transverse slices covering the prostate. It was obtained even in the presence of noise levels far beyond those encountered in iMRI. This is very important for iMRI, where magnetic fields are low and imaging is fast. It was also determined that coronal images work fairly well. This could be useful, because two orientations might provide more flexibility for clinical applications.

There are several reasons for the robustness. First, using both CC and MI at different resolutions was an important feature that increased robustness. When only MI was used, registrations at low resolution very often gave false solutions that misled registration at the next-highest resolution. Fortunately, CC performed well and gave many fewer local maxima at low resolution.[7] However, MI gave a more accurate solution at high resolution due to the peaked MI surface.[7] Our registration algorithm combined advantages from the two similarity mea-
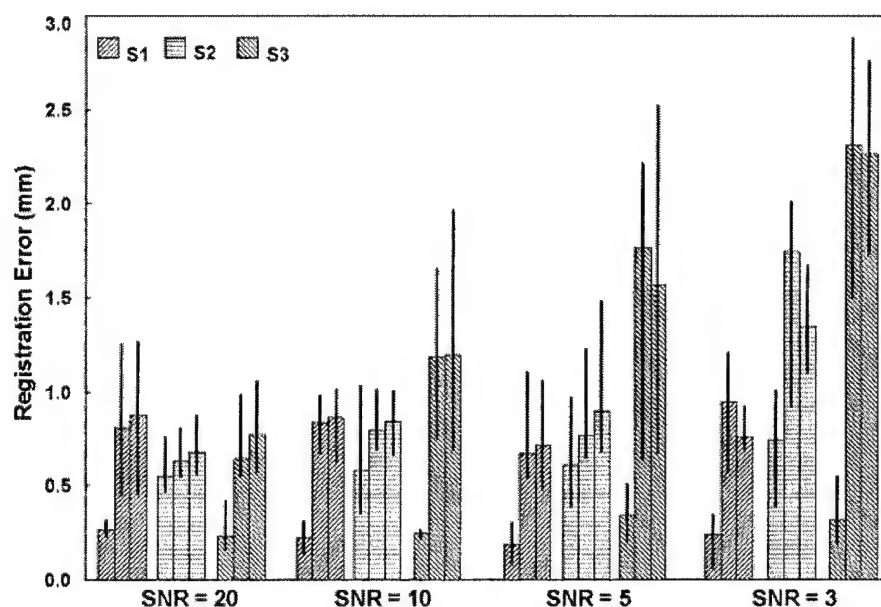
Fig. 8. SV registration at different noise levels. The simulated iMRI image slice had SNR values of 20, 10, 5, and 3, corresponding to added noise levels of 4, 8, 16, and 27 standard deviation gray levels, respectively. The transverse slices from Figure 4 were used. Other details are given in the legend of Figure 4. Even though noise greatly exceeds that found in iMRI, registration was little affected.

sures. Second, the restarting mechanism was also quite important. Without restarting, it was found that registrations sometimes failed in cases of volumes with a large mismatch of 54 mm and high noise. Even these cases resulted in a proper solution when restarting was employed.

The simulation provided a realistic, simple, and efficient way to evaluate the algorithm for our application. The simulated iMRI images are good representations of images from our low-field-strength iMRI system. However, there are other practical aspects of iMRI imaging that were not covered in the simulations. For instance, we did not reproduce the susceptibility artifact of an RF treatment needle in our simulations. From previous experience,[19] we think this is not a problem, because the needle artifact occupies a relatively small percentage of voxels in most cases.

Another practical aspect is possible deformation in the pelvic region. When images were acquired under much different conditions, such as supine or with legs raised, it was determined that warping was required to successfully register the prostate.[28,29] The warping registration method was based upon independent optimization of many interactively placed control points using MI and a thin-plate spline transformation. About 180 strategically placed control points were sufficiently ex-

pressive to capture important features of the deformation. In the event that a device such as an endorectal MR coil is used, warping registration will be required.

Finally, we conclude that the slice-to-volume registration algorithm is quite robust for transverse slice images covering the prostate, and that registration accuracy is probably sufficiently accurate to aid iMRI-guided thermal ablation of prostate cancer. It is quite feasible to include previously acquired high-resolution MRI or nuclear images in iMRI-guided treatment procedures, and we are beginning to explore this application in animal experiments.

ACKNOWLEDGMENT

REFERENCES

1. Lewin JS, Connell CF, Duerk JL, Chung YC, Clampitt ME, Spisak J, Gazelle GS, Haaga JR. Interactive MRI-

guided radiofrequency interstitial thermal ablation of abdominal tumors: clinical trial for evaluation of safety and feasibility. J Magn Reson Imaging 1998;8:40–47.

2. Merkle EM, Shonk JR, Zheng L, Duerk JL, Lewin JS. MR imaging-guided radiofrequency thermal ablation in the porcine brain at 0.2T. Radiology 1999;213P: 1131.

3. Wilson DL, Carrillo A, Zheng L, Genc A, Duerk JL, Lewin JS. Evaluation of 3D image registration as applied to MR-guided thermal treatment of liver cancer. J Magn Reson Imaging 1998;8:77–84.

4. Sodee DB, Malguria N, Faulhaber P, Resnick MI, Albert J, Bakale G. Multicenter ProstaScint imaging findings in 2154 patients with prostate cancer. Urology 2000;56:988–993.

5. Scheidler J, Hricak H, Vigneron DB, Yu KK, Sokolov DL, Huang LR, Zaloudek CJ, Nelson SJ, Carroll PR, Kurhanewicz J. Prostate cancer: localization with three-dimensional proton MR spectroscopic imaging—clinicopathologic study. Radiology 1999;213:473–480.

6. Lee Z, Sodee DB, Duerk JL, Nelson AD, Berridge MS. Automatic registration of SPECT-MRI in the pelvis. J Nuclear Med 2000;41:232.

7. Fei BW, Wheaton A, Lee Z, Duerk JL, Wilson DL. Automatic MR volume registration and its evaluation for the pelvis and prostate. Phys Med Biol 2002;47: 823–838.

8. Hill DLG, Langsaeter LA, Poynter-Smith PN, Summers PE, Keevil SF, Walsh R, Hawkes DJ, Gleeson MJ. Feasibility study of magnetic resonance imaging-guided intranasal flexible microendoscopy. Comp Aid Surg 1997;2:264–275.

9. Kim B, Boes JL, Bland PH, Chenevert TL, Meyer CR. Motion correction in fMRI via registration of individual slices into an anatomical volume. Magn Reson Med 1999;41:964–972.

10. Rohlfing T, West JB, Beier J, Liebig T, Taschner CA, Thomale UW. Registration of functional and anatomical MRI: accuracy assessment and application in navigated neurosurgery. Comp Aid Surg 2000;5:414–425.

11. Kim TS, Singh M, Sungkarat W, Zarow C, Chui H. Automatic registration of postmortem brain slices to MRI reference volume. IEEE Trans Nuclear Sci 2000; 47:1607–1613.

12. Zhengping J, Mowforth PH. Mapping between MR brain images and voxel model. Med Inform (Lond) 1991;16:183–193.

13. Herk MV, Bruce A, Kroes APG, Shouman T, Touw A, Lebesque JV. Quantification of organ motion during conformal radiotherapy of the prostate by three dimensional image registration. Int J Radiat Oncol Biol Phys 1995;33:1311–1320.

14. Tenhaken RK, Forman JD, Heimburger DK, Gerhardsson A, McShan DL, Pereztamayo C, Schoeppel SL, Lichter AS. Treatment planning issues related to prostate movement in response to differential filling of the rectum and bladder. Int J Radiat Oncol Biol Phys 1991;20:1317–1324.

15. Gray H. Anatomy, Descriptive and Surgical. New York: Gramercy Books, 1977. p 1010.

16. Fei BW, Wheaton A, Lee Z, Nagano K, Duerk JL, Wilson DL. Robust registration algorithm for interventional MRI guidance for thermal ablation of prostate cancer. In: Mun SK, editor: Proceedings of SPIE Medical Imaging: Visualization, Display, and Image-Guided Procedures 2001. SPIE Vol 4319. p 53–60.

17. Collignon A, Maes F, Delaere D, Vandermeulen D, Suetens P, Marchal G. Automated multimodality image registration using information theory. In: BizaisY, Barillot C, DiPaola R, editors: Information Processing in Medical Imaging: Proceedings of 14th International Conference (IPMI'95). Computat Imaging Vis 1995. p 287–298.

18. Press WH, Teukolsky SA, Vellerling WT, Flannery BP. Numerical Recipes in C: The Art of Scientific Computing (2nd ed.). New York: The Press Syndicate of the University of Cambridge, 1992. p 636.

19. Carrillo A, Duerk JL, Lewin JS, Wilson DL. Semiautomatic 3-D image registration as applied to interventional MRI liver cancer treatment. IEEE Trans Med Imaging 2000;19:175–185.

20. Nelder J, Mead RA. A simplex method for function minimization. Comput J 1965;7:308–313.

21. Macovski A. Noise in MRI. Magn Reson Med 1996; 36:494–497.

22. Gregg RC, Nowak RD. Noise removal methods for high resolution MRI. IEEE Nuclear Sci Symp 1997; 2:1117–1121.

23. Henkelman RM. Measurement of signal intensities in the presence of noise in MR images. Med Phys 1985; 12:232–233.

24. Kaufman L, Kramer DM, Crooks LE, Ortendahl DA. Measuring signal-to-noise ratios in MR imaging. Radiology 1989;173:265–267.

25. Forbes LK, Crozier S, Doddrell DM. Rapid computation of static fields produced by thick circular solenoids. IEEE Trans Magnet 1997;33:4405–4410.

26. Lewin JS, Duerk JL, Jain VR, Petersilge CA, Chao CP, Haaga JR. Needle localization in MR-guided biopsy and aspiration: effects of field strength, sequence design, and magnetic field orientation. Am J Roentgenol 1996;166:1337–1345.

27. Merkle EM, Shonk JR, Zheng L, Duerk JL, Lewin JS. MR imaging-guided radiofrequency thermal ablation in the porcine brain at 0.2 T. Eur Radiol 2001;11:884–892.

28. Fei BW, Kemper C, Wilson DL. Three-dimensional warping registration of the pelvis and prostate. In: Sonka M, Fitzpatrick JM, editors: Proceedings of SPIE Medical Imaging Image Processing 2002. SPIE Vol 4684. p 528–537.

29. Fei BW, Kemper C, Wilson DL. A comparative study of warping and rigid body registration for the prostate and pelvic MR volumes. Comp Med Imaging and Graphics 2003 (in press).

Automatic MR volume registration and its evaluation for the pelvis and prostate

Baowei Fei[1]**, Andrew Wheaton**[1]**, Zhenghong Lee**[1,2]**, Jeffrey L Duerk**[1,2]
and David L Wilson[1,2]

[1] Department of Biomedical Engineering, Case Western Reserve University, Cleveland,
OH 44106, USA
[2] Department of Radiology, University Hospitals of Cleveland and Case Western Reserve
University, Cleveland, OH 44106, USA

E-mail: DLW@po.cwru.edu

Abstract
A three-dimensional (3D) mutual information registration method was created
and used to register MRI volumes of the pelvis and prostate. It had special
features to improve robustness. First, it used a multi-resolution approach
and performed registration from low to high resolution. Second, it used two
similarity measures, correlation coefficient at lower resolutions and mutual
information at full resolution, because of their particular advantages. Third,
we created a method to avoid local minima by restarting the registration
with randomly perturbed parameters. The criterion for restarting was a
correlation coefficient below an empirically determined threshold. Experiments
determined the accuracy of registration under conditions found in potential
applications in prostate cancer diagnosis, staging, treatment and interventional
MRI (iMRI) guided therapies. Images were acquired in the diagnostic (supine)
and treatment position (supine with legs raised). Images were also acquired as
a function of bladder filling and the time interval between imaging sessions.
Overall studies on three patients and three healthy volunteers, when both
volumes in a pair were obtained in the diagnostic position under comparable
conditions, bony landmarks and prostate 3D centroids were aligned within
1.6 ± 0.2 mm and 1.4 ± 0.2 mm, respectively, values only slightly larger
than a voxel. Analysis suggests that actual errors are smaller because of
the uncertainty in landmark localization and prostate segmentation. Between
the diagnostic and treatment positions, bony landmarks continued to register
well, but prostate centroids moved towards the posterior 2.8–3.4 mm. Manual
cropping to remove voxels in the legs was necessary to register these images. In
conclusion, automatic, rigid body registration is probably sufficiently accurate
for many applications in prostate cancer. For potential iMRI-guided treatments,
the small prostate displacement between the diagnostic and treatment positions

can probably be avoided by acquiring volumes in similar positions and by reducing bladder and rectal volumes.

1. Introduction

We are investigating three-dimensional (3D) image registration to be used in applications of prostate cancer diagnosis, staging and therapy. In particular, we are interested in applications related to the minimally invasive interventional MRI (iMRI) guided treatment of prostate cancer. Our group currently uses iMRI on a low-field open magnet system to guide radiofrequency (RF) thermal ablation of abdominal cancer (Lewin *et al* 1998), and we are investigating this method for prostate cancer treatment. A unique feature of iMRI-guided thermal ablation is that therapy can be monitored either by acquiring images of the thermally induced lesion or by measuring temperature. In addition, MR imaging of the prostate is desirable because it more accurately delineates the prostate than does CT (Milosevic *et al* 1998), which can overestimate the prostate volume (Roach *et al* 1996), and ultrasound, which has a tendency to underestimate the extent of lesions (Boni *et al* 1995).

Several important applications require registration of images of the prostate. First, comparison of registered MR images acquired before and immediately after RF ablation can be used to determine whether a tumour is adequately treated. This is particularly helpful in instances where the edematous response to treatment can be confused with a highly perfused tumour. Second, registration of serial examinations can be used to follow regression/progression of tumour. Third, registration of functional, biochemical images such as single photon emission computed tomography (SPECT), positron emission tomography (PET) and MR spectroscopy with anatomical MR images is useful for detecting and localizing cancer. Fourth, incorporating the functional, biochemical images into the iMRI paradigm will aid image-guided treatments. Fifth, on a low-field magnetic system during iMRI treatments where fast imaging is important, it might be highly desirable to register high-quality MR image from a conventional MR scanner to the live-time iMRI images (Fei *et al* 2001). In this study, we investigate registration of high-resolution MR volumes. Multi-modality image registration results were reported elsewhere (Fei *et al* 2001, Lee *et al* 2000, 2001a).

Many reports describe methods and evaluations for registration in the brain (Hill *et al* 2001); far fewer describe results for the pelvis or prostate. For example, manual registration has been used where an operator cues on segmented vascular structures (Hamilton *et al* 1999) or other anatomical landmarks (Balter *et al* 1995, Liehn *et al* 1992, Narayana *et al* 1997). Others have used automated 3D schemes that match contours of bones and sometimes other structures that are extracted using manual or interactive segmentation (Antolak *et al* 1998, Herk *et al* 1998, Remeijer *et al* 2000). Manual segmentation has also been used to create surfaces for automatic registration (Roeske *et al* 1995, Scott *et al* 1994). All of these methods require either segmentation or visual identification of structures. Voxel-based methods, particularly those based upon mutual information, are robust, require no segmentation that can be prone to error, are suitable for multi-modality registration, are highly accurate for brain registration (Maes *et al* 1997), and are suitable for abdominal registration (Carrillo *et al* 2000). There are no reports of using such methods for pelvis and/or prostate registration. For registration of brain and other organs, registration accuracy has been assessed using fiducial markers (Maurer *et al* 1997, Wang *et al* 1996) and anatomical landmarks (Fitzpatrick *et al* 1998, Peters *et al* 2000, Wilson *et al* 1998).

There are challenges for registration in the pelvis and prostate that might reduce the effectiveness of automatic voxel-based registration. First, the abdomen has irregular boundaries, unlike the head to which registration has been most often applied. Second, the normal prostate is a small organ, which when healthy, measures only about 38.0 mm in its widest dimension transversely across the base (Gray 1977). Third, there are potential factors such as different patient positions, and rectal and bladder filling (Herk *et al* 1995) that can stress registration. In addition, it is more difficult to evaluate pelvic and/or prostate registration because no external markers are available.

In the present study, we perform experiments to determine the potential accuracy of registering prostate MR images using a modified mutual information algorithm that uses rigid-body transformations. High-quality, 3D MR image volumes from a commercially available 1.5 T system are used to determine the best possible results. We examine conditions found in potential applications described previously. We develop and use a variety of assessment methods that include measuring displacements of bony landmarks and of the segmented prostate. One goal is to obtain baseline accuracy measurements for planning future applications of registration in prostate cancer management.

2. Methods

2.1. Data acquisition

All MRI volumes were acquired using a 1.5 T Siemens MRI system (Magnetom Symphony, Siemens Medical Systems, Erlangen, Germany). An 8-element phased array body coil was used to ensure coverage of the prostate with a uniform sensitivity. Typically, two anterior and two posterior elements were enabled for signal acquisition. We used two different MR sequences. First, we used a 3D RF spoiled gradient echo steady-state pulse sequence (FLASH) with TR/TE/flip parameters of 12/5.0/60 which give $256 \times 256 \times 128$ voxels over a $330 \times 330 \times 256$ mm field of view (FOV) to yield $1.29 \times 1.29 \times 2.0$ mm voxels oriented to give the highest resolution for transverse slices. The acquisition time was 5.63 min. This sequence was good for pelvic imaging but was not ideal for the prostate. Second, we used a 3D rapid gradient echo sequence (PSIF) designed to acquire the spin–echo component of the steady-state response, rather than the free induction decay. The spin–echo component was formed immediately prior to the RF pulse and it was shifted towards the prior RF pulse through appropriate gradient waveform design. The sequence with 9.4/5.0/60 (TR/TE/flip) yielded $160 \times 256 \times 128$ voxels over a $219 \times 350 \times 192$ mm rectangular FOV and $1.37 \times 1.37 \times 1.5$ mm voxels oriented to give the highest resolution for transverse slices. There was over sampling at 31% in the slice direction to reduce aliasing artifacts. The acquisition time was 4.25 min. Most often, we used the second sequence, which gave excellent image contrast for the prostate and its surroundings.

2.2. Image volumes for registration

We acquired 3D MRI volume images from three prostate cancer patients and three normal volunteers under four conditions simulating anticipated situations in diagnostic and treatment applications. They are *diagnostic position*, *treatment position*, *empty bladder* and *diagnosis 1 week*. In the diagnostic position, the subject lay supine throughout MR scanning. The *reference* volume was always obtained in the diagnostic position. In the treatment position, the subject was supine and his legs were supported at 30°–60° relative to the horizontal position and separated in a 'V' with an angle of 60°–90° between the legs. This is similar

to the lithotomy position used in some prostate therapies and it should provide access for needle insertion in brachytherapy or RF thermal ablation. In some experiments, the subject micturated to create an empty bladder prior to imaging. For each subject, volumes were typically obtained within an imaging session of 1–2 h. We imaged one subject (V2) a week before the standard imaging session and we refer to this volume as diagnosis 1 week. Between volume acquisitions, subjects got off the MRI table, stretched and walked around to ensure that they would assume a different position on the table. The coil array was centred on the prostate. All images of a subject were acquired using the same pulse sequence and acquisition parameters so as to ensure very similar grey values. In total, we registered 22 volume pairs consisting of one pair for each patient, six pairs for each volunteer and one additional pair for volunteer V2.

There are several preprocessing details. Isotropic voxels are created using 3D linear interpolation or higher order interpolation methods (Carrillo *et al* 2000). From the top and bottom of the volume, we optionally crop transverse slices that are over 35 mm away from the prostate rim. Cropping is done to remove slices having reduced brightness due to sensitivity fall off from the receiver coils, artifacts from a small field of view, displacement of the legs in the treatment position, and/or bladder deformation.

2.3. Similarity measurements

We used two similarity measures, mutual information (MI) and correlation coefficient (CC), in our registration. Suppose one volume R is the *reference*, and the other F is *floating*. Their mutual information MI(R,F) is given below (Maes *et al* 1997):

$$\mathrm{MI}(R, F) = \sum_{r,f} p_{RF}(r, f) \log \frac{p_{RF}(r, f)}{p_R(r) \cdot p_F(f)}$$

The joint probability $p_{RF}(r, f)$ and the marginal probabilities $p_R(r)$ of the reference image and $p_F(f)$ of the floating image, can be estimated from the normalized joint and marginal intensity histogram, respectively. The correlation coefficient CC(R, F) is given below (Press *et al* 1993):

$$\mathrm{CC}(R, F) = \frac{\sum(R(r) - \bar{R}(r))(F(f) - \bar{F}(f))}{\sqrt{\sum(R(r) - \bar{R}(r))^2 \sum(F(f) - \bar{F}(f))^2}}$$

Here $\bar{R}(r)$, $\bar{F}(f)$ denote the average intensities of the reference and floating volumes and the summation includes all voxels within the overlap of both volumes.

2.4. Registration algorithm with special features

The registration algorithm includes special features to improve the robustness for MR pelvic images. We use a multi-resolution approach and perform registration from low to high resolution. At low resolution, we resample both images at 1/4 or 1/2 number of voxels along each linear dimension, respectively. Iterative optimization of the similarity is used to vary the six rigid-body transformation parameters (three translations and three angles). We use the correlation coefficient at the two lower resolutions because it gives fewer local maximums and because it can be calculated faster than MI. We use MI at full resolution because the peaked similarity function gives a more precise solution than CC.

We created a method to avoid local minima by restarting the registration with randomly perturbed parameters obtained from a uniform distribution about the very first initial guess at each resolution. The distribution was centred on the initial guess because we wanted to use the

best solution from the lower resolution. The algorithm restarts until the absolute correlation coefficient between the reference and registered volumes is above a threshold or the maximum number of restarts is reached. The perturbation range is $\pm 5°$ and ± 5 voxels corresponding to ± 27.3, ± 13.7 or ± 6.8 mm for resolutions 1/4, 1/2, or full voxels, respectively. Absolute CC is used for the restart test rather than MI because CC has a well-defined range between 0 and 1, because CC provides an independent check of the MI result, and because, as described later, CC has fewer problems with local and incorrect global maximums for registrations at low resolution far from the optimum value.

We record all important results following an optimization cycle including the CC and/or MI values, the number of restarts and the transformation parameters. At the end of processing at a lower resolution, we always select the transformation parameters having the maximum CC value. We then scale the translation parameters appropriately and assign the new parameters to be initial values at the next higher resolution. At the highest resolution, we select the final transformation parameters to be those with the maximum MI value.

There are several implementation details. We used rigid-body transformation (three translations and three angles) and trilinear interpolation. For optimization, we use the downhill simplex method of Nelder and Mead (1965) and the Powell method (1962), but we prefer the former method as described later. Optimization of alignment ends either when the maximum number of MI calculations is reached (typically 500) or the fractional change in MI is smaller than a tolerance (typically 0.001). For the 22 volume pairs reported here, the maximum number of calculations was reached once and this was only at the lowest resolution. Our very first initial guess at the lowest resolution is all zeros for the three displacements and three angles. Based on our experience, we set the CC thresholds at 0.65, 0.70 and 0.75, and the maximum numbers of restarts at 20, 10 and 5, from low to high resolutions, respectively.

3. Evaluation of registration

3.1. Registration accuracy based on bony landmarks

We evaluated registration of the pelvis by measuring the displacement of bony landmarks following registration. We used six easily found bony landmarks consisting of two great sciatic notches, two lesser sciatic notches, the pubic symphysis, and the coccyx, some of which are illustrated in figure 1. Previously, sciatic notches and the pubic symphysis were used to register CT and MRI images for prostate conformal radiation (Kagawa *et al* 1997). To measure landmark displacements, we used *RegViz*, a program written in IDL (Interactive Data Language, Research System Inc., USA) and created in our laboratory for visualizing and analysing registered image volumes. We navigated transverse, coronal and sagittal MR images slice-by-slice to search the landmarks. The same unique features such as corners and intersections were identified with a cursor on magnified images. A single person repeated this six times over a few weeks and results were averaged to give a 3D location for each landmark. A radiologist confirmed the landmark selection. Following registration, we calculated the root-mean-squared (RMS) distance over the six landmarks (Wang *et al* 1996).

Although this method provides an independent means for evaluating skeletal registration accuracy, there is error in localizing the bony landmarks. To determine the effect of localization error, we performed least-squares point-to-point registration (Maurer *et al* 1997) and compared results to MI registration. The rationale is that if we could identify point landmarks without error on the bony pelvis, point-to-point registration would be perfect. Hence, any displacement left after registration is introduced by localization error. We determined the optimal transformation for matching the six corresponding landmarks. Points were
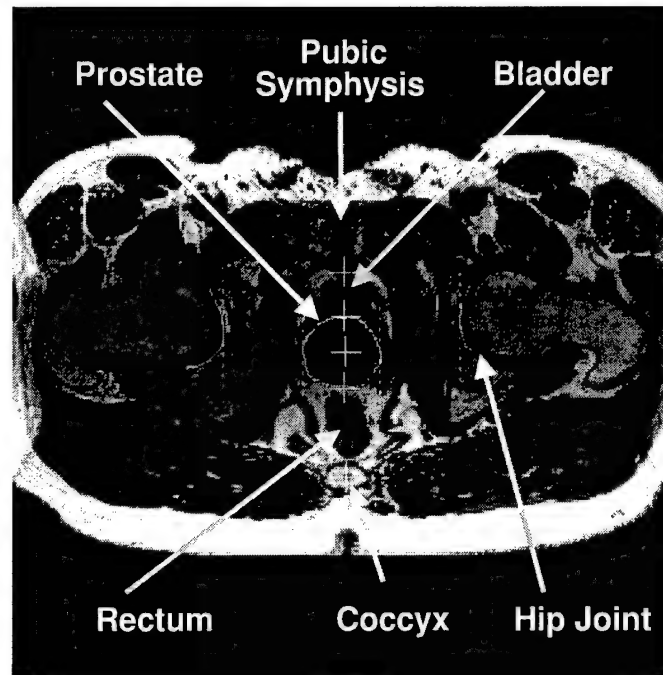
Figure 1. MR prostate image with labelled features used to analyse registration error. This transverse image is from the reference volume of prostate cancer patient P3. The prostate boundary was manually segmented near the image centre. The four vertical dash lines from left to right indicate the rim of the right acetabular socket, the right and left rims of the prostate and the rim of the left acetabular socket, respectively. The five crosses from bottom to top indicate the coccyx, the prostate posterior rim, the 2D centroid automatically calculated from the segmented prostate area, the anterior rim and the pubic symphysis. The image also shows the bottom of the bladder, the rectum, the pubic symphysis and hip joints.

transformed and distances between corresponding points were determined. RMS values were computed and compared to the RMS values from MI registration.

3.2. Registration consistency

We calculated the registration consistency as proposed by Freeborough *et al* (1996). For each of the three volunteers, we used three volumes: reference, diagnosis and empty bladder, all of which were obtained with the subject in the supine position. We call these three volumes A, B and C, respectively. They give three pairs of registrations (A–B, B–C and C–A) and three sets of transformation parameters (T_{ab}, T_{bc}, T_{ca}). Using the transformation parameters, we transformed voxel positions in A to B, and then to C, and then back to A. The distance between the original location and the final position is calculated. Since this is introduced by three transformations, we estimate the error for a single transformation, by multiplying by $3^{-1/2}$ (Freeborough *et al* 1996).

3.3. Voxel displacements

To test the dependency of registration on algorithmic features such as image cropping, one can compare transformation parameters. However, we chose a more meaningful approach

that consisted of finding the average displacement of voxels in a region-of-interest (ROI) (Carrillo *et al* 2000). The 3D distances between transformed voxels were calculated in millimetres and averaged over a cubic ROI just covering the prostate.

3.4. Other evaluation methods including displacement of prostate centroids

We used a variety of other methods to evaluate the registration of the pelvis and prostate. First, we measured potential displacements of the 3D centroid of manually segmented prostates. Second, we used multiple visualization and analysis methods found in RegViz and MIM^{TM} (Zalen LLC, Novelty, OH 44072) such as contour overlap and colour overlay. Third, we calculated the intensity difference between the reference and registered volumes on a voxel-by-voxel basis and computed statistics. Fourth, we calculated the correlation coefficient between corresponding voxels to measure the quality of registration of two MR volumes acquired with identical parameters.

4. Results

4.1. Comparison of mutual information and correlation coefficient

In figure 2, we compare the two similarity measures at different resolutions. Plotted are MI and CC values as a function of translation along the transverse axis where the origin is the optimal transformation. For images at a resolution of 1/4 voxels along a linear dimension, the CC curves are much smoother than MI, which is noisy and contains many local maximums as shown in figure 2(a). In addition, there is a false global maximum in Figure 2(a) at 18 voxels. At full resolution, figure 2(c) shows that MI is much more peaked than CC, but there is high-frequency noise in the MI curves far from the optimum that gives rise to local maximums that must be avoided. From these figures, we infer that CC is better at low resolution and that MI is better at full resolution when one is close to the optimum value. As described in section 2, our registration algorithm makes use of these features.

4.2. Assessments of pelvic registration

Following registration, we determined displacements between the six bony landmarks. For each subject, there was no consistent displacement of landmarks in one direction versus another. Hence, we measured 3D distances and determined RMS values over the six landmarks. Registration results are plotted in figure 3. The smallest errors are obtained when subjects are in the diagnostic position for both imaging sessions, labelled diagnosis–reference. The average error across the three patients and three volunteers is only 1.6 ± 0.2 mm. Consistently larger errors are obtained when we compare volumes acquired in the treatment position with those in the reference position. Even though the MR acquisition technique used for the patients gave inferior image quality as compared to that for the volunteers, the errors were small.

Additional error analyses are performed on the volunteer images to assess the accuracy of point landmark localization. We used images obtained with the rapid-gradient echo sequence, which have improved the contrast between the prostate and bony landmarks and which give us more confidence in measurements. The isotropic voxels are 1.4 mm on a side, almost as large as the 1.7 ± 0.5 mm error obtained for the volunteer diagnosis–reference data. We assess the error in localizing the bony landmarks by performing point-based registration on 4–6 points per volume pair. The RMS distances after registration averaged across the three volunteers was 1.5 ± 0.2 mm, very nearly the value obtained with MI registration. Hence, the 'error' reported for MI is probably overestimated due to landmark location error. This analysis was
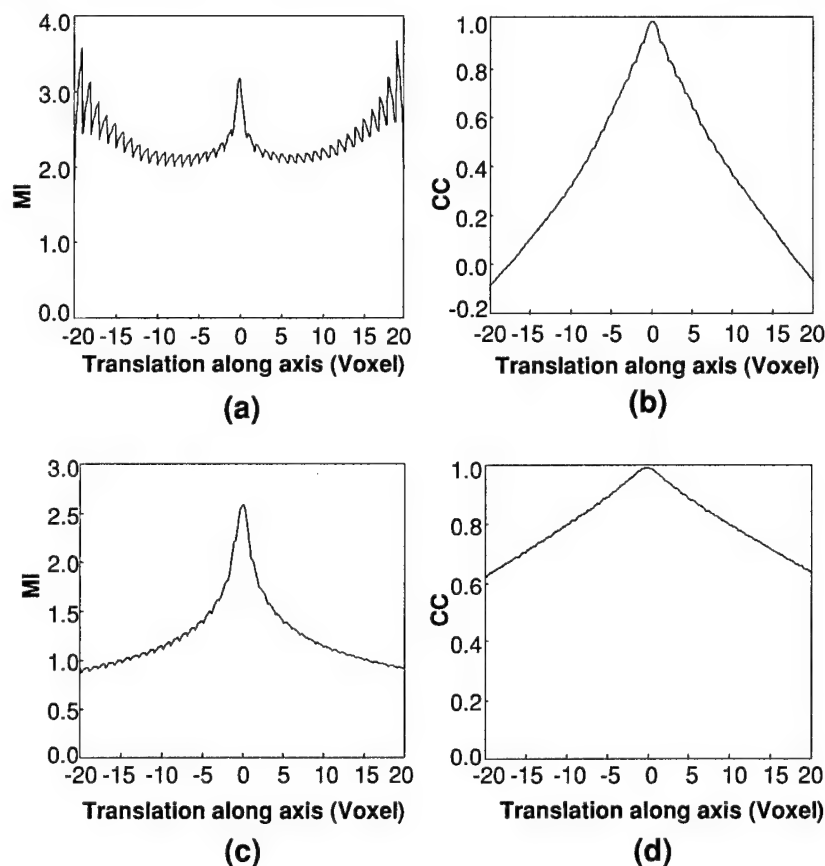
Figure 2. MI and CC similarity functions are plotted to show their relative advantages for registration at different resolutions. Two high-resolution MRI volumes were registered to obtain the optimal parameters. We then computed similarity values as a function of translation along the transverse axis. MI is plotted in (a) and (c); CC is plotted in (b) and (d). Graphs on the top (a) and (b) are at a resolution of 1/4 voxels along a linear dimension, giving a distance between voxel centres of ≈5.5 mm. MI gives a noisy plot having many local maximums and a false global maximum occurs at 18 voxels. Graphs at the bottom are obtained at full resolution. MI has a much sharper peak than CC, which is relatively flat. The voxel size is 1.4 mm. Images are from volunteer V2 in the diagnostic and reference conditions.

prompted by ideas in a previous report (Maurer *et al* 1997) that numerically demonstrated the relationship between point localization uncertainty and point-based registration uncertainty.

Figure 4 shows image intensity differences between reference and registered volumes. The means are quite small with 8 out of 10 registrations giving a mean absolute value <1.5 grey levels, or only 1.7% of typical mean values of 90 grey levels for these 3D MR acquisitions. Again, the only consistent outliers occur when we compare the treatment position to the reference. For the case diagnosis–reference, extremely small image differences are found with V1 giving 0.1 ± 1.6 grey values, a standard deviation that compares favourably with the expectation from image noise alone, or 1.5 grey values. For this volume pair, the subtracted images have very little structure except at the skin surface, indicating excellent registration (not shown). We know that 3D alignment is achieved because all slices across the entire pelvis are well aligned and because rendered images show that the prostate matches well.
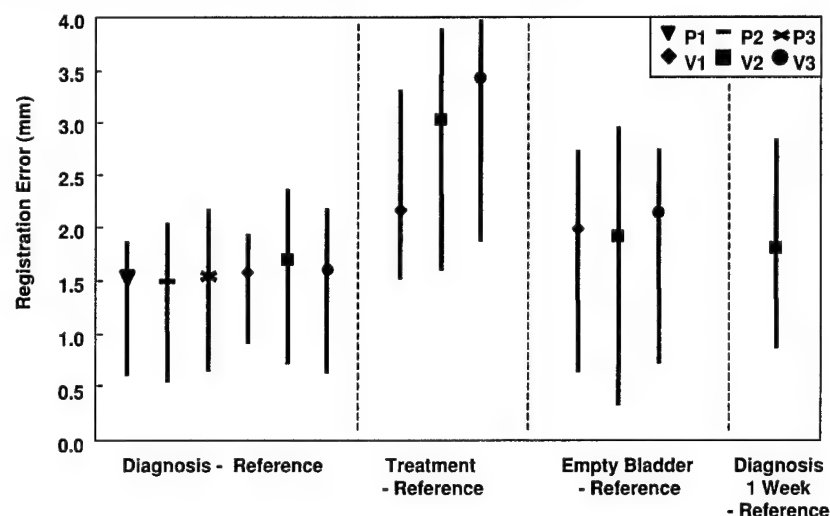
Figure 3. Registration error as determined from bony landmarks. RMS distances as well as maximums and minimums are plotted that show the spread of the data. Conditions along the *x*-axis such as the 'treatment' position are described in section 2. P's and V's refer to patients and volunteers, respectively. Averaging data across all subjects for the best case (diagnosis–reference) gives 1.6 ± 0.2 mm. Averages are 2.9 ± 0.7 mm and 2.0 ± 0.1 mm for treatment–reference and empty bladder–reference respectively.
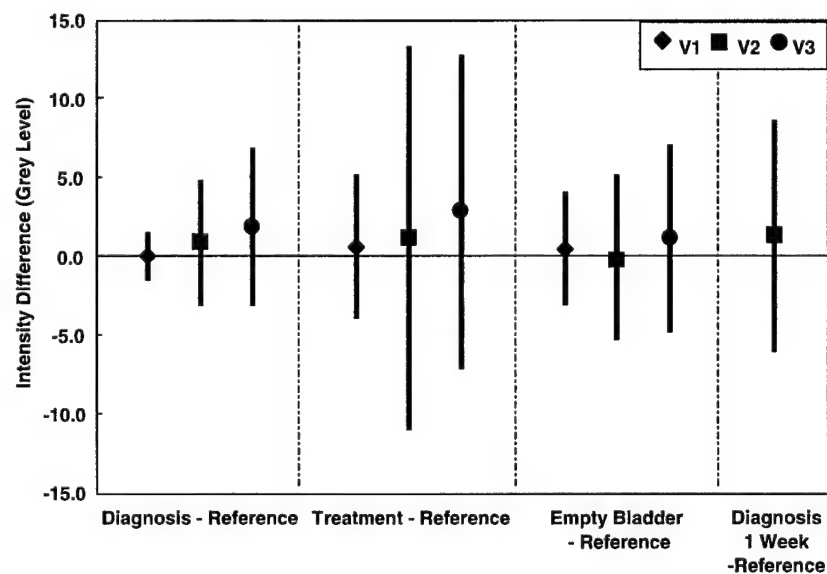
Figure 4. Image intensity difference between registered volume pairs. Means and standard deviations calculated over the entire volumes are plotted. Other details are given in the legend of figure 3. Eight out of ten registrations have a mean absolute grey level difference less than 1.5 grey levels. Average results are 0.9 ± 1.8, 1.5 ± 3.9, and 0.4 ± 2.6 grey levels, or 1.0, 1.7 and 0.4% of typical mean values of 90 grey levels, for diagnosis–reference, treatment–reference and empty bladder–reference respectively.

Registration consistency, as described in section 3, provides yet another means of evaluating the quality of registration. Values were 0.4, 0.8 and 0.7 mm for volunteers V1, V2, and V3, respectively. The average is 0.6 ± 0.2 mm, a value less than half the dimension of a voxel indicating excellent registration consistency.

4.3. Assessment of prostate registration

We determined the quality of prostate registration by visually examining nearly all of the roughly 800 registered image slices using one or more of the methods found in RegViz and MIM^{TM}. A typical example for the case of diagnosis–reference is shown in figure 5 where the boundary overlap is excellent and probably within the manual segmentation error. In some other cases such as treatment–reference, small displacements of the prostate were observed. In a typical volume pair, the prostate is displaced to the posterior direction by ≈ 3.0 mm when the legs are raised. There are no obvious displacements in other directions.

Centroid vector displacements can also be analysed following registration. For the case of diagnosis–reference, centroid displacements are only 1.4 ± 0.2 mm. In the case of treatment–reference, there is a consistent displacement (≈ 3 mm) in the posterior direction with relatively little change in the two orthogonal directions. In the case of empty bladder–reference, two of the three volume pairs show a displacement in the posterior direction while the other is displaced in the anterior direction. Finally, in the case of a diagnostic volume obtained 1 week before the reference, there was a 4 mm displacement in the caudal direction due mostly to changes in rectal and bladder filling. Because the 3D centroid of the prostate averages over a large region, we believe these measurements to be relatively insensitive to segmentation error. Even so, we consider the uncertainty to be at least 1 mm, and displacements less than this should be disregarded. All significant results above can be visually confirmed.

Prostate volumes were measured for each subject. The typical difference between volumes in an imaging session was $<1.5\%$, indicating that segmentation errors were small and that prostate volumes did not change. The average prostate volume for the healthy volunteers was 23.9 ± 3.2 cm^3. Volume measurements are particularly useful for clinicians when assessing the response of prostate cancer treatments such as brachytherapy, chemo- or radiation therapy.

4.4. Effects of image cropping

In figure 6, we plot registration error as determined from bony landmarks with and without the cropping operation described in section 2. For the case treatment-reference, cropping always improved registration accuracy, and for V3, error reduced greatly from 12.6 mm to 3.4 mm. For all other cases, subjects were always in the supine position with legs flat on the table, and there was no consistent effect of cropping. If anything, cropping tends to increase error in these cases, with an increase in five of seven volume pairs. Correlation coefficient always improves with image cropping.

Displacements of bony landmarks might significantly overestimate the change near the prostate. Hence, as described in section 3, we investigated the displacement of voxels in a ROI surrounding the prostate between registrations with and without cropping. For nine of ten analysed volume pairs, the average voxel displacement was <0.5 mm indicating that prostate registration is fairly insensitive to cropping. However, for V3 treatment–reference, a much larger voxel displacement of 7.4 mm was obtained indicating that cropping is critical for this volume pair.
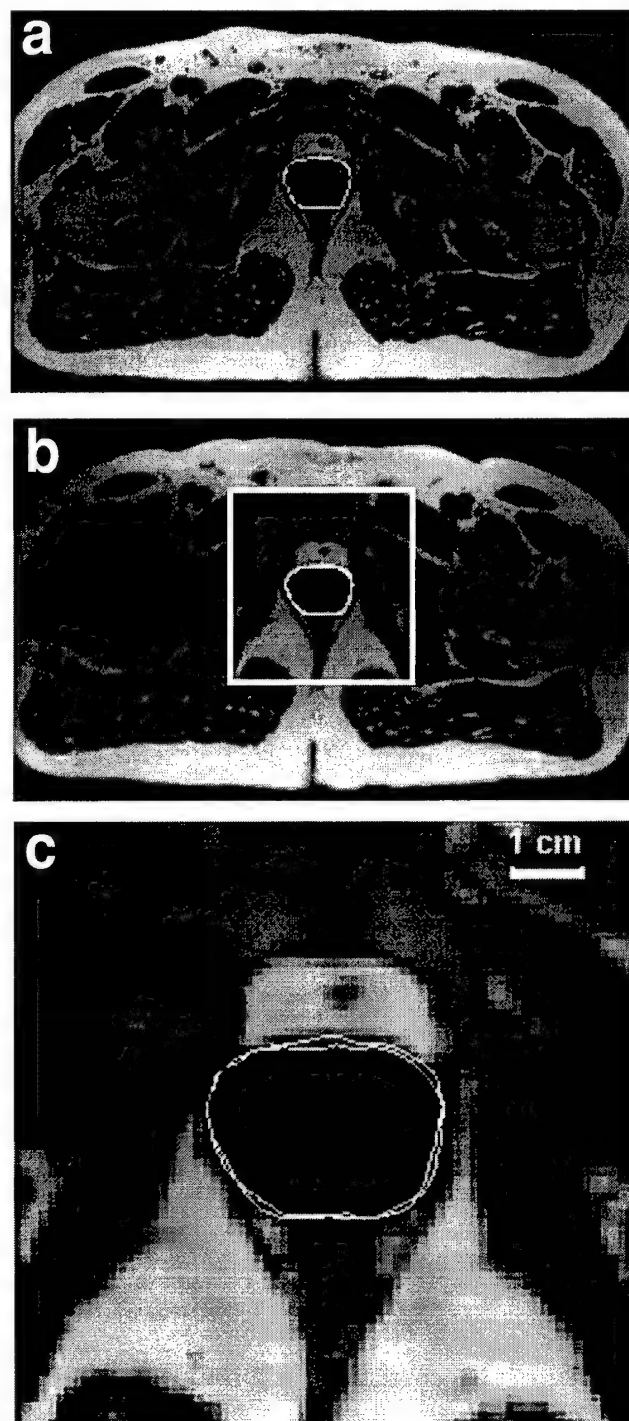
Figure 5. The prostate overlap between reference and registered images. Following registration, the prostate was manually segmented in reference (a) and diagnosis (b) images. The rectangular region in (b) is zoomed in (c) with both boundaries superimposed. Images are from volunteer V2.
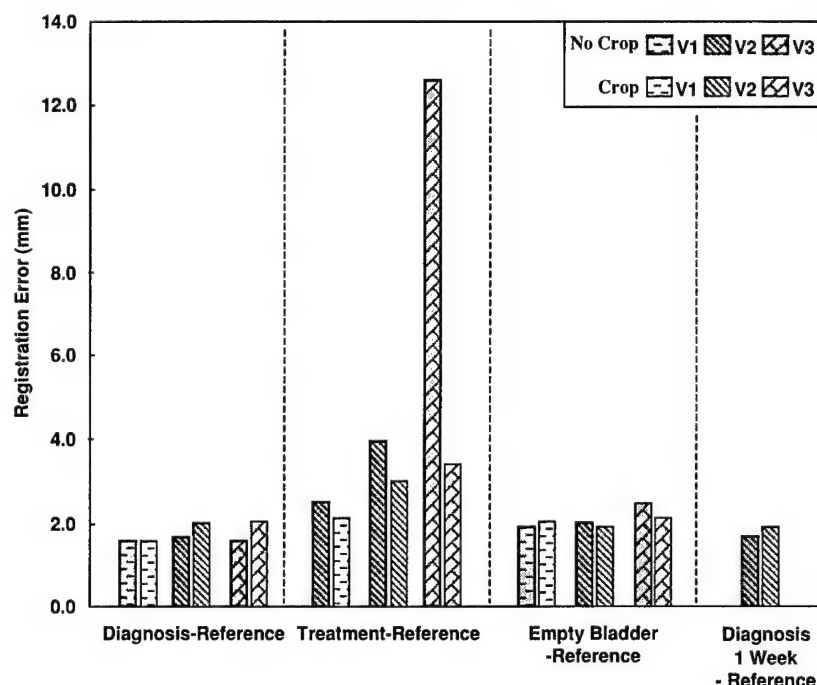
Figure 6. The effect of image cropping on registration accuracy. The light and dark bars are RMS distances between bony landmarks with and without image cropping, respectively, as defined in section 2. Conditions on the *x*-axis are described in section 2.

4.5. Implementation issues

The algorithm was quite robust and always gave very nearly the same transformation parameters (less than 0.01 voxels and 0.01°) for the 22 volume pairs in this study using a wide variety of initial guesses. The restarting and multi-resolution features are important and we report some results for a typical volume pair registration. The multi-resolution approach enabled the program to get close to the final value quickly because of the reduced number of calculations. That is, the time for reformatting at the lowest resolution (1/4) was 9.8 s, which was less than 1/59 times that at the highest resolution, a value nearly equal to 1/64 expected from the change in the number of voxels. The number of restarts was 5, 1 and 1 for resolutions at 1/4, 1/2 and the full number of voxels. Each call to the Simplex optimization resulted in 55 to 94 MI evaluations before the tolerance (0.001) was reached. The simplex optimization method worked about 1.5–2.0 times faster than the Powell method in our implementation. The time for registration using Simplex, typically 10 mines on a Pentium IV, 1.7 GHz CPU, with 1 Gbytes of memory, could probably be greatly improved with optimized C code rather than IDL.

5. Discussion

5.1. Registration accuracy

Our results suggest that MI can be used to accurately register, with an error on the order of a voxel, MR pelvic images obtained under similar conditions. Because it gives an independent,

true 3D measurement, we like to use the method of point bony landmarks to assess accuracy. However, as argued in section 4.2, the true MI registration accuracy might be better than our ability to measure it with point bony landmarks. That is, following point landmark registration, the distance between registered, corresponding landmarks was on the order of that following MI registration. Very possibly, MI is more accurate than point registration using bony landmarks. Additional, independent evidence of excellent MI accuracy comes from the very low error value from the registration consistency measurement (0.6 ± 0.2 mm). Interestingly, this is obtained even though the interpolation artifact present in MI similarity surfaces should reduce the likelihood of sub-voxel accuracy (Pluim *et al* 2000a). Our results for the pelvis with image volumes obtained under the same conditions compare favourably with those for the brain, where MI registers images very accurately giving errors as small as 0.7–0.8 mm for CT-MR (West *et al* 1997).

Visual and quantitative evaluation of prostate organ movement showed good registration even when we acquired images under conditions that greatly stressed the ability to register the images. The small prostate displacements in our study are consistent with earlier reports on respiration-induced prostate movement of $\leqslant 1$ mm for most patients in supine position with 'quiet' respiration (figure 3(b) of the report by Malone *et al* (2000)). The difference between the treatment and diagnostic positions resulted in the most consistent and largest displacement of the prostate. When images were acquired in the diagnostic position 1 week apart, there was significant displacement of the prostate due to a change in rectal filling. This is consistent with previously reported results (Herk *et al* 1995, Tenhaken *et al* 1991), which found rectal filling to be a significant factor in prostate displacement.

There are ways of limiting the small displacements of the prostate. One obvious remedy is to acquire images in the same position. That is, if we want to register an image with that obtained in the treatment position, we should obtain it in the treatment position. Although it is unknown how accurately one must repeat the treatment position, a device to support and constrain the legs is probably required. In addition, there is a dependence of registration error on bladder and rectum content. One solution is use clinical preparations often employed to void the bladder and rectum prior to prostate imaging or therapy. We anticipate that this might even lessen prostate displacements between the diagnostic and treatment positions.

We must consider our results with regard to potential applications such as those described in the section 1. First, registered images acquired before and immediately after treatment can be used to determine whether a tumour is adequately treated. Second, serial examinations can be registered to determine tumour progression or regression. Third, registration of functional images from other modalities such as nuclear medicine or from MR spectroscopy can give molecular markers for prostate cancer (Lee *et al* 2001a, 2001b). Fourth, we want to register high-quality MR images with a few live-time interventional MR images to aid treatment decisions (Fei *et al* 2001). Our results indicate that registering images from the treatment and diagnostic positions can lead to errors and potential steps are described above to limit this error. With images acquired in the same position, our results place a lower limit on registration error of about 1 voxel. Experiments are being conducted to see if this can be achieved with interventional MR images (Fei *et al* 2001).

5.2. Assessment of registration

We are involved in a long-term effort to use registration for detection, assessment and therapy of prostate cancer. Hence, we have developed and used several methods to assess pelvic and prostate registration.

It is highly desirable to have an automatic method for evaluating the quality of a registration so that a poor one can be flagged before it is used clinically. The correlation coefficient would be applicable whenever one uses MR images obtained with identical pulse sequences. It compares favourably with the bony landmark results. Registration consistency provides an additional means to evaluate registration accuracy that does not rely on operator interaction.

Other evaluation methods are applicable for clinical or research applications. RegViz and MIM^{TM} provided visual inspection tools for quick evaluation of the quality of registration and potential prostate displacement. Such methods can be used to verify the quality of registration and possibly account for small displacements in some applications. Boundary overlays provide a good means to evaluate organ deformation as well as displacement. Point anatomical landmarks provide a useful, independent test; but it is time consuming to identify them; and MI might be more accurate than the point landmarks. Centroids are obtained reliably because small segmentation errors are removed by integrating over the entire prostate volume. Centroids provide a good means of quantifying prostate displacements.

5.3. Algorithm with combined similarity measures

Using both CC and MI at different resolutions was an important feature that increased robustness. When only mutual information was used, registrations at low resolution sometimes gave false solutions that misled registration at the next higher resolution. However, CC performed well and gave many fewer local maximums at the lower resolutions (figure 2(a) and (b)). But MI gave a more accurate solution at the full resolution due to the peaked MI surface (figure 2(c) and 2(d)). Our registration algorithm combined advantages from the two similarity measures.

There are probably several reasons why mutual information does not work well at low resolution. First, the similarity curve is noisy with periodic oscillations from the so-called interpolation artifact (Pluim *et al* 2000a) that is accentuated at reduced resolutions (Pluim *et al* 2000b). This results in the many local maximums in figure 2(a) that can trap the optimization. A similar result was reported for brain registration (Lau *et al* 2001, Maes *et al* 1997). Second, when images are of low resolution and there is only a small region of overlap, the mutual information function can even contain incorrect global maximmums (Pluim *et al* 2000b). Such a result was found in figure 2(a) where the global maximum was obtained at very large displacements where the overlap was reduced. This occurs because MI is not only a function of how well the images match in the overlap, but also by how much information is provided by the two images in the overlap (Studholme *et al* 1997).

5.4. Computer implementation

Accuracy is an important issue for automatic registration, but there are others such as robustness, speed, and requirements for operator interaction. With the multi-resolution and restarting features, our modified MI algorithm is quite robust. For a wide range of initial guesses, it worked well for all 22 volume pairs reported here. Three of the volume pairs were from patients and we are confident that routinely acquired clinical images will have sufficient quality for registration. Because good starting values are unimportant, operator interaction is minimal. In one instance, cropping of the legs was important for registering an image volume obtained in the treatment position with that in the diagnostic position. It is not surprising that legs in a very different position have to be cropped. Although this is easy to do manually, we can probably determine an automated method if it is deemed desirable.

The mutual information similarity measure is quite robust. Even though our images are very similar, we had less success with some other measures such as the sum of the squared image difference. An advantage of MI is that it can be used with images from different modalities, a feature that we are starting to use.

6. Conclusion

We have developed an automatic volume registration algorithm with special features for the pelvis and prostate MR volumes. When both volumes in a pair were obtained in the diagnostic position under comparable conditions, our internal registration measures showed accuracy on the order of a voxel. We believe that the MR image registration method is sufficiently accurate and robust for a variety of applications of interest in the pelvis and prostate. We are beginning to explore these applications in clinical procedures and animal experiments.

Acknowledgments

References

Antolak J A, Rosen II, Childress C H, Zagars G K and Pollack A 1998 Prostate target volume variations during a course of radiotherapy *Int. J. Radiat. Oncol. Biol. Phys.* **42** 661–72
Balter J M, Sandler H M, Lam K, Bree R L, Lichter A S and Ten Haken R K 1995 Measurement of prostate movement over the course of routine radiotherapy using implanted markers *Int. J. Radiat. Oncol. Biol. Phys.* **31** 113–8
Boni R A H, Boner J A, Debatin J F, Trinkler F, Knonagel H, Vonhochstetter A, Helfenstein U and Krestin G P 1995 Optimization of prostate carcinoma staging-comparison of imaging and clinical methods *Clin. Radiol.* **50** 593–600
Carrillo A, Duerk J L, Lewin J S and Wilson D L 2000 Semiautomatic 3-D image registration as applied to interventional MRI liver cancer treatment *IEEE Trans. Med. Imaging* **19** 175–85
Fei B, Wheaton A, Lee Z, Nagano K, Duerk J L and Wilson D L 2001 Robust registration algorithm for interventional MRI guidance for thermal ablation of prostate cancer *Proc. SPIE* **4319** 53–60
Fitzpatrick J M, Hill D L G, Shyr Y, West J, Studholme C and Maurer C R 1998 Visual assessment of the accuracy of retrospective registration of MR and CT images of the brain *IEEE Trans. Med. Imaging* **17** 571–85
Freeborough P A, Woods R P and Fox N C 1996 Accurate registration of serial 3D MR brain images and its application to visualizing change in neurodegenerative disorders *J. Comput. Assist. Tomogr.* **20** 1012–22
Gray H 1977 *Anatomy, Descriptive and Surgical (The Classic Collector's Edition)* (New York: Gramercy Books) p 1010
Hamilton R J, Blend M J, Pelizzari C A, Milliken B D and Vijayakumar S 1999 Using vascular structure for CT-SPECT registration in the pelvis *J. Nucl. Med.* **40** 347–51
Herk M V, Bruce A, Kroes A P G, Shouman T, Touw A and Lebesque J V 1995 Quantification of organ motion during conformal radiotherapy of the prostate by three dimensional image registration *Int. J. Radiat. Oncol. Biol. Phys.* **33** 1311–20
Herk M V, de Munck J C, Lebesque J V, Muller S, Rasch C and Touw A 1998 Automatic registration of pelvic computed tomography data and magnetic resonance scans including a full circle method for quantitative accuracy evaluation *Med. Phys.* **25** 2054–67
Hill D L G, Batchelor P G, Holden M and Hawkes D J 2001 Medical image registration *Phys. Med. Biol.* **46** 1–45
Kagawa K, Lee W R, Schultheiss T E, Hunt M A, Shaer A H and Hanks G E 1997 Initial clinical assessment of CT-MRI image fusion software in localization of the prostate for 3D conformal radiation therapy *Int. J. Rad. Oncol. Biol. Phys.* **38** 319–25
Lau Y H, Braun M and Hutton B F 2001 Non-rigid image registration using a median-filtered coarse-to-fine displacement field and a symmetric correlation ratio *Phys. Med. Biol.* **46** 1297–1319
Lee Z, Kemper C, Muzic R F, Berridge M S and Wilson D L 2001a Quantitative pulmonary imaging based on PET-CT co-registration with warping *J. Nucl. Med.* **42** 10–11.

Lee Z, Sodee D B, Duerk J L, Nelson A D and Berridge M S 2000 Automatic registration of SPECT-MRI in the pelvis *J. Nucl. Med.* **41** 232

Lee Z, Sodee D B, Faulhaber P F, Lancaster T L, MacLennan G T and Wilson D L 2001b Comparison of SPECT and PET imaging for prostate cancer with histological correlation *J. Nucl. Med.* **42** 1226

Lewin J S, Connell C F, Duerk J L, Chung Y C, Clampitt M E, Spisak J, Gazelle G S and Haaga J R 1998 Interactive MRI-guided radiofrequency interstitial thermal ablation of abdominal tumors: clinical trial for evaluation of safety and feasibility *J. Magn. Reson. Imaging* **8** 40–7

Liehn J C, Loboguerrero A, Perault X and Demange L 1992 Superimposition of computed-tomography and single photon emission tomography immunoscintigraphic images in the pelvis—validation in patients with colorectal or ovarian carcinoma recurrence *Eur. J. Nucl. Med.* **19** 186–94

Maes F, Collignon A, Vandermeulen D, Marchal G and Suetens P 1997 Multimodality image registration by maximization of mutual information *IEEE Trans. Med. Imaging* **16** 187–98

Malone S, Crook J M, Kendal W S and Szanto J 2000 Respiratory-induced prostate motion: quantification and characterization *Int. J. Radiat. Oncol. Biol. Phys.* **48** 105–9

Maurer C R, Fitzpatrick J M, Wang M Y, Galloway R L, Maciunas R J and Allen G S 1997 Registration of head volume images using implantable fiducial markers *IEEE Trans. Med. Imaging* **16** 447–62

Milosevic M, Voruganti S, Blend R, Alasti H, Warde P, McLean M, Catton P, Catton C and Gospodarowicz M 1998 Magnetic resonance imaging (MRI) for localization of the prostatic apex: comparison to computed tomography (CT) and urethrography *Radiother. Oncol.* **47** 277–84

Narayana V, Roberson P L, Winfield R J and McLaughlin P W 1997 Impact of ultrasound and computed tomography prostate volume registration on evaluation of permanent prostate implants *Int. J. Radiat. Oncol. Biol. Phys.* **39** 341–6

Nelder J and Mead R A 1965 A simplex method for function minimization *Comput. J.* **7** 308–13

Peters A R, Muller S H, de Munck J C and van Herk M 2000 The accuracy of image registration for the brain and the nasopharynx using external anatomical landmarks *Phys. Med. Biol.* **45** 2403–16

Pluim J P W, Maintz J B A and Viergever M A 2000a Interpolation artefacts in mutual information-based image registration *Comput. Vis. Image Understanding* **77** 211–32

Pluim J P W, Maintz J B A and Viergever M A 2000b Image registration by maximization of combined mutual information and gradient information *IEEE Trans. Med. Imaging* **19** 809–14

Powell M J D 1962 An iterative method for finding stationary values of a function of several variables *Comput. J.* **5** 147–51

Press W H, Flannery B P, Teukolsky S A and Vellerling W T 1993 *Numerical Recipes in C: The Art of Scientific Computing* 2nd edn (New York: Cambridge University Press)

Remeijer P, Geerlof E, Ploeger L, Gilhuijs K, van Herk M and Lebesque J V 2000 3-D portal image analysis in clinical practice: an evaluation of 2-D and 3-D analysis techniques as applied to 30 prostate cancer patients *Int J. Radiat. Oncol. Biol. Phys.* **46** 1281–90

Roach M, FaillaceAkazawa P, Malfatti C, Holland J and Hricak H 1996 Prostate volumes defined by magnetic resonance imaging and computerized tomographic scans for three-dimensional conformal radiotherapy *Int. J. Radiat. Oncol. Biol. Phys.* **35** 1011–8

Roeske J C, Forman J D, Mesina C F, He T, Pelizzari C A, Fontenla E, Vijayakumar S and Chen G T Y 1995 Evaluation of changes in the size and location of the prostate, seminal vesicles, bladder, and rectum during a course of external beam radiation therapy *Int. J. Radiat. Oncol. Biol. Phys.* **33** 1321–9

Scott A M *et al* 1994 Clinical validation of SPECT and CT/MRI image registration in radiolabeled monoclonal-antibody studies of colorectal carcinoma *J. Nucl. Med.* **35** 1976–84

Studholme C, Hill D L G and Hawkes D J 1997 Automated three-dimensional registration of magnetic resonance and positron emission tomography brain images by multiresolution optimization of voxel similarity measures *Med. Phys.* **24** 25–35

Tenhaken R K, Forman J D, Heimburger D K, Gerhardsson A, Mcshan D L, Pereztamayo C, Schoeppel S L and Lichter A S 1991 Treatment planning issues related to prostate movement in response to differential filling of the rectum and bladder *Int. J. Radiat. Oncol. Biol. Phys.* **20** 1317–24

Wang M Y, Maurer C R, Fitzpatrick J M and Maciunas R J 1996 An automatic technique for finding and localizing externally attached markers in CT and MR volume images of the head *IEEE Trans. Biomed. Eng.* **43** 627–37

West J *et al* 1997 Comparison and evaluation of retrospective intermodality brain image registration techniques *J. Comput. Assist. Tomogr.* **21** 554–66

Wilson D L, Carrillo A, Zheng L, Genc A, Duerk J L and Lewin J S 1998 Evaluation of 3D image registration as applied to MR-guided thermal treatment of liver cancer *J. Magn. Reson. Imaging* **8** 77–84

Semiautomatic Non-Rigid Registration for the Prostate and Pelvic MR Volumes

David L Wilson [*]

Departments of Biomedical Engineering and Radiology
Case Western Reserve University & University Hospitals of Cleveland
Cleveland, OH 44106

Baowei Fei

Department of Biomedical Engineering
Case Western Reserve University
Cleveland, OH 44106

Running Title:

Prostate and Pelvis Image Registration

* Corresponding author:
David L. Wilson, Ph.D., Professor
Department of Biomedical Engineering
Case Western Reserve University
10900 Euclid Avenue
Cleveland, OH 44106
Telephone: 216-368-4099
Facsimile: 216-368-4969
Email: dlw@po.cwru.edu,
http://imaging.ebme.cwru.edu

ABSTRACT

We created and evaluated an almost fully automated, three-dimensional non-rigid registration algorithm using mutual information and a thin plate spline (TPS) transformation for MR images of the prostate and pelvis. In the first step, an automatic rigid body registration was used to capture the global transformation. Algorithm features included a multi-resolution approach, two similarity measures, and automatic restarting to avoid local minimums. In the second step, local feature points were registered. An operator entered only five feature points (FP's) located at the prostate center, the left and right hip joints, and the left and right distal femurs. The program automatically determined other FP's at the external pelvic skin surface and along the femurs. The program optimized mutual information of a small cubic volume of interest (VOI) centered on each FP by varying three translations and three rotations. From each optimized VOI, nine control points (CP's) were obtained at the center and the corners of the VOI. More than 600 CP's were used to establish a TPS transformation for the deformation of the pelvic region and the prostate. Experiments on healthy volunteers determined the quality of registration under conditions found in potential applications in prostate cancer treatment and interventional MRI guided therapies. Images were acquired in the diagnostic (supine) and treatment position (supine with legs raised). For 10 volume pairs obtained in much different positions, non-rigid registration was much better than rigid body registration. Using various visualization techniques, it was clear that warping rectified the sometimes significant pelvic misalignment by the rigid body method. Gray value measures of registration quality including mutual information, correlation coefficient, and intensity difference all improved with warping. Importantly, the prostate tended to be more accurately registered with warping; the distance between prostate volume centroids was only 0.7 ± 0.2 mm following warping as compared to 4.9 ± 3.4 mm with rigid body registration. From visual and quantitative measurements, we found that our almost fully automatic method worked as well as a previously reported method using non-rigid registration with manually placed control points. The method was computationally efficient for the 600 control points typically used. We believe that the non-rigid registration method will provide a powerful tool for many applications in pelvic and prostate imaging.

Key words: automatic non-rigid image registration, mutual information, thin plate spline, interventional magnetic resonance imaging (iMRI), prostate cancer.

I. INTRODUCTION

We are investigating three-dimensional (3D) non-rigid image registration to be used in applications of prostate cancer diagnosis, staging, and therapy. In particular, we are interested in applications related to the minimally invasive interventional MRI (iMRI) guided treatment of prostate cancer. At our institution, we currently use iMRI on a low-field open magnet system to guide radiofrequency (RF) thermal ablation of abdominal cancer[1]-[3] and we are investigating this method for prostate cancer treatment. A unique feature of iMRI-guided thermal ablation is that therapy can be monitored with MR either by acquiring images of thermally induced lesions or by measuring temperature. In addition, MR imaging of the prostate is desirable because it more accurately delineates the prostate than does CT [4][5] which can overestimate prostate volume [6][7] and ultrasound, which has a tendency to underestimate the extent of lesions [8].

Several applications in prostate imaging require registration. First, comparison of registered MR images acquired before and immediately after RF ablation can be used to determine whether a tumor is adequately treated. This is particularly helpful in instances where the edematous response to treatment can be confused with a highly perfused tumor. Second, other treatment methods such as radiation therapy, brachytherapy, and surgery, will also be aided by registration of images from pre-, intra-, and post-therapy for treatment planning, guidance, and assessment. Third, inter-modality registration will be useful because there are emerging techniques in nuclear medicine [9] and MR spectroscopy [10] that promise to detect and delineate prostate tumor. We have an active project aimed at registering and fusing SPECT monoclonal antibody images with MR to

aid interventional MRI guided treatments. Fourth, registration of serial examinations can be used to follow regression/progression of tumors.

There are challenges to the pelvis and prostate registration. First, pelvic regions can change shape significantly, unlike the brain to which registration has been most often applied. Different patient positions such as legs up and down can cause the movement and deformation of internal organs. Second, the normal prostate is a small organ that when healthy measures only about 3.8 cm in its widest dimension transversely across the base [11]. Third, the small prostate is located below a much larger bladder that can change shape and size. The prostate might move relative to the pelvic bones due to changes in bladder and rectal filling [12][13]. The alignment of the pelvic bones, a most prominent anatomical feature in MR gray-scale images, does not necessarily mean that the prostate is aligned.

Some reports describe methods for rigid body registration in the pelvis or prostate [12][14]-[21]. Some of these methods require either segmentation or visual identification of structures. For example, manual registration has been used where an operator cues on segmented vascular structures [22] or other anatomical landmarks [14]-[16]. Others have used automated 3D schemes that match contours of bones and sometimes other structures that are extracted using manual or interactive segmentation [23].[18][19] Manual segmentation has also been used to create surfaces for automatic registration [20][21].

We previously described a gray-scale, mutual information, rigid body volume-to-volume (VV) registration method for the pelvic and prostate MR images [24]. For volume pairs acquired over a short time span with the volunteer in a similar position, rigid body

registration accuracy of both the prostate centroid (typically < 1 mm) and bony landmarks (average 1.6 mm) was on the order of a voxel (~ 1.4 mm). The centroid error was slightly smaller because the prostate was at the volume center and rotation errors had less effect on it. The localization error in finding 3D points from bony landmarks is probably greater than that of finding centroids of relatively large prostate volumes where segmentation errors average out. With rigid body registration, we obtained larger prostate centroid displacements (2.8 to 10.0 mm) when acquisitions were obtained under much different conditions (e.g., legs flat and legs raised) giving large anatomical deformations. Rigid body registration of the pelvis is inadequate under such conditions [24].

Non-rigid registration is a solution, and there are a number of relevant reports [25]-[33]. However, these applications were mainly for brain [29][31][33]-[35] and breast [27][30][36]; far fewer applications have been described for the abdomen [28][32][37]. As for the prostate, a finite element model was used to deform the gland during brachytherapy treatments and this method also requires manual segmentation of the gland [38].

We recently reported a non-rigid registration method that used many manually selected control points [39][40]. After automatic global rigid body registration, the operator manually selected over 180 control points at the prostate center, pelvic surface and internal structures. The program automatically optimized each control point location by displacing it in the x, y, and z directions with respect to the reference volume until the mutual information computed over a small cube of voxels was maximized. The thin plate spline (TPS) transformation was then applied to express the deformation of the pelvic

region and the prostate. This interactive method was applied to pelvic MR images and lung CT-PET images [41]. The time required for control point selection was a limitation.

In this study, we build upon our previous experience and develop an almost fully automatic non-rigid registration method. Our goal is to automate the algorithm to save time and labor without losing registration quality. In registration experiments, we use high-resolution MR image volumes of the pelvis and prostate in order to determine any uncompensated deformation following registration. We use image data that shows considerable deformation; e. g., images acquired in the diagnostic (supine) and treatment positions (supine with legs raised). We qualitatively and quantitatively compare results of the new non-rigid registration algorithm to the previous, more manual version, and to rigid body registration.

II. REGISTRATION ALGORITHM

A. Similarity Measurements

We used two similarity measures, mutual information (MI) and correlation coefficient (CC) to perform a gray-scale registration. Suppose one volume R is the *reference*, and the other F is *floating*. Their mutual information $MI(R,F)$ is given below [42].

$$MI(R,F) = \sum_{r,f} p_{RF}(r,f) \log \frac{p_{RF}(r,f)}{p_R(r) \cdot p_F(f)}$$

The parameters r and f are the intensity values of the reference and floating volumes, respectively; and their value can range from zero to the maximum image intensity. The joint probability $p_{RF}(r,f)$ and the marginal probabilities $p_R(r)$ of the reference image

and $p_F(f)$ of the floating image, can be estimated from the normalized joint intensity histogram.

The correlation coefficient is a measure of the interdependence of two random variables; it ranges from -1 to +1, indicating perfect negative correlation at -1, absence of correlation at zero, and perfect positive correlation at +1. For the reference and floating images, R and F, their correlation coefficient $CC(R,F)$ is given below [43].

$$CC(R,F) = \frac{\sum_{i=0}^{N-1}(R(i)-\overline{R})(F(i)-\overline{F})}{\sqrt{\left[\sum_{i=0}^{N-1}(R(i)-\overline{R})^2\right]\left[\sum_{i=0}^{N-1}(F(i)-\overline{F})^2\right]}}$$

Here $\overline{R}$, $\overline{F}$ denote the average intensities of the reference and floating volumes and the summation includes all N voxels within the overlap of both volumes.

B. Global Rigid Body Registration Algorithm with Special Features

Rigid body registration is the first step, and it captures the global transformation of two volumes. We previously reported a similar method includes special features to improve robustness for MR pelvic images [24]. We use a multi-resolution approach and perform registration from low to high resolution. At low resolution, we resample both images at 1/4 or 1/2 number of voxels along each linear dimension, respectively. The similarity measure is iteratively optimized by varying the six rigid body transformation parameters (three translations and three angles). We use CC at the two lower resolutions because it gives fewer local maximums [44]-[46], and because it can be calculated faster

than MI. We use MI at full resolution because the peaked similarity function gives a more precise solution than CC [45]. To avoid local maximums, we include a restarting feature where registration is restarted with randomly perturbed parameters obtained from a uniform distribution about the initial transformation values at the current resolution. The algorithm restarts until the absolute CC is above a threshold of 0.5 or the maximum number of restarts is reached. Absolute CC is used for the restart test rather than MI because CC has a well-defined range between 0 and 1, and because CC has fewer problems with local and incorrect global maximums for registrations at low resolution far from the optimum value [24][47].

We record all important results following an optimization cycle including the CC and/or MI values, the number of restarts, and the transformation parameters. At the end of processing at a lower resolution, we always select the transformation parameters having the maximum CC value. We then scale the translation parameters appropriately and assign the new parameters to be initial values at the next higher resolution. At the highest resolution, we select the final transformation parameters to be those with the maximum MI value.

We now describe initial parameter values for the algorithm. We use an initial guess of all zeros for the transformation because the patient is normally oriented approximately the same way from one scan to the next. We set the maximum numbers of restarts at 10, 5, and 3, from low to high resolution, respectively.

C. Non-rigid Registration by Optimizing Control Points

Following the global rigid body transformation, we perform local non-rigid registration to rectify the misalignment of the pelvic region and the prostate. Below we describe details of the various steps of the algorithm outlined in Figure 1.

C.1. Semi-Automatic Detection of Feature Points

After global transformation, we manually selected five corresponding pairs of feature points (Figure 2) from the two volumes. Locations are: the prostate center (PF0), the two hip joints (PF1 and PF2), and the two distal femurs (PF3 and PF4). We first selected feature points PF0, PF1 and PF2. We then browsed images slice-by-slice to locate PF3 and PF4. We placed feature point at the femur center. Because of the subsequent optimization later, the point pairs do not have to exactly lie on corresponding features; an error of up to 15 mm or $\approx$ 10 voxels is well tolerated. These feature points are especially useful when registering volumes obtained in the diagnostic (supine) and treatment (supine with legs raised) positions [24][39]. Transverse slices are used to select these points because they better show displacement of the legs. Images from both volumes are displayed side by side to aid interpretation.

Using these five FP's, the program creates all other FP's automatically. First, for each volume, a line segment is created between the FP's at the hip joint and the distal femur (dashed lines in Figure 2). Each segment is divided into 8 equal lengths to obtain 7 additional FP's. Altogether, we obtained 9 corresponding FP pairs for each femur.

Second, the prostate center is used to create FP's at the pelvic surfaces (Figure 3a). Many radial lines are drawn through the prostate center in a two-dimensional (2D) transverse slice. The angle between lines, the *angle increment,* was normally 18, 20, or 30 degrees. Note that we exclude the vertical line because it normally intersects the buttock groove and/or the penis, regions of relatively little interest that can change considerably from one acquisition to the next. The gray-scale intensity of the pixels along each line is obtained (Figure 3b). The signal in air is noise and normally less than 15 gray levels as compared to a mean signal of about 90 and maximum signal of about 500 in the tissues. The pelvic skin surface gives high intensity signals, above 30 gray levels, because of the fat beneath the skin. We searched each line for the most distant point above a threshold, T (Figure 3b) and set this position to be a surface feature point (Figure 3a). We normally choose a threshold of 20 gray levels. After processing all lines in an image slice, the program repeats the procedure for 4 other transverse slices that are selected with a gap of about 10-mm away from each other. These transverse slices span ~ 40 mm, much of a typical prostate.

For a typical registration with an angle increment of 18 degrees, there are 91 pairs of FP's: one at the prostate center, 18 at the femurs, and 72 at the exterior pelvic surface. Their 3D coordinates are stored. Because of the subsequent optimization, the FP pairs do not have to exactly lie on corresponding features; an error of up to 15 mm or $\approx$ 10 voxels is well tolerated.

C.2. Optimization of Corresponding Feature Points

Corresponding feature points are optimized using a mutual information similarity measure. A small cubic volume of interest (VOI) is centered at each feature point. The VOI can be 32, 48 or 64 voxels on a side, and as reported later, the selection of VOI size depends on the amount of warping required. In both the reference and floating volumes, each corresponding feature point has its own VOI. The one in the reference volume is the reference VOI that is known and fixed. The corresponding VOI in the floating volume is the floating VOI. To perform the optimization, we translate and rotate the floating VOI with respect to the reference VOI and compute their mutual information over corresponding voxels. There are six transformation parameters to optimize: three displacements in x, y, and z, and three angles about each of these three axes. We used the Nelder-Mead Simplex algorithm [48] for optimization, which has previously been used to successfully optimize non-linear problems such as mutual information registration [49][50] and other nonlinear model [51].

Optimal transformation parameters are independently obtained and recorded for each of the floating feature points. On rare occasion, one or more of the translation or rotation parameters of a floating FP are larger than a reasonable value (e.g., 40 mm or 45 degrees), and we eliminate it.

C.3. Determination of Control Points

For each optimized feature point VOI, we create nine optimal control points (CP's). As shown in Figure 4, there is a smaller cube about half the dimensions of a bigger cube

that is used to compute MI. The nine CP's are the eight corners and the center of the small cube. These CP's encode the position and orientation of the VOI. For feature points near the MR image volume border, some CP's may not be in the volume, and we exclude them. The total number of CP's is usually > 600 for an angle increment of 18 degrees.

C.4. TPS Transformation Using Optimal Points

The final major step is to obtain the warped volume from the floating volume. We used backward warping that includes two steps to obtain the warped volume [52]. The first step is a spatial transformation that maps each voxel in the target image to its source in the source image [52]. We use the optimal coordinates of control points to establish a three-dimensional (3D) TPS transformation [53][54] between the floating (source) and warped (target) image volumes. For example, a voxel with 3D coordinates of (64, 78, 24) in the target image is mapped to its source at (63.2, 76.3, 22.1). The second step is the computation of the intensity value at each source location. Since the position of the source can often be real valued, for example, (63.2, 76.3, 22.1), we use tri-linear interpolation to obtain its intensity value. We then copy the intensity value and assign it to the target voxel in the warped volume. Finally, we obtain the warped volume from the floating image.

We summarize parameter values for the non-rigid registration. The 3D coordinates of the five features points are manually selected by user. The angle increment is 18 degrees; the intensity threshold for pelvic surface detection is 20 gray scales; and the VOI size is 32 or 64.

D. Additional Details

There are several preprocessing details. The input MR volume is a 3D MR acquisition giving 256 x 256 x 128 nearly isotropic voxels over a field of view covering the whole pelvis. We create isotropic voxels of about 1.4 mm on a side using tri-linear interpolation. Before optimization, we optionally bin the gray scale values of two volumes to 256; this procedure helps the algorithm perform better for multi-modality registrations such as CT/PET where their gray scales are tremendously different [41]. For both rigid body registration and VOI optimization, we use tri-linear interpolation to obtain samples at real-valued voxel locations. Optimization of similarity ends either when the maximum number of calculations is reached (typically 500) or the fractional change in the similarity function is smaller than a tolerance (typically 0.001). The program is written in IDL (Interactive Data Language, Research System Inc., Boulder, CO).

III. EXPERIMENTAL METHODS

A. Image Acquisition

All MRI volumes were acquired using a 1.5 T Siemens MRI system (Magnetom Symphony, Siemens Medical Systems, Erlangen, Germany). An 8-element phased array body coil was used to ensure coverage of the prostate with a uniform sensitivity. Typically two anterior and two posterior elements were enabled for signal acquisition.

We used two different MR sequences. First, we used a 3D RF spoiled gradient echo steady state pulse sequence (FLASH) with TR/TE/flip parameters of 12/5.0/60 which give 256x256x128 voxels over a 330x330x256-mm field of view (FOV) to yield 1.3x1.3x2.0-mm voxels oriented to give the highest resolution for transverse slices. The acquisition time was 5.6 min. This sequence was good for pelvic imaging but was not ideal for the prostate. It was used for volunteer S1. Second, we used a 3D rapid gradient echo sequence (PSIF) designed to acquire the spin-echo component of the steady state response. The spin echo component formed immediately prior to the RF pulse, and it was shifted toward the prior RF pulse through appropriate gradient waveform design. The sequence with 9.4/5.0/60 (TR/TE/flip) yielded 160x256x128 voxels over a 219x350x192-mm rectangular FOV and 1.4x1.4x1.5-mm voxels oriented to give the highest resolution for transverse slices. There was over sampling at 31% in the slice direction to reduce aliasing artifacts. The acquisition time was 4.3 min. Most often, we used the second sequence, which gave excellent image contrast for the prostate and its surroundings. It was used for volunteers S2 and S3.

B. Imaging Experiments

We acquired 3D MRI volume images from three normal volunteers under a variety of conditions simulating anticipated conditions in diagnostic and treatment applications. In the *diagnostic position,* the volunteer laid supine throughout MR scanning. In the *treatment position,* the volunteer was supine, and his legs were supported at 30°-60° relative to the horizon and separated in a "V" with an angle of 60°-90° between two legs.

This is similar to the lithotomy position used in prostate therapies, and it should provide access for needle insertion in brachytherapy or RF thermal ablation. For each volunteer, image volumes were typically obtained on the same day within an imaging session. The coil array was centered on the prostate. All images of a volunteer were acquired with the same MRI acquisition parameters so as to ensure very similar gray values. In total, there are 4, 4, and 5 volumes for each volunteer, S1, S2, and S3, respectively. For each volunteer, one volume was in the treatment position; the other was in the diagnostic position.

We performed registration experiments using treatment-diagnosis volume pairs. For volunteers S1, S2, and S3, there were 3, 3, and 4 treatment-diagnosis volume pairs, respectively. Rigid body and non-rigid registration were applied to each pair. Additionally, we tested the methods on 10 volume pairs obtained in the same diagnostic position.

C. Registration Evaluation

We used multiple visualization features of RegViz, a program written in IDL and created in our laboratory for visualizing and analyzing registered image volumes. First, color overlay displays were used to evaluate overlap of structures. One image was rendered in gray and the other in the "hot - iron" color scheme available in IDL. To visualize potential differences, it was quite useful to interactively change the contribution of each image using the transparency scale. Second, we used a sector display, which divided the reference and registered images into rectangular sectors and created an output

image by alternating sectors from the two input images. Even subtle shifts of edges could be clearly seen. Third, we manually segmented prostate boundaries in image slices and copied them to corresponding slices from the other volume. This enabled visual determination of the overlap of prostate boundaries over the entire volume. We applied the same method to evaluate pelvic registration.

Correlation coefficient and mutual information were calculated as indicators of registration quality. Since volumes to be registered were acquired using the same acquisition parameters, high absolute CC values were obtained when registration was good [30]. The higher the MI values, the better the two volumes are registered.

We compared the new semi-automatic method with a non-rigid registration that used manually selected control points as reported by us [39]. Briefly, in the previous method, we first performed a rigid body registration, then manually selected about 180 control points, automatically optimized their locations, and finally warped the volume using TPS interpolation. The principal change in the current algorithm is the automation of control point selection after identification of five feature points. A rigid body method was also previously described [24].

We measured potential displacements of the 3D centroid of the prostate to assess prostate registration error. We used RegViz to manually segment the prostate across all image slices and calculated a 3D centroid.

IV. RESULTS

A. Determination of Feature Points

The method for finding corresponding FP's was quite successful. After rigid body registration, our visualization tool made it easy to approximately locate the prostate center, hip joints, and the femurs. The automatic detection method for identifying the external pelvic surface was quite reliable. For all volume pairs, the program correctly detected all surface points using all angle increments and a threshold of 20 gray levels. Figure 5 shows surface FP's for a typical treatment-diagnostic volume pair. The method for finding FP's along the femurs also worked in a robust fashion.

In over 60 non-rigid registration experiments using 10 treatment-diagnosis volume pairs, we found that more FP's generally improved registration quality. Figure 6 plots MI values of registered volumes after warping as a function of angle increment. When the angle increment is less than 20 degrees, MI saturates. As the angle increment increases, less FP's are used and the MI value decreases. The downside of adding more CP's is the increased time for registration. We use an angle increment of 18 degrees in subsequent experiments.

Adding feature points along the femurs was important for good registration of internal structures. When only surface FP's were used, the femurs and its surrounding structures did not register well (not shown) even with a very large number of surface points as obtained with an angle increment of 9 degrees. Experiments showed that fewer feature points along the femurs did not satisfactorily remove deformations when the legs were raised in the treatment position.

B. Registration Quality of Non-Rigid versus Rigid Body Registration

In Figure 7, we compare non-rigid and rigid body registration for a typical volume pair from the treatment and diagnostic positions. Following non-rigid registration, the prostate boundary overlap is excellent (Figure 7e) and within manual segmentation error as assessed by an experienced operator. Using rigid body registration, there is significant misalignment throughout large regions in the pelvis as shown in the overlap image (Figure 7f), and alignment is greatly improved with warping (Figure 7g) where the pelvis matched very well even at the outer surfaces. Similar results were obtained in transverse slices throughout the prostate. Other visualization methods such as two-color overlays and difference images (not presented) also show excellent matching of structures.

Visual inspections were further verified by quantitative measurements. Figure 8 shows the prostate centroid displacement following rigid body and non-rigid registration. Warping significantly decreased the displacement, indicating much better registration of the prostate. Following warping, the mean displacement was only 0.7 mm ± 0.2 mm cross all volume pairs. The later number is the standard deviation. However, the mean was 4.9 ± 3.4 mm for rigid body registration.

A typical example is the second pair of volunteer S2. Following rigid body registration, the prostate was misaligned with a displacement to the posterior of about 13.6 mm when in the treatment position (Figure 7d). A prostate rotation of about 14 degree along left-right axis was also found following rigid body registration. Following non-rigid registration, the 3D prostates matched very well and the centroid calculated from segmented images displaced by only 0.9 mm, or 0.7 voxels.

Additionally, we examined 10 volume pairs with both volumes acquired in the diagnostic position. In all such cases, rigid body registration worked as well as non-rigid registration. There were no noticeable deformations in the pelvic region, and prostate centroids typically displaced less than 1.0 mm between the two registered volumes. Note that this was obtained even though volunteers always got up from the table and moved around before being imaged again. In what follows, we only report results of treatment-diagnosis volume pairs.

In Figure 9, we compare rigid body, manual warping, and our new almost fully automatic non-rigid methods. Correlation coefficient (CC) values between registered volumes of treatment-diagnosis are plotted. Both semi-automatic and manual non-rigid registration significantly increased CC values in every case, and a paired two-tailed t test indicated a significant effect of warping at $p < 0.5\%$. The semi-automatic non-rigid registration worked better than the manual one in 7 out of 10 cases. This is probably because we used more (~ 600) CP's with the semi-automated method than the manual method (~ 180). Recall that with the manual method each FP was optimized for translation and not rotation and each FP gave one CP

C. Algorithmic Implementation

The rigid body registration is robust as previously reported by us [24]. For 10 volume pairs acquired in the same diagnostic position, registration was 100% successful with prostate centroids typically displaced < 1 mm following registration. For 10 treatment-diagnosis volume pairs, the pelvic region was aligned except for local deformations and

displacements. The time for rigid body registration was typically 5 minutes on a Pentium IV, 1.8 GHz CPU, with 1.0 G Bytes of memory.

We report some details on non-rigid registration for a typical volume pair from volunteer S2. The angle increment was 18 degrees and the total number of FP's was 91. After FP optimization, 21 FP's were rejected, and 70 FP's remained that produced 630 CP's. Excluding 17 invalid CP's outside the volume region, there were 613 useful CP's for the TPS transformation. Following rigid body registration, the mean distance between the reference and floating FP's was 18.6 ± 12.4 mm, where the latter number is the standard deviation. The maximum distance was 58.2 mm. The maximum rotation of a VOI was 40.3 degrees. Using the same computer as described above, for volumes with 256x256x140 voxels, the non-rigid registration took about 30 minutes with TPS warping occupying ~ 86% of the time. Very probably, the time could be greatly improved with optimized C code rather than the high level language, IDL.

VOI size was an important parameter to control the amount of warping. We performed experiments to find the optimal VOI size using sizes of 16, 32, 64, and 72 voxels. We quickly found that a VOI size of 16 or 72 voxels on a side gave unsatisfactory results because warping that was either too much or too little, respectively. A VOI size of 64 worked somewhat better than other VOI sizes for S1 and S3 because there was relatively little deformation between volume pairs. However, a VOI size of 32 voxels on a side performed best for volunteer S2 because there was more deformation in this case (Figure 7).

The method for obtaining CP's from FP's satisfactorily encoded the local position and orientation for warping. As described previously, we used the corners and the center of a *small* cubic volume contained within the FP VOI. Using the corners of the FP VOI gave unsatisfactory results from visual inspection as well as CC and MI values.

V. DISCUSSION

A. Applicability of Non-rigid Registration

For MR images of the pelvis and prostate, non-rigid registration is desirable whenever images are acquired in different positions. Local deformations throughout the pelvis can be corrected, and, more importantly, the prostate can be accurately registered. However, when images are acquired in the same position under comparable conditions such as the case called diagnosis-diagnosis, rigid body registration worked satisfactorily [24]. Similarly, if one were to reproduce the treatment position reasonably well, one could probably again get very good results with rigid body registration.

The high-resolution MR images provide a very stringent test for warping. Many anatomical details are evident, and even a small mismatch can clearly be seen. With a sufficient number of control points, the TPS transformation excellently approximated the deformations of the pelvis and internal structures of our MR images. Even when we warped the volume in the diagnostic position to one in the treatment position, most organs were closely aligned, despite very significant movements.

With non-rigid registration, we have to be concerned about potential warping errors affecting the application of interest. For the prostate, we used only one CP at the prostate center because we desired to maintain the spatial integrity of the organ and to preserve the tissue volume. We placed many CP's around the pelvic surface to produce reasonable warping.

The semi-automatic method is fast and reliable. A user only needs to place 5 feature points in a procedure that is straightforward with our graphical user interface. All other tasks are automated. Further, the localization error of feature points up to 15 mm or ≈ 10 voxels is well tolerated. As compared to the manual non-rigid method, the almost fully automated method saved time and labor, and gave registrations that were as good as or better than the manual method. An interesting semiautomatic method was previously reported for landmark localization in the brain [29] that would be time-consuming for use in the pelvis. A user manually specified a region of interest (ROI), a 3D differential operator was applied to obtain landmark candidates within the ROI, and the user selected the most promising candidate. Unlike the brain images, the pelvic volume needs hundreds of points (600 in our study) to correct the huge deformation not seen in the brain.

The flexibility of the semi-automatic method makes the current software suitable for non-rigid registration in many applications in addition to the clinical procedures described in the Introduction. We believe that the registration method can be applied to other modalities and inter-subject images. In addition, the general approach can probably be modified for other organ systems.

B. Algorithmic Robustness and Efficiency

For rigid body registration, two principal design features greatly improved the robustness of the global registration [24]. First, using both CC and MI at different resolutions was an important feature that increased robustness. CC gave fewer local minimums at low resolutions and MI was more accurate at high resolution [45][46]. Our registration algorithm combined these advantages from the two similarity measures. Second, the restarting mechanism was important. Without restarting, we found that registrations sometimes failed in cases of volumes with large mismatches and significant deformation. Even these cases resulted in a proper solution when restarting was employed.

The non-rigid registration algorithm is designed to be very computationally efficient for TPS warping with hundreds of CP's. We optimized each CP separately because the optimization of six parameters (three translations and three rotations) is simple and fast. Simultaneous optimization of many control points is another approach [55]. However, our experiments shows that 600 control points with 1800 free parameters are needed; hence, simultaneous optimization would be extraordinarily complex and time consuming. We applied the TPS transformation once to the final optimal CP's; this saved considerable time and gave satisfactory warping. If TPS was applied during each iteration of the optimization process [55], the registration time would be quite unacceptable. If we were to use optimized C code instead of IDL, the rigid body and non-rigid registration should be more time efficient.

C. Evaluation of Non-rigid Registration

Since there is no standard method, we used a variety of methods to evaluate non-rigid registration quality. First, for routine evaluation, a color overlay is simple, fast, and intuitive. To better visualize the two data sets, we interactively adjust the transparency scale of each image. Second, for illustration of subtle difference along an edge, we use a sector display because it best shows small shifts [45]. Third, for visual evaluation of a specific organ such as the prostate, we like to superimpose manually marked contours from one image onto another as shown in Figure 7. This clearly shows any displacement or deformation. Fourth, a more quantitative approach is obtained by calculating the displacement of a 3D centroid of the segmented prostate. Finally, when images have comparable gray levels, a difference image, and statistics on the difference image, provides yet another approach. A downside with MR images is that the inhomogeneity of the signal response and interpolation can introduce artifacts in the difference images. Since MR image intensity can vary with different MR sequence parameters and the signal response of MR coil, the gray value statistic may have some limitations when image acquisitions are not carefully repeated. Similarly, there are other gray-level measures such as the correlation coefficient. Although the absolute value of CC, and other gray-scale measures, might not predict registration quality, it is probably a very good way to compare registrations on a single volume pair, as done in Figure 9.

We conclude that the semi-automatic non-rigid registration works better than rigid body registration when patient position is greatly changed between acquisitions. It also

compares favorably to non-rigid registration with manual selection of control points. We believe it will be a useful tool for many applications.

ACKNOWLEDGEMENTS

REFERENCE LIST

[1] A.Carrillo, J.L.Duerk, J.S.Lewin, and D.L.Wilson, "Semiautomatic 3-D image registration as applied to interventional MRI liver cancer treatment," *IEEE Transactions on Medical Imaging*, vol. 19, pp. 175-185, 2000.

[2] J.S.Lewin, C.F.Connell, J.L.Duerk, Y.C.Chung, M.E.Clampitt, J.Spisak, G.S.Gazelle, and J.R.Haaga, "Interactive MRI-guided radiofrequency interstitial thermal ablation of abdominal tumors: Clinical trial for evaluation of safety and feasibility," *Journal of Magnetic Resonance Imaging*, vol. 8, pp. 40-47, 1998.

[3] E.M.Merkle, J.R.Shonk, J.L.Duerk, G.H.Jacobs, and J.S.Lewin, "MR-guided RF thermal ablation of the kidney in a porcine model," *American Journal of Roentgenology*, vol. 173, pp. 645-651, 1999.

[4] K.Kagawa, W.R.Lee, T.E.Schultheiss, M.A.Hunt, A.H.Shaer, and G.E.Hanks, "Initial clinical assessment of CT-MRI image fusion software in localization of the prostate for 3D conformal radiation therapy," *International Journal of Radiation Oncology Biology Physics*, vol. 38, pp. 319-325, 1997.

[5] M.Milosevic, S.Voruganti, R.Blend, H.Alasti, P.Warde, M.McLean, P.Catton, C.Catton, and M.Gospodarowicz, "Magnetic resonance imaging (MRI) for localization of the prostatic apex: comparison to computed tomography (CT) and urethrography," *Radiotherapy and Oncology*, vol. 47, pp. 277-284, 1998.

[6] M.Roach, P.FaillaceAkazawa, C.Malfatti, J.Holland, and H.Hricak, "Prostate volumes defined by magnetic resonance imaging and computerized tomographic

scans for three-dimensional conformal radiotherapy," *International Journal of Radiation Oncology Biology Physics*, vol. 35, pp. 1011-1018, 1996.

[7] C.Rasch, I.Barillot, P.Remeijer, A.Touw, M.van Herk, and J.V.Lebesque, "Definition of the prostate in CT and MRI: A multi-observer study," *International Journal of Radiation Oncology Biology Physics*, vol. 43, pp. 57-66, 1999.

[8] R.A.H.Boni, J.A.Boner, J.F.Debatin, F.Trinkler, H.Knonagel, A.Vonhochstetter, U.Helfenstein, and G.P.Krestin, "Optimization of prostate carcinoma staging - comparison of imaging and clinical methods," *Clinical Radiology*, vol. 50, pp. 593-600, 1995.

[9] D.B.Sodee, G.T.MacLennan, M.I.Resnick, P.F.Faulhaber, Z.Lee, A.D.Nelson, J.P.Molter, and G.Bakale, "Comparison of CT- or MRI-fused PET-FDG and SPECT-ProstaScint (R) imaging of prostate cancer with the gold standard of histology," *Journal of Nuclear Medicine*, vol. 42, pp. 1222-1222, 2001.

[10] J.Scheidler, H.Hricak, D.B.Vigneron, K.K.Yu, D.L.Sokolov, L.R.Huang, C.J.Zaloudek, S.J.Nelson, P.R.Carroll, and J.Kurhanewicz, "Prostate cancer: Localization with three-dimensional proton MR spectroscopic imaging - Clinicopathologic study," *Radiology*, vol. 213, pp. 473-480, 1999.

[11] H.Gray. *Anatomy, Descriptive and Surgical (The classic collector's edition).* New York: Gramercy Books, 1977.

[12] M.vanHerk, A.Bruce, A.P.G.Kroes, T.Shouman, A.Touw, and J.V.Lebesque, "Quantification of organ motion during conformal radiotherapy of the prostate by three dimensional image registration," *International Journal of Radiation Oncology Biology Physics*, vol. 33, pp. 1311-1320, 1995.

[13] R.K.Tenhaken, J.D.Forman, D.K.Heimburger, A.Gerhardsson, D.L.Mcshan, C.Pereztamayo, S.L.Schoeppel, and A.S.Lichter, "Treatment planning issues related to prostate movement in response to differential filling of the rectum and bladder," *International Journal of Radiation Oncology Biology Physics*, vol. 20, pp. 1317-1324, 1991.

[14] J.C.Liehn, A.Loboguerrero, X.Perault, and L.Demange, "Superimposition of computed-tomography and single photon emission tomography immunoscinti-graphic images in the pelvis - validation in patients with colorectal or ovarian carcinoma recurrence," *European Journal of Nuclear Medicine*, vol. 19, pp. 186-194, 1992.

[15] J.M.Balter, H.M.Sandler, K.Lam, R.L.Bree, A.S.Lichter, and R.K.Ten Haken, "Measurement of prostate movement over the course of routine radiotherapy using implanted markers," *International Journal of Radiation Oncology Biology Physics*, vol. 31, pp. 113-118, 1995.

[16] V.Narayana, P.L.Roberson, R.J.Winfield, and P.W.McLaughlin, "Impact of ultrasound and computed tomography prostate volume registration on evaluation of permanent prostate implants," *International Journal of Radiation Oncology Biology Physics*, vol. 39, pp. 341-346, 1997.

[17] M.van Herk, J.C.de Munck, J.V.Lebesque, S.Muller, C.Rasch, and A.Touw, "Automatic registration of pelvic computed tomography data and magnetic resonance scans including a dull circle method for quantitative accuracy evaluation," *Medical Physics*, vol. 25, pp. 2054-2067, 1998.

[18] J.A.Antolak, I.I.Rosen, C.H.Childress, G.K.Zagars, and A.Pollack, "Prostate target volume variations during a course of radiotherapy," *International Journal of Radiation Oncology Biology Physics*, vol. 42, pp. 661-672, 1998.

[19] P.Remeijer, E.Geerlof, L.Ploeger, K.Gilhuijs, M.van Herk, and J.V.Lebesque, "3-D portal image analysis in clinical practice: An evaluation of 2-D and 3-D analysis techniques as applied to 30 prostate cancer patients," *International Journal of Radiation Oncology Biology Physics*, vol. 46, pp. 1281-1290, 2000.

[20] J.C.Roeske, J.D.Forman, C.F.Mesina, T.He, C.A.Pelizzari, E.Fontenla, S.Vijayakumar, and G.T.Y.Chen, "Evaluation of changes in the size and location of the prostate, seminal vesicles, bladder, and rectum during a course of external beam radiation therapy," *International Journal of Radiation Oncology Biology Physics*, vol. 33, pp. 1321-1329, 1995.

[21] A.M.Scott, H.A.Macapinlac, C.R.Divgi, J.J.Zhang, H.Kalaigian, K.Pentlow, S.Hilton, Graham.M.C, G.Sgouros, C.Pelizzari, G.Chen, J.Schlom, S.J.Goldsmith, and S.M.Larson, "Clinical validation of SPECT and CT/MRI image registration in radiolabeled monoclonal-antibody studies of colorectal carcinoma," *Journal of Nuclear Medicine*, vol. 35, pp. 1976-1984, 1994.

[22] R.J.Hamilton, M.J.Blend, C.A.Pelizzari, B.D.Milliken, and S.Vijayakumar, "Using vascular structure for CT-SPECT registration in the pelvis," *Journal of Nuclear Medicine*, vol. 40, pp. 347-351, 1999.

[23] M.V.Herk, J.C.de Munck, J.V.Lebesque, S.Muller, C.Rasch, and A.Touw, "Automatic registration of pelvic computed tomography data and magnetic resonance scans including a full circle method for quantitative accuracy evaluation," *Medical Physics*, vol. 25, pp. 2054-2067, 1998.

[24] B.W.Fei, A.Wheaton, Z.Lee, J.L.Duerk, and D.L.Wilson, "Automatic MR volume registration and its evaluation for the pelvis and prostate," *Physics in Medicine and Biology*, vol. 47, pp. 823-838, 2002.

[25] C.R.Meyer, J.L.Boes, B.Kim, P.H.Bland, G.L.LeCarpentier, J.B.Fowlkes, N.A.Roubidoux, and P.L.Carson, "Semiautomatic registration of volumetric

ultrasound scans," *Ultrasound in Medicine and Biology*, vol. 25, pp. 339-347, 1999.

[26] J.F.Krucker, C.R.Meyer, G.L.LeCarpentier, J.B.Fowlkes, and P.L.Carson, "3D spatial compounding of ultrasound images using image-based nonrigid registration," *Ultrasound in Medicine and Biology*, vol. 26, pp. 1475-1488, 2000.

[27] M.H.Davis, A.Khotanzad, D.P.Flamig, and S.E.Harms, "A physics-based coordinate transformation for 3-D image matching," *IEEE Transactions on Medical Imaging*, vol. 16, pp. 317-328, Jun, 1997.

[28] G.E.Christensen, R.D.Rabbitt, and M.I.Miller, "Deformable templates using large deformation kinematics," *IEEE Transactions on Image Processing*, vol. 5, pp. 1435-1447, 1996.

[29] K.Rohr, H.S.Stiehl, R.Sprengel, T.M.Buzug, J.Weese, and M.H.Kuhn, "Landmark-based elastic registration using approximating thin- plate splines," *IEEE Transactions on Medical Imaging*, vol. 20, pp. 526-534, 2001.

[30] D.Rueckert, L.I.Sonoda, C.Hayes, D.L.G.Hill, M.O.Leach, and D.J.Hawkes, "Nonrigid registration using free-form deformations: Application to breast MR images," *IEEE Transactions on Medical Imaging*, vol. 18, pp. 712-721, 1999.

[31] S.K.Kyriacou and C.Davatzikos, "A biomechanical model of soft tissue deformation, with applications to non-rigid registration of brain images with tumor pathology," *Medical Image Computing and Computer-Assisted Intervention - Miccai'98*, vol. 1496, pp. 531-538, 1998.

[32] S.Kimiaei, M.Noz, E.Jonsson, J.Crafoord, and G.Q.Maguire, "Evaluation of polynomial image deformation using anatomical landmarks for matching of 3D-abdominal MR-images and for atlas construction," *IEEE Transactions on Nuclear Science*, vol. 46, pp. 1110-1113, 1999.

[33] M.Otte, "Elastic registration of fMRI data using Bezier-spline transformations," *IEEE Transactions on Medical Imaging*, vol. 20, pp. 193-206, 2001.

[34] G.E.Christensen, P.Yin, M.W.Vannier, K.S.C.Chao, J.F.Dempsey, and J.F.Williamson, "Large-deformation image registration using fluid landmarks,"Proceedings of 4th IEEE Southwest Symposium on Image Analysis and Interpretation,pp. 269-273, 2000.

[35] C.R.Maurer, D.L.G.Hill, A.J.Martin, H.Y.Liu, M.McCue, D.Rueckert, D.Lloret, W.A.Hall, R.E.Maxwell, D.J.Hawkes, and C.L.Truwit, "Investigation of intraoperative brain deformation using a 1.5-t interventional MR system: Preliminary results," *IEEE Transactions on Medical Imaging*, vol. 17, pp. 817-825, 1998.

[36] E.R.E.Denton, L.I.Sonoda, D.Rueckert, S.C.Rankin, C.Hayes, M.O.Leach, D.L.G.Hill, and D.J.Hawkes, "Comparison and evaluation of rigid, affine, and nonrigid registration of breast MR images," *Journal of Computer Assisted Tomography*, vol. 23, pp. 800-805, 1999.

[37] D.L.Wilson, A.Carrillo, L.Zheng, A.Genc, J.L.Duerk, and J.S.Lewin, "Evaluation of 3D image registration as applied to MR-guided thermal treatment of liver cancer," *Journal of Magnetic Resonance Imaging*, vol. 8, pp. 77-84, 1998.

[38] A.Bharatha, M.Hirose, N.Hata, S.K.Warfield, M.Ferrant, K.H.Zou, E.Suarez-Santana, J.Ruiz-Alzola, A.D'Amico, R.A.Cormack, R.Kikinis, F.A.Jolesz, and C.M.C.Tempany, "Evaluation of three-dimensional finite element-based deformable registration of pre- and intraoperative prostate imaging," *Medical Physics*, vol. 28, pp. 2551-2560, 2001.

[39] B.W.Fei, C.Kemper, and D.L.Wilson, "A comparative study of warping and rigid body registration for the prostate and pelvic MR volumes," *Computerized Medical Imaging and Graphics*, vol. 27, pp. 267-281, 2003.

[40] B.W.Fei, C.Kemper, and D.L.Wilson, "Three-dimensional warping registration of the pelvis and prostate," Proceedings of SPIE Medical Imaging on Image Processing, vol. 4684, pp. 528-537, 2002.

[41] Z.Lee, C.Kemper, R.F.uzic, M.S.erridge, and D.L.ilson, Quantitative pulmonary imaging based on PET-CT co-registration with warping *Journal of Nuclear Medicine*, vol. 42, no. Suppl, pp. 10-11, 2001.(Abstract)

[42] A.Collignon, F.Maes, D.Delaere, D.Vandermeulen, P.Suetens, and G.Marchal, "Automated multimodality image registration using information theory,"*Information Processing in Medical Imaging: Proc. 14th International Conference (IPMI'95)*, Computational Imaging and Vision,pp. 287-298, 1995.

[43] W.H.Press, S.A.Teukolsky, W.T.Vellerling, and B.P.Flannery. *Numerical Recipes in C: The Art of Scientific Computing, Second Edition.* New York: The Press Syndicate of the Cambridge University, 1992.

[44] J.P.W.Pluim, J.B.A.Maintz, and M.A.Viergever, "Interpolation artefacts in mutual information-based image registration," *Computer Vision and Image Understanding*, vol. 77, pp. 211-232, 2000.

[45] B.W.Fei, J.L.Duerk, D.T.Boll, J.S.Lewin, and D.L.Wilson, "Slice to volume registration and its potential application tointerventional MRI guided radiofrequency thermal ablation of prostate cancer," *IEEE Transactions on Medical Imaging*, vol. 22, no. 4, pp. 515-525, 2003.

[46] B.W.Fei, A.Wheaton, Z.Lee, K.Nagano, J.L.Duerk, and D.L.Wilson, "Robust registration algorithm for interventional MRI guidance for thermal ablation of

prostate cancer," Proceedings of SPIE Medical Imaging on Visualization, Display, and Image-Guided Procedures, vol. 4319, pp. 53-60, 2001.

[47] J.P.W.Pluim, J.B.A.Maintz, and M.A.Viergever, "Image registration by maximization of combined mutual information and gradient information," *IEEE Transactions on Medical Imaging*, vol. 19, pp. 809-814, 2000.

[48] J.Nelder and R.A.Mead, "A simplex method for function minimization," *Computer Journal*, vol. 7, pp. 308-313, 1965.

[49] Y.M.Zhu and S.M.Cochoff, "Influence of implementation parameters on registration of MR and SPECT brain images by maximization of mutual information," *Journal of Nuclear Medicine*, vol. 43, pp. 160-166, 2002.

[50] P.J.Slomka, J.Mandel, D.Downey, and A.Fenster, "Evaluation of voxel-based registration of 3-D power Doppler ultrasound and 3-D magnetic resonance angiographic images of carotid arteries," *Ultrasound in Medicine and Biology*, vol. 27, pp. 945-955, 2001.

[51] N.Yildirim, F.Akcay, H.Okur, and D.Yidirim, "Parameter estimation of nonlinear models in biochemistry: a comparative study on optimization methods," *Applied Mathematics and Computation*, vol. 140, pp. 29-36, 2003.

[52] J.Gomes, B.Costa, L.Darsa, and L.Velho. *Warping & morphing of graphical objects.* Morgan Kaufman, 1999.

[53] A.Goshtasby, "Registration Of Images With Geometric Distortions," *IEEE Transactions on Geoscience and Remote Sensing*, vol. 26, pp. 60-64, 1988.

[54] F.L.Bookstein, "Principal warps - thin-plate splines and the decomposition of deformations," *IEEE Transactions on Pattern Analysis and Machine Intelligence*, vol. 11, pp. 567-585, 1989.

[55] C.R.Meyer, J.L.Boes, B.Kim, P.H.Bland, K.R.Zasadny, P.V.Kison, K.Koral, K.A.Frey, and R.L.Wahl, "Demonstration of accuracy and clinical versatility of mutual information for automatic multimodality image fusion using affine and thin-plate spline warped geometric deformations," *Medical Image Analysis*, vol. 1, pp. 195-206, 1996.

FIGURE LEGENDS

Figure 1. Flow chart of the non-rigid registration algorithm. The first four steps are to create features points in both volumes following global rigid body registration. The loop from FOR to END is to optimize the volumes of interest (VOI) as centered at corresponding feature points using mutual information. The optimal VOI is then used to determine nine control points that represent the position and orientation of the VOI. The position information of all control points is used to establish a three-dimensional TPS transformation for the entire volume. See text for details.

Figure 2. Locations of the manually selected five feature points. FP_0 is at the prostate center; FP_1 and FP_2, the hip joints; and FP_3 and FP_4; the distal femurs. The dash lines connecting FP_1 and FP_3, and FP_2 and FP_4 are along the femurs.

Figure 3. Automatic detection of the pelvic surfaces. Image (a) is a transverse image slice covering the prostate. The dash lines pass thought the prostate with an equal angle increment. The dots are at the pelvic exterior surfaces. Graph (b) plots the intensity signals along one dash line in (a). A threshold T is used to determine the pelvic surfaces along this line.

Figure 4. Nine control points for each feature point and volume of interest (VOI). The big cubic volume is the VOI that is used to calculate mutual information and optimize the feature point FP. The small cubic volume is with the same center and the same orientation but half size on a side. The center and the eight corners of the *smaller* cubic volume are the control points that will be used to establish thin plate spline transformation.

Figure 5. Feature points for images acquired in the treatment and diagnostic positions. Image (a) is from the reference volume acquired in the treatment position with legs raised. Image (b) is to be warped and is from the volume acquired in the diagnostic position with legs flat on the table. Feature points are located at the prostate center, femurs, and pelvic surfaces. Each feature point is located at one voxel but displayed much larger for improved visualization. Volumes are of volunteer S2.

Figure 6. Mutual information as a function of angle increment. The y-axis was MI values between registered volumes. The x-axis was the angle increments that were used to detect pelvic surfaces. Generally, MI values decreased when the angle increment increased because less FP's participated non-rigid registration. MI values saturate when the angle increment is smaller than 20 degree. The number of FP's varied from 15 to 60 for angle increments of 107 to 43, respectively.

Figure 7. Comparison of non-rigid and rigid body registration for volumes acquired in the treatment and diagnostic positions. Image (a) is from the reference volume acquired in the treatment position, and the prostate is manually segmented. Images in the left and right columns are from the floating volume acquired in the diagnostic position following rigid body and non-rigid registration, respectively. To show potential mismatch, the prostate contour from the reference in (a) is copied to (b) and (c) and magnified as the dashed contours in (d) and (e). The movement of the prostate to the posterior is corrected with warping (e) but not rigid body registration (d). Pelvic boundaries manually segmented from the reference show significant misalignment with rigid body (f) that is greatly improved with warping (g). Images are transverse slices from volunteer S2.

Figure 8. Prostate centroid displacement following rigid body and non-rigid registration. Ten treatment-diagnosis volume pairs from three volunteers were registered using rigid body and non-rigid registration, respectively. Following rigid body registration, the mean displacement of prostate centroid between registered volumes was 4.9 ± 3.4 mm cross all volume pairs. The latter number is the standard deviation. Following warping, the mean displacement was only 0.7 ± 0.2 mm. Warping significantly decreased the displacement indicating much better registration of the prostate.

Figure 9. Comparison of rigid body, semi-automatic, and manual non-rigid registration for treatment-diagnosis volume pairs. Correlation coefficient following registration is plotted. Both semi-automatic and manual non-rigid registration increased the correlation coefficient as compared to rigid body registration in each case and this effect was significant as determined from all data ($p < 0.5\%$). The semi-automatic method is better than the manual non-rigid registration with 180 control points in 7 out of 10 trials. There are a total 10 volume pairs from three volunteers as described previously.

Create reference and floating volumes following global rigid body registration

Place five feature points (FP) at prostate center, hip joints, and femurs in both volumes

Create feature points along femur using line segment approximation

Create feature points on skin surface using the prostate center and radial lines

Initialize the size of volume of interest (VOI) centered at FP's

FOR *FP* **FROM** *0* to *N-1* **DO BEGIN**

   Optimize mutual information (MI) between the reference and floating VOI's

     1. **Transform** the floating VOI using three translations and three rotations

     2. **Interpolate** to get a reformatted VOI

     3. **Calculate** MI between the reference and reformatted VOI's

     4. **Vary** the three translation and three rotation parameters

     5. **Repeat** steps 1-4 until meeting function tolerance or maximum iteration number

   Record the optimized FP coordinates in the floating volume

END

Determine control points (CP) using the feature points and VOI's

Calculate thin plate spline transformation using the reference and optimized CP's

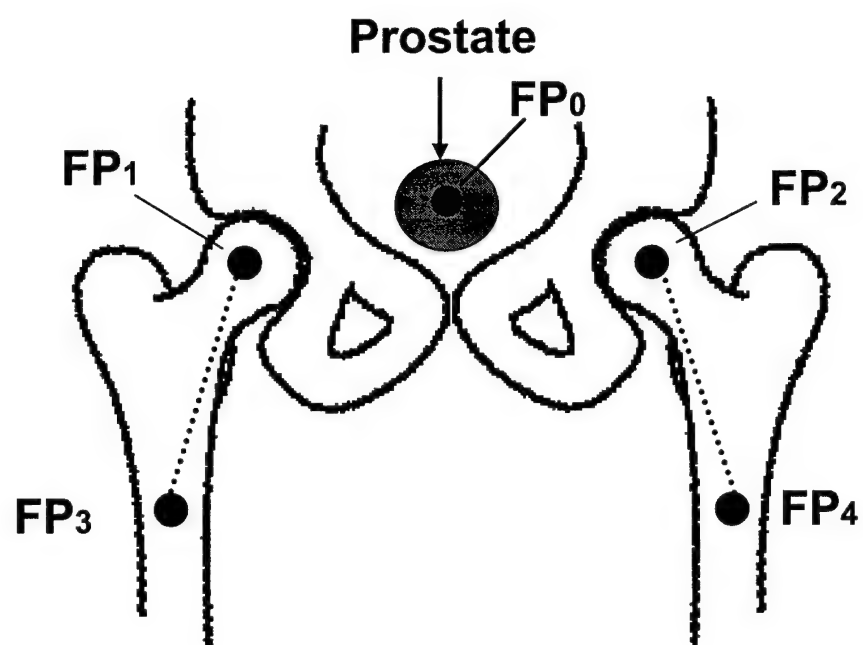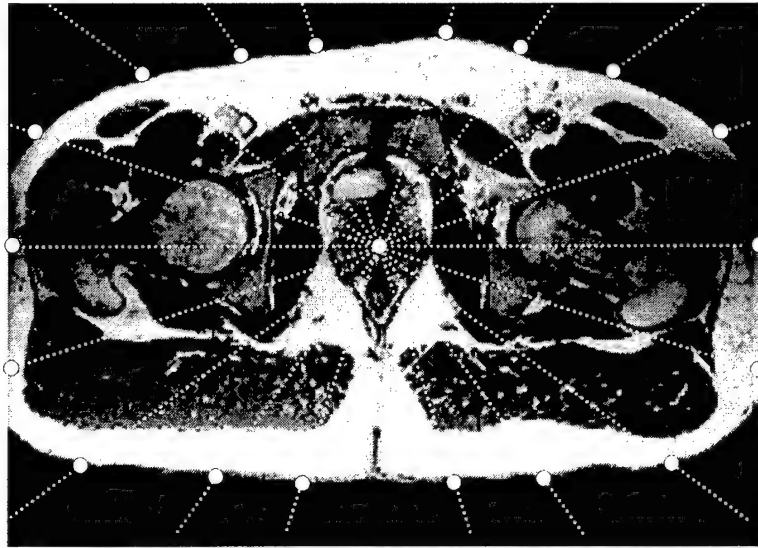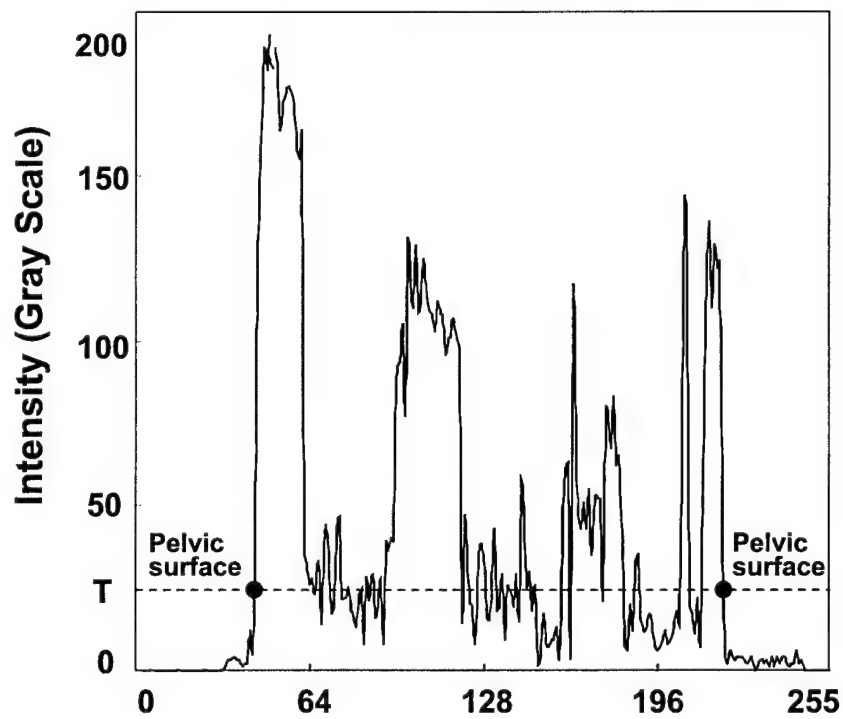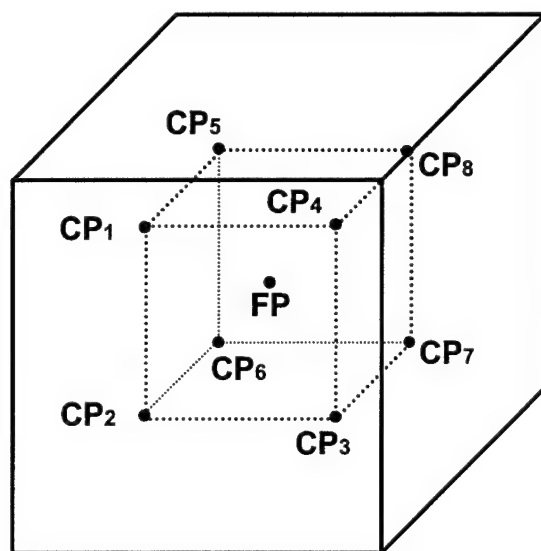**Interpolate** the floating volume and get a warped volume

Figure 1

Figure 2

(a)

(b)

Figure 3

Figure 4
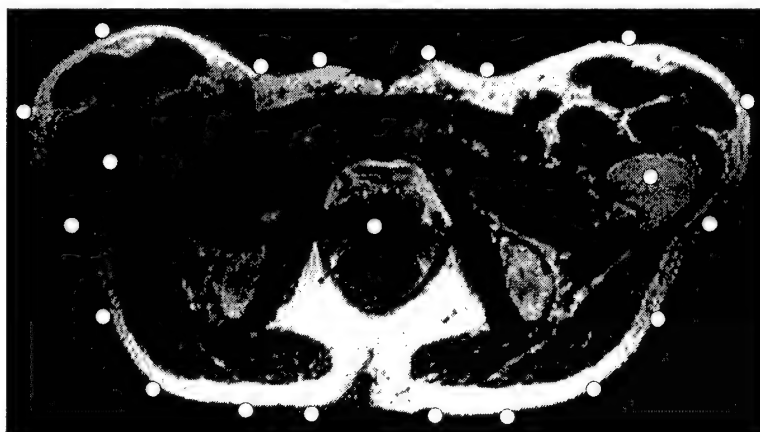
(a)
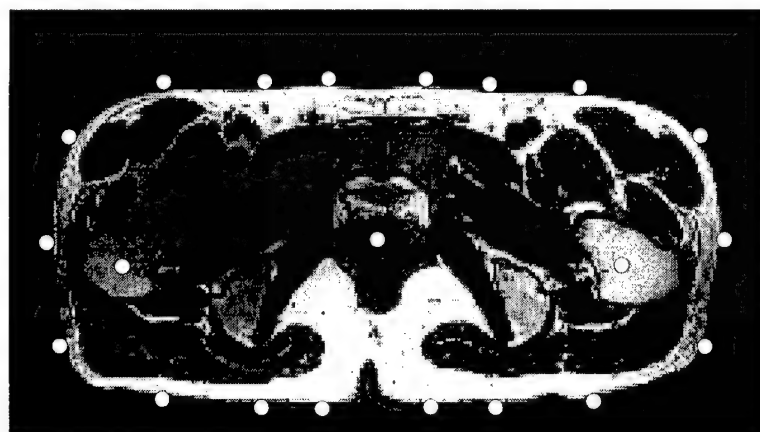
(b)
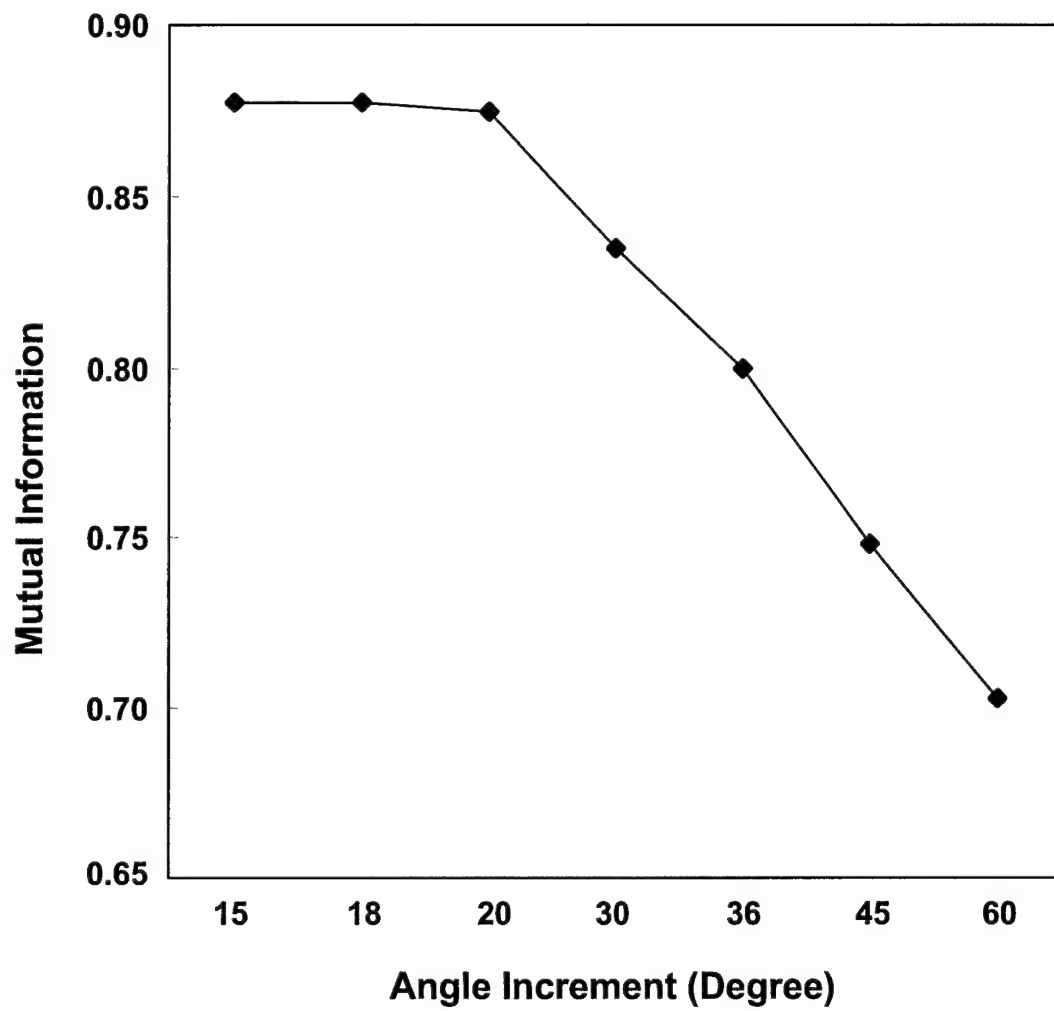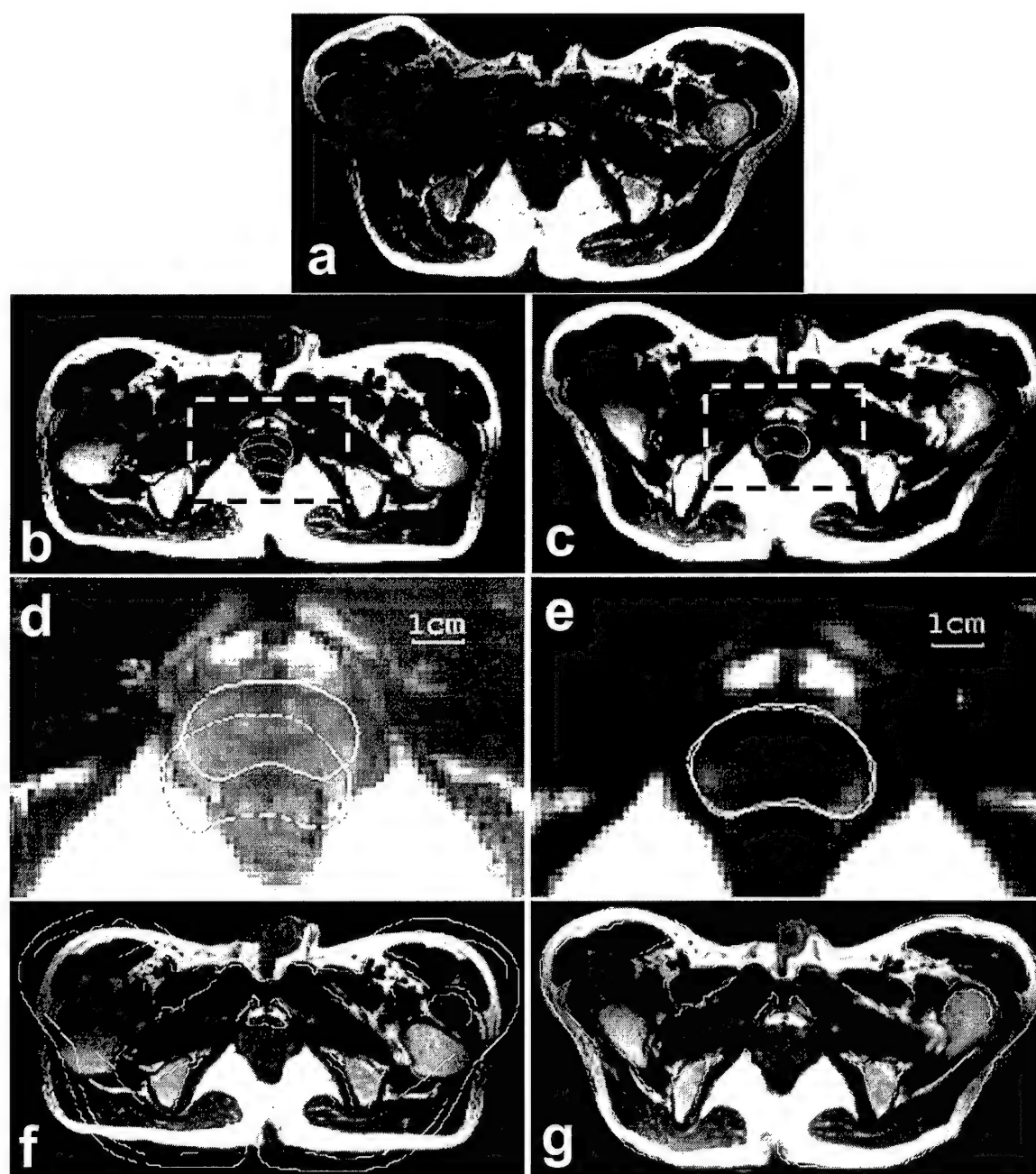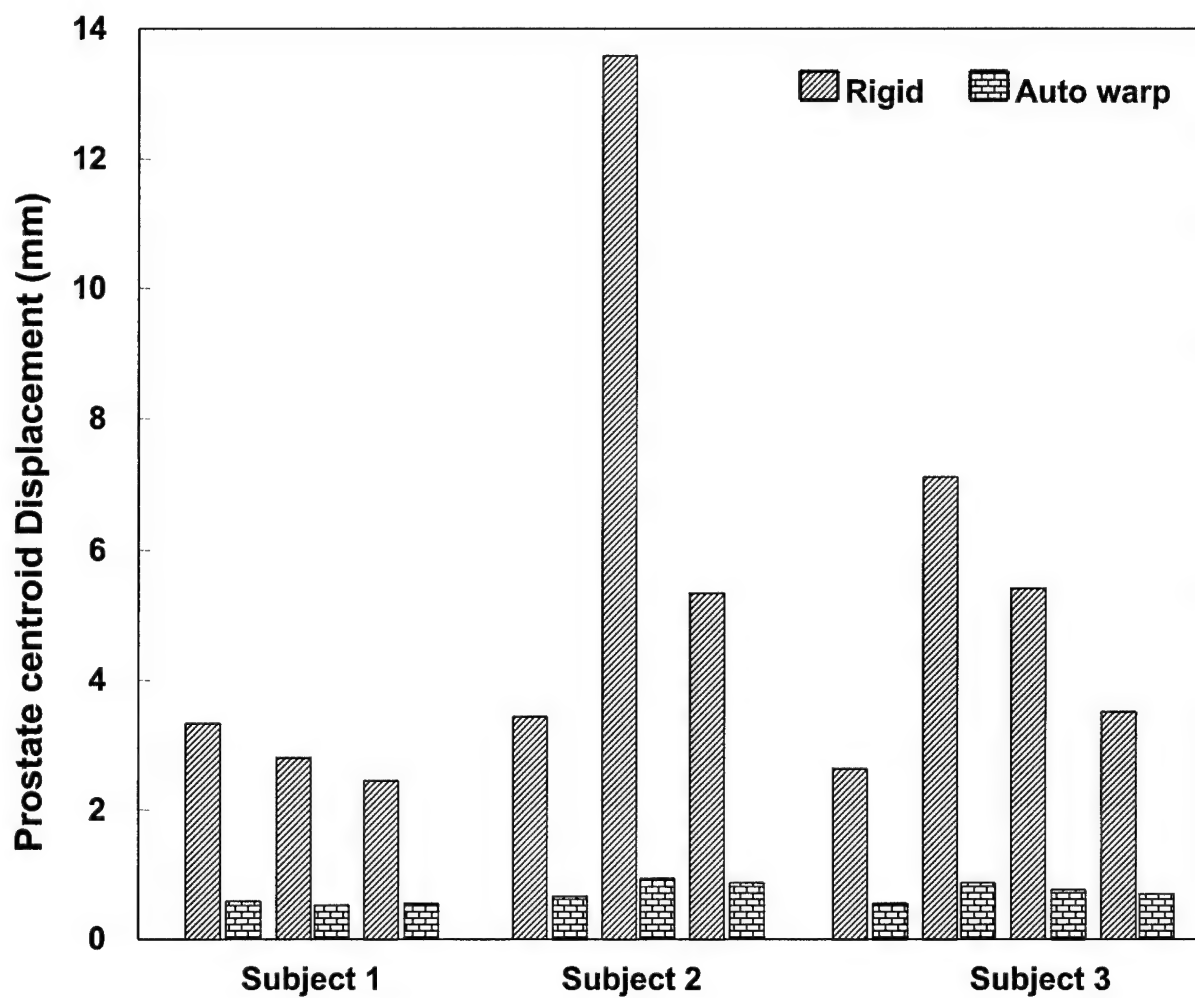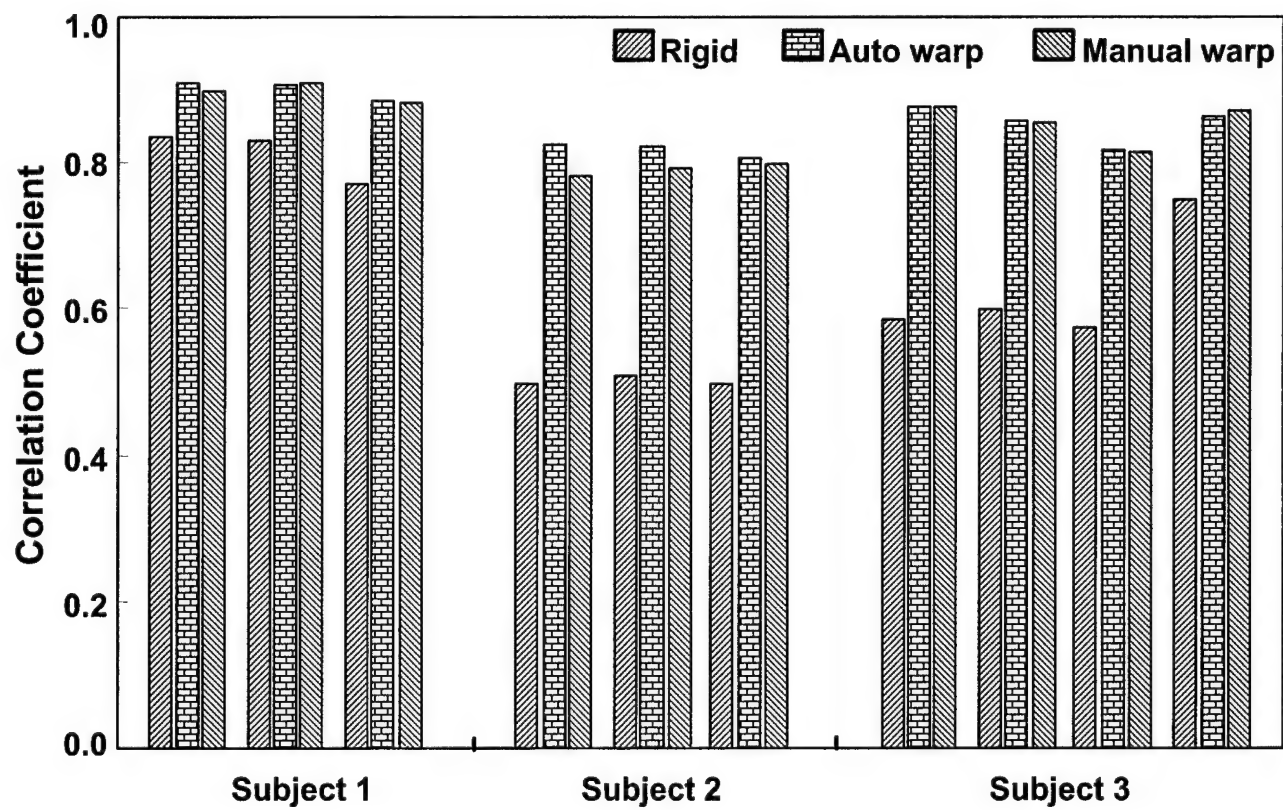
Figure 5

Figure 6

Figure 7

Figure 8

Figure 9

Registration of Micro-PET and High Resolution MR Images of Mice for Monitoring Photodynamic Therapy

Baowei Fei [a*], Raymond F. Muzic [b,a], Zhenghong Lee [b,a], Chris A. Flask [b,a],
Rachel L. Morris [c], Jeffery L. Duerk [b,a], Nancy Oleinick [c], David L. Wilson [a b**]

[a] Department of Biomedical Engineering, Case Western Reserve University, OH 44106
[b] Department of Radiology, University Hospitals of Cleveland, OH 44106
[c] Department of Radiation Oncology, Case Western Reserve University, OH 44106

ABSTRACT

We are investigating imaging techniques to study the rapid biochemical and physiological response of tumors to photodynamic therapy (PDT). Positron emission tomography (PET) can provide physiological and functional images of cancers. While MRI can provide high resolution anatomical images and generate serial, noninvasive, in vivo observations of morphological changes. In this study, we investigate image registration methods to combine MRI and micro-PET (μPET) images for improved tumor monitoring. We acquired high resolution MR and PET ^{18}F-fluorodeoxyglucose (FDG) images from mice with RIF-1 tumors. We used rigid body registration with three translations and three angular variables. We used normalized mutual information as the similarity measure. To assess the quality of registration, we performed slice by slice review of both image volumes, manually segmented feature organs such as the left and right kidneys and the bladder in each slice, and computed the distance between corresponding centroids of the organs. We also used visual inspection techniques such as color overlay displays. Over 40 volume registration experiments were performed with MR and μPET images acquired from three C3H mice. The color overlays showed that the MR images and the PET images matched well. The distance between corresponding centroids of organs was 1.5 ± 0.4 mm which is about 2 pixels of μPET. In conclusion, registration of high resolution MR and μPET images of mice may be useful to combine anatomical and functional information that could be used for the potential application in photodynamic therapy.

Keywords: Image registration, mutual information, magnetic resonance imaging (MRI), positron emission tomography (PET), photodynamic therapy (PDT), micro-PET (μPET), cancers.

1. INTRODUCTION

Photodynamic therapy (PDT) is USFDA approved (with the photosensitizer Photofrin) for advanced esophageal, early lung and late lung cancer.[1,2] In PDT, a tumor-localized photosensitizer is irradiated with visible light to generate reactive oxygen that efficiently kills cells and ablates tumors. PDT is a three-component treatment.[1,2] It requires (a) a photosensitizer, often a porphyrin-related macrocycle, that tends to accumulate in tumors; (b) non-thermal visible light

---

* Baowei.Fei@case.edu, ** dlw@po.cwru.edu, Wickenden Building 319, 10900 Euclid Avenue, Cleveland, OH 44106.

of a wavelength absorbed by the photosensitizer and generally in the red region of the spectrum (since longer wavelengths penetrate human tissue best); and (c) molecular oxygen. With an adequate oxygen supply and light intensity, the site of photodamage depends on the location of the photosensitizer. An important advantage of PDT is that both the photosensitizer and the light are inert by themselves, and the light can be precisely focused onto a selected region, allowing extreme specificity in the localization of the photodynamic effect. Consequently, systemic toxicities are minimized.

Imaging techniques are used for the study of cancer. Positron emission tomography (PET) is widely used to study the physiology of many types of cancer.[3,4] Since tissue uptake of ^{18}F-fluorodeoxyglucose (FDG) depends on both blood flow and hexokinase activity, it can be a good probe to investigate the mechanisms of PDT that dependent on the two parameters. However, because FDG uptake depends on both, it is difficult to differentiate on the basis of FDG alone. We had planned to also do water (perfusion) and carbon monoxide (blood volume). Lapointe et al. reported the study of PET FDG imaging for monitoring the response of tumors to PDT.[3] A micro-PET (μPET) imager was designed and built to perform dynamic in vivo PET scans of tumor-bearing mice after PDT. Reductions in FDG uptake of a treated tumor relative to an untreated tumor in the same animal were observed.[3] Magnetic resonance imaging (MRI) has also been used to evaluate PDT-induced hemorrhagic necrosis in the murine M1 tumor within 72 hours of treatment of male DBA/2 mice.[5-7]

In this project, we investigate using both μPET and high-resolution MR imaging techniques for improved tumor monitoring. Though PET images can provide the dynamic functional information, MR has superior anatomical information for the locations of tumors and organs and can make serial, noninvasive, in vivo observations of morphological changes. Conversely, PET can provide functional information that is not available in normal anatomical MR images. The goal of this project is to apply PET imaging to study the rapid biochemical and physiological response of tumors to PDT and to use MR to monitor the anatomical and morphological changes of tumors.

The combination of μPET and high-resolution MRI has several advantages. First, MRI scans provide anatomical reference to the PET images. Second, registration of PET and MRI images can enhance our ability to visualize the location of the FDG uptake. Third, MRI provides tumor shape and size information that can be used to improve the accuracy of the PET data analysis such as drawing region of interests (ROIs) and performing quantitative analyses. Fourth, MRI can be used to correct PET data for partial volume effects to clarify that the PET-measured changes induced by PDT are due to metabolic and hemodynamic changes and not artifacts due to changes in tumor size.

In this study, we focus on image registration methods for the alignment of MRI and μPET images. Several reports described the registration of MRI and PET for the cat brain,[8] the rat brain,[9] a brain phantom,[10] and radiotherapy planning.[11] There is no report on mutual information image registration of μPET and MRI for the study of photodynamic therapy. We acquired both PET and MR images from mice with tumors and performed over 40 registration experiments. Evaluation results from visual inspection and quantitative measurements are reported.

2. REGISTRATION ALGORITHM

2.1 Similarity Measurements

Based on our previous experience,[12,13] we chose normalized mutual information (NMI) as the similarity measure in our registration because it is robust and suitable for multi-modality image registration.[14,15] One image R is the *reference*, and the other F is *floating*. Their normalized mutual information (NMI) is given by the following equation.[15]

$$NMI(R,F) = \frac{2MI(R,F)}{H(R)+H(F)}$$

where

$$H(R) = -\sum_r p_R(r)\log p_R(r)$$

$$H(F) = -\sum_f p_F(f)\log p_F(f)$$

$$MI(R,F) = \sum_{r,f} p_{RF}(r,f)\log \frac{p_{RF}(r,f)}{p_R(r)\cdot p_F(f)}.$$

The joint probability $p_{RF}(r,f)$ and the marginal probabilities $p_R(r)$ of the reference image and $p_F(f)$ of the floating image, can be estimated from the normalized joint intensity histograms. When two images are geometrically aligned, NMI is maximal.[15]

2.2 Registration Algorithm

The input data include the PET transmission, emission, and high-resolution MR images. We normally discretize the image intensity to 256 levels. We combine the PET transmission and emission images and form one data set by taking a weighted sum. We assume that there is no movement between the transmission and emission scans. We use the combined PET data and the high-resolution MR image for mutual information registration.

We used rigid body transformation (three translations and three rotations) and trilinear interpolation as described previously.[16] For optimization, we used the downhill simplex method of Nelder and Mead.[17] Optimization of similarity ends either when the maximum number (800) of calculations is reached or the fractional change in similarity function is smaller than a tolerance (0.001). Typically the latter is achieved within about 200 iterations. Our very first initial guess is all zeros for the 3 displacements and 3 angles.

3. EXPERIMENTAL METHODS

3.1 Animal Preparation

RIF (Radiation-induced fibrosarcoma)-1 cells were grown as monolayers in E-MEM supplemented with 15% fetal bovine serum (ref. 18). Prior to inoculation, C3H/HeN mice were shaved and depilated. Two tumors were initiated in

each mouse by injection of 10^5 - 10^6 RIF-1 cells intradermally on the shoulder flanks, as far from the bladder and kidneys as possible to minimize spillover in PET images. Tumors were treated and imaged when they reach 3-5 mm in diameter, which required 7-10 days after implantation. Animals were given the photosensitizer Pc 4 (1 mg/kg) by tail vein injection. After 24 hours, one of the tumors was exposed to red light (670 nm) from a diode laser (150 J/cm^2; 150 mW/cm^2).

Three animals were studied for µPET and MR imaging. We know from experience that neither the light nor the photosensitizer alone produces any response, so initially, one of the two tumors in each animal served as a control (receiving photosensitizer but no light), and the other tumor was exposed to laser light.

3.2 MR Image Acquisition

Two days after photosensitizer injection, the animals were taken to the MR imaging facility. The mouse images were acquired using a Siemens Sonata 1.5 T scanner (Siemens Medical Systems, Erlangen, Germany). A custom-designed whole-body mouse coil (2-element phased-array, ID = 32 mm) was used to minimize noise levels. A T1-weighted spin echo pulse sequence (TR/TE=600/13ms) with a slice thickness of 1-mm was used to generate high-resolution coronal images (Matrix = 256 x 120, FOV = 80 x 36-mm). The number of signal averages was typically set at six to obtain low noise images. In these T1 images, the tumors are clearly delineated by the bright subcutaneous fat signal. During each imaging session, the animals were mounted on a plastic holder and were provided with a continuous supply of 2% isoflurane (EZAnesthesia, Palmer, PA) in oxygen to minimize motion artifacts in MR images.

3.3 Micro-PET Image Acquisition

After MR image acquisition, the animals with the plastic holder and the lasers were taken to the PET imaging facility. We used a MicroPET R4 scanner (Concorde Microsystems, Inc., Knoxville, TN 37932) designed specifically for imaging small rodents.[20] The in vivo functional imaging with microPET® allows both serial and longitudinal studies to be conducted in the same animal. We followed a single animal over 90-minute period of time and monitored the response of PDT and the outcome.

We used ^{18}F-FDG (fludeoxyglucose) that is the standard radiopharmaceutical used in PET scanning for tumor diagnosis and assessment, for cerebral glucose metabolism, and for myocardial metabolic assessment. It has become a standard commodity and is obtained commercially as well as being produced on the premises. It was produced for this experiment in standard fashion.[21,22]

The control tumor was shielded with black cloth, and the animals were placed in plastic holders to restrain them during imaging. The mouse was studied for FDG accumulation, blood flow and blood volume. Depending upon the simulations, ^{18}F-FDG was injected as a bolus or by continuous infusion into the tail vein. About 6 min later, laser light was focused onto a 1-cm spot encompassing the non-shielded tumor. FDG accumulation in both tumors was measured during the 15-min light exposure.

We acquired both transmission and emission images from the same mouse. Since the animal did not move during the image session, we assume the there is no movement between the two scans. The PET images include 63 transverse slices covering the whole mouse. Each slice has 128x128-pixel with an in-plane pixel size of 0.85 x 0.85-mm and a thickness of 1.2 mm.

3.4 Preprocessing

The input MR volume is a 2D MR acquisition giving 256 x120 with an in-plane resolution of 0.3x0.3-mm and a slice thickness of 1.0-mm. Twenty nine coronal slices over a field of view cover the whole mouse. Using tri-linear interpolation, we create isotropic voxels of 0.3 mm on a side for both PET and MR image volumes. We optionally discretize the intensity to 256 levels. We use IDL (Interactive Data Language, Research System Inc., Boulder, CO) as the programming language.

For purposes of registration, we optionally cropped image slices that were not of interest. For example, the tumors were on the mouse back near the shoulder, we cropped out images at the abdomen and tail. Before cropping, the image volume was 350x250x250-voxel covering the whole mouse. After cropping, we created a volume with 128x128x248-voxel near the region of interest. Cropping processing can bring two advantages for the mouse registration. First, cropping out regions that are not of interest can increase image consistency for the mutual information registration. Since the mouse body is very flexible, the deformation at the abdomen can cause inconsistency for the rigid body registration. Second, the small number of voxels after cropping can increase the speed of image registration.
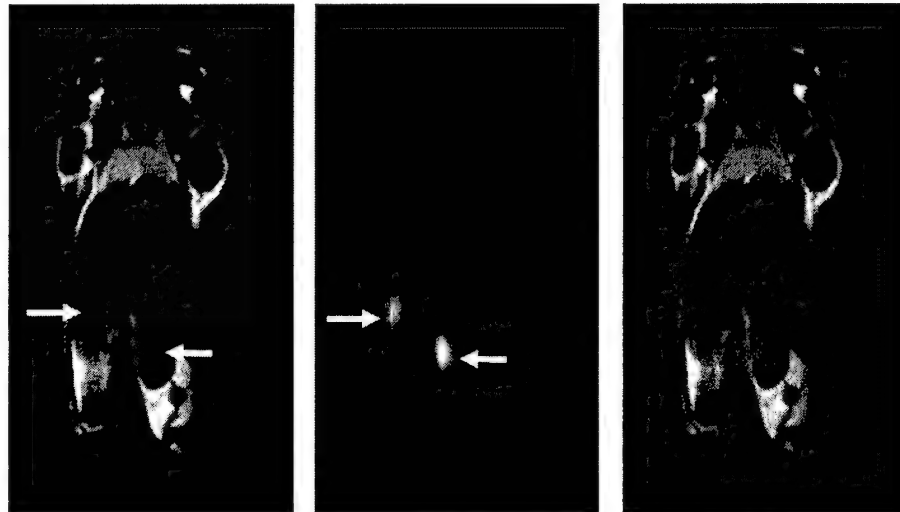

Figure 1. Visual inspection of the kidney registration. Image on the left is the high-resolution MR image. The white arrows indicate the left and right kidneys of the mouse. Image at the center is the PET FDG image.The white arrows indicate the kidneys. Image on the right is the overlay of the two images, which indicate good registration at the organs. Images are from the Mouse No.3.
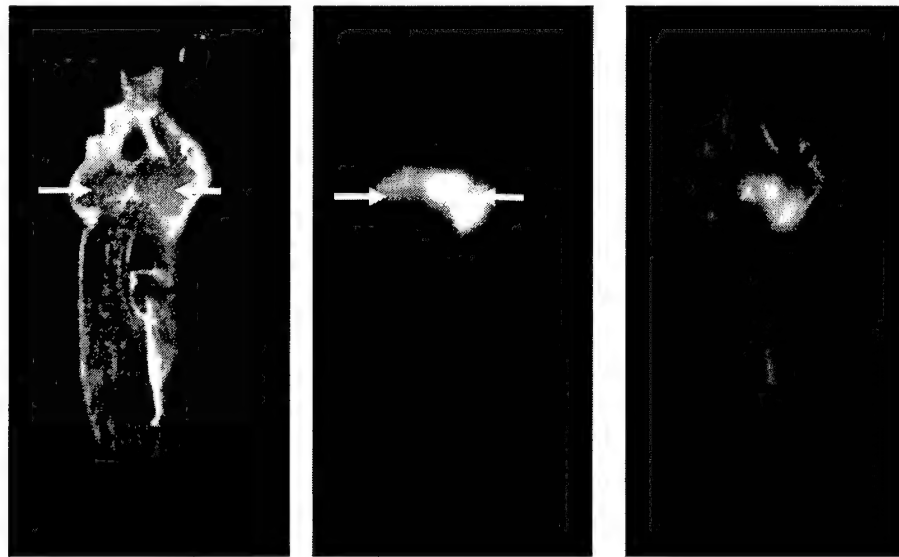
Figure 2. Registration of tumors. Image on the left is the coronal MR image. The white arrows indicate two tumors on the back of the mouse. Image at the center is the PET FDG image. The white arrows indicate two tumors. Image on the right is the overlay image. The tumors are registered well. Images are from the Mouse No.3.

Figure 3. The effect of intensity scaling on image registration. The X-axis is the gray levels from 32 to 512. The Y-axis it the normalized mutual information values between MR and PET transmission images. The dash line indicates the NMI values before registration. The real line is the NMI values after registration.

4. Results and Discussion
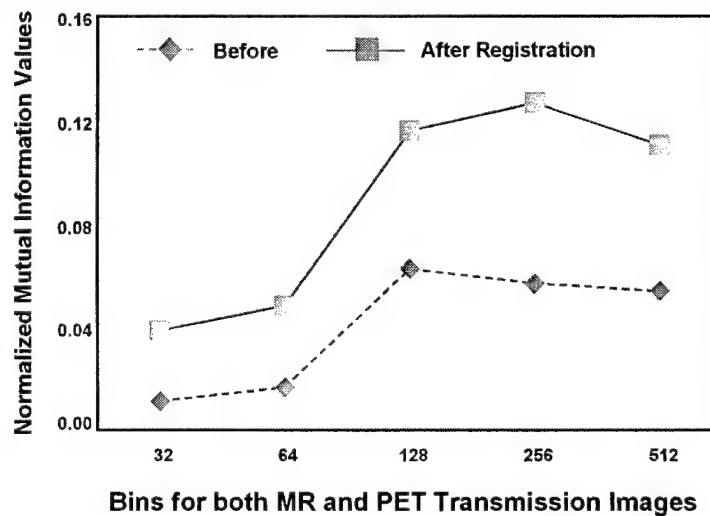
4.1 Visual Inspection

Figure 1 shows the registration of the left and right kidneys of a mouse. The MR image provides the shape of the kidneys. The PET image shows the FDG uptake of the organs. The fused image combines both anatomic and functional information. We also examined other slices in different positions. The kidneys were well-aligned in three dimensions. The kidneys are good anatomic markers for registration evaluation. Other feature organs such as the bladder and heart were also aligned.

Figure 2 shows the registration of two tumors. The high resolution MR image contains the anatomic structure of the tumors. The PET image shows the radioactivity of the tumors. The overlay image indicates good registration of the tumors. We also used other visualization methods found in MIM ^{TM} (MIMvista Corp., Cleveland, Ohio 44122) for the image display and analysis.

4.2 Effects of Intensity Scaling

We tested the effect of intensity scaling on image registration. Since PET images are stored as float data, we normally discretize the data to 256 gray levels for image display and processing. We then use the scaled data and apply the mutual information algorithm. Different intensity scaling creates different joint histograms that affect the mutual information calculation. We performed registration experiments using different intensity scaling such as 512, 256, 128, 64, or 32 bins for both volume data sets. Scaling was linear between zero and the maximum value. Registration was examined by analyzing the normalized mutual information values and visual inspection.

In Figure 3, we show the NMI values between the PET transmission image and MR image volume. First, the NMI values increased after registration. Second, when the bin size is 256, the NMI is the maxim indicating the gray level of 256 is the best for the registration. The visual inspection confirmed the results.

4.3 Quantitative Evaluation

We used features identifiable in both PET and MR images to evaluate the mouse registration. We manually segmented feature organs such as the left and right kidneys and the bladder in each slice for both MR and PET image volumes. We calculated the area and the center point for each slice. Then, we compute the three-dimensional centroid of the organs. To evaluate the registration error, we computed the distance between corresponding centroids. For three mice, the registration error is 1.5 ± 0.4 mm, about 2 μPET pixels. More importantly, μPET resolution is about 2 mm.[20]

4.4 Combining PET Emission and Transmission Images

We found that only using PET emission image led to the registration failure and that it is important to add transmission image for the registration. We think the anatomic information from transmission image may be good for the mutual information image registration. However, increasing the percentage of transmission image from 10% to 100% made no significant difference.

5. CONCLUSION

We created a rigid body image registration method for µPET and high MR images for a new application in small animal imaging. The registration and fusion provided both functional and anatomic information that could be useful for the potential application in photodynamic therapy. We are going to perform more imaging experiments and we are developing deformable registration method for small animals.

ACKNOWLEDGEMENTS

REFERENCE

1   T.J.Dougherty, "An update on photodynamic therapy applications," *J Clin.Laser Med Surg.*, vol. 20, pp. 3-7, Feb, 2002.

2   T.J.Dougherty, C.J.Gomer, B.W.Henderson, G.Jori, D.Kessel, M.Korbelik, J.Moan, and Q.Peng, "Photodynamic therapy," *J Natl.Cancer Inst.*, vol. 90, pp. 889-905, Jun 17, 1998.

3   D.Lapointe, N.Brasseur, J.Cadorette, C.La Madeleine, S.Rodrigue, J.E.van Lier, and R.Lecomte, "High-resolution PET imaging for in vivo monitoring of tumor response after photodynamic therapy in mice," *J Nucl.Med*, vol. 40, pp. 876-882, May, 1999.

4   J.V.Moore, M.L.Waller, S.Zhao, N.J.Dodd, P.D.Acton, A.P.Jeavons, and D.L.Hastings, "Feasibility of imaging photodynamic injury to tumours by high-resolution positron emission tomography," *Eur.J Nucl.Med*, vol. 25, pp. 1248-1254, Sep, 1998.

5   B.G.Winsborrow, H.Grondey, H.Savoie, C.A.Fyfe, and D.Dolphin, "Magnetic resonance imaging evaluation of photodynamic therapy-induced hemorrhagic necrosis in the murine M1 tumor model," *Photochem.Photobiol.*, vol. 66, pp. 847-852, Dec, 1997.

6   S.Gross, A.Gilead, A.Scherz, M.Neeman, and Y.Salomon, "Monitoring photodynamic therapy of solid tumors online by BOLD-contrast MRI," *Nat.Med*, vol. 9, pp. 1327-1331, Oct, 2003.

7   S.D.Kennedy, L.S.Szczepaniak, S.L.Gibson, R.Hilf, T.H.Foster, and R.G.Bryant, "Quantitative MRI of Gd-DTPA uptake in tumors: response to photodynamic therapy," *Magn Reson Med*, vol. 31, pp. 292-301, Mar, 1994.

8   Y.Shimada, K.Uemura, B.A.Ardekani, T.Nagaoka, K.Ishiwata, H.Toyama, K.Ono, and M.Senda, "Application of PET-MRI registration techniques to cat brain imaging," *J Neurosci.Methods*, vol. 101, pp. 1-7, Aug 15, 2000.

9   N.Hayakawa, K.Uemura, K.Ishiwata, Y.Shimada, N.Ogi, T.Nagaoka, H.Toyama, K.Oda, A.Tanaka, K.Endo, and M.Senda, "A PET-MRI registration technique for PET studies of the rat brain," *Nucl.Med Biol.*, vol. 27, pp. 121-125, Feb, 2000.

10   M.Koole, Y.D'Asseler, K.Van Laere, W.R.Van de, W.C.Van de, I.Lemahieu, and R.A.Dierckx, "MRI-SPET and SPET-SPET brain co-registration: evaluation of the performance of eight different algorithms," *Nucl.Med Commun.*, vol. 20, pp. 659-669, Jul, 1999.

11   S.J.Kiebel, J.Ashburner, J.B.Poline, and K.J.Friston, "MRI and PET coregistration--a cross validation of statistical parametric mapping and automated image registration," *Neuroimage.*, vol. 5, pp. 271-279, May, 1997.

12 B.W.Fei, A.Wheaton, Z.Lee, J.L.Duerk, and D.L.Wilson, "Automatic MR volume registration and its evaluation for the pelvis and prostate," *Physics in Medicine and Biology*, vol. 47, pp. 823-838, 2002.

13 B.W.Fei, J.L.Duerk, D.T.Boll, J.S.Lewin, and D.L.Wilson, "Slice to volume registration and its potential application to interventional MRI guided radiofrequency thermal ablation of prostate cancer," *IEEE Transactions on Medical Imaging*, vol. 22, pp. 515-525, 2003.

14 A.Collignon, F.Maes, D.Delaere, D.Vandermeulen, P.Suetens, and G.Marchal, "Automated multimodality image registration using information theory,"*Information Processing in Medical Imaging: Proc. 14th International Conference (IPMI'95)*, Computational Imaging and Vision,pp. 287-298, 1995.

15 F.Maes, A.Collignon, D.Vandermeulen, G.Marchal, and P.Suetens, "Multimodality image registration by maximization of mutual information," *IEEE Transactions on Medical Imaging*, vol. 16, pp. 187-198, 1997.

16 B.W.Fei, Z.Lee, J.L.Duerk, and D.L.Wilson, "Image Registration for Interventional MRI Guided Procedures: Similarity Measurements, Interpolation Methods, and Applications to the Prostate," *Lecture Notes of Computer Science (LNCS)*, vol. 2717, pp. 3292003.

17 J.Nelder and R.A.Mead, "A simplex method for function minimization," *Computer Journal*, vol. 7, pp.308-313, 1965.

18 S.I.Zaidi, N.L.Oleinick, M.T.Zaim, and H.Mukhtar, "Apoptosis during photodynamic therapy-induced ablation of RIF-1 tumors in C3H mice: electron microscopic, histopathologic and biochemical evidence," *Photochem.Photobiol.*, vol. 58, pp. 771-776, Dec, 1993.

19 C.H.Sibata, V.C.Colussi, N.L.Oleinick, and T.J.Kinsella, "Photodynamic therapy in oncology," *Expert. Opin. Pharmacother.*, vol. 2, pp. 917-927, Jun, 2001.

20 C.Knoess, S.Siegel, A.Smith, D.Newport, N.Richerzhagen, A.Winkeler, A.Jacobs, R.N.Goble, R.Graf, K.Wienhard, and W.D.Heiss, "Performance evaluation of the microPET R4 PET scanner for rodents," *Eur.J Nucl.Med Mol. Imaging*, vol. 30, pp. 737-747, May, 2003.

21 R.F.Muzic, Jr., B.Landmeier, Z.Zhang, L.Zheng, and M.S.Berridge, "Solid-phase analysis method for (S)-[18F]fluorocarazolol and its metabolites," *J Chromatogr.B Biomed Sci.Appl.*, vol. 759, pp. 355-359, Aug 15, 2001.

22 R.F.Muzic, Jr. and S.Cornelius, "COMKAT: compartment model kinetic analysis tool," *J Nucl.Med*, vol. 42, pp. 636-645, Apr, 2001.

Three-Dimensional Automatic Volume Registration of Carotid MR Images

Baowei Fei [1], Shaoxiong Zhang [2], Olivier Savado [1], Jasjit Suri [1],
Jonathan S. Lewin [2,1], David L. Wilson [1,2]

[1]Department of Biomedical Engineering, Case Western Reserve University, Cleveland, OH, USA
[2]Department of Radiology, University Hospitals of Cleveland, Cleveland, OH, USA

Abstract — We created an automatic three-dimensional registration algorithm for magnetic resonance images of carotid vessels. Potential applications include atherosclerotic plaque characterization and plaque burden quantification vector-based segmentation using dark blood MR images having multiple contrast weightings (proton density (PD), T1, and T2). Another application is measurement of disease progression and regression with drug trials. We used mutual information registration algorithm to compensate movements between image acquisitions. PD, T1, and T2 images were acquired from patients and volunteers and then matched for image analysis. Visualization methods such as contour overlap showed that vessels well aligned after registration. Distance measurements from the landmarks indicated that the registration method worked well with an error of 1.09 ± 0.42 mm.

Keywords—Image registration, dark blood MR image, carotid plaque classification

I. Introduction

Atherosclerotic disease of the carotid artery is the leading cause of stroke [1]. MRI has emerged as a potential leading in vivo imaging modality for atherosclerotic plaque characterization [2][3]. Black blood high-resolution MRI techniques with multiple contrast weightings (proton density (PD), T1, and T2) have been shown to be useful for atherosclerotic plaque characterization and plaque burden assessment [4].

Quantification during disease progression and after therapeutic intervention may improve our knowledge of the natural history of the disease and lead to improved therapeutic strategies. However, the spatial location mismatching of different scans from serial examination will impair the accuracy of quantified analysis of atherosclerotic disease using MRI. Image registration has the potential to improve the quantification and characterization [5]. Combination of multiple images such as proton density (PD), T1, and T2 could verify lesions and provide more information for diagnosis and treatment. Further, registration of serial examinations can follow up the progression and regression of diseases [6]. In this study, we perform registration experiments for MR images from patients with carotid stenosis and volunteers.

II. Methodology

A. Registration Algorithm

We are investigating voxel-based methods for automatic three-dimensional (3D) registration because they do not depend on possibly inaccurate image segmentation and because they can be extended to non-rigid registration [7]-[9].

We used normalized mutual information (NMI) as the similarity measures in our registration because they are robust and suitable for multi-modality image registration [7]. Suppose one image R is the *reference*, and the other F is *floating*. NMI is given by the following equation [7].

$$NMI(R,F) = \frac{2MI(R,F)}{H(R) + H(F)}$$

where

$$H(R) = -\sum_r p_R(r)\log p_R(r), \quad H(F) = -\sum_f p_F(f)\log p_F(f)$$

$$MI(R,F) = \sum_{r,f} p_{RF}(r,f)\log\frac{p_{RF}(r,f)}{p_R(r)\cdot p_F(f)}.$$

The joint probability $p_{RF}(r,f)$ and the marginal probabilities $p_R(r)$ of the reference image and $p_F(f)$ of the floating image, can be estimated from the normalized joint intensity histograms. When two images are geometrically aligned, NMI is maximal.

We used rigid body transformation (three translations and three angles) and trilinear interpolation. For optimization, we use the downhill simplex method of Nelder and Mead [10]. Optimization of alignment ends either when the maximum number of NMI calculations is reached (typically 500) or the fractional change in NMI is smaller than a tolerance (typically 0.0001). Our very first initial guesses are all zeros for the 3 displacements and 3 angles.

B. Image Acquisitions

All MR scans were conducted on a 1.5 T system (Magnetom Sonata, Siemens Medical Solutions, Erlangen, Germany) with a custom-built phased array coil to improve the local image signal-to-noise ratio. Patients were positioned supine on the scanner table. After axial, sagittal and coronal localizer images were acquired; a set of double oblique localizer images was then acquired to monitor the phased array coil position and to roughly identify the carotid

artery bifurcation. A transverse three-dimensional (3D) multiple overlapping thin slab angiography (MOTSA) sequence with TR/TE/flip/partition thickness of 20ms/3.4ms/25°/1mm, was used to locate the exact level of the carotid bifurcation. Dark blood images were then obtained using ECG-triggered double inversion recovery (DIR) turbo spin echo sequences. The imaging parameters (TR/TE/TI/NSA/thickness/FOV) were as follows: 1R-R/7.1ms/500ms/2/3mm/13cm (T1), 2R-R/7.1ms/600ms/2/3mm/13cm (PD), 2R-R/68ms/600ms/2/3mm/13cm (T2). Fat saturation was applied for all dark blood images. The in plane resolution was 0.51×0.51mm^2. We acquired PD, T1, and T2 images from one patient P1 and two volunteers S1 and S2.

C. Registration Experiments

We have nine pairs of volumes for registration experiments. For each subject, we have PD, T1 and T2 image volumes. We used PD as the reference image and we registered T1 and T2 with PD. We also matched T2 with T1 to test the registration algorithm. There are three registration experiments for each subject. We performed two registration trials for volunteers S1 and S2. In total, we conducted 15 registration experiments, three for the patient P1 and three for each of the volunteers S1 and S2.

D. Registration Evaluation

We used visual inspections to evaluate the registration. We used *RegViz,* a program written in IDL (Interactive Data Language, Research System Inc., Boulder, CO) and created in our laboratory for visualizing and analyzing registered image volumes. First, we manually segmented carotid vessel walls in image slices and copied them to corresponding slices. This enabled visual determination of the overlap of vessel walls over the entire volume. Second, color overlay displays were used to evaluate overlap of structures. One image was rendered in gray and the other in the "hot-iron" color scheme available in IDL. To visualize potential differences, it was quite useful to interactively change the contribution of each image using the transparency scale. Third, we used a sector display, which divided the reference and registered images into rectangular sectors and created an output image by alternating sectors from the two input images. Even subtle shifts of edges would be clearly seen.

We evaluated registration of the vessels by measuring the displacement of the landmarks following registration. We used the left and right bifurcations as the landmarks. To measure displacements, we navigated transverse, coronal, and sagittal MR images slice-by-slice to search bifurcations in both reference and registered volumes. Using consistent rules and magnified images, a radiologist used a cursor to identify unique features on both images. The 3D locations for each landmark were recorded and 3D distance between corresponding landmarks is computed.

III. RESULTS

A. Visual Inspection

We determined the quality of vessel registration by visually examining all image slices of registered volume pairs using one or more of the methods found in RegViz. A typical example is shown in Fig.1 where the contour overlap is excellent and probably within the manual segmentation error. Other transverse images were also well aligned indicating that the registration was successful in three dimensions. Other visual inspection techniques such as color overlay and sector display also demonstrate excellent registration.

B. Assessments of Bifurcations

Following registration, we measured 3D distances between corresponding bifurcations. Registration results are shown in Table I. The average error across the three subjects with 15 registration experiments is only 1.09 ± 0.42 mm. The isotropic voxel size of the volumes is 0.51 mm. The measured error reported for NMI registration is probably overestimated due to landmark location error.

TABLE I
DISPLACEMENT OF BIFURCATIONS
MEAN (STANDARD DEVIATION) IN mm

	PD-T1	PD-T2	T1-T2
Left bifurcation	1.04 (0.63)	1.49 (0.56)	1.02 (0.27)
Right bifurcation	0.97 (0.34)	1.04 (0.24)	0.98 (0.31)

C. Implementation Issues

The algorithm was quite robust for nine volume pairs in this study. Each call to the Simplex optimization resulted in 120 to 250 NMI evaluations before the tolerance (0.0001) was reached. The time for a single registration, typically 5 minutes for the volumes with 256x256x59-voxels on a Pentium IV, 1.8GHz CPU, with 1Gbytes of memory, could probably be greatly improved with optimized C code rather than IDL.

IV. DISCUSSION & CONCLUSION

We have developed an automatic volume registration algorithm for multiple contrast weighted MR images of carotid vessels. Our internal measures showed the registration is quite robust and accurate. It will probably be a useful tool for many applications of interest in vascular imaging.

REFERENCES

[1] G.W.Petty, R.D.Brown, J.P.Whisnant, J.D.Sicks, W.M.O'Fallon, and D.O.Wiebers, "Ischemic stroke subtypes - A population-based study of functional outcome, survival, and recurrence," *Stroke*, vol. 31, pp. 1062-1068, 2000.

[2] Z.A.Fayad and V.Fuster, "Clinical imaging of the high-risk or vulnerable atherosclerotic plaque," *Circulation Research*, vol. 89, pp. 305-316, 2001.

[3] C.Yuan, L.M.Mitsumori, K.W.Beach, and K.R.Maravilla, "Carotid atherosclerotic plaque: Noninvasive MR characterization and identification of vulnerable lesions," *Radiology*, vol. 221, pp. 285-299, 2001.

[4] S.X.Zhang, T.S.Hatsukami, N.L.Polissar, C.Han, and C.Yuan, "Comparison of carotid vessel wall area measurements using three different contrast-weighted black blood MR imaging techniques," *Magnetic Resonance Imaging*, vol. 19, pp. 795-802, 2001.

[5] V.L.Stevenson, S.M.Smith, P.M.Matthews, D.H.Miller, and A.J.Thompson, "Monitoring disease activity and progression in primary progressive multiple sclerosis using MRI: sub-voxel registration to identify lesion changes and to detect cerebral atrophy," *Journal of Neurology*, vol. 249, pp. 171-177, 2002.

[6] D.Rey, G.Subsol, H.Delingette, and N.Ayache, "Automatic detection and segmentation of evolving processes in 3D medical images: Application to multiple sclerosis," *Medical Image Analysis*, vol. 6, pp. 163-179, 2002.

[7] F.Maes, A.Collignon, D.Vandermeulen, G.Marchal, and P.Suetens, "Multimodality image registration by maximization of mutual information," *IEEE Transactions on Medical Imaging*, vol. 16, pp. 187-198, 1997.

[8] B.W.Fei, C.Kemper, and D.L.Wilson, "A comparative study of warping and rigid body registration for the prostate and pelvic MR volumes," *Computerized Medical Imaging and Graphics*, vol. 27, pp. 267-281, 2003.

[9] B.W.Fei, A.Wheaton, Z.Lee, J.L.Duerk, and D.L.Wilson, "Automatic MR volume registration and its evaluation for the pelvis and prostate," *Physics in Medicine and Biology*, vol. 47, pp. 823-838, 2002.

[10] J.Nelder and R.A.Mead, "A simplex method for function minimization," *Computer Journal*, vol. 7, pp. 308-313, 1965.
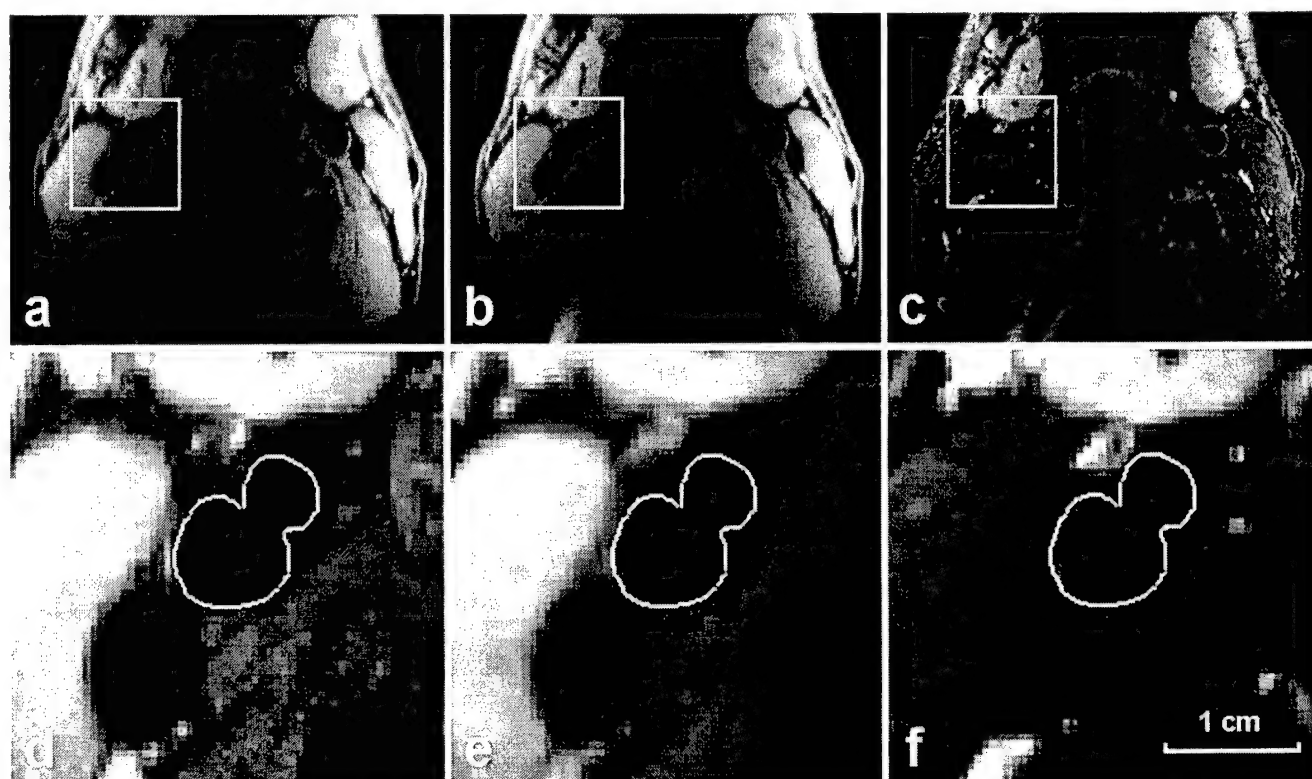
Fig.1. MR images of carotid vessels. The top images from left to right are proton density (PD), T1, and T2 images, respectively. Both T1 and T2 images were registered with the PD image. The rectangular regions are magnified and displayed at the bottom. The carotid vessel walls were manually segmented from the PD image (left) and copied to the T1 (center) and T2 images (right). The contour overlaps at the bottom shows that the vessel boundaries from PD well aligned with those in T1 and T2 images. Images are from Volunteer S1.

Automatic Registration and Fusion of High Resolution Micro-CT and Lung Perfusion SPECT Images of the Rat

Baowei Fei [1], Christian Wietholt [2], Anne V. Clough [3],
Christopher A. Dawson [2,4], David L. Wilson [1,5]

[1]Department of Biomedical Engineering, Case Western Reserve University, Cleveland, OH, USA
[2]Department of Biomedical Engineering, Marquette University, Milwaukee, WI, USA
[3]Department of Computer Science and Mathematics, Marquette University, Milwaukee, WI, USA
[4]Department of Physiology, Medical College of Wisconsin, Milwaukee, WI, USA
[5]Department of Radiology, University Hospitals of Cleveland, Cleveland, OH, USA

Abstract — **Small animal imaging can provide high-throughput phenotypic data for functional genomic studies and better mechanistic understanding of disease. Fusion of anatomical and functional images will aid interpretation of functional images having relatively little anatomical detail. In this study, we are investigating automatic registration and fusion visualization methods for micro-CT and SPECT images of rat lung. The immediate application is studies of pulmonary perfusion in a healthy rat and one with an occluded left pulmonary artery. Registration experiments were performed on images acquired from rats and a phantom. Fusion visualization showed excellent registration results. Quantitative measures such as distances and perimeters from phantom results show that the registration is quite accurate.**

Keywords—**Image registration and fusion, small animal imaging, SPECT, micro-CT, lung perfusion**

I. INTRODUCTION

Small animal imaging is a fast growing field that has numerous applications in the studies of functional genomics, the biology of disease, and therapeutics [1][2]. Since commonly, functional imaging modalities such as single photon emission tomography (SPECT), positron emission tomography (PET) and functional magnetic resonance imaging (fMRI) have little anatomic information, images acquired from computed tomography (CT) or MRI are used to provide structural identification and localization of organs/regions of interest and may also provide additional diagnostic information [5]. In this particular study, we investigate automatic image registration and fusion visualization methods applied to SPECT and micro-CT images for this new important application. The model application used to demonstrate the registration/fusion methods is the localization of a lung perfusion image obtained with SPECT within the anatomical lung field image obtained with micro-CT. We performed registration experiments using image volumes acquired both from rats and a gamma emitting, x-ray absorbing phantom.

II. MATERIALS AND METHODS

A. Registration Algorithm

Based on our previous experiences [6][7], we chose normalized mutual information (NMI) as the similarity measures in our registration because it is robust and suitable for multi-modality image registration [8]. We used rigid body transformation (three translations and three angles) and trilinear interpolation. For optimization, we used the downhill simplex method of Nelder and Mead [9]. Optimization of alignment ends either when the maximum number of NMI calculations is reached (typically 500) or the fractional change in NMI is smaller than a tolerance (typically 0.0001). Our very first initial guesses are all zeros for the three displacements and three angles. We use IDL (Interactive Data Language, Research System Inc., Boulder, CO) as the program language.

B. Image Acquisitions

We used the SPECT and micro-CT systems developed by Marquette University and Medical College of Wisconsin as described previously [4]. For SPECT data acquisition, a mobile gamma camera was positioned in front of the specimen stage and perpendicular to the x-ray beam. The center of the pinhole collimator was positioned at the height of the x-ray source focal spot. The SPECT data were acquired in a step-and-shoot fashion using 128 equiangular increments over a full 360° at 40 sec/view and reconstructed using ordered subset expectation maximization (OSEM) [4]. Subsequently, micro-CT images were acquired at 1° increments over 360°. Seven frames were averaged at each position. This data was reconstructed using Feldkamp [3] conebeam reconstruction.

We performed imaging experiments with a phantom consisting of three test tubes filled with technetium (Tc99m), which were embedded within a larger cylinder. The phantom was placed on the specimen stage and imaged as described above. After the SPECT acquisitions were completed, the phantom was imaged using micro-CT.

We acquired image sets from two rats that were anesthetized with 40mg per kg pentobarbital sodium [4]. One rat underwent surgery in which the left pulmonary

artery was occluded 8 days prior to the imaging. The other rat was untreated. A femoral venous catheter was used to inject 0.6 ml of Tc99m labeled macro-aggregated albumin with a total radioactivity of 2.0 mCi. After allowing the compound enough time to distribute and accumulate in the rat's lungs, the animals were sacrificed using an overdose of the anesthetic. The rats were then placed head down in a plastic tube with diameter of 52mm, and were positioned on the specimen stage. The center of rotation was set so that the right and left lungs were within the field of view at all angular positions. SPECT and micro-CT data were acquired as described above.

C. Registration Experiments

Before we performed image registration experiments, we preprocessed both micro-CT and SPECT image volumes. The original CT image volume has 512x512x497 voxels with 497 transverse slices. The voxel size is 0.10x0.10x0.10-mm. The SPECT image volume is 128x128x128-voxel with voxel size of 0.48x0.48x0.48-mm. We resample CT images and interpolated SPECT images generating two volumes with the same voxel size of 0.2x0.2x0.2-mm. We cropped both SPECT and CT images that have no signal of interest. The final volume images are 256x256x156 for phantom data and 256x256x232 for rats, respectively. We transform CT volumes and registered with corresponding SPECT volumes using our 3D registration algorithm.

D. Registration Evaluation

We used visual inspections to evaluate the registration. We used *RegViz*, a program written in IDL and created in our laboratory for visualizing and analyzing registered image volumes. First, color overlay displays were used to evaluate overlap of structures. One image was rendered in gray and the other in the "hot-iron" color scheme available in IDL. To visualize potential differences, it was quite useful to interactively change the contribution of each image using the transparency scale. Second, we manually segmented regions of interest (ROI) in image slices and copied them to corresponding slices. This enabled visual determination of the overlap of ROI over the entire volume. To evaluate registration of the phantom, we manually segmented the three tubes within the phantom from both CT and SPECT images. We calculated the central positions and computed the distance between corresponding central positions and the perimeters of the segmented tubes.

III. RESULTS

The fusion visualization of registered micro-CT and SPECT images shows that the tubes within the phantom are well matched (Fig.1c). The distances between corresponding central points are less than 0.25-mm and the perimeter

differences are less than 0.33-mm. Hence, the phantom registration is quite accurate.

We determined the registration quality of the rat images by visually examining all image slices of registered volume pairs using one or more of the methods found in RegViz. A typical example is shown in Fig.1 where the color overlays show that the rat lung aligned very well. Other transverse images were also well aligned indicating that the registration was successful in three dimensions. Contour overlap and sector display also demonstrate excellent registration.

IV. DISCUSSION & CONCLUSION

Using our three dimensional automatic registration method, we successfully registered high resolution micro-CT images with lung perfusion SPECT images of the rat. Phantom results show that the registration is quite accurate. As we are performing more rat imaging experiments, we believe that the registration and fusion visualization method could be a useful tool for many applications in small animal imaging.

REFERENCES

[1] J.S.Lewis, S.Achilefu, J.R.Garbow, R.Laforest, and M.J.Welch, "Small animal imaging: current technology and perspectives for oncological imaging," *European Journal of Cancer*, vol. 38, pp. 2173-2188, 2002.

[2] M.J.Paulus, S.S.Gleason, S.J.Kennel, P.R.Hunsicker, and D.K.Johnson, "High resolution X-ray computed tomography: An emerging tool for small animal cancer research," *Neoplasia*, vol. 2, pp. 62-70, 2000.

[3] R.H.Johnson, H.Hu, S.T.Haworth, P.S.Cho, C.A.Dawson, and J.H.Linehan, "Feldkamp and circle-and-line cone-beam reconstruction for 3D micro-CT of vascular networks," *Physics in Medicine and Biology*, vol. 43, pp. 929-940, 1998.

[4] C.Wietholt, R.C.Molthen, Johnson R.H., C.A.Dawson, and A.V.Clough, "SPECT imaging of pulmonary blood flow in a rat," Proceedings of SPIE Medical Imaging on Physiology and Function: Methods, Systems, and Applications, vol. 5031, 2003.

[5] G.J.Forster, C.Laumann, O.Nickel, P.Kann, O.Rieker, and P.Bartenstein, "SPECT/CT image co-registration in the abdomen with a simple and cost-effective tool," *European Journal of Nuclear Medicine and Molecular Imaging*, vol. 30, pp. 32-39, 2003.

[6] B.W.Fei, A.Wheaton, Z.Lee, J.L.Duerk, and D.L.Wilson, "Automatic MR volume registration and its evaluation for the pelvis and prostate," *Physics in Medicine and Biology*, vol. 47, pp. 823-838, 2002.

[7] B.W.Fei, J.L.Duerk, and D.L.Wilson, "Automatic 3D Registration for Interventional MRI-Guided Treatment of Prostate Cancer," *Computer Aided Surgery*, vol. 7, pp. 257-267, 2002.

[8] F.Maes, A.Collignon, D.Vandermeulen, G.Marchal, and P.Suetens, "Multimodality image registration by maximization of mutual information," *IEEE Transactions on Medical Imaging*, vol. 16, pp. 187-198, 1997.

[9] J.Nelder and R.A.Mead, "A simplex method for function minimization," *Computer Journal*, vol. 7, pp. 308-313, 1965.
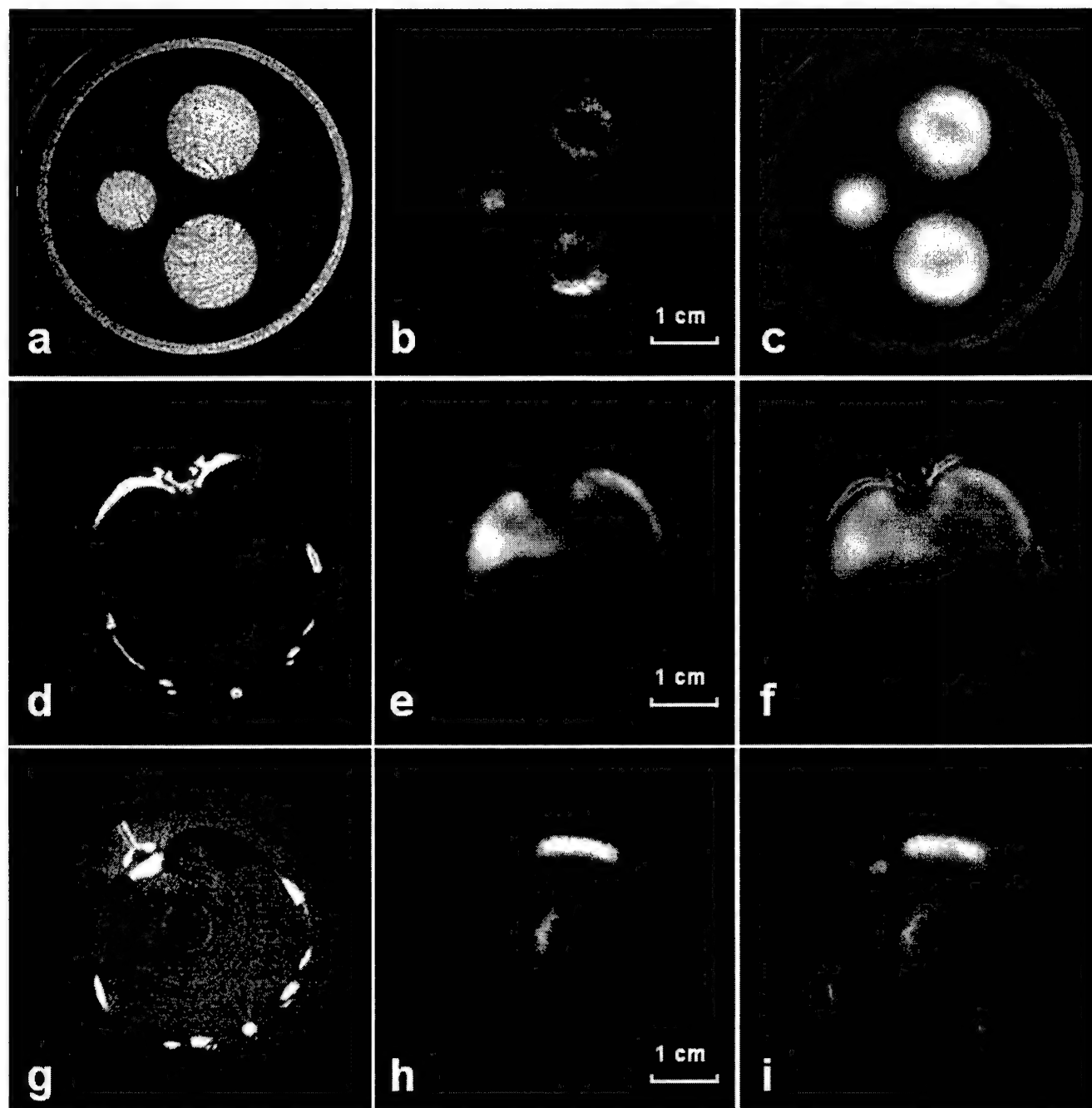
Fig.1. Images of Micro-CT (a,d,g), SPECT (b,e,h), and fusion visualization (c,f,i). a,b,c: Images of the phantom. In the fused image (c), the three tubes within the phantom are well aligned. d,e,f: Normal lung images showing the lung field (d) and perfusion (e) of both the left and right lungs of the rat. g,h,i : Images obtained from a rat with occluded left pulmonary artery. Perfusion (h) is observable only in the right lung in this case. The registered fusion visualization (i) excellently represents both structural and functional information.

Registration Algorithms for Interventional MRI-guided Treatment of the Prostate

Baowei Fei [a*], Kristin Frinkley[a], David L Wilson [a b**]

[a] Department of Biomedical Engineering, Case Western Reserve University, OH 44106

[b] Department of Radiology, University Hospitals of Cleveland, OH 44106

ABSTRACT

We are investigating interventional MRI (iMRI) guided radiofrequency thermal ablation for the minimally invasive treatment of prostate cancer. Nuclear medicine and MR spectroscopy can detect and localize tumor in the prostate not reliably seen in MR. We are investigating methods to combine the advantages of functional images such as SPECT with iMRI-guided treatments. Our concept is to first register the low-resolution functional images with a high resolution MR volume. Then by registering the high-resolution MR image with live-time iMRI acquisitions, we can, in turn, map the functional data and high-resolution anatomic information to iMRI images for improved tumor targeting. In this study, we registered noisy, thick iMRI image slices with high-resolution MR volumes and called this slice-to-volume registration. We investigated two similarity measures, i.e., mutual information and correlation coefficient, and three interpolation methods, i.e., tri-linear, re-normalized sinc, and nearest neighbor. To assess the quality of registration, we calculated 3D displacement on a voxel-by-voxel basis over a volume of interest (VOI) between slice-to-volume registration and volume-to-volume registration that was previously shown to be quite accurate for these image pairs. Over 300 registration experiments showed that transverse slice images covering the prostate work best with a registration error of only 0.4 ± 0.2 mm. Error was greater at other slice orientations and positions. Since live-time iMRI images are used for guidance and registered images are used for adjunctive information, the accuracy and robustness of slice-to-volume registration is very probably adequate.

Keywords: Image registration, medical imaging, interventional magnetic resonance imaging (iMRI), mutual information, thermal ablation, prostate cancer.

1. INTRODUCTION

We are investigating interventional MRI (iMRI) guided radiofrequency (RF) thermal ablation for the minimally invasive treatment of prostate cancer. Nuclear medicine and MR spectroscopy can detect and localize tumor in the prostate not reliably seen in MR. We are investigating methods to combine the advantages of functional images such as SPECT with iMRI-guided treatments. Our concept is to first register the low-resolution functional images with a high resolution MRI. Then by registering the high-resolution MR volume with live-time iMRI acquisitions, we can, in turn, map the functional data and high-resolution anatomic information to iMRI images to aid tumor targeting.

Previous success with registering one MR prostate volume to another [1] encourages us to pursue this plan. We call this volume-to-volume registration, or VV. We used a rigid body, mutual information registration method with some features to improve robustness.[1] We carefully evaluated registration quality using a variety of methods. For volume pairs acquired over a short time span from a supine subject with legs flat on the table, registration accuracy of both

---

prostate centroids (typically < 1 mm) and bony landmarks (average 1.6 mm) was on the order of a voxel (≈ 1.4 mm). For volumes acquired under very different conditions, e.g., legs flat and legs raised into the treatment position, or with and without bladder or rectal filling, we obtained somewhat larger prostate centroids registration errors of about 3.0 mm.

In this study, we are investigating methods to register live-time iMRI image slices with a previously obtained, high resolution MRI volume. We call this slice-to-volume (SV) registration. Because of our success with VV prostate registration, we can determine SV accuracy by comparing results to VV registration for volume pairs having low VV registration error.

The application of SV registration methods to iMRI-guided treatment of prostate cancer raises several challenges. First, iMRI images often have lower signal to noise ratio (SNR) than diagnostic MR images because of the emphasis on fast imaging and because of the typically lower field strength of open iMRI magnets. Second, a single slice, or a few slices, provides many fewer structures than an entire volume for voxel based matching. Third, the prostate can move relative to the pelvic bones due to changes in rectal and bladder filling [2,3] or changes in patient posture for treatment.[1] That is, alignment of the pelvic bones, prominent anatomical features in MR gray-scale images, does not necessarily ensure that the prostate is aligned. Fourth, the normal prostate is a small organ; when healthy, it measures only ≈ 3.8 cm in its widest dimension.[4] The small prostate is located below the much larger bladder that can change its shape and size during imaging. Finally, times for registration and algorithm robustness are of particular concern for this application.

Previously reported methods for SV registration were mainly applied to the brain for applications of functional MRI,[5,6] postmortem pathology studies,[7] and anatomical modeling.[8]

We previously reported an SV registration method for the application of iMRI-guided treatment of the prostate.[9-12] In this report, we further investigated the algorithms by comparing three interpolation methods and two similarity measures. We registered noisy, thick iMRI image slices with high-resolution MR volumes. Over 300 registration experiments were performed with 9 pairs of MR volume images acquired from three health volunteers.

2. REGISTRATION ALGORITHM

2.1. Similarity Measurements

We used two similarity measures, mutual information and correlation coefficient (CC), in our registration. One image R is the *reference*, and the other F is *floating*. Their mutual information $MI(R,F)$ is given below.[13]

$$MI(R,F) = \sum_{r,f} p_{RF}(r,f) \log \frac{p_{RF}(r,f)}{p_R(r) \cdot p_F(f)}$$

The joint probability $p_{RF}(r,f)$ and the marginal probabilities $p_R(r)$ of the reference image and $p_F(f)$ of the floating image, can be estimated from the normalized joint intensity histograms. When two images are geometrically aligned, MI is maximal.[13] The correlation coefficient $CC(R,F)$ is given below.[14]

$$CC(R,F) = \frac{\sum (R(r) - \overline{R}(r))(F(f) - \overline{F}(f))}{\sqrt{\sum (R(r) - \overline{R}(r))^2 \sum (F(f) - \overline{F}(f))^2}}$$

Here $\overline{R}(r)$, $\overline{F}(f)$ denote the average intensities of the reference and floating images and the summation includes all voxels within the overlap of both images.

2.2. Interpolation Methods

We used three interpolation methods, i.e., nearest neighbor (NN), tri-linear, and re-normalized sinc interpolation.[15,16] The conventional sinc interpolation with a cosine Hamming window is described as below.[15]

$$I'(x,y,z) = \sum_X \sum_Y \sum_Z I(X,Y,Z) \cdot HS(x,X,R) \cdot HS(y,Y,R) \cdot HS(z,Z,R)$$

with
$$HS(\alpha, A, R) = \frac{\sin[\pi(\alpha - A)]}{2\pi(\alpha - A)} \cdot \left\{ 1 + \cos[\pi(\alpha - A)/R + 1] \right\},$$

where X, Y, Z, are the coordinates of the original data set (I); x, y, z are the coordinates of the re-formatting data set (I'); A is a symbol representing X, Y, or Z, and a represents x, y, or z; and R is the kernel size. The Hamming function eliminates problems with oscillatory effects at discontinuities and guarantees that the convolution coefficients fall of to zero at the edge of the sinc kernel (i.e., at $|a|=R+1$, where $R=5$ in this study).[15]

A previous report [15] showed that re-normalizing the interpolation kernel for a constant integral could make significant improvement in performance of the conventional sinc interpolation. In our implementation, we used the re-normalized sinc interpolation method.[15] We replaced HS in the above equation with

$$HS'(\alpha, A, R) = HS(\alpha, A, R) \Big/ \sum_A HS(\alpha, A, R) = HS(\alpha, A, R) \Big/ |HS(\alpha)|.$$

2.3. Comparison of Different Similarity Measures and Interpolation Methods

We compared two similarity measures, CC and MI, at different resolutions in order to determine their suitability for SV registration. At *1/4 resolution*, we resampled images so as to give 1/4 number of the voxels along each linear dimension. At *full resolution*, we used the full number of voxels. We plot the two similarity measures as a function of translations. After two typical high-resolution MR volumes were registered,[1] values were plotted with the origin as the optimal transformation. We calculated CC and MI values while moving the simulated iMRI image relative to the high-resolution MR image along coronal (anterior-posterior) axis. When obtaining floating images, we used the three different interpolation methods.

Features of MI and CC demonstrate their suitability at high and low resolutions, respectively. At 1/4 resolution, CC curves are much smoother than MI, which is noisy and contains many local maxima as shown in Figures 1. At full resolution, Figures 2 shows that MI curves are much peaked than CC, but once again there is high frequency noise in the MI curves, far from the optimum, that gives rise to local maxima that must be avoided. From these figures, we infer that CC is better at low resolution and MI is better at full resolution, when one is close to the optimum value.

We also compared the effects interpolation methods. At 1/4 resolution (Figure 1), the MI curves with sinc had more local maximums than those with tri-linear; however, CC plots with sinc were smoother than tri-linear. This indicates that CC and sinc are possibly the best choices for robust registration at low resolution. At full resolution (Figure 2), MI and sinc gave the sharpest peak at the optimum; nearest neighbor interpolation gave a flat peak with a width of one voxel; and tri-linear gave a result between the other two. These results imply that MI and sinc interpolation should provide the best registration accuracy at full resolution. However, tri-linear interpolation is about 100 times faster than sinc interpolation in our implementations.
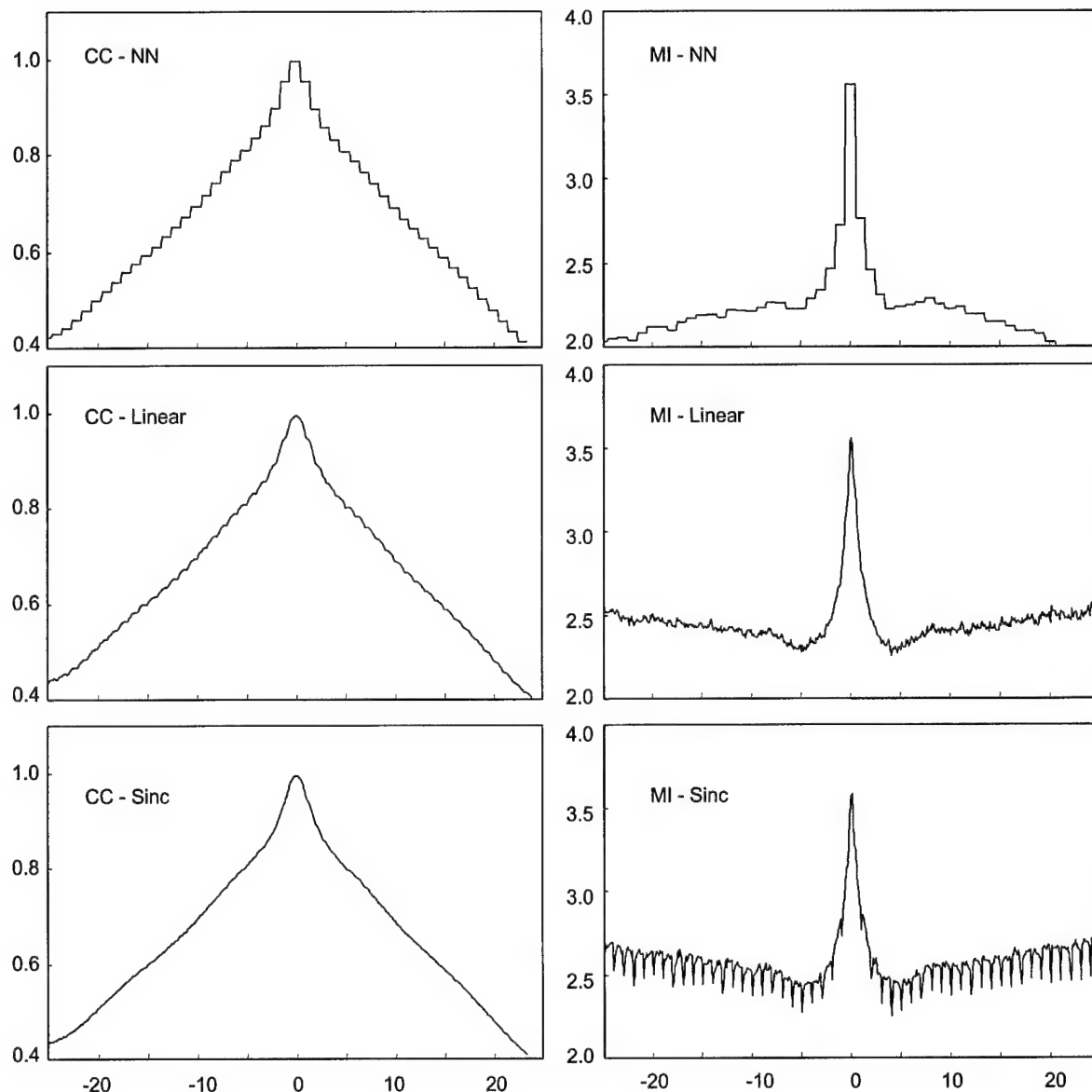
Figure 1. Similarity functions are plotted as a function of translations at the 1/4 resolution in the multi-resolution registration process. Two high-resolution MRI volumes were registered, and they are down sampled by 1/4 along each linear dimension, giving a distance between voxel centers of ≈ 5.5 mm. From the optimal parameters, we computed the similarity of the simulated iMRI and MRI images as a function of translations along the coronal (anterior-posterior) axis. Correlation coefficient (CC) is plotted in the left column. Mutual information (MI) is plotted in the right column. From the top to bottom, nearest neighbor (NN), tri-linear and re-normalized sinc interpolation methods are used to obtain the floating images, respectively. The noisey MI curves in the right column show many local maxima, especially with sinc interpolation. CC curves in the left column are much smoother indicating its suitability for low resolution. Nearest neighbor has a flat peak with a width of one voxel in both similarity curves. The unit of the X-axis is voxel. Images are from volunteer S2.
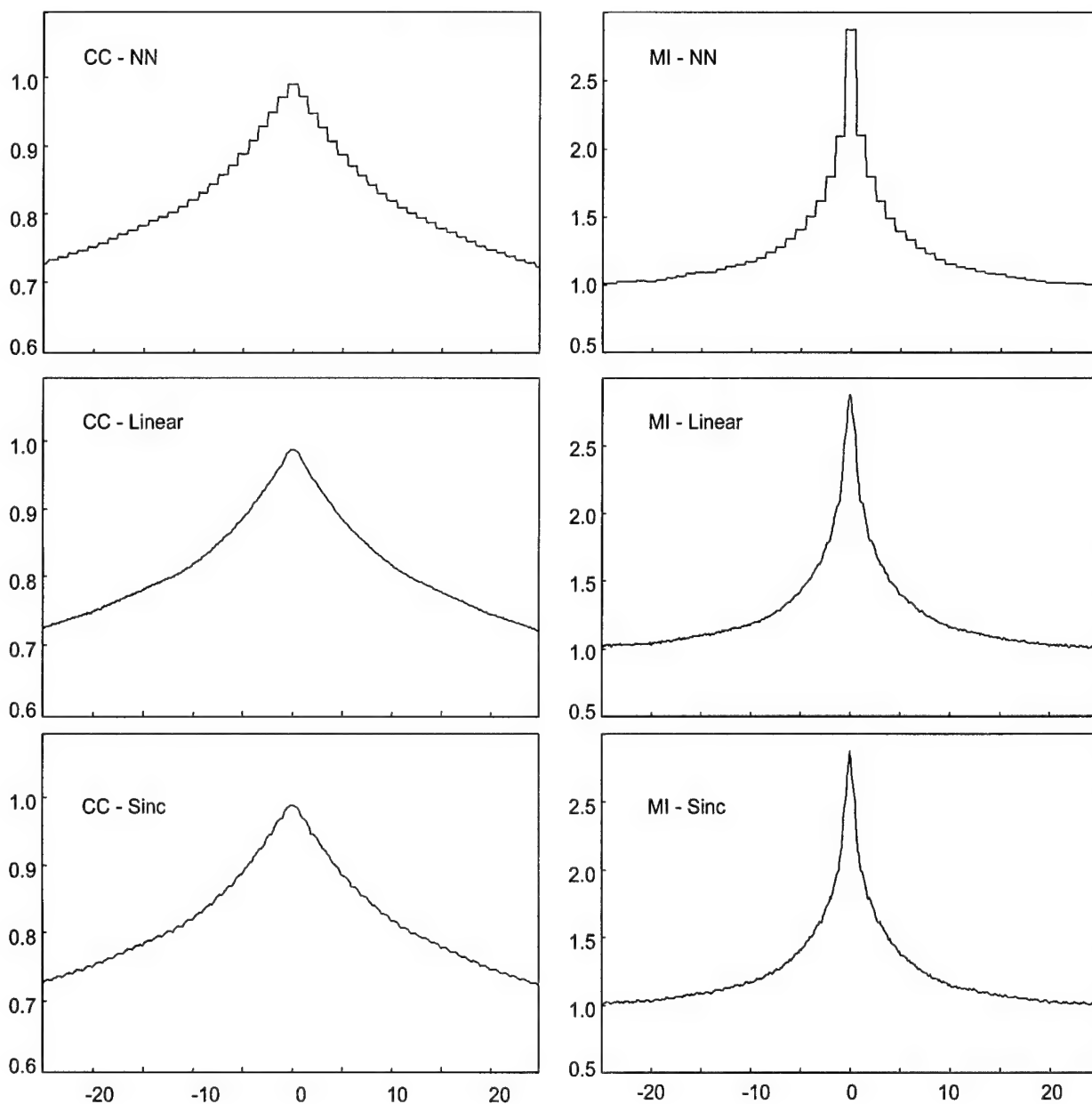
Figure 2. Similarity functions are plotted as a function of translations at full resolution. Many details are given in the legend of Figure 1. Again, CC is plotted in the left column. MI is plotted in the right column. From the top to bottom, nearest neighbor (NN), tri-linear, and re-normalized sinc interpolation methods are used to obtain floating images, respectively. MI curves are much peaked than CC, especially with sinc and tri-linear interpolation. The voxel is isotropic with 1.4 mm on a side. Image data are the same used in Figure 1.

2.4. Rigid Body Registration Algorithm with Special Features

The algorithm includes special features to improve robustness for registration of MR prostate images.[1] Suppose the iMRI image slice is the *reference* image, the matching slice extracted from the high-resolution MRI volume is the *floating* image. We use a multi-resolution approach and perform registration from low to high resolution. We use CC at the two lower resolutions because it gives fewer local maxima and because it can be calculated faster than MI. We use MI at full resolution because of its peaked surface. To avoid local maxima, we include a restarting feature where registration is restarted with randomly perturbed parameters obtained from a uniform distribution about the initial transformation values at the current resolution being used. The algorithm restarts until the absolute CC is above a threshold of 0.5 as experimentally determined or the maximum number of restarts is reached. Absolute CC is used rather than MI because it has a well-defined range between 0 and 1 and because it provides an independent check of the MI result at the highest resolution.[11]

We record all important results following an optimization cycle including the CC and/or MI values and the transformation parameters. At the end of processing at a lower resolution, we always select the transformation parameters having the maximum CC value. We then scale the translation parameters appropriately and assign the new parameters to be initial values at the next higher resolution. At the highest resolution, MI instead of CC is the similarity measure, and we select the final transformation parameters to be those having the maximum MI value.

Additional algorithm details are now described. For registration, we use rigid body transformation (three translations and three rotations). We chose tri-linear interpolation instead of sinc because it is much faster and because it has comparable performance, as observed from Figures 1 and 2. For optimization, we use the downhill simplex method of Nelder and Mead.[17] Optimization of similarity ends either when the maximum number of calculations is reached (typically 500) or the fractional change in the similarity function is smaller than a tolerance (typically 0.001). The input MRI volume is a 3D MR acquisition giving 256 x 256 x 128 nearly isotropic voxels over a field of view covering the whole pelvis. We create isotropic voxels of about 1.4 mm on a side using 3D linear interpolation. We use IDL (Interactive Data Language, Research System Inc., Boulder, CO.) as the programming language. We use an initial guess assuming an identity transformation, i.e., all initial translation and rotation parameters are zero, because the patient is normally oriented approximately the same way from one scan to the next. We set the maximum numbers of restarts at 10, 5, and 3, from low to high resolution, respectively.

2.5. Simulation of iMRI Slice Images

We used high-resolution MRI volumes to simulate iMRI images by creating thick slices and adding noise and receive coil inhomogeneity.[11] Clinically, we typically use an iMRI slice thickness of 4.0 - 6.0 mm. We averaged 3 slices 1.4 mm thick to create a 4.2 mm thick slice.

We added noise to the simulated iMRI image. MR noise is described by the Rician distribution,[18] but at reasonably high signal values, the noise is accurately approximated with Gaussian white noise.[19] We measured typical SNR on our open magnet system using a homogenous phantom and methods described elsewhere.[20,21] We then added Gaussian noise to the simulated iMRI slice images either to match the measured SNR or to give much greater noise to further stress registration. We report noise experiments using the SNR of the simulated slice images.

2.6. Registration Evaluation

Our standard evaluation method was to compare SV and VV registration. Since this relies on VV registration accuracy, we now review our previous results.[1] For volume pairs acquired over a short time span from a supine subject with legs flat on the table, prostates were well aligned and prostate centroid displacements were typically < 1 mm. The registration accuracy as determined from displacements of pelvic bony landmarks was 1.6 ± 0.2 mm. This error might be overestimated because it includes the uncertainty of locating the bony landmarks. The centroid error was slightly smaller because the prostate was at the volume center and rotation errors had less effect. From our success with VV prostate registration, we decided that we could obtain SV accuracy by comparing to VV registrations for those volume pairs having low VV registration error.

To compare SV and VV registration, we defined a rectangular volume of interest (VOI) just covering the prostate and calculated voxel displacements between the two registrations. To voxels within the VOI, we applied the transformations obtained by VV and by SV registrations. We then calculated the 3D displacements between the transformed voxels. The mean voxel distance was used as our metric of SV registration error. For the evaluation of algorithm robustness, we defined the SV registration as being *successful* when the 3D displacement was less than 2.0 mm.

We used the multiple visualization features of RegViz, a program created in IDL in our laboratory, to visually evaluate registration results. First, we manually segmented prostate boundaries in image slices and copied them to corresponding slices from the other volume. This enabled visual determination of the overlap of prostate boundaries over the entire volume. We applied the same method to evaluate pelvic registration. Second, color overlay displays were used to evaluate overlap of structures. One image was rendered in gray and the other in the "hot - iron" color scheme available in IDL. To visualize potential differences, it was quite useful to interactively change the contribution of each image using the transparency scale. Third, we used a sector display, which divided the reference and registered images into rectangular sectors and created an output image by alternating sectors from the two input images. Even subtle shifts of edges could be clearly seen.[1]

3. EXPERIMENTAL METHODS

3.1. Image Acquisition

All MRI volumes were acquired using a 1.5 T Siemens MRI system (Magnetom Symphony, Siemens Medical Systems, Erlangen, Germany). An 8-element phased array body coil was used to ensure coverage of the prostate with a uniform sensitivity. Typically two anterior and two posterior elements were enabled for signal acquisition. We used two different MR sequences. First, we used a 3D RF spoiled gradient echo steady state pulse sequence (FLASH) with TR/TE/flip parameters of 12/5.0/60 which give 256 x 256 x 128 voxels over a 330 x 330 x 256-mm field of view (FOV) to yield 1.3 x 1.3 x 2.0-mm voxels oriented to give the highest resolution for transverse slices. The acquisition time was 5.6 min. This sequence was good for pelvic imaging but was not ideal for the prostate. Second, we used a 3D rapid gradient echo sequence (PSIF) designed to acquire the spin-echo component of the steady state response, rather then the free induction decay. The spin echo component formed immediately prior to the RF pulse, and it was shifted toward the prior RF pulse through appropriate gradient waveform design. The sequence with 9.4/5.0/60 (TR/TE/flip) yielded 160 x 256 x 128 voxels over a 219 x 350 x 192-mm rectangular FOV and 1.4 x 1.4 x 1.5-mm voxels oriented to give the highest resolution for transverse slices. There was over sampling at 31% in the slice direction to reduce aliasing

artifacts. The acquisition time was 4.3 min. Most often, we used the second sequence, which gave excellent image contrast for the prostate and its surroundings.

3.2. Imaging Experiments

We acquired high-resolution MRI volumes from three volunteers. For each volunteer, three image volumes were obtained with an imaging session. Each volume was acquired with compatible conditions. Volunteers laid supine with legs flat similar to the position in routine MR scanning. Between volume acquisitions, volunteers got off the MRI table, stretched, and walked around to ensure that they would assume a different position when they laid back on the table. The coil array was centered on the prostate. All images of a volunteer were acquired with the same MRI acquisition parameters. In total, there are 9 pairs of high-resolution MRI volumes for registration.

4. RESULTS AND DISCUSSION

4.1. Slice Orientation and Position

As described in Section 2, we obtained relatively low noise, high-resolution MR images and simulated SV registration results. These data sets allowed us to test effects of noise and receive coil inhomogeneity in a controlled fashion. And, because we had substantial previous experience showing the accuracy of VV registration under comparable conditions, we could easily determine SV error by comparing results to VV registration.

We determined SV registration results for slices near the prostate in the three standard orthogonal orientations. Comparing to VV, mean and standard deviation registration errors across 9 volume pairs and 45 SV registration experiments were 0.4 mm ± 0.2 mm, 0.5 mm ± 0.2 mm, and 2.6 mm ± 1.6 mm for transverse, coronal and sagittal slices covering the prostate, respectively. Transverse slices worked best because they contain many relatively rigid anatomical structures. Coronal slices worked next best. Sagittal slices gave the largest error because they contained a large portion of the deformable bladder and rectum. We further found that transverse slices centered on the prostate produced better results than those above or below the prostate. Image slices above included the deformable bladder that could give an inconsistent structure from one volume to the next. Image slices below the prostate mainly contained muscle and fatty regions from the hips that could deform, again giving inconsistent image data.

4.2. Noise Level

The typical iMRI SNR under clinical conditions is about 25. Even when noise much exceeded this normal situation, registration results were quite good. A 100% success rate was achieved with an acceptance criterion of < 2.0 mm even when SNR was as bad as 10.

4.3. Robustness

The registration algorithm was quite robust for transverse slices covering the prostate. Using the nine volume pairs from three volunteers, the algorithm never failed for any transverse slice covering the prostate. In addition, the final registration result was insensitive to initial guesses within a large range, [-60, +60] mm for translations and [-20, +20] degrees for rotations. With the restarting algorithm, we even successfully registered slices as much as 80 mm from the

optimum. This working range is probably sufficient for clinical applications where we can ensure good starting values. Using the pelvic bones as markers and needle localization methods,[22] we should be able to position the prostate within about ± 20 mm. In addition, the patient normally lies supine in the MR bed with very little rotation (< ± 5 degrees).

4.4. Comparison of Different Interpolation Methods

Computation time and registration accuracy are two main factors to consider when choosing interpolation methods. Using tri-linear interpolation, the time for an SV registration was typically about 5 sec on a Pentium IV, 1.8 GHz CPU, with 1Gbyte of memory. If the re-normalized sinc interpolation method was used, the time was ˜ 10 min, a duration not acceptable for our application. The algorithm was written in IDL and could probably be made faster in a lower level language such as C. We did not use nearest neighbor because of the obvious insufficient accuracy as induced from its flat peak of the similarity curves in Figure 2. A call to the Simplex optimization typically resulted in 50 to 105 similarity evaluations before the tolerance value (0.001) was reached.

4.5. Comparison of Three Alignment Techniques

When registering iMRI image slices with high-resolution MR volumes, we compared three alignment techniques: (1) an iMRI thick slice to an MR thin slice, (2) an iMRI thick slice to the average of three MR thin slices, and (3) three copies of the iMRI thick slice to three MR thin slices. The second and third methods were tested because they were thought to better match the resolution of the high resolution volume to the the thick slide. There were no significant differences (voxel displacements < 0.1 mm) among the three methods. Hence, we used the first method because of its simplicity.

5.   CONCLUSION

The slice to volume registration algorithm is quite robust for transverse slice images covering the prostate. Since live-time iMRI images are used for guidance and registered images are used for adjunctive information, the registration accuracy is very probably adequate. It is quite feasible to include previously acquired high-resolution MRI or nuclear images into iMRI-guided treatment procedures. We are beginning to explore this application in animal experiments.

ACKNOWLEDGEMENTS

REFERENCE

1   B.W.Fei, A.Wheaton, Z.Lee, J.L.Duerk, and D.L.Wilson, "Automatic MR volume registration and its evaluation for the pelvis and prostate," *Physics in Medicine and Biology*, vol. 47, pp. 823-838, 2002.

2   M.V.Herk, A.Bruce, A.P.G.Kroes, T.Shouman, A.Touw, and J.V.Lebesque, "Quantification of organ motion during conformal radiotherapy of the prostate by three dimensional image registration," *International Journal of Radiation Oncology Biology Physics*, vol. 33, pp. 1311-1320, 1995.

3 R.K.Tenhaken, J.D.Forman, D.K.Heimburger, A.Gerhardsson, D.L.Mcshan, C.Pereztamayo, S.L.Schoeppel, and A.S.Lichter, "Treatment planning issues related to prostate movement in response to differential filling of the rectum and bladder," *International Journal of Radiation Oncology Biology Physics*, vol. 20, pp. 1317-1324, 1991.

4 H.Gray. *Anatomy, Descriptive and Surgical (The classic collector's edition)*. New York: Gramercy Books, pp. 1010, 1977.

5 B.Kim, J.L.Boes, P.H.Bland, T.L.Chenevert, and C.R.Meyer, "Motion correction in fMRI via registration of individual slices into an anatomical volume," *Magnetic Resonance in Medicine*, vol. 41, pp. 964-972, 1999.

6 Rohlfing, Torsten, West, Jay B., Beier, Jürgen, Liebig, Thomas, Taschner, Christian A., and Thomale, Ulrich Wilhelm. Registration of functional and anatomical MRI: Accuracy assessment and application in navigated neurosurgery. Computer Aided Surgery 5(6), 414-425. 2000.

7 T.S.Kim, M.Singh, W.Sungkarat, C.Zarow, and H.Chui, "Automatic registration of postmortem brain slices to MRI reference volume," *IEEE Transactions on Nuclear Science*, vol. 47, pp. 1607-1613, 2000.

8 J.Zhengping and P.H.Mowforth, "Mapping between MR brain images and voxel model," *Medical Informatics*, vol. 16, pp. 183-193, 1991.

9 B.W.Fei, A.Wheaton, Z.Lee, K.Nagano, J.L.Duerk, and D.L.Wilson, "Robust registration algorithm for interventional MRI guidance for thermal ablation of prostate cancer," Proceedings of SPIE Medical Imaging on Visualization, Display, and Image-Guided Procedures, vol. 4319, pp. 53-60, 2001.

10 B.W.Fei, J.L.Duerk, and D.L.Wilson, "Automatic 3D Registration for Interventional MRI-Guided Treatment of Prostate Cancer," *Computer Aided Surgery*, (In Press), 2003.

11 B.W.Fei, J.L.Duerk, D.T.Boll, J.S.Lewin, and D.L.Wilson, "Slice to volume registration and its potential application tointerventional MRI guided radiofrequency thermal ablation of prostate cancer," *IEEE Transactions on Medical Imaging*, (In Press), 2003.

12 B.W.Fei, D.T.Boll, J.L.Duerk, and D.L.Wilson, "Image registration for interventional MRI-guided minimally invasive treatment of prostate cancer,"Proceedings of the Second Joint EMBS/BMES Conference, Houston, TX, USA, October 23-26, pp. 1185, 2002.

13 F.Maes, A.Collignon, D.Vandermeulen, G.Marchal, and P.Suetens, "Multimodality image registration by maximization of mutual information," *IEEE Transactions on Medical Imaging*, vol. 16, pp. 187-198, 1997.

14 W.H.Press, S.A.Teukolsky, W.T.Vellerling, and B.P.Flannery. *Numerical Recipes in C: The Art of Scientific Computing, Second Edition*. New York: The Press Syndicate of the Cambridge University, 1992.

15 N.A.Thacker, A.Jackson, D.Moriarty, and E.Vokurka, "Improved quality of re-sliced MR images using re-normalized sinc interpolation," *Journal of Magnetic Resonance Imaging*, vol. 10, pp. 582-588, 1999.

16 J.V.Hajnal, N.Saeed, E.J.SOAR, A.Oatridge, I.R.Young, and G.M.Bydder, "A registration and interpolation procedure for subvoxel matching of serially acquired mr-images," *Journal of Computer Assisted Tomography*, vol. 19, pp. 289-296, 1995.

17 J.Nelder and R.A.Mead, "A simplex method for function minimization," *Computer Journal*, vol. 7, pp. 308-313, 1965.

18 A.Macovski, "Noise in MRI," *Magnetic Resonance in Medicine*, vol. 36, pp. 494-497, 1996.

19 R.C.Gregg and R.D.Nowak, "Noise removal methods for high resolution MRI," *IEEE Nuclear Science Symposium*, vol. 2, pp. 1117-1121, 1997.

20 R.M.Henkelman, "Measurement of signal intensities in the presence of noise in MR mages," *Medical Physics*, vol. 12, pp. 232-233, 1985.

21 L.Kaufman, D.M.Kramer, L.E.CROOKS, and D.A.Ortendahl, "Measuring signal-to-noise ratios in MR imaging," *Radiology*, vol. 173, pp. 265-267, 1989.

22 J.S.Lewin, J.L.Duerk, V.R.Jain, C.A.Petersilge, C.P.Chao, and J.R.Haaga, "Needle localization in MR-guided biopsy and aspiration: Effects of field strength, sequence design, and magnetic field orientation," *American Journal of Roentgenology*, vol. 166, pp. 1337-1345, 1996.

IMAGE REGISTRATION FOR INTERVENTIONAL MRI-GUIDED MINIMALLY INVASIVE TREATMENT OF PROSTATE CANCER

Baowei Fei [1], Daniel T. Boll [2], Jeffery L Duerk [1,2], David L Wilson [1,2]

[1] Department of Biomedical Engineering, Case Western Reserve University, Cleveland, OH, USA
[2] Department of Radiology, University Hospitals of Cleveland, Cleveland, OH, USA

Abstract - **We are investigating automatic image registration methods that can be used for interventional magnetic resonance imaging (iMRI) guided radiofrequency (RF) thermal ablation of prostate cancer. We tested the ability of slice-to-volume registration between iMRI slice images and high-resolution MRI volumes. Images were acquired from a conventional 1.5 T and an interventional 0.2 T MRI system. We evaluated the registration quality by calculating 3D displacement on a voxel-by-voxel basis over a volume of interest between slice-to-volume registration and volume-to-volume registration that was previously shown to be quite accurate. Visual inspections such as color overlay and contour overlap were also used for registration evaluation. More than 300 registration experiments were performed on MR images of volunteers. Results showed that the registration was quite robust and accurate (< 2 mm) for the transverse images covering the prostate.**

Keywords: medical imaging, image registration, interventional magnetic resonance imaging (iMRI), prostate cancer.

I. INTRODUCTION

We currently use interventional MRI as guidance for RF thermal ablation of abdominal cancer. In the case of the prostate, the tumor is not reliably identified with MRI. Other functional imaging techniques are required. Potential methods include SPECT imaging and MR spectroscopy. To incorporate the functional images with interventional MRI tumor targeting, one can first register the low-resolution functional images with high-resolution MR volumes. Then by registering high-resolution MR volume with nearly real-time iMRI acquisitions, we can map both the functional data and high-resolution anatomic information to interventional images for improved tumor targeting. From our previous success with MR volume-to-volume (VV) registration [1] and slice-to-volume (SV) registration using simulated iMRI images [2], we are further testing the SV registration ability using real iMRI images in this study.

II. MATERIALS AND METHODS

We acquired high-resolution MR volumes from three volunteers using a 3D rapid gradient echo sequence (PSIF) with 9.4/5.0/60 (TR/TE/FA) and a conventional 1.5 T MR system (Siemens Magnetom Symphony,Erlangen, Germany). Volunteers laid supine similar to the diagnostic position in routine MR scanning. Two volumes were acquired for each volunteer. Volume images were normally 256x256x128 with the voxel size of 1.4x1.4x1.5-mm.

We also acquired images from the same volunteers using a clinical 0.2 T C-arm interventional MR system (Siemens Open Symphony, Erlangen, Germany). Volunteers were supine with the legs supported similar to the lithotomy position used in prostate therapies. This position should provide access for needle insertion in brachytherapy or RF thermal ablation. We used a 3D PSIF with 25/13/60 (TR/TE/FA) for volume acquisitions and 2D PSIF with 15.2/7.4/45 (TR/TE/FA) for slice acquisitions. Slice images were 128x128 with pixel size of 2.8x2.8-mm and with effective slice thickness of 5 mm. For each volunteer, we acquired 2 volumes and 25 slices covering the prostate. They included 15 transverse, 5 coronal, and 5 sagittal slices. We called these images as iMRI volume or real iMRI slices. We call them real iMRI slices to differentiate from previous experiments on simulated iMRI slices.

We performed registration experiments using an automatic algorithm with special features important for robustness for MR pelvic images [1]. First, we performed VV registration between high-resolution MRI and iMRI volumes. Second, we extracted slices from an iMRI volume and registered the slices with the high-resolution MRI volume. We evaluated SV registrations by calculating 3D displacement on a voxel-by-voxel basis over a volume of interest (VOI) between SV and VV registration [2]. Third, we tested the SV registration between real iMRI slices and high-resolution MRI volumes. We used visual inspections such as color overlay and contour overlap to evaluate the SV registration quality.

III. RESULTS

We performed over 300 registration experiments. The VV registration of MRI and iMRI volumes is quite accurate with prostate centroid typically less than 1 mm. As compared to the VV results, the VOI displacement of SV registration is less than 2 mm for all transverse slices covering the prostate. Most coronal slices (86%) gave an accuracy of less than 2.5 mm. Nearly half of sagittal slices (46%) gave an accuracy of less than 5 mm. This suggested that transverse slices were the best. Inspection indicates that bladder and/or rectal filling interfered with registration of coronal and sagittal slices because of deformation. Visual inspection of SV registration between iMRI slices and high-resolution MRI volumes demonstrated similar results.

IV. CONCLUSION

It is quite feasible to use SV image registration to aid the application of interventional MRI-guided RF thermal ablation of prostate cancer. We are beginning to explore these applications in dog experiments.

REFERENCES

[1] B. Fei, A. Wheaton, Z. Lee, J.L. Duerk, D.L. Wilson. "Automatic MR volume registration and its evaluation for the pelvis and prostate." *Physics in Medicine and Biology,* 47: 823-838, 2002.
[2] B. Fei, A. Wheaton, Z. Lee, K. Nagano, J.L. Duerk, D.L. Wilson. "Robust registration algorithm for interventional MRI guidance for thermal ablation of prostate cancer." *Proceedings of SPIE Medical Imaging on Visualization, Display, and Image-Guided Procedures,* 4319: 53-60, 2001.

Three-Dimensional Warping Registration
of the Pelvis and Prostate

Baowei Fei [a*], Corey Kemper [a], David L Wilson [a b**]

[a] Department of Biomedical Engineering, Case Western Reserve University, OH 44106
[b] Department of Radiology, University Hospitals of Cleveland, OH 44106

ABSTRACT

We are investigating interventional MRI guided radiofrequency (RF) thermal ablation for the minimally invasive treatment of prostate cancer. Among many potential applications of registration, we wish to compare registered MR images acquired before and immediately after RF ablation in order to determine whether a tumor is adequately treated. Warping registration is desired to correct for potential deformations of the pelvic region and movement of the prostate. We created a two-step, three-dimensional (3D) registration algorithm using mutual information and thin plate spline (TPS) warping for MR images. First, automatic rigid body registration was used to capture the global transformation. Second, local warping registration was applied. Interactively placed control points were automatically optimized by maximizing the mutual information of corresponding voxels in small volumes of interest and by using a 3D TPS to express the deformation throughout the image volume. Images were acquired from healthy volunteers in different conditions simulating potential applications. A variety of evaluation methods showed that warping consistently improved registration for volume pairs whenever patient position or condition was purposely changed between acquisitions. A TPS transformation based on 180 control points generated excellent warping throughout the pelvis following rigid body registration. The prostate centroid displacement for a typical volume pair was reduced from 3.4 mm to 0.6 mm when warping was added.

Keywords: Warping image registration, medical imaging, interventional magnetic resonance imaging (iMRI), mutual information, thin plate spline, prostate cancer.

1. INTRODUCTION

We are investigating three-dimensional (3D) image registration to be used in applications of prostate cancer diagnosis, staging, and therapy. In particular, we are interested in applications related to the minimally invasive interventional magnetic resonance imaging (iMRI) guided treatment of prostate cancer. At our institution, we currently use iMRI on a low-field open magnet system to guide radiofrequency (RF) thermal ablation of abdominal cancer,[1,2] and we are investigating this method for prostate cancer treatment. A unique feature of iMRI-guided thermal ablation is that therapy can be monitored with MR either by acquiring images of the thermally induced lesion or by measuring temperature. In addition, MR imaging of the prostate is desirable because it more accurately delineates the prostate than does CT,[3,4] which can overestimate the prostate volume,[5,6] and ultrasound, which has a tendency to underestimate the extent of lesions.[7]

Several applications in prostate imaging require registration. First, comparison of registered MR images acquired before and immediately after RF ablation can be used to determine whether a tumor is adequately treated. This is

---

Proceedings of SPIE Vol. 4684 (2002) @ 2002 SPIE × 1605-7422/01/$15.00
Image Processing, Milan Sonka, J. Michael Fitzpatrick, Editor,

528

particularly helpful in instances where the edematous response to treatment can be confused with a highly perfused tumor. Second, registration of serial examinations can be used to follow regression/progression of tumor. Third, incorporating the functional, biochemical images into the iMRI paradigm will aid image-guided treatments, as recently reported by us.[8,9]

Several reports describe methods for registration in the pelvis or prostate.[10-15] These methods required either segmentation or visual identification of structures and they were based on rigid body transformation. We recently reported a mutual information rigid body transformation method for prostate registration.[16] For volume pairs acquired over a short time span from a supine subject with legs flat on the table, registration accuracy of both prostate centroids (typically < 1 mm) and bony landmarks (average 1.6 mm) was on the order of a voxel ($\approx$ 1.4 mm). We obtained somewhat larger prostate registration errors of about 3.0 mm when volume pairs were obtained under very different conditions, e.g., legs flat and legs raised, or with and without bladder or rectal filling. Rigid body registration of the pelvis cannot follow prostate movements due to changes in the postures of legs and deformation of the bladder and rectum, as reported by us [16] and others.[14,17]

There are a number of reports on warping registration.[18-20] These applications were mainly on the brain and breast; and far few described results for the abdomen.[21,22] For our application, we are developing voxel-based warping registration in the pelvis and prostate.

There are challenges to the pelvis and prostate registration. First, pelvic regions can change shape significantly, unlike the brain to which registration has been most often applied. Different patient positions such as displacement of the legs can cause the movement and deformation of internal organs. Second, the normal prostate is a small organ that when healthy measures only about 3.8 cm in its widest dimension transversely across the base.[23] Third, the prostate might move relative to the pelvic bones due to changes in bladder and rectal filling.[14,17]

In the present study, we perform experiments to determine if warping can improve registration of pelvic MR. High quality, 3D MR image volumes from a commercially available 1.5 T system are used to determine the best possible results. We examine conditions found in the potential clinical applications described previously. We will qualitatively and quantitatively compare results of warping and rigid body registration using 9 volume pairs from three volunteers.

2. REGISTRATION ALGORITHM

2.1. Similarity Measurements

We used two similarity measures, mutual information and correlation coefficient (CC), in our registration. One volume R is the *reference*, and the other F is *floating*. Their mutual information $MI(R,F)$ is given below.[24]

$$MI(R,F) = \sum_{r,f} p_{RF}(r,f) \log \frac{p_{RF}(r,f)}{p_R(r) \cdot p_F(f)}$$

The joint probability $p_{RF}(r,f)$ and the marginal probabilities $p_R(r)$ of the reference image and $p_F(f)$ of the floating image, can be estimated from the normalized joint intensity histograms. When two images are geometrically aligned, MI is maximal.[24] The correlation coefficient $CC(R,F)$ is given below.[25]

$$CC(R,F) = \frac{\sum (R(r) - \overline{R}(r))(F(f) - \overline{F}(f))}{\sqrt{\sum (R(r) - \overline{R}(r))^2 \sum (F(f) - \overline{F}(f))^2}}$$

Here $\overline{R}(r)$, $\overline{F}(f)$ denote the average intensities of the reference and floating volumes and the summation includes all voxels within the overlap of both volumes.

2.2. Rigid Body Registration Algorithm with Special Features

The rigid body registration algorithm includes special features to improve robustness for MR pelvic images. Reference is matched to the *reformatted* volume obtained by transforming the floating volume. We use a multi-resolution approach and perform registration from low to high resolution. At low resolution, we resample both images at 1/4 or 1/2 number of voxels along each linear dimension, respectively. A simplex algorithm varies the six rigid body transformation parameters (three translations and three angles) to optimize the similarity measure.[26] We use CC at the two lower resolutions because it gives fewer local maximums [8,9,16] and because it can be calculated faster than MI. We use MI at full resolution because the peaked similarity function gives a more precise solution than CC.[9,16] To avoid local maximums, we include a restarting feature where registration is restarted with randomly perturbed parameters. The algorithm restarts until the absolute CC is above an experimentally determined threshold or the maximum number of restarts is reached. Absolute CC is used for the restart test rather than MI because CC has fewer problems with local and incorrect global maximums at low resolution.[9,16]

We record all important results following an optimization cycle including the CC and/or MI values, the number of restarts, and the transformation parameters. At the end of processing at a lower resolution, we always select the transform-ation parameters having the maximum CC value. We then scale the translation parameters appropriately and assign the new parameters to be initial values at the next higher resolution. At the highest resolution, we select the final transformation parameters to be those with the maximum MI value.

Typical parameter values are now described. We use an initial guess at the lowest resolution of all zeros because the patient is normally oriented approximately the same way from one scan to the next. Based on experience, we set the CC thresholds at 0.50, 0.55, and 0.65, and the maximum numbers of restarts at 10, 5, and 3, from low to high resolution, respectively.

2.3. Warping Registration Using Optimized Control Points

The warping registration algorithm includes three major steps: control point (CP) selection, control point optimization, and thin plate spline (TPS) warping. Again, the unchanging volume is the *reference*, and the one to be warped is *floating*.

The manual selection of CP's is an important step. We used *RegViz*, a program written in IDL (Interactive Data Language, Research System Inc., Boulder, CO) and created in our laboratory for visualizing and analyzing image volumes. Following rigid body registration, the aligned two volumes are displayed in two rows slice-by-slice. Corresponding CP's in the two volumes are placed using a cursor, and sometimes they are in different image slices. The 3D coordinates are automatically stored in a file. Because of the optimization that occurs later, the correspondence can be up to 15 mm or ≈ 10 voxels in error. More experience with CP selection is described in Results. Typically, we used 180 CP's for a volume with 256 x 256 x 140 isotropic voxels.

The next step of the warping algorithm is the CP optimization. We define a small cubic volume of interest (VOI) centered at each CP. The VOI can be 16 or 64 voxels on a side. A simplex optimization algorithm varies the x, y, and z transformation parameters of the floating VOI until the mutual information with the reference VOI is optimized. Each control point is optimized independently.

The final major step is to warp the floating volume using the optimal CP's coordinates to establish a TPS transformation. We extended the two-dimensional TPS transformation method reported by Bookstein[27] to three dimensions in a manner similar to that of Davis et al.[19]

2.4. Additional Details

There are several preprocessing details. The input MRI volume is a 3D MR acquisition giving 256 x 256 x 128 nearly isotropic voxels over a field of view covering the whole pelvis. We create isotropic voxels of about 1.4 mm on a side using 3D linear interpolation. From the top and bottom of the volume, we optionally crop transverse slices that are over 35 mm away from the prostate rim. Cropping is done to remove slices having reduced brightness due to sensitivity fall off from the receiver coils and/or artifacts from a small field of view. For both rigid body registration and VOI optimization, we use trilinear interpolation. Optimization of similarity ends either when the maximum number of calculations is reached (typically 500) or the fractional change in the similarity function is smaller than a tolerance (typically 0.001). We use IDL as the programming language.

3. EXPERIMENTAL METHODS

3.1. Image Acquisition

All MRI volumes were acquired using a 1.5 T Siemens MRI system (Magnetom Symphony, Siemens Medical Systems, Erlangen, Germany). An 8-element phased array body coil was used to ensure coverage of the prostate with a uniform sensitivity. Typically two anterior and two posterior elements were enabled for signal acquisition. We used two different MR sequences. First, we used a 3D RF spoiled gradient echo steady state pulse sequence (FLASH) with TR/TE/flip parameters of 12/5.0/60 which give 256 x 256 x 128 voxels over a 330 x 330 x 256-mm field of view (FOV) to yield 1.3 x 1.3 x 2.0-mm voxels oriented to give the highest resolution for transverse slices. The acquisition time was 5.6 min. This sequence was good for pelvic imaging but was not ideal for the prostate. Second, we used a 3D rapid gradient echo sequence (PSIF) designed to acquire the spin-echo component of the steady state response, rather then the free induction decay. The spin echo component formed immediately prior to the RF pulse, and it was shifted toward the prior RF pulse through appropriate gradient waveform design. The sequence with 9.4/5.0/60 (TR/TE/flip) yielded 160 x 256 x 128 voxels over a 219 x 350 x 192-mm rectangular FOV and 1.4 x 1.4 x 1.5-mm voxels oriented to give the highest resolution for transverse slices. There was over sampling at 31% in the slice direction to reduce aliasing artifacts. The acquisition time was 4.3 min. Most often, we used the second sequence, which gave excellent image contrast for the prostate and its surroundings.

3.2. Imaging Experiments

We acquired 3D MRI volume images from three normal volunteers under a variety of conditions simulating anticipated conditions in diagnostic and treatment applications. Before image acquisition, each volunteer drank water and had a relatively *full bladder*. In the *diagnostic position,* the subject laid supine throughout MR scanning. In the *treatment position,* the subject was supine, and his legs were supported at 30°-60° relative to the horizon and separated in a "V" with an angle of 60°-90° between two legs. This position should provide access for needle insertion in brachytherapy or RF thermal ablation. In some experiments, the subject micturated to create an *empty bladder* prior to imaging. For each subject, image volumes were obtained on the same day within one imaging session. Between volume acquisitions,

volunteers got off the MRI table, stretched, and walked around to ensure that they would assume a different position when they laid back on the table. All images of a volunteer were acquired with the same MRI acquisition parameters so as to ensure very similar gray values. In total, there are 3 volumes for each volunteer.

3.3. Volume Pairs for Registration

We registered 9 volume pairs under different conditions. Three pairs are *treatment-diagnosis;* three pairs are *full-empty bladder;* and three pairs are *diagnosis-diagnosis*. Rigid body and warping registration were applied to each of the volume pairs. Results were evaluated as described next.

3.4. Registration Evaluation

We used the multiple visualization features of RegViz to visually evaluate registration results. First, we manually segmented prostate boundaries in image slices and copied them to corresponding slices from the other volume. This enabled visual determination of the overlap of prostate boundaries over the entire volume. We applied the same method to evaluate pelvic registration. Second, color overlay displays were used to evaluate overlap of structures. One image was rendered in gray and the other in the "hot - iron" color scheme available in IDL. To visualize potential differences, it was quite useful to interactively change the contribution of each image using the transparency scale. Third, we used a sector display, which divided the reference and registered images into rectangular sectors and created an output image by alternating sectors from the two input images. Even subtle shifts of edges could be clearly seen.[16]

Voxel gray value measures were calculated as indicators of regitration quality. Mutual information and correlation coefficient between registered volumes were computed. The higher the MI values, the more likely the two volumes are well registered. Since volumes to be registered were acquired using the same acquisition parameters, high absolute CC values were obtained when registration was good.[20] Because voxel intensities were comparable, we created difference images and calculated statistics such as the voxel mean and standard deviation following registration.

Finally, to assess prostate registration error, we measured potential displacements of the 3D centroid of the prostate. We used RegViz to manually segment the prostate across all image slices and calculated the 3D centroid. A similar method was used by West et al. to evaluate rigid body registration of the brain.[28]

4. RESULTS AND DISCUSSION

4.1. Control Point Selection

In well over 50 registration experiments, we investigated the number and placement of CP's on warping registration quality. We quickly determined that many CP's are required in order to get good visual matching of our very high-resolution MR images showing great anatomical detail, especially when large deformations occurred as in the case of diagnosis-treatment. We progressively increased the number of CP's from 15 to 250. We found that less than 120 CP's did not produce smooth and reasonable warps. Warping with 180 CP's excellently approximated the deformation of the pelvis and internal organs. More than 220 CP's did not give significant improvement but needed more time for manual selection and optimization. As a result of this experience, we modified the registration method to be more suitable for many CP's (see Section 2).
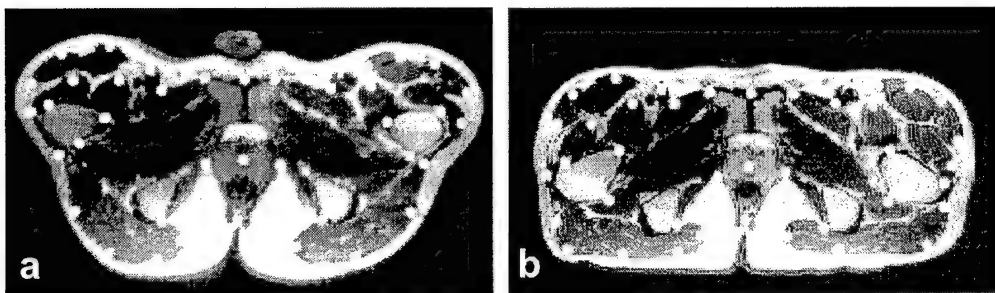
Figure 1. Control point selection when images are acquired in the treatment and diagnostic positions. Image (a) is from the reference volume acquired in the treatment position with legs raised. Image (b) is to be warped and is from the volume acquired in the diagnostic position with the subject supine on the table. Transverse slices best show the deformations, especially at the legs. As described in the text, control points indicated by the white dots are selected around the pelvic surface and the prostate. Each control point is located at one voxel but displayed much bigger for better visualization. Volumes are from volunteer S2.

We also determined that it was necessary to place the CP's in strategic locations, and some rules follow. For registration of treatment and diagnostic image volumes, most CP's were selected using transverse slices because they best showed the pelvic displacement when moving the legs to the treatment position (Figure 1). About 30 CP pairs were placed near edge and point features having recognizable correspondence on each of 5-8 transverse slices with a z interval of ~ 8 mm, covering the entire prostate region. Additionally, we placed about 25 CP's from sagittal slices because they provided other structures that can be missed in the transverse images. It was also important to include CP's from organs other than the prostate because they constrained warps. We always placed CP's at critical regions such as the prostate center, pelvic surface, bladder border, and rectal walls.

4.2. Registration Quality of Warping and Rigid Body Registration

In Figure 2, we compare warping and rigid body registration for a typical volume pair in the treatment and diagnostic positions. Using rigid body registration, there is significant misalignment throughout large regions in the pelvis (Figure 2a) that is greatly reduced with warping (Figure 2b). Note that warping even allows the outer surfaces to match well. Other visualization methods such as two-color overlays and difference images, quickly show matching of structures without segmentation but do not reproduce well on a printed page. The prostate 3D centroid calculated from segmented images displaced by only 0.6 mm, or 0.4 voxels, following warping. Following rigid body registration, the prostate was misaligned with a displacement to the posterior of ≈ 3.4 mm when in the treatment position

We examined the effect of conditions such as bladder and rectal filling that might change from one imaging session to the next (not shown). Contour overlap showed that warping registration perfectly aligns the prostate while rigid body does not. In addition, rigid body registration does not align the bladder. With warping, the bladder perfectly matches the reference. Other visualization methods showed excellent alignment of internal and surface edges. Difference images show that warping greatly improves alignment of internal structures as compared to rigid body registration.

We also examined volume pairs with both volumes acquired in the diagnostic position under comparable conditions. In all such cases, rigid body registration worked as well as warping. There were no noticeable deformations in the pelvis, and prostate centroids typically displaced less than 1.0 mm between the two registered volumes.
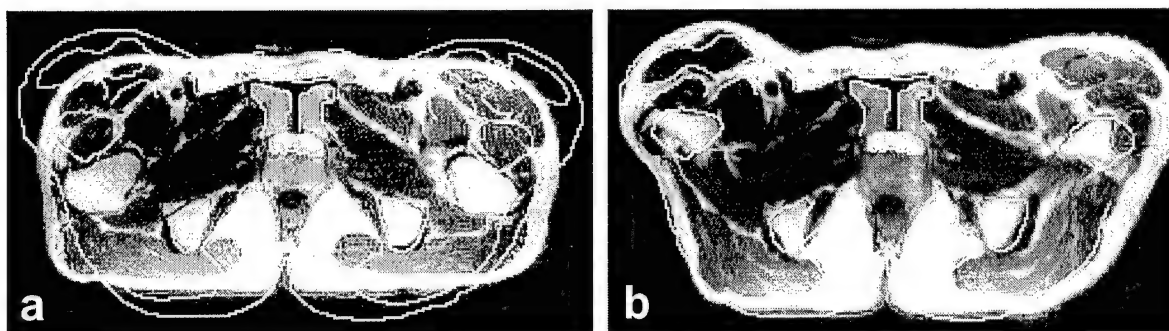
Figure 2. Comparison of warping and rigid body registration for volumes acquired in the treatment and diagnostic positions. Image (a) is from the floating volume acquired in the diagnostic position following rigid body registration. Pelvic contours manually segmented from the reference show significant misalignment. Image (b) is from the floating volume acquired in the diagnostic position following warping registration. The misalignment is greatly improved with warping. Images are transverse slices from subject S2.
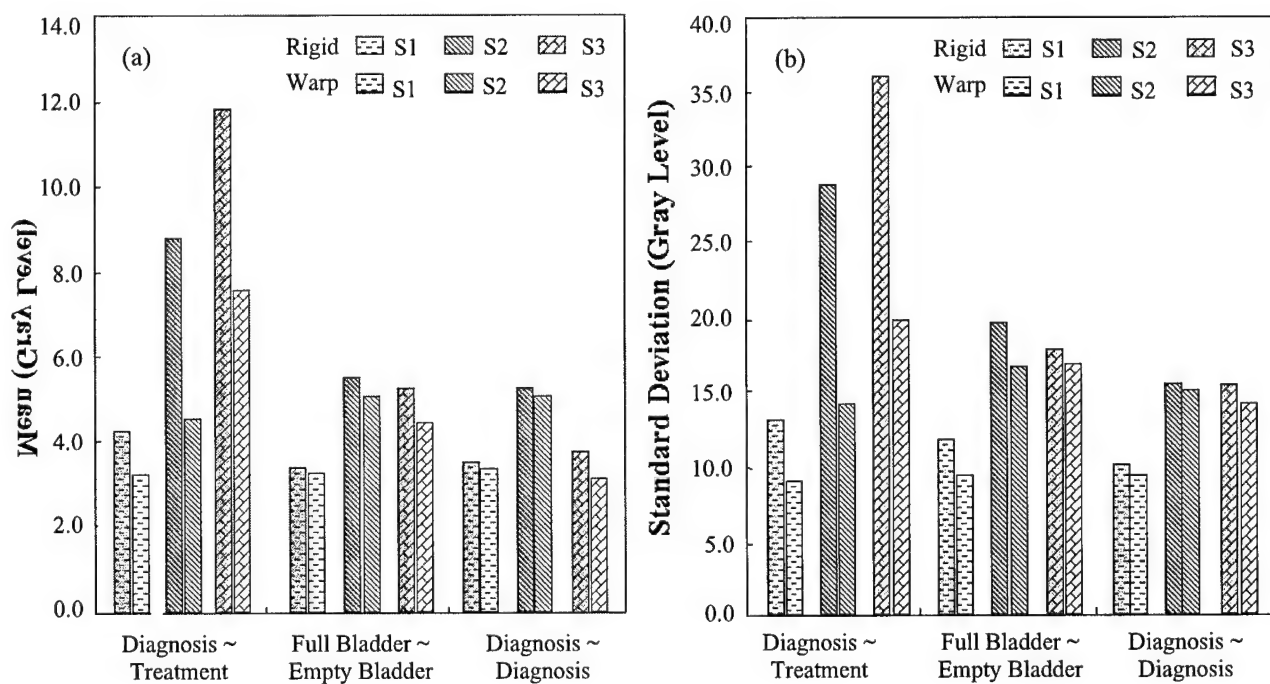

Figure 3. Image statistics of absolute intensity difference images for rigid body and warping registration. The mean (a) and standard deviation (b) are plotted. See the legend of Figure 3 for other details. Warping decreased the mean and standard deviation in each case, but the most significant decreases occurred in the case of the treatment-diagnosis volume pairs.

4.3. Quantitative Evaluation of Warping Registration

Statistics of image differences following rigid body and warping registration are shown in Figure 3. Warping reduces the absolute intensity difference between corresponding voxels (Figure 3a). We did not use non-absolute differences as evaluation criteria because the positive and negative differences can be canceled. The standard deviation of absolute difference is also reduced (Figure 3b). We also calculated the correlation coefficient and mutual information values between registered volumes. Warping increased CC and MI values in every case.

4.4. Algorithmic Robustness and Efficiency

The rigid body algorithm gives robust registration. Because of two principal design features, the algorithm is quite robust and accurate for volume pairs acquired in the same positions and with comparable conditions.[16] First, using both CC and MI at different resolutions was an important feature that increased robustness. CC gave fewer local minimums at low resolutions and MI was more accurate at high resolution.[8,9] Second, the restarting mechanism was also quite important. Without restarting, we found that registrations sometimes failed in cases of volumes with large mismatches and significant deformation. Even these cases resulted in a proper solution when restarting was employed. The time for rigid body registration, typically 5 minutes on a Pentium IV, 1.8 GHz CPU, with 1.0 GBytes of memory, could be greatly improved with C rather than IDL.

The interactive warping registration algorithm is designed to be very computationally efficient for TPS warping with hundreds of CP's. First, the optimization of small VOI's is very fast. Second, we optimized each CP separately because the optimization of three parameters (x, y, and z) is simple and fast. Third, we applied the TPS transformation once to the final, optimal CP's; this saved considerable time. Using the same computer above, for a volume with 256x256x140 voxels and 180 CP's, the warping registration typically takes about 15-45 minutes depending on the VOI size. If we were to use optimized C code, the total time for rigid body and warping registration should reduce to within 5 minutes.

5. CONCLUSION

The mutual information warping registration works better than rigid body registration whenever the subject position or condition is greatly changed between acquisitions. It will probably be a useful tool for many applications in prostate diagnosis, staging, and therapy. It is fast for hundreds of control points and can be applied to a variety of applications.

ACKNOWLEDGEMENTS

REFERENCES

1   J.S.Lewin, C.F.Connell, J.L.Duerk, Y.C.Chung, M.E.Clampitt, J.Spisak, G.S.Gazelle, and J.R.Haaga, "Interactive MRI-guided radiofrequency interstitial thermal ablation of abdominal tumors: Clinical trial for evaluation of safety and feasibility," *Journal of Magnetic Resonance Imaging*, vol. 8, pp. 40-47, 1998.

2   E.M.Merkle, J.R.Shonk, J.L.Duerk, G.H.Jacobs, and J.S.Lewin, "MR-guided RF thermal ablation of the kidney in a porcine model," *American Journal of Roentgenology*, vol. 173, pp. 645-651, 1999.

3   K.Kagawa, W.R.Lee, T.E.Schultheiss, M.A.Hunt, A.H.Shaer, and G.E.Hanks, "Initial clinical assessment of CT-MRI image fusion software in localization of the prostate for 3D conformal radiation therapy," *International Journal of Radiation Oncology Biology Physics*, vol. 38, pp. 319-325, 1997.

4   M.Milosevic, S.Voruganti, R.Blend, H.Alasti, P.Warde, M.McLean, P.Catton, C.Catton, and M.Gospodarowicz, "Magnetic resonance imaging (MRI) for localization of the prostatic apex: comparison to computed tomography (CT) and urethrography," *Radiotherapy and Oncology*, vol. 47, pp. 277-284, 1998.

5   M.Roach, P.FaillaceAkazawa, C.Malfatti, J.Holland, and H.Hricak, "Prostate volumes defined by magnetic resonance imaging and computerized tomographic scans for three-dimensional conformal radiotherapy," *International Journal of Radiation Oncology Biology Physics*, vol. 35, pp. 1011-1018, 1996.

6   C.Rasch, I.Barillot, P.Remeijer, A.Touw, M.van Herk, and J.V.Lebesque, "Definition of the prostate in CT and MRI: A multi-observer study," *International Journal of Radiation Oncology Biology Physics*, vol. 43, pp. 57-66, 1999.

7   R.A.H.Boni, J.A.Boner, J.F.Debatin, F.Trinkler, H.Knonagel, A.Vonhochstetter, U.Helfenstein, and G.P.Krestin, "Optimization of prostate carcinoma staging - comparison of imaging and clinical methods," *Clinical Radiology*, vol. 50, pp. 593-600, 1995.

8   B.Fei, A.Wheaton, Z.Lee, K.Nagano, J.L.Duerk, and D.L.Wilson, "Robust registration algorithm for interventional MRI guidance for thermal ablation of prostate cancer," Proceedings of SPIE Medical Imaging on Visualization, Display, and Image-Guided Procedures, vol. 4319, pp. 53-60, 2001.

9   B.Fei, J.L.Duerk, and D.L.Wilson, "Slice to volume registration for interventional MRI guided treatment of prostate cancer," *IEEE Transactions on Medical Imaging*, (Submitted), 2001.

10 R.J.Hamilton, M.J.Blend, C.A.Pelizzari, B.D.Milliken, and S.Vijayakumar, "Using vascular structure for CT-SPECT registration in the pelvis," *Journal of Nuclear Medicine*, vol. 40, pp. 347-351, 1999.

11 J.M.Balter, H.M.Sandler, K.Lam, R.L.Bree, A.S.Lichter, and R.K.Ten Haken, "Measurement of prostate movement over the course of routine radiotherapy using implanted markers," *International Journal of Radiation Oncology Biology Physics*, vol. 31, pp. 113-118, 1995.

12 V.Narayana, P.L.Roberson, R.J.Winfield, and P.W.McLaughlin, "Impact of ultrasound and computed tomography prostate volume registration on evaluation of permanent prostate implants," *International Journal of Radiation Oncology Biology Physics*, vol. 39, pp. 341-346, 1997.

13 M.van Herk, J.C.de Munck, J.V.Lebesque, S.Muller, C.Rasch, and A.Touw, "Automatic registration of pelvic computed tomography data and magnetic resonance scans including a dull circle method for quantitative accuracy evaluation," *Medical Physics*, vol. 25, pp. 2054-2067, 1998.

14 M.vanHerk, A.Bruce, A.P.G.Kroes, T.Shouman, A.Touw, and J.V.Lebesque, "Quantification of organ motion during conformal radiotherapy of the prostate by three dimensional image registration," *International Journal of Radiation Oncology Biology Physics*, vol. 33, pp. 1311-1320, 1995.

15 A.M.Scott, H.A.Macapinlac, C.R.Divgi, J.J.Zhang, H.Kalaigian, K.Pentlow, S.Hilton, Graham.M.C, G.Sgouros, C.Pelizzari, G.Chen, J.Schlom, S.J.Goldsmith, and S.M.Larson, "Clinical validation of SPECT and CT/MRI image registration in radiolabeled monoclonal-antibody studies of colorectal carcinoma," *Journal of Nuclear Medicine*, vol. 35, pp. 1976-1984, 1994.

16 B.Fei, A.Wheaton, Z.Lee, J.L.Duerk, and D.L.Wilson, "Automatic MR volume registration and its evaluation for the pelvis and prostate," *Physics in Medicine and Biology*, (In Press), 2002.

Proceedings of SPIE Vol. 4684 (2002) @ 2002 SPIE × 1605-7422/01/$15.00
Image Processing, Milan Sonka, J. Michael Fitzpatrick, Editor,

536

17   R.K.Tenhaken, J.D.Forman, D.K.Heimburger, A.Gerhardsson, D.L.Mcshan, C.Pereztamayo, S.L.Schoeppel, and A.S.Lichter, "Treatment planning issues related to prostate movement in response to differential filling of the rectum and bladder," *International Journal of Radiation Oncology Biology Physics*, vol. 20, pp. 1317-1324, 1991.

18   C.R.Meyer, J.L.Boes, B.Kim, P.H.Bland, K.R.Zasadny, P.V.Kison, K.Koral, K.A.Frey, and R.L.Wahl, "Demonstration of accuracy and clinical versatility of mutual information for automatic multimodality image fusion using affine and thin-plate spline warped geometric deformations," *Medical Image Analysis*, vol. 1, pp. 195-206, 1996.

19   M.H.Davis, A.Khotanzad, D.P.Flamig, and S.E.Harms, "A physics-based coordinate transformation for 3-D image matching," *IEEE Transactions on Medical Imaging*, vol. 16, pp. 317-328, 1997.

20   D.Rueckert, L.I.Sonoda, C.Hayes, D.L.G.Hill, M.O.Leach, and D.J.Hawkes, "Nonrigid registration using free-form deformations: Application to breast MR images," *IEEE Transactions on Medical Imaging*, vol. 18, pp. 712-721, 1999.

21   G.E.Christensen, P.Yin, M.W.Vannier, K.S.C.Chao, J.F.Dempsey, and J.F.Williamson, "Large-deformation image registration using fluid landmarks,"Proceedings of 4th IEEE Southwest Symposium on Image Analysis and Interpretation,pp. 269-273, 2000.

22   D.L.Wilson, A.Carrillo, L.Zheng, A.Genc, J.L.Duerk, and J.S.Lewin, "Evaluation of 3D image registration as applied to MR-guided thermal treatment of liver cancer," *Journal of Magnetic Resonance Imaging*, vol. 8, pp. 77-84, 1998.

23   H.Gray, T.Pickering Pick, and R.Howden. *Gray Anatomy: The classic collector's edition.* New York: Gramercy Books, 1977.

24   F.Maes, A.Collignon, D.Vandermeulen, G.Marchal, and P.Suetens, "Multimodality image registration by maximization of mutual information," *IEEE Transactions on Medical Imaging*, vol. 16, pp. 187-198, 1997.

25   W.H.Press, B.P.Flannery, S.A.Teukolsky, and W.T.Vellerling. *Numerical Recipes in C: The Art of Scientific Computing, Second Edition.* New York: Cambridge University Press, 1993.

26   J.Nelder and R.A.Mead, "A simplex method for function minimization," *Computer Journal*, vol. 7, pp. 308-313, 1965.

27   F.L.Bookstein, "Principal warps - thin-plate splines and the decomposition of deformations," *IEEE Transactions on Pattern Analysis and Machine Intelligence*, vol. 11, pp. 567-585, 1989.

28   J.West, J.M.Fitzpatrick, M.Y.Wang, B.M.Dawant, C.R.Maurer, R.M.Kessler, R.J.Maciunas, C.Barillot, D.Lemoine, A.Collignon, F.Maes, P.Suetens, D.Vandermeulen, P.A.vandenElsen, S.Napel, T.S.Sumanaweera, B.Harkness, P.F.Hemler, D.L.G.Hill, D.J.Hawkes, C.Studholme, J.B.A.Maintz, M.A.Viergever, G.Malandain, X.Pennec, M.E.Noz, G.Q.Maguire, M.Pollack, C.A.Pelizzari, R.A.Robb, D.Hanson, and R.P.Woods, "Comparison and evaluation of retrospective intermodality brain image registration techniques," *Journal of Computer Assisted Tomography*, vol. 21, pp. 554-566, 1997.

Robust Registration Method for Interventional MRI-Guided Thermal Ablation of Prostate Cancer

Baowei Fei [a*], Andrew Wheaton [a], Zhenghong Lee [b], Kenichi Nagano [a]
Jeffrey L Duerk [b a], David L Wilson [a b**]

[a] Department of Biomedical Engineering, Case Western Reserve University, OH 44106
[b] Department of Radiology, University Hospitals of Cleveland, OH 44106

ABSTRACT

We are investigating methods to register live-time interventional magnetic resonance imaging (iMRI) slice images with a previously obtained, high resolution MRI image volume. The immediate application is for iMRI-guided treatments of prostate cancer. We created and evaluated a slice-to-volume mutual information registration algorithm for MR images with special features to improve robustness. Features included a multi-resolution approach and automatic restarting to avoid local minima. We acquired 3D volume images from a 1.5 T MRI system and simulated iMRI images. To assess the quality of registration, we calculated 3D displacement on a voxel-by-voxel basis over a volume of interest between slice-to-volume registration and volume-to-volume registrations that were previously shown to be quite accurate. More than 500 registration experiments were performed on MR images of volunteers. The slice-to-volume registration algorithm was very robust for transverse slice images covering the prostate. A 100% success rate was achieved with an acceptance criterion of < 1.0 mm displacement error over the prostate. Our automatic slice-to-volume mutual information registration algorithm is robust and probably sufficiently accurate to aid in the application of iMRI-guided thermal ablation of prostate cancer.

Keywords: Image registration, mutual information, magnetic resonance imaging (MRI), interventional MRI, prostate cancer, minimally invasive treatment, thermal ablation.

1. INTRODUCTION

We are investigating methods for registering slice images obtained on a low field iMRI system to high-resolution MR volumes obtained on a traditional 1.5 T scanner. Immediate applications involve the treatment of prostate cancer as described below. To be useful for an interventional procedure, a registration method must be automatic, accurate, robust, and fast. Currently, we are investigating voxel-based methods because of their ease of use and reported accuracy for other applications.

There are important reasons for this investigation. At our institution, we have extensive experience with minimally invasive treatment of abdominal cancer using iMRI-guided radiofrequency thermal abaltion.[1,2,3] In the case of the prostate, the tumor is not reliably identified with MR. Hence, other functional imaging techniques are required, and potential methods include SPECT antibody imaging and MR spectroscopy. To incorporate the functional images with iMRI tumor targeting, one can first register the low-resolution functional images with a high-resolution MRI. Then by registering the high-resolution MR volume with live-time iMRI acquisitions, we can map both the functional data and high-resolution anatomic information to live-time iMRI images for improved tumor targeting. Image guided biopsies are another important application of iMRI in those cases where the tumor is more readily seen in MR than in CT or ultrasound. [4,5,6]

Previously reported methods on slice to volume registration were mainly applied to the brain. [7,8,9] For the case of volume to volume registration, there are many reports of accurate voxel-based registration in the brain [10,11,12,13] and abdominal and pelvic organs.[1,14]

There are challenges to successful slice to volume registration for the prostate. They include:

1) A single slice, or a few slices, provides much less information than an entire volume for voxel based matching.

2) There is a low signal to noise ratio (SNR) in iMRI because of the emphasis on fast imaging typically with a low field scanner.

3) The pelvic region has irregular boundaries and can deform, unlike the brain to which registration has been most often applied. The prostate might move relative to the pelvic bones due to changes in rectal and bladder filling [15,16] or movement of the patient for treatment.

4) The normal prostate is a small organ that when healthy measures only about 3.8 cm in its widest dimension transversely across the base, [17] and the small prostate is located below a much larger bladder that can change shape and size.

5) The non-homogenous receive coil response can change from one acquisition to next.

We are investigating the use of voxel-based registration for this important application. We created a mutual information algorithm modified to include some features to improve robustness. We performed registration experiments under conditions found with low field open MR imaging.

2. REGISTRATION ALGORITHM

2.1. Similarity Measurement

Two similarity measurements, mutual information (MI) and correlation coefficient (CC), are used in our algorithm. The MI-based registration method is robust and suitable for multi-modality registration, is highly accurate for brain registration,[18] and is suitable for abdominal registration where there can be deformation.[1,14] However, the MI method has the problem of interpolation artifacts, which are especially serious in the case of down sampling in a multi-resolution approach.[19] Fortunately, CC produces fewer locally optimum values than does MI.[20] Our method combines both similarity measures to use the good attributes of each.

MI quantifies interdependency of two variables, such as image gray intensities of image A and B. When A and B are exactly aligned, MI is maximal.[18] We calculate MI using Equations 9 to 12 in the report by Maes et al.[18] CC is a measure of the relation between the statistical distributions of the two images. The absolute of CC has the range of 0 to 1. The higher the absolute value of CC, the more dependence the two images have.[21] We calculate CC using the equation 10 in the report by Rueckert et al.[21]

The algorithm shown in Figure 1 included special features to improve robustness for registration of MR prostate images. In the pseudo-code, the iMRI slice image is the *reference slice,* the slice image extracted from the high-resolution MRI volume is the *reformatted slice,* and the final reformatted slice is the *registered slice.* We used a multi-resolution approach and performed registration from low to high resolution. We used MI at the highest resolution because it gave a more robust solution, and we used CC at the lower resolutions because it gives few local optima and because it calculates faster than MI. We created a method to avoid local minima by restarting the registration with randomly perturbed parameters obtained from a uniform distribution about the very first initial guess. The algorithm restarts until the absolute CC between the reference and registered images is above a threshold or the maximum number of restarts is reached. Absolute CC is used for the restart test rather than MI because it has a well-defined range between 0 and 1 and because it provides an independent check of the MI result.

We used rigid body transformation (three translations and three rotations) and trilinear interpolation as described previously.[1] For optimization, we used the downhill simplex method of Nelder and Mead [22] and the Powell method,[23] but we prefer the former method as described later. Optimization of similarity ends either when the maximum number of calculations is reached (typically 500) or the fractional change in similarity function is smaller than a tolerance (typically 0.001). Our very first initial guess at the lowest resolution is all zeros for the 3 displacements and 3 angles. Based on our

Set an initial reformatted_slice in high-resolution MR volume and CC_thresholds
DO registration **FROM** lowest resolution **TO** highest resolution **BEGIN**
  Resample volume and slice to ¼, ½ or full number of voxels along linear dimension
  Initialize registration_results and number_restarts to zero for restarting registrations
  REPEAT
    Optimize similarity (CC* or MI**) between the reference slice and reformatted_slice
      1. **Transform** the initial reformatted_slice and **interpolate** to get a new reformatted_slice
      2. **Calculate** similarity between the reference slice and the new reformatted_slice
      3. **Repeat** 1 and 2 until meeting function tolerance or maximum iteration number
    Calculate CC between the reference slice and the optimal reformatted_slice
    Record CC, MI** values and transformation parameters to registration_results
    Perturb the initial transformation parameters:
      initial_transformation_parameters = initial_transformation_parameters + random • factor
    Trace the number of restarts: number_restarts = number_restarts + 1
  UNTIL (CC > CC_threshold) **OR** (number_restarts > maximum_restarts)
  Select the final transformation_parameters based on CC* or MI** among registration_results
  Scale the parameters and **assign** to initial_transformation_parameters of next higher resolution
END

Figure 1. Registration algorithm. Capital bold words are computer language.   The outer loop from DO to END gives the multi-resolution approach. The inter loop from REPEAT to UNTIL is for restarting registration. Registration_results and number_restarts are used to store temporary values in the program. See text for details.
* CC is used at lower resolutions, ¼ or ½ number of voxels.
** MI is used only at high resolution, full number of voxels.

experience, we set the CC thresholds at 0.60, 0.65 and 0.70, and the maximum numbers of restarts at 25, 15, and 5, from low to high resolution, respectively.

In Figure 1, there are several differences between low and high resolutions. At lower resolutions, we resample the volume and slice to 1/4 or 1/2 size along the linear dimension. We optimize the CC between reference and reformatted slices to obtain optimal transformation parameters. We record important results such as all CC optimized values, the number of restarts, and the transformation parameters following an optimization. At the end of either of these resolutions, we select the transformation parameters that have the maximum CC value. We then scale the parameters and assign them to be initial values at the next higher resolution. At the highest resolution, MI instead of CC is chosen to be the similarity measurement method, and we select the final transformation parameters with maximum MI instead of CC.

There are several preprocessing details. The input MRI volumes are 256 x 256 x 128 voxels that have an almost isotropic size over a field of view covering the whole pelvis. Isotropic voxels are created using 3D linear interpolation or higher order interpolation methods.[1]

3.   EXPERIMENTAL METHODS

3.1.   Data Acquisition

All MRI volumes were acquired using a 1.5 T Siemens MRI system (Magnetom Symphony, Siemens Medical Systems in Erlangen, Germany). An 8-element phased array body coil was used to ensure coverage of the prostate with a uniform sensitivity. Typically two anterior and two posterior elements were enabled for signal acquisition. We used a 3D PSIF sequence with 9.4/5.0/60 (TR/TE/flip) yields 160 x 256 x 128 voxels over a 219 x 350 x 192-mm rectangular FOV and 1.37 x 1.37 x 1.5-mm voxels oriented to give the highest resolution for transverse slices. There is over-sampling at 31% in

the slice direction to reduce aliasing artifacts. This sequence gave excellent image contrast for the prostate and its surroundings.

3.2. Creation of Images for Testing

To test the ability of the slice-to-volume (SV) registration, we obtained high-resolution MRI volumes and simulated iMRI images by adding noise and receive coil inhomogeneity. We compared SV registration to volume-to-volume (VV) registration results.

We simulated iMRI slice images. We averaged 3 slices together to simulate an iMRI 4-mm thick slice. We used a homogenous phantom to measure the SNR of iMRI images on our 0.2 T open magnet system (Magnetom Open, Siemens Medical Systems in Erlangen, Germany). We used simulated iMRI images to test the dependence of registration on noise levels. Figure 2 shows the simulated iMRI slice images.

3.3. Registration Experiments

We acquired high-resolution MR volumes from three volunteers. Each has two pairs of volumes for registration. We extracted three slices from one volume and used these slices to simulate an iMRI image. We tested multiple ways to acquire slices for SV registration. First, we used transverse, sagittal and coronal slices for registration, respectively. The objective was to optimize the slice orientation for image guidance. Second, we extracted slices from different positions such as centered at the prostate, and above and below the prostate by 35 mm. This experiment was performed to investigate the range for reliable slice registration. Third, we tested the dependence of the registration on noise levels.
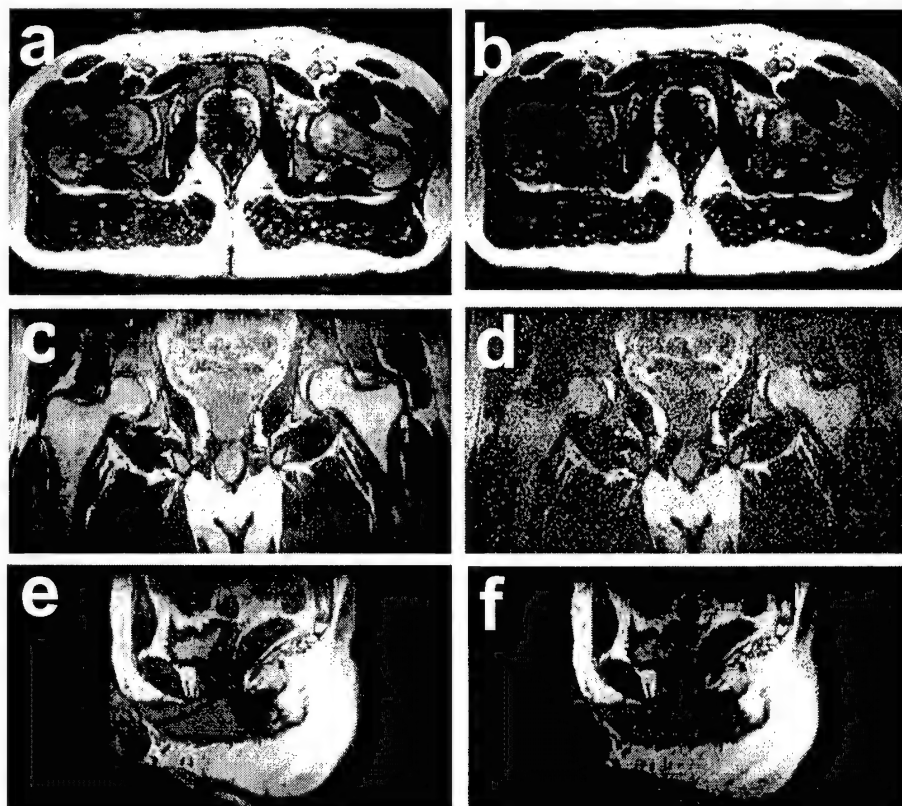

Figure 2. Simulated iMRI images. Images on the left, (a), (c) and (e), are the high-resolution MR images in transverse, coronal and sagittal planes, respectively. Images on the right are corresponding simulated iMRI images with SNR = 8. The images are of volunteer V2.
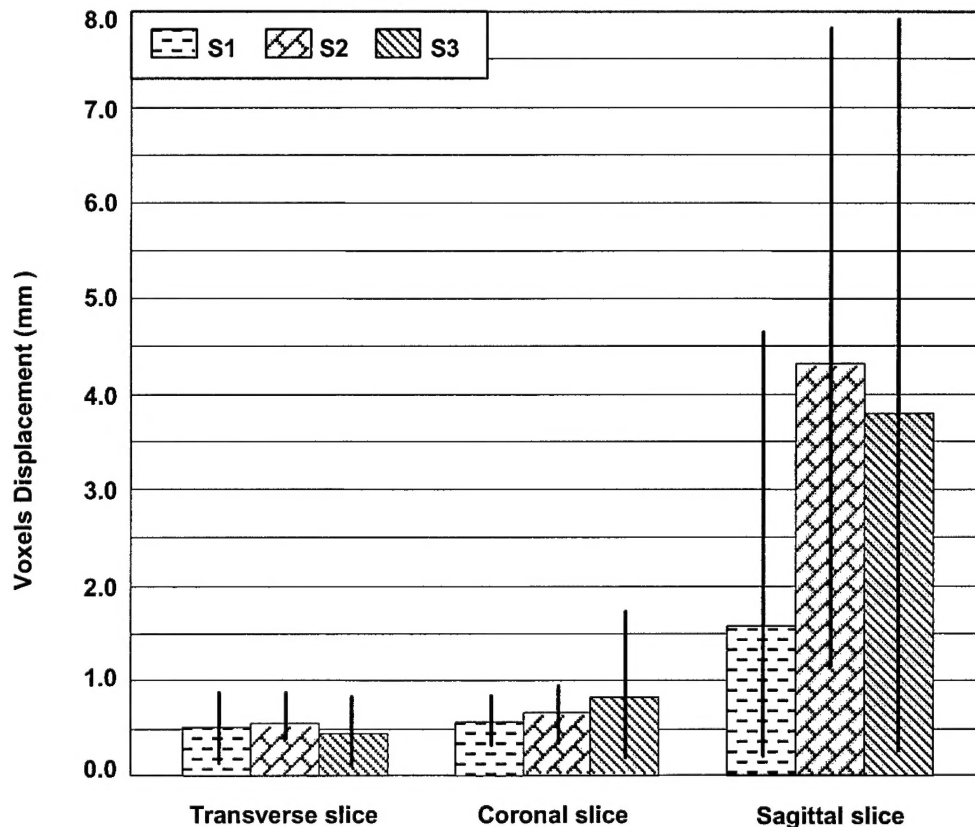
Figure 3. SV registration using slices at different orientations. The error metric is voxel displacement between the SV and VV results. Plotted are mean errors as well as maximums and minimums that show the spread of the data. S1, S2, and S3 refer to volunteers. Each volunteer has two volume pairs. For each pair, five transverse slices centered at the prostate were extracted from one volume and registered to the other. The same procedures were applied to coronal and sagittal slices.

3.4.   Evaluation Methods

To test the program, we transformed a reference volume using known parameters to obtain a *digital phantom*. We extracted slices from the digital phantom and registered them to the reference volume. Because the transformation was known, we could validate the performance of the software.

Our standard evaluation method was to compare SV and VV registration. The VV registration accuracy was previously evaluated to be on the order of one voxel (1.37 mm) [14]. We defined a volume of interest (VOI) just covering the prostate and applied the transformations obtained by VV and SV registrations to voxels within the VOI. We calculated the 3D displacement on a voxel-by-voxel basis over the two transformed VOIs. The mean voxel displacement was used as our metric of SV registration error.

4.   RESULTS AND DISCUSSIONS

More than 300 SV registration experiments were performed under a variety of conditions expected for applications in iMRI-guided treatment of the prostate. First, we report the effect of slice orientation and position on registration. Second, we describe the results associated with image noise. At the end, we describe some details on the algorithm implementation.
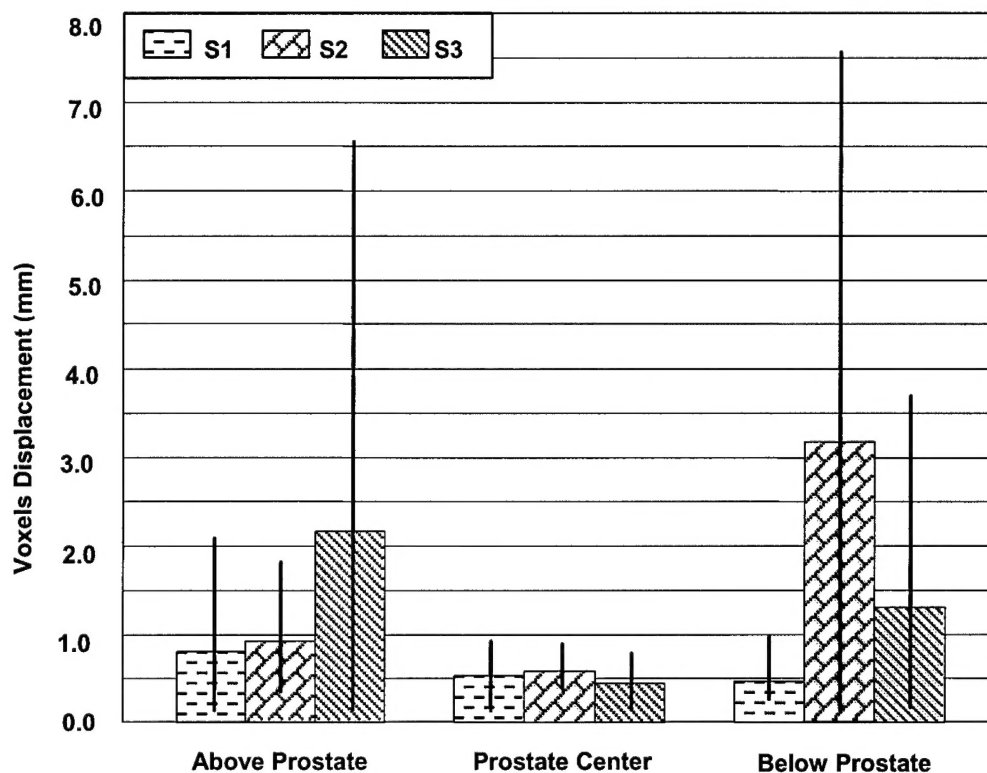
Figure 4. SV registration using transverse slices at different positions. Relative to the prostate, five iMRI slices each were extracted near its center, ≈ 35 mm above its center, and ≈ 35 mm below its center. Other details are given in Figure 3. Slices at the prostate center work best.

4.1. Slice Orientation and Position

Figure 3 shows registration results for single slices oriented in different directions. All slices intersect the prostate. Transverse slices give the lowest average error across the three volunteers, 0.39 ± 0.19 mm. The reason for this result is that a transverse slice contains more anatomical structures than do slices in other orientations. A transverse slice also excludes the bladder and portions of the rectum that can deform and create inconsistent matches for registration. The following analyses are all based on transverse slices.

Figure 4 shows registration results for transverse slices at different heights relative to the prostate. Slices centered on the prostate produced the best results with the displacement error always being less than 1.0 mm. On the one hand, slices centered at the prostate are good because they include an abundance of bony structures that provide adequate information for registration. Slices above the prostate include the bladder, which can deform and stress the registration algorithm. Slices below the prostate mainly contain fatty regions from the hips that can also deform and have less information for registration.

4.2. Noise Level and Robustness

We performed preliminary experiments using different noise levels in the simulated iMRI images. When SNR values were 30, 15 and 5, registration errors were always less than 0.9 mm for three volunteers in all conditions. For more than 200 registration experiments, the algorithm was very robust and never failed even with these large noise values. We believe the algorithm to be insensitive to noise.

4.3. Program Implementation

We implemented the registration program using IDL (Interactive Data Language, Research System Inc., Boulder, CO.). The time for an SV registration, typically 40 to 90 sec on a Pentium III, 800 MHz CPU, with 512 Mbytes of memory, could

be improved using optimized C code rather than IDL. The simplex optimization method worked faster than the Powell method in our implementation. This result is contrary to our previous experience.[1] We think that this phenomenon occurred because the Powell method depends on the order that parameters are optimized. Because we do not require preprocessing to determine initial values, there are no clear choices for which parameters to optimize first. Each call to the Simplex optimization for restarts or optimization at a finer resolution resulted in 50 to 105 similarity evaluations before the tolerance value (0.001) was reached.

The restarting and multi-resolution features are important. Using normal clinical transverse images covering the prostate, the algorithm always gave very nearly the same transformation parameters (less than 0.01 voxels and 0.01 degrees) using a wide variety of initial guesses. The multi-resolution approach enabled the program to get close to the final value quickly because of the reduced number of calculations. Althought serious motion artifacts may stress the registration, our experience is that these can be controlled with appropriate subject compliance and with the proper acquisition technique. Organ motion and deformation from one acquisition to the next are other factors that can affect the performance of the algorithm, especially when subject is in a different position or there is rectal and bladder filling. [14] Again, our experience is that these errors can be controlled. [14]

5. CONCLUSION

The automatic slice-to-volume mutual information registration algorithm was quite robust for transverse slice images covering the prostate. There were no registration failures in over 200 experiments on MRI images without obvious artifacts. The registration error of < 1.0 mm should be sufficiently accurate to aid in the application of iMRI-guided minimal invasive thermal ablation of prostate cancer. We are beginning to explore these applications in clinical procedures and animal experiments.

ACKNOWLEDGEMENTS

REFERENCES

1. A. Carrillo, J. L. Duerk, J. S. Lewin, and D. L. Wilson, "Semiautomatic 3-D image registration as applied to interventional MRI liver cancer treatment," *IEEE Trans. Med. Imag.*, vol. 19, no. 3, pp. 175-185, Mar. 2000
2. J. S. Lewin, C. F. Connell, J. L. Duerk, Y. C. Chung, M. E. Clampitt, J. Spisak, G. S. Gazelle, and J. R. Haaga, "Interactive MRI-guided radiofrequency interstitial thermal ablation of abdominal tumors: clinical trial for evaluation of safety and feasibility," *JMRI*, vol. 8, no.1, pp. 40-47, Jan. 1998.
3. E. M. Merkle, J. R. Shonk, J. L. Duerk, G. H. Jacobs, and J. S. Lewin, "MR-guided RF thermal ablation of the kidney in a porcine model," *Am. J. Roentgenol.*, vol.173, no. 3, pp. 645-651, Sep, 1999.
4. K. Kagawa, W.R. Lee, T. E. Schultheiss, M. A. Hunt, A. H. Shaer, G. E. Hanks, "Initial clinical assessment of CT-MRI image fusion software in localization of the prostate for 3D conformal radiation therapy," *Int. J. Radiation Oncology Biol. Phys.*, vol. 38, no. 2, pp. 319-325, 1997.
5. M. Milosevic, A. Voruganti, R. Blend, H. Alasti, P. Warde, M. McLean, P. Catton, C. Catton, M. Gospodarowicz, "Magnetic resonance imaging (MRI) for localization of the prostatic apex: comparison to computed tomography (CT) and urethrography," *Radiotherapy and Oncology,* vol. 47, no.3, pp. 277-284, Jun. 1998.
6. R.A.H. Boni, J.A. Boner, J.F. Debatin, F. Trinkler, H. Knonagel, A. Vonhochstetter, U. Helfenstein, G.P. Krestin, "Optimization of prostate carcinoma staging - comparison of imaging and clinical methods," *Clinical Radiology*, vol. 50, no. 9, pp. 593-600, Sep. 1995
7. B. Kim, J.L. Boes, P.H. Bland, T.L. Chenevert, C.R. Meyer, "Motion correction in fMRI via registration of individual slices into an anatomical volume," *Magnetic Resonance in Medicine*, vol. 41, pp. 964-972, 1999.

8. T.S. Kim, M. Singh, W. Sungkarat, C. Zarow, H. Chui, "Automatic registration of postmortem brain slices to MRI reference volume," *IEEE Trans. Nuclear Science*, vol. 47, no. 4, Aug. 2000.

9. J. Zhengping, P.H. Mowforth, "Mapping between MR brain images and a voxel model," *Medical Informatics*, vol. 16, no. 2, pp. 183-193, Apr-Jun., 1991

10. D.L.G. Hill, L.A. Langsaeter, P.N. Poynter-Smith, C.L. Emery, P.E. Summers, S.F. Keevil, J.P.M. Pracy, R. Walsh, D.J. Hawkers, M.J. Gleeson, "Feasibility study of magnetic resonance image-guided intranasal flexible miroendoscopy," *Computer Aided Surgery*, vol. 2, pp. 264-275, 1997.

11. P. A. Freeborough, R. P. Woods, and N. C. Fox, "Accurate registration for 3D MR brain images and its application to visualizing change in neurodegenerative disorders," *J CAT*, vol. 20, no. 6, pp. 1012-1022, 1996.

12. M. Holden, D. L. G. Hill, E. R. E. Denton, J. M. Jarosz, T. C. S. Cox, T. Rohlfing, J. Goodey, D. J. Hawkes, "Voxel similarity measures for 3-D serial MR brain image registration," *IEEE Trans. Med. Imag.*, vol. 19, no. 2, pp. 94 – 102, Feb. 2000

13. R.W. Cox, A. Jesmanowicz, "Real-time 3D image registration for functional MRI," *Magnetic Resonance in Medicine*, vol. 42, pp. 1014-1018, 1999.

14. B.W. Fei, A. Wheaton, Z. Lee, J.L. Duerk, and D.L. Wilson, "Registration of MR images of the prostate," Submitted to *IEEE Trans. Med. Imag.*, Jan. 2001.

15. M.V. Herk, A. Bruce, A.P.G. Kroes, T. Shouman, A. Touw, J.V. Lebesque, "Quantification of organ motion during conformal radiotherapy of the prostate by three dimensional image registration," *Int. J. Radiation Oncology Biol. Phys.*, vol. 33, no. 5, pp. 1311-1320, 1995.

16. R.K. Ten Haken, J.D. Forman, D.K. Heimburger, A. Gerhardsson, D.L. McShan, C. Perez Tamayo, S.L. Schoeppel, A.S. Litchter, "Treatment planning issues related to prostate movement in response to differential filling of the rectum and bladder," *Int. J. Radiation Oncology Biol. Phys.*, vol. 20, no. 6, pp. 1317-1324, Jun. 1991.

17. H. Gray, T. Pickering Pick, R. Howden, "Gray Anatomy: The classic collector's edition," New York: Gramercy Books, 1977, p. 1010.

18. F. Maes, A. Collignon, D. Vandermeulen, G. Marchal, P. Suetens, "Multimodality image registration by maximization of mutual information," *IEEE Trans. Med. Imag.*, vol. 16, no.2, pp. 187 –198, April 1997

19. J.P.W. Pluim, J.B.A. Maintz, M.A. Viergever, "Interpolation artifacts in mutual information-based image registration," *Computer vision and image understanding*, vol. 77, no.2, pp. 211-232, Feb. 2000

20. B.W. Fei, Z. Lee, J.L. Duerk, and D.L. Wilson, "Slice to volume registration as applied to interventional MRI-guided treatment of prostate cancer," In preparation.

21. D. Rueckert, L. I. Sonoda, C. Hayes, D. L. G. Hill, M.O. Leach, D. J. Hawkes, "Nonrigid registration using free-form deformations: application to breast MR images," *IEEE Trans. Med. Imag.*, vol. 18, no. 8, pp. 712 –721, 1999

22. J. Nelder and R.A. Mead, "A simplex method for function minimization," *Comp. J.*, vol. 7, pp. 308-313, 1965

23. M. J. D. Powell, "An iterative method for finding stationary values of a function of several variables," *Comp. J.*, vol. 5, pp. 147-151, 1962